Catalytic Conversion of Bio-oil to Fuel for Transportation

Mortensen, Peter Mølgaard

Publication date:
2013

Document Version
Publisher's PDF, also known as Version of record

Catalytic Conversion of Bio-oil to Fuel for Transportation

Ph.D. Thesis
Denmark, 2010–2013

Written by

Peter Mølgaard Mortensen

Combustion and Harmful Emission Control
Department of Chemical and Biochemical Engineering
Technical University of Denmark

Supervised by

Professor Anker Degn Jensen
Professor Jan-Dierk Grunwaldt
and Associate Professor Peter Arendt Jensen

Abstract

The incitement for decreasing the modern society's dependency on fossil based fuel and energy is both environmentally and politically driven. Development of bio-fuels could be part of the future solution. The combination of flash pyrolysis and catalytic upgrading of the produced bio-oil has been identified as a prospective route to bio-fuels. The upgrading is most favorably done by hydrodeoxygenation (HDO), producing bio-fuels at a quality equivalent to conventional fossil fuels. The topic of this Ph.D. thesis has been the development of active and stable catalysts for this reaction.

In the search for new HDO catalyst 23 catalytic systems were screened in a batch reactor at 100 bar H_2 and 275 °C with phenol as bio-oil model compound, comparing different combinations of active phase and support. Among the tested catalysts, reduced metal catalysts displayed the highest activity, with the apparent order of activity for some of the most active catalysts being: $Ni/ZrO_2 > Ru/C > Ni/Al_2O_3 > Ni/SiO_2 \gg Pd/C > Pt/C$. Catalysts should be effective in both hydrogenation and deoxygenation to effectively convert phenol at the applied conditions. Ni/SiO_2 was further investigated by varying the Ni particle size, showing that deoxygenation was linked to low coordinated sites (e.g. steps and corners), favored at small nickel particles. Hydrogenation was also influenced by particle size, where the reaction was hindered at small particles due to competitive adsorption of alcohols on the nickel sites. However, the support was found to have the largest effect on the hydrogenation rate. A good support should have high availability of Lewis acid sites. Overall Ni/ZrO_2 prepared with small (<10 nm) nickel particles was found as a very prospective catalyst for HDO, displaying both good hydrogenation and deoxygenation activity.

With Ni/ZrO_2 identified as a prospective HDO catalyst, the stability and resistance toward bio-oil impurities was investigated in a high pressure gas and liquid continuous flow setup with bio-oil model compounds and compared to the more traditional hydrotreating catalysts Mo_2C/ZrO_2 and Ni-MoS_2/ZrO_2. The investigated bio-oil impurities included water (up to 30 wt% in bio-oil), chlorine, potassium and sulfur. Of the tested catalysts, Ni/ZrO_2 displayed the highest activity, requiring only 250 °C for performing HDO of aromatic compounds, followed by Ni-MoS_2/ZrO_2 (requiring 280 °C), and then Mo_2C/ZrO_2, which required temperatures >320 °C.

Ni/ZrO_2 and Ni-MoS_2/ZrO_2 displayed good stability for HDO of pure model compounds over periods of more than 100 h. However, Ni-MoS_2/ZrO_2 required a significant co-feed of sulfur (as dimethyl disulfide or H_2S) to remain stable, as oxidation of the sulfide phase took place in the absence of sulfur. Part of the sulfur was

incorporated in the liquid product as thiols if the residence time was not sufficiently high.

Mo_2C/ZrO_2 displayed poor stability during HDO of a mixture of phenol and 1-octanol at 300 °C, loosing roughly 50% activity over 74 h of operation. The loss of activity was found to be due to oxidation of the catalyst by the water formed from the HDO reaction. This was evidenced in a separate experiment co-feeding water, where all activity was lost over only 12 h of operation, and further verified by thermodynamic calculations showing the affinity for oxidation of Mo_2C with water at the given operating conditions.

Ni-MoS_2/ZrO_2 was also found to be unstable in the presence of water if not co-fed with sufficient sulfur. The best stability of the catalyst was obtained when co-feeding sulfur in a H_2O/H_2S ratio of 9.4, but in this case still 36% loss of activity occurred over 94 h of operation. This loss of activity was probably linked to the loss of edge sulfur atoms during exposure to water.

Potassium was found to severely deactivate both Ni/ZrO_2 and Ni-MoS_2/ZrO_2, as the activity of the catalyst decreased by 88% and 94%, respectively, when impregnated with potassium (in a stoichiometric ratio between active metal and potassium) compared to the un-poisoned cases. Chlorine was inhibiting both catalysts but the activity could be regained when removing it from the feed. Sulfur was found as the overall worst poison for Ni/ZrO_2, as this transformed the nickel to a NiS_x phase leading to fast and complete loss of activity. This is in contrast to the Ni-MoS_2/ZrO_2 catalyst where sulfur was a requirement to maintain the activity.

Overall, Ni-MoS_2/ZrO_2 displayed the best resistance, but the somewhat high temperature requirement and heavy dependency of a sulfur source are drawbacks. Ni/ZrO_2 was in contrast more easily poisoned by especially sulfur, but is an attractive catalyst as it catalyzes HDO at relative low temperatures. However, in general a lot of work is still needed in catalyst development.

Resumé

Incitamentet for at sænke det moderne samfunds afhængighed af fossile brændstoffer og energi er både miljømæssigt og politisk drevet. Bio-brændstoffer kan være en del af den fremtidige løsning. Kombinationen af flash pyrolyse og katalytisk opgradering af den producerede bio-olie er blevet identificeret som en lovende vej til bio-brændstoffer. Hydrodeoxygenering (HDO) er den mest favorable opgraderingsproces, da bio-brændstoffer kan produceres i en kvalitet der svarer til den af konventionelle fossile brændstoffer. Dette Ph.D. projekt omhandler udvikling af aktive og stabile katalysatorer til denne reaktion.

For at finde nye HDO katalysatorer blev 23 katalytiske systemer undersøgt i en batchreaktor ved 100 bar H_2 og 275 °C med phenol som bio-olie modelkomponent, hvor forskellige kombinationer af aktivfase og bærer blev sammenlignet. Imellem disse katalysatorer var det de reducerede metal katalysatorer der havde den højeste aktivitet, med en aktivitetsrækkefølge for de mest aktive katalysatorer som følger: $Ni/ZrO_2 > Ru/C > Ni/Al_2O_3 > Ni/SiO_2 \gg Pd/C > Pt/C$. Katalysatorerne skulle være effektive til både hydrogenering og deoxygenering for effektivt at omdanne phenol ved de anvendte betingelser. Ni/SiO_2 blev yderligere undersøgt med varierende Ni partikel størrelse, hvilket viste at deoxygenering foregik på nikkel sites med lavt koordinationstal (dvs. trin eller hjørne sites) som var mest udbredt på små nikkel nano-partikler. Hydrogeneringen var også påvirket af partikel størrelsen, da reaktionen blev forhindret på små nano-partikler på grund af konkurrerende adsorption af alkoholer på nikkel sites. Hydrogeneringen var imidlertid mere påvirket af den anvendte bærer, hvor en god bærer skulle have høj tilgængelighed af Lewis syre-sites. Overordnet var Ni/ZrO_2 fremstillet med små (<10 nm) nikkel nano-partikler en lovende HDO katalysator der udviste både god hydrogenering- og deoxygenering-aktivitet.

Stabiliteten og modstandsdygtigheden mod bio-olie urenheder blev undersøgt i en højtryks gas og væske kontinuert opstilling med Ni/ZrO_2 som katalysator og sammenlignet med de mere traditionelle hydrogenerings katalysatorer, Mo_2C/ZrO_2 og Ni-MoS_2/ZrO_2. Vand (op imod 30 wt% i bio-olie), chlor, kalium og svovl blev undersøgt som bio-olie urenheder. Ni/ZrO_2 udviste den højeste aktivitet, da denne kunne udføre HDO af aromatiske stoffer ved kun 250 °C. Til sammenligning krævede Ni-MoS_2/ZrO_2 en temperatur på 280 °C og Mo_2C/ZrO_2 krævede temperaturer >320 °C.

Ni/ZrO_2 og Ni-MoS_2/ZrO_2 udviste god stabilitet ved HDO af rene modelkomponenter igennem mere end 100 h drift. God stabilitet af Ni-MoS_2/ZrO_2 krævede imidlertid en høj koncentration af svovl (enten som dimethyldisulfid eller H_2S) i fø-

den for at undgå oxidation af sulfidfasen. Svovl i føden betød dog at produktet også ville indeholde thioler hvis opholdstiden i reaktoren ikke var tilstrækkelig lang.

Stabiliteten for HDO af en blanding af phenol i 1-octanol over en Mo_2C/ZrO_2 katalysator var lav, da rundt regnet 50% af aktiviteten blev tabt i løbet af 74 h drift. Deaktiveringen var forårsaget af oxidation af katalysatoren med det vand der blev dannet under HDO reaktionen. Dette blev klargjort i et separat eksperiment, hvor ekstra føde med vand medførte komplet tab af aktivitet for Mo_2C/ZrO_2 katalysatoren i løbet af 12 h drift. Termodynamiske beregninger underbyggede yderligere at der er en drivende kraft for oxidation af Mo_2C med vand ved de givne drift betingelser.

Vand påvirkede også stabiliteten af Ni-MoS_2/ZrO_2, hvis der ikke var tilstrækkelig svovl i føden. Den bedste stabilitet blev opnået ved en føde rate på 9.4 H_2O/H_2S, men dette betød stadig et tab på 36% aktivitet over 94 h drift. Denne deaktivering var højst sandsynligt et resultat af tab af kant svovl-atomer ved vandeksponering.

Eksponering af både Ni/ZrO_2 og Ni-MoS_2/ZrO_2 til kalium medførte markant deaktivering. Aktiviteten faldt med respektive 88% og 94% efter imprægnering af katalysatorerne med kalium (i støkiometrisk forhold mellem aktivt metal og kalium), sammenlignet med uforgiftede eksperimenter. Chlor inhiberede begge katalysatorer, men aktiviteten kunne genvindes ved at fjerne chlor fra føden. Svovl var den værste urenhed for Ni/ZrO_2, da dette medførte en omdannelse af metallisk nikkel til en NiS_x fase og derved hurtig og fuldstændig tab af aktivitet. Dette var i kontrast til Ni-MoS_2/ZrO_2 katalysatoren, hvor svovl var en nødvendighed for at opretholde aktivitet.

For at opsummere havde Ni-MoS_2/ZrO_2 den bedste modstandsdygtighed overfor bio-olie urenheder, men den relativt høje påkrævede temperatur og afhængigheden af svovl i føden er markante svagheder. I modsætning var modstandsdygtigheden af Ni/ZrO_2 mindre, men katalysatoren var attraktiv da HDO reaktionen kunne forløbe effektivt ved relativt lave temperaturer. Meget arbejde er dog stadig nødvendigt i udviklingen af HDO katalysatorer.

Preface & Acknowledgment

Kgs. Lyngby, Denmark, December 2013

This thesis has been written as a part of the Ph.D. project by Peter Mølgaard Mortensen carried out in the period from August 2010 to December 2013 at the Technical University of Denmark (DTU) at the Department of Chemical and Biochemical Engineering (KT) in the research group Combustion and Harmful Emission Control (CHEC). Professor Anker Degn Jensen from KT has been main supervisor throughout the project, with Associate Professor Peter Arendt Jensen also from KT and Professor Jan-Dierk Grunwaldt from Institute for Chemical Technology and Polymer Chemistry at Karlsruhe Institute of Technology (KIT) as co-supervisors.

I greatly acknowledge funding from DTU and The Catalysis for Sustainable Energy (CASE) initiative, funded by the Danish Ministry of Science, Technology and Innovation.

I owe a lot of gratitude to all the people whom have been involved and influenced the progress of this project and my personal development as a researcher and a person in the past three years. First of all I would like to thank Anker Degn Jensen for being my primary and competent feedback throughout this project. Your door has always been open and you have always taken the time to discuss issues in all sizes, ranging from professional to personal. You have been as much a friend as an employer to me in these last three years, and for this I am you very grateful. Big thanks also goes to Peter Arendt Jensen and Jan-Dierk Grunwaldt, I cherished your opinion on my work and your often alternative view on my work helped shape this work to be much more thorough.

Ph. D. student Diego Gardini from Center of Electron Nanoscopy (CEN) at DTU joined the project in the autumn 2012. His project intended to support the work on development of hydrodeoxygenation (HDO) catalysts, but with emphasis on catalyst characterization. I appreciate your eager in learning and understanding the challenges of this project.

Senior Researcher Thomas Willum Hansen and Professor Jakob Birkedal Wagner suggested a collaborate project between CEN and KT in modeling their ETEM with CFD. I appreciate this opportunity, and I think we ended up with a nice output as a side project during this Ph.D. Additionally I would like to thank Thomas for his assistance in performing TEM analysis on some of my catalysts in the early stage of this project.

Hudson Wallace Pereira de Carvalho from KIT performed XAS analysis of some of the catalysts and also made the subsequent analysis, I appreciate the enthusiasm you displayed in our collaboration.

Sterlin Hansraj, Agnete Gørløv, Andreas Hofer, Christian Evald Hessel, Kyle Hancock, and Magnus Stummann, supervising you helped me shape my experiments and the experimental setups to where they are today. Despite your results have not found way to this thesis, your refreshing points of view were very much appreciated and I enjoyed the informal discussion I had with many of you.

During the daily struggles with experimental facilities, analytical equipment, and similar I would like to point out Anders Tiedje's patient and pleasant assistance in any issue, small or large. You were an irreplaceable help in this work and a phenomenal support in the building of the continuous flow setup (POC). Also Mette Larsen, Nikolaj Vinterberg Nissen, and Emine Yüksel Coskun deserve a notice for their good spirit and always helpful attitude. Especially Mette's works is cherished for her help in administrating my many and sometimes foul smelling chemicals.

The workshop at KT deserves special gratitude for their assistance in building the POC. I would like to highlight the pleasant nature of Jens Henry Poulsen and his energetic work in the construction of the POC.

In the past three years my Ph.D. project has been a large part of my life, but fortunately I have a lot of friends to help me remember the other fun aspects of life. First of all thanks to the more social part of CHEC: Rasmus, Claus, Martin, Kristian, Xiao, Jakob, Joachim, Thomas, and Dominik, you made the daily work more fun and especially the daily lunch was a nice break in the sometimes busy days. Also the Staff club at KT deserves to be mentioned: Lars, Karin, Claus, Peter, and Peter, I enjoyed our meetings and the always fun spirit.

Jon, Nicklas, and Philip, you are and have been my daily core of friends for as long as I can remember. You have supported me the past eight years at DTU and always tried to listen interested when I talked about my education and work, despite I often had the feeling that you did not have a clue about the context. Bugge, G, Gordon, Jimmy, Kristian, Kåre, and Mads deserve gratitude for all the good times we shared and hopefully will share in the future. Also Sebastian should be mentioned, despite you left my life way to early you still was a big part of it until the very last moment. We should have shared a future of experiences together as friends, but unfortunately life did not intend it this way. May you ever rest in peace my dear friend.

My Morther, Father, and Brother have supported me all the way in my life. I am forever grateful to be of such a warm family.

Last but not least heartfelt thanks are directed toward my two loved girls: Louise and Astrid. Louise, you have been my solid support in all periods of this project. You never got tired of listening to my often nerdy talk about work and supported me in my enthusiasm. Your love is one of the most important things in my life and I hope it will never fade.

I hope I have not forgotten anybody, if so it was not ill intended.

Sincerely,
Peter Mølgaard Mortensen

List of Publications & Conference Contributions

Articles Published in Peer-reviewed Journals

Peter M. Mortensen, Jan-Dierk Grunwaldt, Peter A. Jensen, Kim G. Knudsen, and Anker D. Jensen, *"A Review of Catalytic Upgrading of Bio-oil to Engine Fuels"*, *Applied Catalalysis A: General* **407** (2011) 1-19

Peter M. Mortensen, Jan-Dierk Grunwaldt, Peter A. Jensen, and Anker D. Jensen, *"Screening of Catalysts for Hydrodeoxygenation of Phenol as a Model Compound for Bio-oil"*, *ACS Catalalysis* **3** (2013) 1774-1785

Articles Submitted to Peer-reviewed Journals

Peter M. Mortensen, Jan-Dierk Grunwaldt, Peter A. Jensen, and Anker D. Jensen, *"Structure Sensitivity of Nickel Based Catalysts for the Hydrodeoxygenation of Phenol"*, Submitted to *ChemCatChem*, 2013

Peter M. Mortensen, Diego Gardini, Hudson W. P. de Carvalho, Christian D. Damsgaard, Jan-Dierk Grunwaldt, Peter A. Jensen, Jakob B. Wagner, and Anker D. Jensen, *"Stability and Resistance of Nickel Catalysts for Hydrodeoxygenation: Effects of Sulfur, Potassium, and Chlorine in the Feed"*, Submitted to Applied Catalysis B: Environmental, 2014

Peter M. Mortensen, Thomas W. Hansen, Jakob B. Wagner, and Anker D. Jensen, *"Modeling of Temperature Profiles in an Environmental Transmission Electron Microscope using Computational Fluid Dynamics"*, Submitted to Ultramicroscopy, 2014

Articles in Preparation

Peter M. Mortensen, Hudson W. P. de Carvalho, Jan-Dierk Grunwaldt, Peter A. Jensen, and Anker D. Jensen, *"Activity and Stability of Mo_2C as Catalyst for Hydrodeoxygenation of Bio-oil"*, To be submitted, 2014

Peter M. Mortensen, Diego Gardini, Christian D. Damsgaard, Jan-Dierk Grunwaldt, Peter A. Jensen, Jakob B. Wagner, Anker D. Jensen, *"Inhibition and Deactivation of Ni-MoS_2 by Bio-oil Impurities During Hydrodeoxygenation"*, To be submitted, 2014

Oral Conference Contributions

Peter M. Mortensen, Jan-Dierk Grunwaldt, Peter A. Jensen, and Anker D. Jensen, *"Catalytic Upgrading of Bio-oil"*, Presented at: Energy and Materials from the Sun, 2011, Kerkrade, Netherlands

Peter M. Mortensen, Jan-Dierk Grunwaldt, Peter A. Jensen, and Anker D. Jensen, *"Mechanistic Insight in Hydrodeoxygenation on Nickel Based Catalysts"*, Presented at: 23rd North American Catalysis Society Meeting, 2013, Louisville, Kentucky, United States of America

Peter M. Mortensen, Jan-Dierk Grunwaldt, Peter A. Jensen, and Anker D. Jensen, *"Stability of Nickel-Based Catalysts for Hydrodeoxygenation"*, Presented at: Second International Conference Catalysis for Renewable Sources: Fuel, Energy, Chemicals, 2013, Lund, Sweden

Discussion Symposia Conference Contributions

Peter M. Mortensen, Jan-Dierk Grunwaldt, Peter A. Jensen, and Anker D. Jensen, *"Stability of Nickel-Based Catalysts for Hydrodeoxygenation"*, Presented at: Europacat XI, 2013, Lyon, France

Poster Conference Contributions

Peter M. Mortensen, Jan-Dierk Grunwaldt, Peter A. Jensen, and Anker D. Jensen, *"Screening of Catalysts for Bio-oil Hydrodeoxygenation"*, Presented at: 15th International Congress on Catalysis, 2012, Munich, Germany

Charlotte V. Ovesen, Klas J. Andersson, Peter M. Mortensen, Brian K. Olsen, Anker D. Jensen, and Martin S. Skjøth-Rasmussen, *"Mechanistic and Kinetic Aspects of Steam Reforming of Ethane"*, Presented at: 15th International Congress on Catalysis, 2012, Munich, Germany

Peter M. Mortensen, Jan-Dierk Grunwaldt, Peter A. Jensen, and Anker D. Jensen, *"Stability of Nickel-Based Catalysts for Hydrodeoxygenation"*, Presented at: Europacat XI, 2013, Lyon, France

Peter M. Mortensen, Jan-Dierk Grunwaldt, Peter A. Jensen, and Anker D. Jensen, *"Stability and Resistance of Ni/ZrO_2 for Guiaicol Hydrodeoxygenation: Effect of Sulfur, Chlorine, and Alkali in the Feed"*, Presented at: DTU International Energy Conference, 2013, Kgs. Lyngby, Denmark

Other Publications/Documents

Peter M. Mortensen and Rasmus Trane, *"Affald fra Marken bliver CO_2-neutrale Brændstoffer"*, *Energi på Lager*, Addition to Chapter 4: "Affald på Tanken", `http://www.energi.case.dtu.dk/Biomasse/Laer-mere_kap4`, DTU, (2011)

Peter M. Mortensen and Anker D. Jensen, *"Valorization of Biomass to Chemicals and Fuels: Input to DONG Roadmap"*, *Technical Report*, Department of Chemical and Biochemical Engineering, CHEC, DTU (2012)

Peter M. Mortensen, Rasmus Trane-Restrup, and Anders Tiedje, *"Pyrolysis Oil Converter: High Pressure Liquid and Gas Flow Reactor System"*, *Technical Report 045-28 POC*, Department of Chemical and Biochemical Engineering, CHEC, DTU (2013)

Other Articles Published in Peer-reviewed Journals

Jakob M. Christensen, Peter M. Mortensen, Rasmus Trane, Peter A. Jensen, and Anker D. Jensen, *"Effects of H_2S and Process Conditions in the Synthesis of Mixed Alcohols from Syngas over Alkali Promoted Cobalt-molybdenum Sulfide"*, *Applied Catalalysis A: General* **366** (2009) 29-43

Lars Jensen, Peter M. Mortensen, Rasmus Trane, Pernille Harris, and Rolf W. Berg, *"Reaction Kinetics of Acetone Peroxide Formation and Structure Investigations Using Raman Spectroscopy and X-ray Diffraction"*, *Applied Spectroscopy* **63** (2009) 92-97

Contents

Abstract **II**

Resumé **V**

Preface & Acknowledgment **VII**

List of Publications & Conference Contributions **IX**

Contents **XII**

Abbreviations & Symbols **XVI**

1 Outline **1**

2 A Review of Catalytic Upgrading of Bio-oil to Engine Fuels **4**
2.1 Introduction 5
2.2 Bio-oil 6
2.3 Bio-oil Upgrading - General Considerations 8
2.4 Hydrodeoxygenation 10
2.4.1 Catalysts & Reaction Mechanisms 15
2.4.1.1 Sulphide/Oxide Catalysts 15
2.4.1.2 Transition Metal Catalysts 17
2.4.1.3 Supports 20
2.4.2 Kinetic Models 20
2.4.3 Deactivation 22
2.5 Zeolite Cracking 23
2.5.1 Catalysts & Reaction Mechanisms 25
2.5.2 Kinetic Models 27
2.5.3 Deactivation 28
2.6 General Aspects 31
2.7 Prospect of Catalytic Bio-oil Upgrading 34
2.8 Discussion 37
2.9 Conclusion and Future Tasks 39

3 Experimental Work **41**
3.1 Batch Reactor Setup 41
3.1.1 Setup Description 41

3.1.2 Experimental Procedure 43
3.1.2.1 Alternative Experiments 44
3.2 High Pressure Continuous Flow Fixed Bed Reactor Setup 45
3.2.1 Setup Description 47
3.2.1.1 Gas Feed Section 47
3.2.1.2 Liquid Feed Section 48
3.2.1.3 Reactor 49
3.2.1.4 Liquid Makeup Section 50
3.2.1.5 Gas Makeup Section 51
3.2.2 Experimental Procedure 51
3.3 Product Analysis 53
3.3.1 GC-MS/FID 53
3.3.2 CHN-S 53
3.3.3 Calculations 54
3.4 Catalyst Synthesis and Preparation 56
3.4.1 Catalyst Screening 57
3.4.2 Nickel Catalysts 58
3.4.3 Molybdenum Carbide Catalysts 59
3.4.4 Sulfided Catalysts 60
3.5 Catalyst Characterization 60
3.5.1 Ammonia Temperature Programmed Desorption 60
3.5.2 Brunauer-Emmett-Teller Surface Area 60
3.5.3 Energy Dispersive X-Ray Spectroscopy 60
3.5.4 Environmental Transmission Electron Microscopy 61
3.5.5 Plasma Emission Spectroscopy 61
3.5.6 Temperature Programmed Oxidation 61
3.5.7 Temperature Programmed Reduction 61
3.5.8 X-Ray Absorption Spectroscopy 62
3.5.9 X-Ray Diffraction 63

4 Screening of Catalysts for Hydrodeoxygenation of Phenol as Model Compound for Bio-oil 64
4.1 Introduction 65
4.2 Kinetics of Phenol Hydrodeoxygenation 66
4.3 Oxide and Methanol Synthesis Catalysts 70
4.4 Reduced Noble Metal Catalysts 72
4.5 Reduced Non-noble Metal Catalysts 75
4.5.1 Support Effect on Nickel Catalysts 77
4.6 Conclusion 82

5 Structure Sensitivity of Nickel Based Catalysts for the Hydrodeoxygenation of Phenol 83
5.1 Introduction 84
5.2 Results 84
5.3 Theoretical Distribution of Nickel Sites 86
5.4 Discussion 89
5.5 Conclusion 94

6 Stability and Resistance of Nickel Catalysts for Hydrodeoxygenation: Effects of Sulfur, Potassium, and Chlorine in the Feed 96
6.1 Introduction . . . 97
6.2 Kinetic Model . . . 97
6.3 Reduction Temperature of Ni/ZrO_2 . . . 98
6.4 Long Term stability . . . 99
6.5 Effect of Impurities in the Feed . . . 103
6.5.1 Effect of Sulfur . . . 103
6.5.2 Effect of Chlorine . . . 105
6.5.3 Effect of Potassium . . . 105
6.6 XRD and TEM Characterization of Poisoned Catalysts . . . 106
6.6.1 Sulfur Poisoning . . . 106
6.6.2 Chlorine Poisoning . . . 107
6.6.3 Potassium Poisoning . . . 108
6.7 XAS Analysis of Poisoned Catalysts . . . 108
6.8 Comparison of Deactivation Mechanisms . . . 112
6.9 Conclusion . . . 113

7 Activity and Stability of Mo_2C as Catalyst for Hydrodeoxygenation of Bio-oil 115
7.1 Introduction . . . 116
7.2 Carburization Procedure . . . 116
7.3 Catalyst Activity . . . 118
7.4 Stability . . . 120
7.5 Thermodynamic Evaluation of the Stability of Mo_2C . . . 122
7.6 In situ XRD During Water Deactivation . . . 124
7.7 Conclusion . . . 124

8 Inhibition and Deactivation of Ni-MoS_2 by Bio-oil Impurities During Hydrodeoxygenation 126
8.1 Introduction . . . 127
8.2 The effect of H_2S . . . 127
8.3 The Effect of H_2O . . . 132
8.4 The Effect of Potassium . . . 133
8.5 The Effect of Chlorine . . . 135
8.6 Inhibition Strength of H_2S, H_2O, and HCl . . . 136
8.7 Conclusion . . . 138

9 Perspective on Real Bio-oil Upgrading 140

10 Conclusions & Outlook 142
10.1 Future Work . . . 144

Bibliography 146

Appendices 176

A Modeling of Temperature Profiles in an Environmental Transmission Electron Microscope using Computational Fluid Dynamics 177
A.1 Introduction . . . 178
A.2 CFD Model . . . 178
A.2.1 Weakly Compressible Navier-Stokes Equations . . . 180
A.2.1.1 Boundary conditions . . . 181
A.2.2 General Heat Transfer . . . 181
A.2.2.1 Boundary conditions . . . 183
A.2.3 Mesh and Model Evaluation . . . 184
A.3 Results and Discussion . . . 185
A.3.1 General Model Analysis . . . 185
A.3.2 Parameter Analysis . . . 187
A.4 Operation Recommendations . . . 193
A.5 Conclusion . . . 194

B Evaluation of the Temperature in the Batch Reactor 195

C Transport Limitations of Catalysts 197
C.1 Mears' Criterion . . . 197
C.2 Weisz-Prater Criterion . . . 198
C.3 Effectiveness Factor . . . 200

D Temperature Programmed Reduction of Catalysts 202

E Langmuir-Hinshelwood Model of Phenol Hydrogenation 208

F Plug Flow Reactor Kinetic Model Derivation 212

G Detailed Product Development of Stability Tests with Ni/ZrO_2 214

H EXAFS of Poisoned Ni/ZrO_2 Catalysts 218

I Linear Combination Analysis of XAS Data During Carburization 223

J Thermodynamic Data of MoS_2 Oxidation 226

K Real Bio-oil Tests 227

L Supporting Documents 232

Abbreviations & Symbols

Abbreviations

ANKA	Angström Quelle Karlsruhe
BET	Brunauer-Emmett-Teller
C	Condensator
CFD	Computational Fluid Dynamics
CNF	Carbon Nanofiber
CPA	Cubic Plus Association
CSD	Coherent Scattering Domain
DFT	Density Functional Theory
DMDS	Dimethyl Disulfide
DOD	Degree of Deoxygenation
dP	Differential Pressure Indicator
E	Evaporator
EDX	Energy Dispersive X-Ray
ETEM	Environmental Transmission Electron Microscopy
EXAFS	Extended X-ray Absorption Fine Structure
F	Filter
FCC	Fluid Catalytic Cracking
FI	Flow Indication
FIC	Flow Indication Controller
FID	Flame Ionization Detector
GC	Gas Chromatograph
HAADF	High Angle Annular Dark Field
HDCl	Hydrodechlorination
HDO	Hydrodeoxygenation
HDS	Hydrodesulfurization
HHV	Higher Heating Value
HV	Heating Value
ICP-OES	Inductively Coupled Plasma Atomic Emission Spectroscopy
IR	Infra Red
LHV	Lower Heating Value
LHSV	Liquid Hourly Space Velocity
LP	Liquid Pump
MS	Mass Spectrometer

PI	Pressure Indicator
PIC	Pressure Indicator Controller
PID	Proportional Integral Derivative
PFR	Plug Flow Reactor
POC	Pyrolysis Oil Converter
PSA	Pressure Swing Adsorption
PTFE	Polytetrauoroethylene
PV	Process Value
RON	Research Octane Number
S	Separator
SEM	Scanning Electron Microscopy
SP	Set Point
SSQ	Sum of Squares
STEM	Scanning Transmission Electron Microscopy
T	Temperature Indicator
TEM	Transmission Electron Microscopy
TCD	Thermal Conductivity Detector
TGA	Thermogravimetric Analyzer
TOF	Turn Over Frequency
TOS	Time On Stream
TPD	Temperature Programmed Desorption
TPO	Temperature Programmed Oxidation
TPR	Temperature Programmed Reduction
V	Valve
WHSV	Weight Hourly Space Velocity
XANES	X-ray Absorption Near Edge Structure
XAS	X-Ray Absorption
XRD	X-Ray Diffraction

Symbols

β	Peak broadening
ΔC	Carbon balance deviation
ΔG_i	Gibbs free energy of reaction i
ΔP	Pressure difference
ϵ	Emissivity
η_{eff}	Effectiveness factor
Θ	Bragg angle
Θ_i	Fractional coverage of i
λ	X-ray wavelength
μ_i	Viscosity of i
ν	Kinematic viscosity
ν_{eff}	Effective carbon number
ν_i	Carbon atoms in molecule i
ρ	Misfitting between experimental data and theory
ρ_b	Bulk density of catalyst
ρ_i	Density of i

σ	Stefan-Boltzmann constant
σ^2	Mean-square disorder in the atomic distance
τ	Residence time
τ_c	Tortuosity of catalyst pores
ϕ	Thiele Modulus
ϕ_i	Porosity of i
ψ_B	Association parameter
ϑ_c	Constriction factor
χ_i	Difference in Gibbs free energy for adsorption at step and facet sites of i
A	Cross section area
a	Radius of catalyst pores
A_i	Area of peak i
C°	Standard Concentration
C_{Ab}	Bulk concentration of A
C_i	Concentration of compound i
C_M	Mears' criterion constant
$C_{p,i}$	Heat capacity of i
D	Dispersion
D_{AB}	Diffusion coefficient of A in B
$d_{M,at}$	Atomic diameter of metal M
d_M	Crystallite diameter of metal M
D_e	Effective diffusion coefficient
D_K	Knudsen diffusion coefficient
d_p	Catalyst particle diameter
DOD^i	Degree of deoxygenation of compound i
$E_{(\text{M-O})}$	Metal-Oxygen bond energy
E_A	Activation energy
F_i	Flow of i
G	Irradiation
g	Gravitational acceleration
h	Liquid height
H/C	Molar hydrogen/carbon ratio
$(\mathrm{H/C})_{eff}$	Effective H/C ratio
J	Radiosity
K	Shape factor
k_{corner}	Rate constant at corner sites
k_{facet}	Rate constant at facet sites
k_{step}	Rate constant at step sites
k_c	Mass transfer coefficient
k_i	Rate constant for reaction i
K_i	Equillibrium constant of reaction i
k_i'	Lumped rate constant for reaction i
k_j	Conductivity of compound j
m	Cluster edge length
M_i	Molar mass of compund i
m_i	Mass of i
N	Number of neighboring atoms

n	Reaction order
$\underline{n}$	Normal vector
N_A	Avogadro's constant
N'_{corner}	Available corner sites on a cluster
N'_{facet}	Available facet sites on a cluster
n_i	Moles of i
N_S	Total amount of surface sites per catalyst mass
N'_S	Total amount of surface sites on a cluster
N'_{step}	Available step sites on a cluster
N_T	Total amount of atoms per catalyst mass
N'_T	Total amount of atoms in a cluster
O/C	Molar oxygen/carbon ratio
P	Pressure
P_i	Partial pressure of i
Q	Supplied heat
q	Heat flux
R	Ideal Gas Constant
r	Atomic distance
$r'(obs)$	Observed reaction rate
r_i	Rate of reaction of reaction i
Re	Reynolds number
S_i	Selectivity of i
Sc	Schmidt number
Sh	Sherwood number
t	Time
T	Temperature
T_{iso}	Iso-reactive temperature
V	Volume of liquid phase
v	Volumetric flow
$\tilde{V}_A$	Molar volume of A
W	Mass of catalyst
W	Weight of catalyst
w_{Ni}	Mass percent of nickel on catalyst
$wt\%$	Weight percent
x_{corner}	Fraction of corner sites relative to total amount of surface sites
x_{facet}	Fraction of facet sites relative to total amount of surface sites
x_{step}	Fraction of step sites relative to total amount of surface sites
X_i	Conversion of reaction i
Y_i	Yield of i

Chapter 1

Outline

The work in this thesis is to a large extent a compilation of the articles written during this Ph.D. project and most of the individual chapters are therefore directly connected to one of the scientific papers described on page IX-XI. To help the reader, an exposition of the content of the individual chapters is given below:

- Chapter 2 is almost a reprint of the article "A Review of Catalytic Upgrading of Bio-oil to Engine Fuels" published in Applied Catalysis A: General during the winter of 2011 [1]. This chapter reviews the state of the art of the hydrodeoxygenation (HDO) and zeolite cracking reactions up to 2011 and was used as the foundation for the further work in the project. Of the involved authors, Peter M. Mortensen was the main author and Anker D. Jensen, Jan-Dierk Grunwaldt, Peter A. Jensen, and Kim G. Knudsen read and commented on the work.

- Chapter 3 jointly describes the experimental facilities used during this Ph.D. project. Special emphasis is given to the batch reactor setup and the high pressure gas and liquid continuous flow fixed bed reactor system, which were both established during the project. Also product analysis and synthesis, pretreatment, and characterization of the used catalysts are described.

- Chapter 4 is basically the Results & Discussion section of the article "Screening of Catalysts for Hydrodeoxygenation of Phenol as a Model Compound for Bio-oil" published in ACS Catalysis during the summer of 2013 [2], which summarizes much of the work performed in the batch reactor setup in the period from spring 2011 to spring 2012. Here 23 catalysts were screened to find suitable HDO catalysts. Of the involved authors, Peter M. Mortensen made all experiments and was the main author and Anker D. Jensen, Jan-Dierk Grunwaldt, and Peter A. Jensen participated in discussing the results and proof reading of the work.

- Chapter 5 is basically the Results & Discussion section of the article "Structure Sensitivity of Nickel Based Catalysts for the Hydrodeoxygenation of Phenol" which has been sent to ChemCatChem in November 2013 for review. This summarizes a parallel work to the screening work described in Chapter 4, where the nickel particle size effect on HDO of phenol for Ni/SiO_2 was investigated. Of the involved authors, Peter M. Mortensen made all experiments and was the

main author and Anker D. Jensen, Jan-Dierk Grunwaldt, and Peter A. Jensen participated in discussion of the results and proof reading of the work.

- Chapter 6 is basically the Results & Discussion section of the article "Stability and Resistance of Nickel Catalysts for Hydrodeoxygenation: Effects of Sulfur, Potassium, and Chlorine in the Feed", an article still in preparation but intended for submission to Applied Catalysis B: Environmental. This work summarizes the initial tests performed on the continuous flow reactor system in the period from summer 2012 to winter 2012/2013 concerning stability and resistance of nickel based catalysts, in an attempt to mimic the deactivating environment when feeding real bio-oils to HDO catalysts. Of the involved authors, Peter M. Mortensen was the main author and was responsible for all the continuous flow experiments. Diego Gardini made characterization of the catalysts samples by XRD and SEM/STEM-EDX measurements and he has written the draft to Section 6.6. Hudson Wallace Pereira de Carvalho performed XAS on all of the samples and he has written the draft to Section 6.7 and Appendix H. Anker D. Jensen, Peter A. Jensen, Jan-Dierk Grunwaldt, Christian D. Damsgaard, and Jakob B. Wagner participated in discussing the results and proof reading of the work.

- Chapter 7 is basically the Results & Discussion section of the article "Mo_2C as Catalyst for Hydrodeoxygenation of Bio-oil: Activity and Stability", an article still in preparation phase. This work investigated Mo_2C/ZrO_2 as catalyst for HDO and had special emphasis on the stability of this catalyst in the presence of water. The work was performed during the spring and summer of 2013. Peter M. Mortensen was the main author and was responsible for all the continuous flow experiments. Hudson Wallace Pereira de Carvalho performed XAS on all of the samples and he has written the draft to Section 7.2 and Appendix I. Anker D. Jensen, Peter A. Jensen, and Jan-Dierk Grunwaldt participated in discussing the results and proof reading of the work.

- Chapter 8 is basically the Results & Discussion section of the article "Inhibition and Deactivation of Ni-MoS_2 by Bio-oil Impurities During Hydrodeoxygenation", an article still in preparation phase. This summarizes the work with Ni-MoS_2/ZrO_2 as catalyst for HDO of a model compound system of bio-oil which was contaminated with impurities as water, alkali metals, and chlorine in order to investigate potential deactivation mechanisms of this catalyst during HDO of real bio-oil. This work was performed in the autumn of 2013. Peter M. Mortensen was the main author and was responsible for all the continuous flow experiments. Diego Gardini assisted in the characterization of the catalysts samples by XRD and TEM. Anker D. Jensen, Peter A. Jensen, and Jan-Dierk Grunwaldt participated in discussing the results and proof reading of the work.

- Chapter 9 is a discussion of a series of experiments made with a real bio-oil feed in the end of the Ph.D. project (winter 2013). This section is closely linked to Appendix K where detailed description of the experiments are made. However, as the experiments were used mostly to evaluate the progress made during the Ph.D. project and put the many bio-oil model compound studies in perspective, the discussion of the actual experiments were not included in the main part of the thesis.

Each chapter based on an article starts with the abstract of the respective article. The articles excerpts have been changed slightly to fit better in the overall context of the thesis, but are still in a form very similar to their intended form for publications. Minor updates of references and small changes in comments or discussion have also been done.

Additionally Appendix A is a reprint of an article describing a computational fluid dynamics (CFD) model of an environmental transmission electron microscope (ETEM) developed as a side project during this Ph.D. project. The work was a collaboration between Peter M. Mortensen and Anker D. Jensen from DTU-KT and Thomas W. Hansen and Jakob B. Wagner from DTU-CEN (Center for Electron Nanoscopy). Peter M. Mortensen was responsible for developing the CFD model and the CEN group was responsible for acquiring drawings of the microscope and generally outlining the tasks of the work.

Chapter 2

A Review of Catalytic Upgrading of Bio-oil to Engine Fuels

Abstract

As the oil reserves are depleting the need of an alternative fuel source is becoming increasingly apparent. One prospective method for producing fuels in the future is conversion of biomass into bio-oil and then upgrading the bio-oil over a catalyst, this method is the focus of this review. Bio-oil production can be facilitated by flash pyrolysis, which has been identified as one of the most feasible routes. The bio-oil has a high oxygen content and therefore low stability over time and a low heating value. Upgrading is desirable to remove the oxygen and in this way make it resemble crude oil. Two general routes for bio-oil upgrading have been considered: hydrodeoxygenation (HDO) and zeolite cracking. HDO is a high pressure operation where hydrogen is used to exclude oxygen from the bio-oil, giving a high grade oil product equivalent to crude oil. Catalysts for the reaction are traditional hydrodesulfurization (HDS) catalysts, such as Co-MoS_2/Al_2O_3, or metal catalysts, as for example Pd/C. However, catalyst lifetimes of much more than 200 h have not been achieved with any current catalyst due to carbon deposition. Zeolite cracking is an alternative path, where zeolites, e.g. HZSM-5, are used as catalysts for the deoxygenation reaction. In these systems hydrogen is not a requirement, so operation is performed at atmospheric pressure. However, extensive carbon deposition results in very short catalyst lifetimes. Furthermore a general restriction in the hydrogen content of the bio-oil results in a low H/C ratio of the oil product as no additional hydrogen is supplied. Overall, oil from zeolite cracking is of a low grade, with heating values approximately 25% lower than that of crude oil. Of the two mentioned routes, HDO appears to have the best potential, as zeolite cracking cannot produce fuels of acceptable grade for the current infrastructure. HDO is evaluated as being a path to fuels in a grade and at a price equivalent to present fossil fuels, but several tasks still have to be addressed within this process. Catalyst development, understanding of the carbon forming mechanisms, understanding of the kinetics, elucidation of sulfur as a source of deactivation, evaluation of the requirement for high pressure, and sustainable sources for hydrogen are all areas which have to be elucidated before commercialization of the process.

2.1 Introduction

Energy consumption has never been higher worldwide than it is today, due to our way of living and the general fact that the World's population is increasing [3, 4]. One of the main fields of energy consumption is the transportation sector, constituting about one fifth of the total [5]. As the World's population grows and means of transportation becomes more readily available, it is unavoidable that the need for fuels will become larger in the future [6]. This requirement constitutes one of the major challenges of the near future [7], as present fuels primarily are produced from crude oil and these reserves are depleting [8].

Substantial research is being carried out within the field of energy in order to find alternative fuels to replace gasoline and diesel. The optimal solution would be an alternative which is equivalent to the conventional fuels, i.e. compatible with the infrastructure as we know it, but also a fuel which is sustainable and will decrease the CO_2 emission and thereby decrease the environmental man-made footprint [9, 10].

Biomass derived fuels could be the prospective fuel of tomorrow, as these can be produced within a relatively short cycle and are considered benign for the environment [6, 11]. So far first generation bio-fuels (bio-ethanol and biodiesel) have been implemented in different parts of the World [12, 13]. However, these technologies rely on food grade biomass; first generation bio-ethanol is produced from the fermentation of sugar or starch and biodiesel is produced on the basis of fats [14–16]. This is a problem as the requirement for food around the World is a constraint and the energy efficiency per unit land of the required crops is relatively low (compared to energy crops) [17]. For this reason new research focuses on developing second generation bio-fuels, which can be produced from other biomass sources such as agricultural waste, wood, etc. and therefore does not influence food supply [18–21]. Table 2.1 summarizes different paths for producing fuels from biomass and display which type of biomass source is required, showing that a series of paths exists which can utilize any source of biomass.

Of the second generation biofuel paths, a lot of efforts are presently spent on the biomass to liquid route via syngas to optimize the efficiency [28–31] and also synthesis of higher alcohols from syngas or hydrocarbons from methanol [24, 29, 32–35]. As an alternative, the estimated production prices shown in Table 2.1 indicate that HDO constitute a feasible route for the production of synthetic fuels. The competitiveness of this route is achieved due to a good economy when using bio-oil as platform chemical (lower transport cost for large scale plants) and the flexibility with respect to the biomass feed [14, 36–38]. Furthermore this route also constitute a path to fuels applicable in the current infrastructure [14].

Jointly, HDO and zeolite cracking are referred to as catalytic bio-oil upgrading and these could become routes for production of second generation bio-fuels in the future, but both routes are still far from industrial application. This review will give an overview on the present status of the two processes and also discuss which aspects need further elucidation. Each route will be considered independently. Aspects of operating conditions, choice of catalyst, reaction mechanisms, and deactivation mechanisms will be discussed. These considerations will be used to give an overview of the two processes compared to each other, but also relative to crude oil as the benchmark. Ultimately, an industrial perspective will be given, discussing the prospective of production of bio-fuels by catalytic bio-oil upgrading in industrial scale.

Table 2.1: *Overview of potential routes for production of renewable fuels from biomass. The prices are based on the lower heating value (LHV). Biomass as feed implies high flexibility with respect to feed source.*

Technology	Feed	Platform Chemical	Price [\$/toe[a]]
Hydrodeoxygenation	Biomass	Bio-oil	740[b]
Zeolite cracking	Biomass	Bio-oil	-[c]
Fischer-Tropsch	Biomass	Syngas	840-1134[d]
H_2	Biomass	Syngas	378-714[ef]
Methanol	Biomass	Syngas	546-588[g]
Higher Alcohols	Biomass	Syngas	1302-1512[h]
Bio-ethanol	Sugar Cane	-	369-922[i]
Bio-ethanol	Corn	-	1107-1475[j]
Bio-ethanol	Biomass	-	1475-2029[k]
Biodiesel	Canola oil	-	586-1171[l]
Biodiesel	Palm oil	-	586-937[m]
Gasoline	Crude oil	-	1046[n]

[a]toe: Tonne of Oil Equivalent, 1 toe = 42 GJ
[b]Published price: 2.04 \$/gallon [22], 1 gallon = 3.79 l, ρ = 719 kg/m^3, LHV = 42.5 MJ/kg.
[c]No economic evaluation has been made for this technology.
[d]Published price: 20-27 \$/GJ [23].
[e]Published price: 9-17 \$/GJ [23, 24].
[f]Expenses for distribution and storage are not considered.
[g]Published price: 13-14 \$/GJ [23].
[h]Published price: 31-36 \$/GJ [23].
[i]Published price: 0.2-0.5 \$/l [25], ρ = 789 kg/m^3, LHV = 28.87 MJ/kg.
[j]Published price: 0.6-0.8 \$/l [25].
[k]Published price: 0.8-1.1 \$/l [25].
[l]Published price: 0.5-1 \$/l [25], ρ = 832 kg/m^3, LHV = 43.1 MJ/kg.
[m]Published price: 0.5-0.8 \$/l [25].
[n]Published price in USA April 2011: 2.88\$/gallon excluding distribution, marketing, and taxes [26]. Crude oil price April 2011: 113.23 \$/barrel [27].

Other reviews within the same field are that by Elliott [39] from 2007 where the development within HDO since the 1980's is discussed, and a review in 2000 by Furimsky [40] where reaction mechanisms and kinetics of HDO are discussed. More general reviews of utilization of bio-oil have been published by Zhang et al. [41], Bridgwater [42], and Czernik and Bridgwater [43], and reviews about bio-oil and production thereof have been published by Venderbosch and Prins [44] and Mohan et al. [45].

2.2 Bio-oil

As seen from Table 2.1, both HDO and zeolite cracking are based on bio-oil as platform chemical. Flash pyrolysis is the most widely applied process for production of bio-oil, as this has been found as a feasible route [29, 39, 46, 47]. In this review, only this route will be discussed and bio-oil will in the following refer to flash pyrolysis oil. For information about other routes reference is made to [29, 48–51].

Flash pyrolysis is a densification technique where both the mass- and energy-density is increased by treating the raw biomass at intermediate temperatures (300-600 °C) with high heating rates (10^3-10^4 K/s) and at short residence times (1-2 seconds) [41, 44, 52]. In this way, an increase in the energy density by roughly a factor of 7-8 can be achieved [53, 54]. Virtually any type of biomass is compatible with pyrolysis, ranging from more traditional sources such as corn and wood to waste products such as sewage sludge and chicken litter [52, 55, 56].

More than 300 different compounds have been identified in bio-oil, where the specific composition of the product depends on the feed and process conditions used [41]. In Table 2.2 a rough characterization of bio-oil from different biomass sources is seen. The principle species of the product is water, constituting 10-30 wt%, but the oil also contains: hydroxyaldehydes, hydroxyketones, sugars, carboxylic acids, esters, furans, guaiacols, and phenolics, where many of the phenolics are present as oligomers [41, 43, 57, 58].

Table 2.2: *Bio-oil composition in wt% on the basis of different biomass sources and production methods.*

	Corn Cobs	Corn Stover	Pine	Softwood	Hardwood
Ref. #	[59]	[59]	[44, 60]	[61]	[61]
T [°C]	500	500	520	500	-
Reactor	Fluidized bed	Fluidized bed	Transport bed	Rotating cone	Transport bed
Water	25	9	24	29-32	20-21
Aldehydes	1	4	7	1-17	0-5
Acids	6	6	4	3-10	5-7
Carbohydrates	5	12	34	3-7	3-4
Phenolics	4	2	15	2-3	2-3
Furan etc.	2	1	3	0-2	0-1
Alcohols	0	0	2	0-1	0-4
Ketones	11	7	4	2-4	7-8
Unclassified	46	57	5	24-57	47-58

Table 2.3 shows a comparison between bio-oil and crude oil. One crucial difference between the two is the elemental composition, as bio-oil contains 10-40 wt% oxygen [41, 44, 59]. This affects the homogeneity, polarity, heating value (HV), viscosity, and acidity of the oil.

The oxygenated molecules of lower molecular weight, especially alcohols and aldehydes, ensure the homogeneous appearance of the oil, as these act as a sort of surfactant for the higher molecular weight compounds, which normally are considered apolar and immiscible with water [62, 63]. Overall this means that the bio-oil has a polar nature due to the high water content and is therefore immiscible with crude oil. The high water content and oxygen content further result in a low HV of the bio-oil, which is about half that of crude oil [41, 43, 44, 64].

The pH of bio-oil is usually in the range from 2-4, which primarily is related to the content of acetic acid and formic acid [65]. The acidic nature of the oil constitutes a problem, as it will entail harsh conditions for equipment used for both storage,

Table 2.3: *Comparison between bio-oil and crude oil. Data are from references [14, 15, 41].*

	Bio-oil	Crude Oil
Water [wt%]	15-30	0.1
pH	2.8-3.8	-
ρ [kg/l]	1.05-1.25	0.86
$\mu_{50°C}$ [cP]	40-100	180
HHV [MJ/kg]	16-19	44
C [wt%]	55-65	83-86
O [wt%]	28-40	<1
H [wt%]	5-7	11-14
S [wt%]	<0.05	<4
N [wt%]	<0.4	<1
Ash [wt%]	<0.2	0.1

transport, and processing. Common construction materials such as carbon steel and aluminium have proven unsuitable when operating with bio-oil, due to corrosion [41, 64].

A pronounced problem with bio-oil is the instability during storage, where viscosity, HV, and density all are affected. This is due to the presence of highly reactive organic compounds. Olefins are suspected to be active for repolymerization in the presence of air. Furthermore, ketones, aldehydes, and organic acids can react to form ethers, acetales, and hemiacetals, respectively. These types of reactions effectively increase the average molecular mass of the oil, the viscosity, and the water content. An overall decrease in the oil quality is therefore seen as a function of storage time, ultimately resulting in phase separation [60, 66, 67].

Overall the unfavorable characteristics of the bio-oil are associated with the oxygenated compounds. Carboxylic acids, ketones, and aldehydes constitute some of the most unfavorable compounds, but utilization of the oil requires a general decrease in the oxygen content in order to separate the organic product from the water, increase the HV, and increase the stability.

2.3 Bio-oil Upgrading - General Considerations

Catalytic upgrading of bio-oil is a complex reaction network due to the high diversity of compounds in the feed. Cracking, decarbonylation, decarboxylation, hydrocracking, hydrodeoxygenation, hydrogenation, and polymerization have been reported to take place for both zeolite cracking and HDO [68–70]. Examples of these reactions are given in Figure 2.1. Besides these, carbon formation is also significant in both processes.

The high diversity in the bio-oil and the span of potential reactions make evaluation of bio-oil upgrading difficult and such evaluation is often restricted to model compounds. To get a general thermodynamic overview of the process, we have eval-

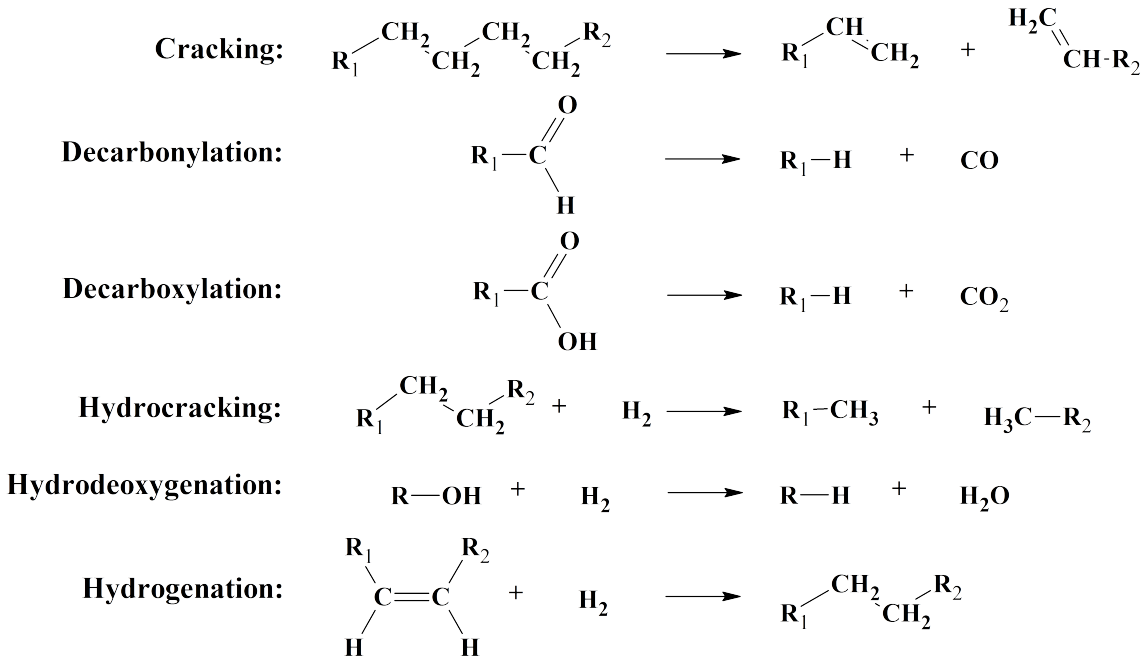

Figure 2.1: *Examples of reactions associated with catalytic bio-oil upgrading. The figure is drawn on the basis of information from references [68, 69].*

uated the following reactions by thermodynamic calculations (based on data from Barin [71]):

$$\text{Phenol} + \text{H}_2 \rightleftharpoons \text{Benzene} + \text{H}_2\text{O} \tag{2.1}$$

$$\text{Phenol} + 4\,\text{H}_2 \rightleftharpoons \text{Cyclohexane} + \text{H}_2\text{O} \tag{2.2}$$

This reaction path of phenol has been proposed by both Massoth et al. [72] and Yunquan et al. [73]. Calculating the thermodynamic equilibrium for the two reactions shows that complete conversion of phenol can be achieved at temperatures up to at least 600 °C at atmospheric pressure and stoichiometric conditions. Increasing either the pressure or the excess of hydrogen will shift the thermodynamics even further towards complete conversion. Similar calculations have also been made with furfural, giving equivalent results. Thus, thermodynamics does not appear to constitute a constraint for the processes, when evaluating the simplest reactions of Figure 2.1 for model compounds.

In practice it is difficult to evaluate the conversion of each individual component in the bio-oil. Instead two important parameters are the oil yield and the degree of deoxygenation:

$$Y_{oil} = \left(\frac{m_{\text{oil}}}{m_{\text{feed}}}\right) \cdot 100\% \tag{2.3}$$

$$\text{DOD} = \left(1 - \frac{wt\%_{\text{O in product}}}{wt\%_{\text{O in feed}}}\right) \cdot 100\% \tag{2.4}$$

Here Y_{oil} is the yield of oil, m_{oil} is the mass of produced oil, m_{feed} is the mass of the feed, DOD is the degree of deoxygenation, and $wt\%_{\text{O}}$ is the weight percent of oxygen in the oil. The two parameters together can give a rough overview of the extent of

reaction, as the oil yield describes the selectivity toward an oil product and the degree of deoxygenation describes how effective the oxygen removal has been and therefore indicates the quality of the produced oil. However, separately the parameters are less descriptive, as it can be seen that a 100% yield can be achieved in the case of no reaction. Furthermore, none of the parameters relate to the removal of specific troublesome species and these would have to be analyzed for in detail.

Table 2.4 summarizes operating parameters, product yield, degree of deoxygenation, and product grade for some of the work conducted within the field of bio-oil upgrading. The reader can get an idea of how the choice of catalyst and operating conditions affect the process. It is seen that a wide variety of catalysts have been tested. HDO and zeolite cracking are split in separate sections in the table, where it can be concluded that the process conditions of HDO relative to zeolite cracking are significantly different, particularly with respect to operating pressure. The two processes will therefore be discussed separately in the following.

2.4 Hydrodeoxygenation

HDO is closely related to the hydrodesulfurization (HDS) process from the refinery industry, used in the elimination of sulfur from organic compounds [57, 82]. Both HDO and HDS use hydrogen for the exclusion of the heteroatom, forming respectively H_2O and H_2S.

All the reactions shown in Figure 2.1 are relevant for HDO, but the principal reaction is hydrodeoxygenation, as the name implies, and therefore the overall reaction can be generally written as (the reaction is inspired by Bridgwater [57, 83] and combined with the elemental composition of bio-oil specified in Table 2.3 normalized to carbon):

$$CH_{1.4}O_{0.4} + 0.7H_2 \longrightarrow 1\text{"}CH_2\text{"} + 0.4H_2O \tag{2.5}$$

Here "CH_2" represent an unspecified hydrocarbon product. The overall thermo chemistry of this reaction is exothermic and simple calculations have shown an average overall heat of reaction in the order of 2.4 MJ/kg when using bio-oil [84].

Water is formed in the conceptual reaction, so (at least) two liquid phases will be observed as product: one organic and one aqueous. The appearance of two organic phases has also been reported, which is due to the production of organic compounds with densities less than water. In this case a light oil phase will separate on top of the water and a heavy one below. The formation of two organic phases is usually observed in instances with high degrees of deoxygenation, which will result in a high degree of fractionation in the feed [15].

In the case of complete deoxygenation the stoichiometry of Eq. 2.5 predicts a maximum oil yield of 56-58 wt% [57]. However, the complete deoxygenation indicated by Eq. 2.5 is rarely achieved due to the span of reactions taking place; instead a product with residual oxygen will often be formed. Venderbosch et al. [15] described the stoichiometry of a specific experiment normalized with respect to the feed carbon as (excluding the gas phase):

$$CH_{1.47}O_{0.56} + 0.39H_2 \longrightarrow 0.74CH_{1.47}O_{0.11} + 0.19CH_{3.02}O_{1.09} + 0.29H_2O \tag{2.6}$$

Table 2.4: Overview of catalysts investigated for catalytic upgrading of bio-oil.

Catalyst	Setup	Feed	Time [h]	P [bar]	T [°C]	DOD [%]	O/C	H/C	Y_{oil} [wt%]	Ref. #
				Hydrodeoxygenation						
Co-MoS_2/Al_2O_3	Batch	Bio-oil	4	200	350	81	0.8	1.3	26	[68]
Co-MoS_2/Al_2O_3	Continuous	Bio-oil	4^a	300	370	100	0.0	1.8	33	[74]
Ni-MoS_2/Al_2O_3	Batch	Bio-oil	4	200	350	74	0.1	1.5	28	[68]
Ni-MoS_2/Al_2O_3	Continuous	Bio-oil	0.5^a	85	400	28	-	-	84	[75]
Pd/C	Batch	Bio-oil	4	200	350	85	0.7	1.6	65	[68]
Pd/C	Continuous	Bio-oil	4^b	140	340	64	0.1	1.5	48	[76]
Pd/ZrO_2	Batch	Guaiacol	3	80	300	-	0.1	1.3	-	[77]
$Pt/Al_2O_3/SiO_2$	Continuous	Bio-oil	0.5^a	85	400	45	-	-	81	[75]
Pt/ZrO_2	Batch	Guaiacol	3	80	300	-	0.2	1.5	-	[77]
Rh/ZrO_2	Batch	Guaiacol	3	80	300	-	0.0	1.2	-	[77]
Ru/Al_2O_3	Batch	Bio-oil	4	200	350	78	0.4	1.2	36	[68]
Ru/C	Continuous	Bio-oil	0.2^a	230	350-400	73	0.1	1.5	38	[15]
Ru/C	Batch	Bio-oil	4	200	350	86	0.8	1.5	53	[68]
Ru/TiO_2	Batch	Bio-oil	4	200	350	77	1.0	1.7	67	[68]
				Zeolite Cracking						
GaHZSM-5	Continuous	Bio-oil	0.32^a	1	380	-	-	-	18	[78]
H-Mordenite	Continuous	Bio-oil	0.56^a	1	330	-	-	-	17	[79]
H-Y	Continuous	Bio-oil	0.28^a	1	330	-	-	-	28	[79]
HZSM-5	Continuous	Bio-oil	0.32^a	1	380	50	0.2	1.2	24	[78]
HZSM-5	Continuous	Bio-oil	0.91^a	1	500	53	0.2	1.2	12	[80]
MgAPO-36	Continuous	Bio-oil	0.28^a	1	370	-	-	-	16	[81]
SAPO-11	Continuous	Bio-oil	0.28^a	1	370	-	-	-	20	[81]
SAPO-5	Continuous	Bio-oil	0.28^a	1	370	-	-	-	22	[81]
ZnHZSM-5	Continuous	Bio-oil	0.32^a	1	380	-	-	-	19	[78]

[a] Calculated as the inverse of the WHSV.
[b] Calculated as the inverse of the LHSV.

Here $CH_{1.47}O_{0.11}$ is the organic phase of the product and $CH_{3.02}O_{1.09}$ is the aqueous phase of the product. Some oxygen is incorporated in the hydrocarbons of the organic phase, but the O/C ratio is significantly lower in the hydrotreated organic phase (0.11) compared to the pyrolysis oil (0.56). In the aqueous phase a higher O/C ratio than in the parent oil is seen [15].

Regarding operating conditions, a high pressure is generally used, which has been reported in the range from 75 to 300 bar in the literature [44, 76, 85]. Patent literature describes operating pressures in the range of 10-120 bar [86, 87]. The high pressure has been described as ensuring a higher solubility of hydrogen in the oil and thereby a higher availability of hydrogen in the vicinity of the catalyst. This increases the reaction rate and further decreases coking in the reactor [15, 88]. Elliott et al. [76] used hydrogen in an excess of 35-420 mol H_2 per kg bio-oil, compared to a requirement of around 25 mol/kg for complete deoxygenation [15].

High degrees of deoxygenation are favored by high residence times [44]. In a continuous flow reactor, Elliott et al. [76] showed that the oxygen content of the upgraded oil decreased from 21 wt% to 10 wt% when decreasing the LHSV from 0.70 h^{-1} to 0.25 h^{-1} over a Pd/C catalyst at 140 bar and 340 °C. In general LHSV should be in the order of 0.1-1.5 h^{-1} [86]. This residence time is in analogy to batch reactor tests, which usually are carried out over time-frames of 3-4 h [68, 77, 89].

HDO is normally carried out at temperatures between 250-450 °C [15, 82]. As the reaction is exothermic and calculations of the equilibrium predicts potential full conversion of representative model compounds up to at least 600 °C, it appears that the choice of operating temperature should mainly be based on kinetic aspects. The effect of temperature was investigated by Elliott et al. [76] for HDO of wood based bio-oil over a Pd/C catalyst in a fixed bed reactor at 140 bar. Here it was found that the oil yield decreased from 75% to 56% when increasing the temperature from 310 °C to 360 °C. This was accompanied by an increase in the gas yield by a factor of 3. The degree of deoxygenation increased from 65% at 310 °C to 70% at 340 °C. Above 340 °C the degree of deoxygenation did not increase further, but instead extensive cracking took place rather than deoxygenation.

The observations of Elliott et al. [76] are due to the reactivity of the different types of functional groups in the bio-oil [36, 90]. Table 2.5 summarizes activation energies, iso-reactivity temperatures (the temperature required for a reaction to take place), and hydrogen consumption for different functional groups and molecules over a Co-MoS_2/Al_2O_3 catalyst. On this catalyst the activation energy for deoxygenation of ketones is relatively low, so these molecules can be deoxygenated at temperatures close to 200 °C. However, for the more complex bound or sterically hindered oxygen, as in furans or ortho substituted phenols, a significantly higher temperature is required for the reaction to proceed. On this basis the apparent reactivity of different compounds has been summarized as [40]:

$$\begin{aligned} &\text{Alcohol} > \text{Ketone} > \text{Alkylether} > \text{Carboxylic Acid} \\ &\approx \text{M-/p-phenol} \approx \text{Naphtol} > \text{Phenol} > \text{Diarylether} \\ &\approx \text{O-phenol} \approx \text{Alkylfuran} > \text{Benzofuran} > \text{Dibenzofuran} \end{aligned} \tag{2.7}$$

Table 2.5: *Activation energy (E_A), iso-reactive temperature (T_{iso}), and hydrogen consumption for the deoxygenation of different functional groups or molecules over a Co-MoS_2/Al_2O_3 catalyst. Data are obtained from Grange et al. [36].*

Molecule/Group	E_A [kJ/mol]	T_{Iso} [°C]	Hydrogen Consumption
Ketone	50	203	$2H_2$/group
Carboxylic acid	109	283	3 H_2/group
Methoxy phenol	113	301	≈6 H_2/molecule
4-Methylphenol	141	340	≈4 H_2/molecule
2-Ethylphenol	150	367	≈4 H_2/molecule
Dibenzofuran	143	417	≈8 H_2/molecule

An important aspect of the HDO reaction is the consumption of hydrogen. Venderbosch et al. [15] investigated hydrogen consumption for bio-oil upgrading as a function of deoxygenation rate over a Ru/C catalyst in a fixed bed reactor. The results are summarized in Figure 2.2. The hydrogen consumption becomes increasingly steep as a function of the degree of deoxygenation. This development was presumed to be due to the different reactivity values of the compounds in the bio-oil. Highly reactive oxygenates, like ketones, are easily converted with low hydrogen consumption, but some oxygen is bound in the more stable compounds. Thus, the more complex molecules are accompanied by an initial hydrogenation/saturation of the molecule and therefore the hydrogen consumption exceeds the stoichiometric prediction at the high degrees of deoxygenation [40]. These tendencies are also illustrated in Table 2.5. Obviously, the hydrogen requirement for HDO of a ketone is significantly lower than that for a furan. Overall this means that in order to achieve 50% deoxygenation (ca. 25 wt% oxygen in the upgraded oil) 8 mol H_2 per kg bio-oil is required according to Figure 2.2. In contrast, complete deoxygenation (and accompanied saturation) has a predicted hydrogen requirement of ca. 25 mol/kg, i.e. an increase by a factor of ca. 3.

The discussion above shows that the use of hydrogen for upgrading bio-oil has two effects with respect to the mechanism: removing oxygen and saturating double bounds. This results in decreased O/C ratios and increased H/C ratios, both of which increase the fuel grade of the oil by increasing the heating value (HV). Mercader et al. [85] found that the higher heating value (HHV) of the final product was approximately proportional to the hydrogen consumed in the process, with an increase in the HHV of 1 MJ/kg per mol/kg H_2 consumed.

In Figure 2.3 the production of oil, water, and gas from a HDO process using a Co-MoS_2/Al_2O_3 catalyst is seen as a function of the degree of deoxygenation. The oil yield decreases as a function of the degree of deoxygenation, which is due to increased water and gas yields. This shows that when harsh conditions are used to remove the oxygen, a significant decrease in the oil yield occurs; it drops from 55% to 30% when increasing the degree of deoxygenation from 78% to 100%. It is therefore an important aspect to evaluate to which extent the oxygen should be removed [91].

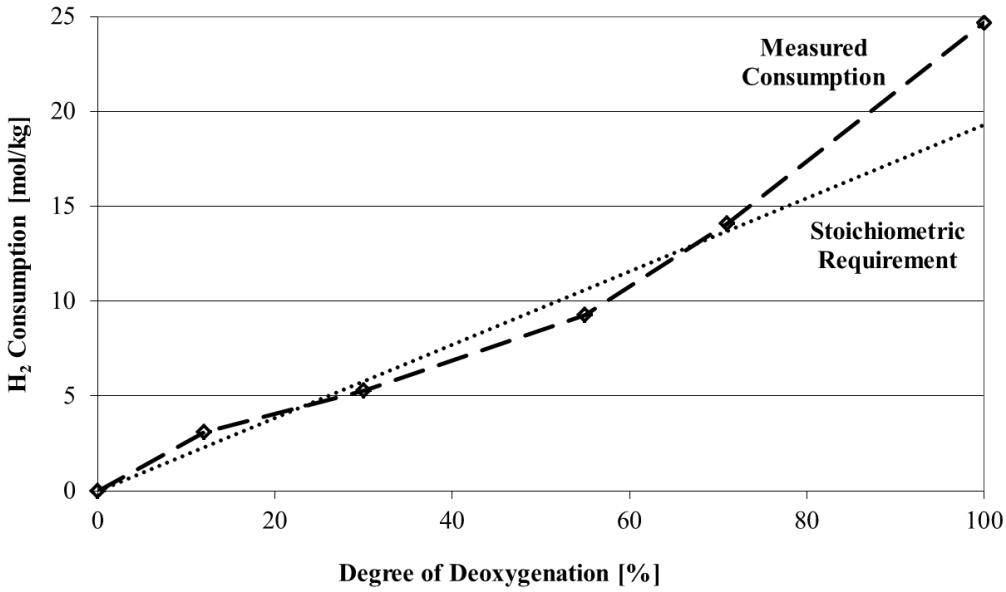

Figure 2.2: *Consumption of hydrogen for HDO as a function of degree of deoxygenation compared to the stoichiometric requirement. 100% deoxygenation has been extrapolated on the basis of the other points. The stoichiometric requirement has been calculated on the basis of an organic bound oxygen content of 31 wt% in the bio-oil and a hydrogen consumption of 1 mol H_2 per mol oxygen. Experiments were performed with a Ru/C catalyst at 175-400 °C and 200-250 bar in a fixed bed reactor fed with bio-oil. The high temperatures were used in order to achieve high degrees of deoxygenation. Data are from Venderbosch et al. [15].*

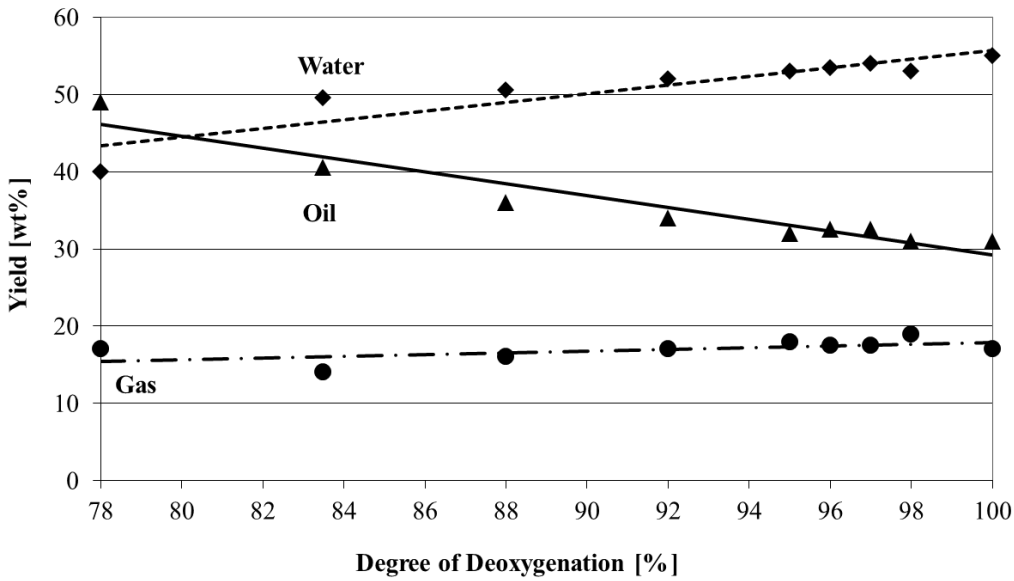

Figure 2.3: *Yields of oil, water, and gas from a HDO process as a function of the degree of deoxygenation. Experiments were performed with eucalyptus bio-oil over a Co-MoS_2/Al_2O_3 catalyst in a fixed bed reactor. Data are from Samolada et al. [92].*

2.4.1 Catalysts & Reaction Mechanisms

As seen from Table 2.4, a variety of different catalysts has been tested for the HDO process. In the following, these will be discussed as either sulphide/oxide type catalysts or transition metal catalysts, as it appears that the mechanisms for these two groups of catalysts are different.

2.4.1.1 Sulphide/Oxide Catalysts

Co-MoS_2 and Ni-MoS_2 have been some of the most frequently tested catalysts for the HDO reaction, as these are also used in the traditional hydrotreating process [39, 40, 74, 88, 90, 92–104].

In these catalysts, Co or Ni serves as promoters, donating electrons to the molybdenum atoms. This weakens the bond between molybdenum and sulfur and thereby generates a sulfur vacancy site. These sites are the active sites in both HDS and HDO reactions [72, 98, 105–107].

Romero et al. [106] studied HDO of 2-ethylphenol on MoS_2-based catalysts and proposed the reaction mechanism depicted in Figure 2.4. The oxygen of the molecule is believed to adsorb on a vacancy site of a MoS_2 slab edge, activating the compound. S-H species will also be present along the edge of the catalyst as these are generated from the H_2 in the feed. This enables proton donation from the sulfur to the attached molecule, which forms a carbocation. This can undergo direct C-O bond cleavage, forming the deoxygenated compound, and oxygen is hereafter removed in the formation of water.

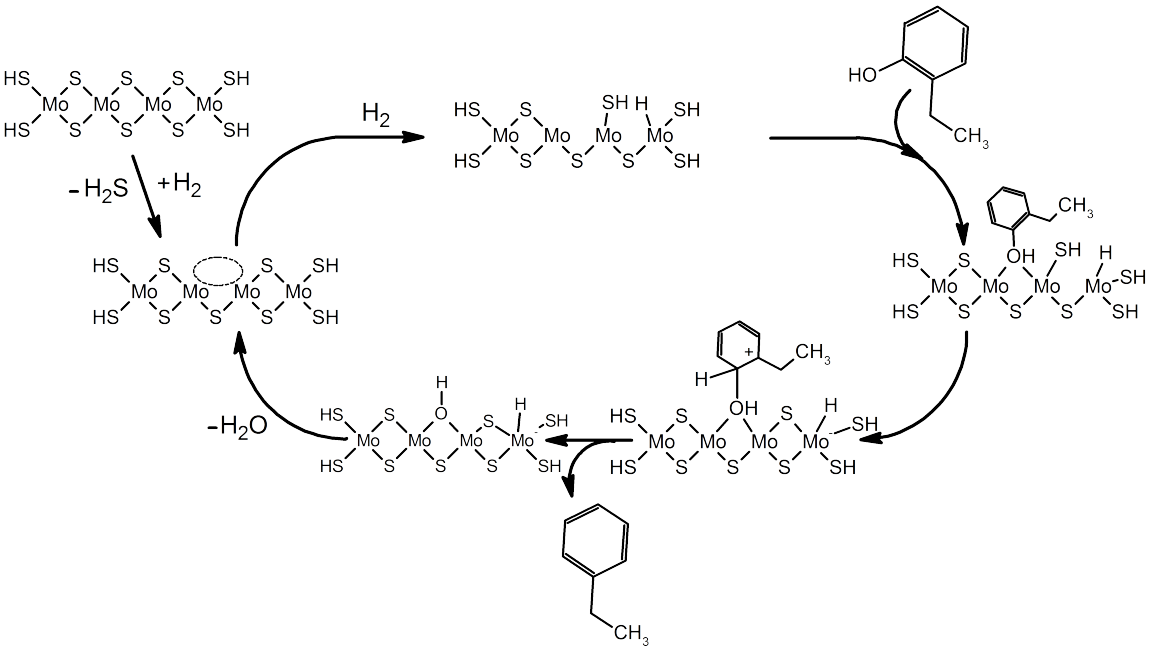

Figure 2.4: *Proposed mechanism of HDO of 2-ethylphenol over a Co-MoS_2 catalyst. The dotted circle indicates the catalytically active vacancy site. The figure is drawn on the basis of information from Romero et al. [106].*

For the mechanism to work, it is a necessity that the oxygen group formed on the metal site from the deoxygenation step is eliminated as water. During prolonged

operation it has been observed that a decrease in activity can occur due to transformation of the catalyst from a sulphide form toward an oxide form. In order to avoid this, it has been found that co-feeding H_2S to the system will regenerate the sulphide sites and stabilize the catalyst [100, 105, 108, 109]. However, the study of Senol et al. [108, 109] showed that trace amounts of thiols and sulphides were formed during the HDO of 3 wt% methyl heptanoate in m-xylene at 15 bar and 250 °C in a fixed bed reactor with Co-MoS_2/Al_2O_3 co-fed with up to 1000 ppm H_2S. Thus, these studies indicate that sulfur contamination of the otherwise sulfur free oil can occur when using sulphide type catalysts. An interesting perspective in this is that Co-MoS_2/Al_2O_3 is used as industrial HDS catalyst where it removes sulfur from oils down to a level of a few ppm [110]. On the other hand, Christensen et al. [32] showed that, when synthesizing higher alcohols from synthesisgas with Co-MoS_2/C co-fed with H_2S, thiols and sulfides were produced as well. Thus, the influence of the sulfur on this catalyst is difficult to evaluate and needs further attention.

On the basis of density functional theory (DFT) calculations, Moberg et al. [111] proposed MoO_3 as catalyst for HDO. These calculations showed that the deoxygenation on MoO_3 occur similar to the path in Figure 2.4, i.e. chemisorption on a coordinatevely unsaturated metal site, proton donation, and desorption. For both oxide and sulphide type catalysts the activity relies on the presence of acid sites. The initial chemisorption step is a Lewis acid/base interaction, where the oxygen lone pair of the target molecule is attracted to the unsaturated metal site. For this reason it can be speculated that the reactivity of the system must partly rely on the availability and strength of the Lewis acid sites on the catalyst. Gervasini and Auroux [112] reported that the relative Lewis acid site surface concentration on different oxides are:

$$Cr_2O_3 > WO_3 > Nb_2O_5 > Ta_2O_5 > V_2O_5 \approx MoO_3 \tag{2.8}$$

This should be matched against the relative Lewis acid site strength of the different oxides. This was investigated by Li and Dixon [113], where the relative strengths were found as:

$$WO_3 > MoO_3 > Cr_2O_3 \tag{2.9}$$

The subsequent step of the mechanism is proton donation. This relies on hydrogen available on the catalyst, which for the oxides will be present as hydroxyl groups. To have proton donating capabilities, Brønsted acid hydroxylgroups must be present on the catalyst surface. In this context the work of Busca showed that the relative Brønsted hydroxyl acidity of different oxides is [111]:

$$WO_3 > MoO_3 > V_2O_5 > Nb_2O_5 \tag{2.10}$$

The trends of Eqs. 2.8-2.10 in comparison to the reaction path of deoxygenation reveals that MoO_3 functions as a catalyst due to the presence of both strong Lewis acid sites and strong Brønsted acid hydroxyl sites. However, Whiffen and Smith [114] investigated HDO of 4-methylphenol over unsupported MoO_3 and MoS_2 in a batch reactor at 41-48 bar and 325-375 °C, and found that the activity of MoO_3 was lower than that for MoS_2 and that the activation energy was higher on MoO_3 than on MoS_2 for this reaction. Thus, MoO_3 might not be the best choice of an oxide type catalyst, but on the basis of Eqs. 2.8-2.10 other oxides seem interesting for HDO. Specifically WO_3 is indicated to have a high availability of acid sites. Echeandia et al. [115] investigated oxides of W and Ni-W on active carbon for HDO of 1 wt%

phenol in n-octane in a fixed bed reactor at 150-300 °C and 15 bar. These catalysts were all proven active for HDO and especially the Ni-W system had potential for complete conversion of the model compound. Furthermore, a low affinity for carbon was observed during the 6 h of experiments. This low value was ascribed to a beneficial effect from the non-acidic carbon support (cf. Section 2.4.1.3).

2.4.1.2 Transition Metal Catalysts

Selective catalytic hydrogenation can also be carried out with transition metal catalysts. Mechanistic speculations for these systems have indicated that the catalysts should be bi-functional, which can be achieved in other ways than the system discussed in Section 2.4.1.1. The bi-functionality of the catalyst implies two aspects. On one hand, the activation of oxy-compounds is needed, which likely could be achieved using the valence of an oxide form of a transition metal or on an exposed cation, often associated with the catalyst support. This should be combined with a possibility for hydrogen donation to the oxy-compound, which could take place on transition metals, as they have the potential to activate H_2 [116–119]. The combined mechanism is exemplified in Figure 2.5, where the adsorption and activation of the oxy-compound are illustrated to take place on the support.

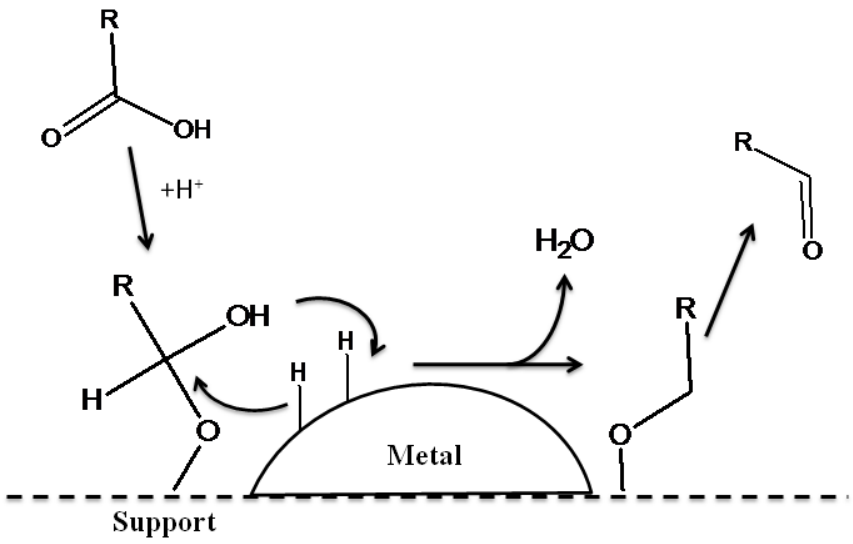

Figure 2.5: *HDO mechanism over transition metal catalysts. This mechanism drawn on the basis of information from references [117, 119].*

The mechanism of hydrogenation over supported noble metal systems is still debated. Generally it is acknowledged that the metals constitute the hydrogen donating sites, but oxy-compound activation has been proposed to either be facilitated on the metal sites [120–122] or at the metal-support interface (as illustrated in Figure 2.5) [122–124]. This indicates that these catalytic systems potentially could have the affinity for two different reaction paths, since many of the noble metal catalysts are active for HDO.

A study by Gutierrez et al. [77] investigated the activity of Rh, Pd, and Pt supported on ZrO_2 for HDO of 3 wt% guaiacol in hexadecane in a batch reactor at 80 bar and 100 °C. They reported that the apparent activity of the three was:

$$Rh/ZrO_2 > Co\text{-}MoS_2/Al_2O_3 > Pd/ZrO_2 > Pt/ZrO_2 \tag{2.11}$$

Figure 2.6 shows the results from another study of noble metal catalysts by Wildschut et al. [68, 125]. Here Ru/C, Pd/C, and Pt/C were investigated for HDO of beech bio-oil in a batch reactor at 350 °C and 200 bar over 4 h. Ru/C and Pd/C appeared to be good catalysts for the process as they displayed high degrees of deoxygenation and high oil yields, relative to Co-MoS_2/Al_2O_3 and Ni-MoS_2/Al_2O_3 as benchmarks.

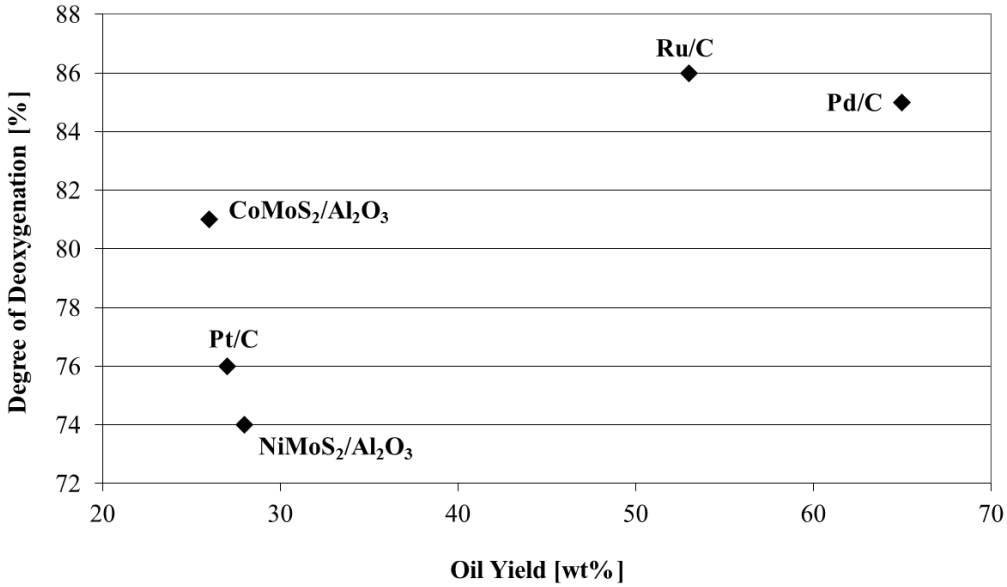

Figure 2.6: *Comparison of Ru/C, Pd/C, Pt/C, Co-MoS_2/Al_2O_3 and Ni-MoS_2/Al_2O_3 as catalysts for HDO, evaluated on the basis of the degree of deoxygenation and oil yield. Experiments were performed with beech bio-oil in a batch reactor at 350 °C and 200 bar over 4 h. Data are from Wildschut et al. [68, 125].*

Through experiments in a batch reactor setup with synthetic bio-oil (mixture of compounds representative of the real bio-oil) at 350 °C and ca. 10 bar of nitrogen, Fisk et al. [126] found that Pt/Al_2O_3 displayed catalytic activity for both HDO and steam reforming and therefore could produce H_2 in situ. This approach is attractive as the expense for hydrogen supply is considered as one of the disadvantages of the HDO technology. However, the catalyst was reported to suffer from significant deactivation due to carbon formation.

To summarize, the noble metal catalysts Ru, Rh, Pd, and possibly also Pt appear to be potential catalysts for the HDO synthesis, but the high price of the metals make them unattractive.

As alternatives to the noble metal catalysts a series of investigations of base metal catalysts have been performed, as the prices of these metals are significantly lower [127]. Yakovlev et al. [116] investigated nickel based catalysts for HDO of anisole in a fixed bed reactor at temperatures in the range from 250-400 °C and pressures in the range from 5-20 bar. In Figure 2.7 the results of these experiments are shown. Specifically Ni-Cu had potential for complete elimination of the oxygen content in anisole. Unfortunately, this comparison only gives a vague idea about how the nickel based catalysts compare to other catalysts. Quantification of the activity and affinity

for carbon formation of these catalysts relative to noble metal catalysts such as Ru/C and Pd/C or relative to Co-MoS_2 would be interesting.

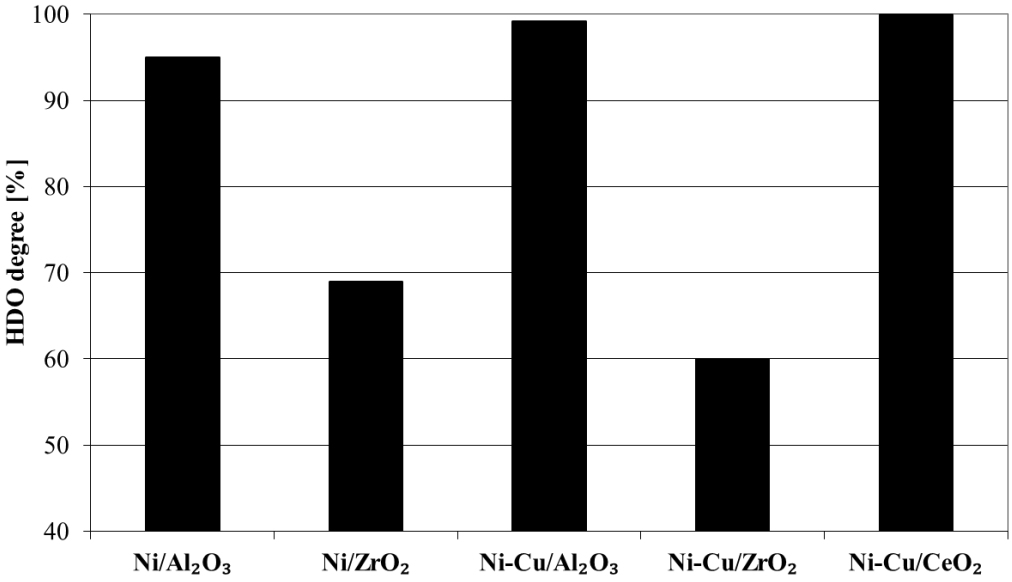

Figure 2.7: *Performance of nickel based catalysts for HDO. HDO degree is the ratio between the concentrations of oxygen free product relative to all products. Experiments performed with anisole in a fixed bed reactor at 300 °C and 10 bar. Data from Yakovlev et al. [116].*

Zhao et al. [128] measured the activity for HDO in a fixed bed reactor where a hydrogen/nitrogen gas was saturated with gaseous guaiacol (H_2/guaiacol molar ratio of 33) over phosphide catalysts supported on SiO_2 at atmospheric pressure and 300 °C. On this basis the following relative activity was found:

$$Ni_2P/SiO_2 > Co_2P/SiO_2 > Fe_2P/SiO_2 > WP/SiO_2 > MoP/SiO_2 \tag{2.12}$$

All the catalysts were found less active than Pd/Al_2O_3, but more stable than Co-MoS_2/Al_2O_3. Thus, the attractiveness of these catalysts is in their higher availability and lower price, compared to noble metal catalysts.

A different approach for HDO with transition metal catalysts was published by Zhao et al. [129–131]. In these studies it was reported that phenols could be hydrogenated by using a heterogeneous aqueous system of a metal catalyst mixed with a mineral acid in a phenol/water (0.01 mol/4.4 mol) solution at 200-300 °C and 40 bar over a period of 2 h. In these systems hydrogen donation proceeds from the metal, followed by water extraction with the mineral acid, whereby deoxygenation can be achieved [129]. Both Pd/C and Raney® Ni (nickel-alumina alloy) were found to be effective catalysts when combined with Nafion/SiO_2 as mineral acid [130]. However, this concept has so far only been shown in batch experiments. Furthermore the influence of using a higher phenol concentration should be tested to evaluate the potential of the system.

Overall it is apparent that alternatives to both the sulfur containing type catalysts and noble metal type catalysts exist, but these systems still need additional development in order to evaluate their full potential.

2.4.1.3 Supports

The choice of carrier material is an important aspect of catalyst formulation for HDO [116].

Al_2O_3 has been shown to be an unsuitable support, as it in the presence of larger amounts of water it will convert to boemite (AlO(OH)) [15, 39, 132]. An investigation of Laurent and Delmon [132] on Ni-MoS_2/γ-Al_2O_3 showed that the formation of boemite resulted in the oxidation of nickel on the catalyst. These nickel oxides were inactive with respect to HDO and could further block other Mo or Ni sites on the catalyst. By treating the catalyst in a mixture of dodecane and water for 60 h, a decrease by two thirds of the activity was seen relative to a case where the catalyst had been treated in dodecane alone [39, 132].

Additionally, Popov et al. [133] found that 2/3 of alumina was covered with phenolic species when saturating it at 400 °C in a phenol/argon flow. The observed surface species were believed to be potential carbon precursors, indicating that a high affinity for carbon formation exists on this type of support. The high surface coverage was linked to the relative high acidity of Al_2O_3.

As an alternative to Al_2O_3, carbon has been found to be a more promising support [68, 115, 134–136]. The neutral nature of carbon is advantageous, as this gives a lower tendency for carbon formation compared to Al_2O_3 [115, 134]. Also SiO_2 has been indicated as a prospective support for HDO as it, like carbon, has a general neutral nature and therefore has a relatively low affinity for carbon formation [128]. Popov et al. [133] showed that the concentration of adsorbed phenol species on SiO_2 was only 12% relative to the concentration found on Al_2O_3 at 400 °C. SiO_2 only interacted with phenol by hydrogen bonds, but on Al_2O_3 dissociation of phenol to more strongly adsorbed surface species on the acid sites was observed [137].

ZrO_2 and CeO_2 have also been identified as potential carrier materials for the synthesis. ZrO_2 has some acidic character, but significantly less than Al_2O_3 [138–140]. ZrO_2 and CeO_2 are thought to have the potential to activate oxy-compounds on their surface, as shown in Figure 2.5, and thereby increase activity. Thus, they seem attractive in the formulation of new catalysts, see also Figure 2.7 [77, 116, 138, 141].

Overall two aspects should be considered in the choice of support. On one hand the affinity for carbon formation should be low, which to some extent is correlated to the acidity (which should be low). Secondly, it should have the ability to activate oxy-compounds to facilitate sufficient activity. The latter is especially important when dealing with base metal catalysts, as discussed in Section 2.4.1.2.

2.4.2 Kinetic Models

A thorough review of several model compound kinetic studies has been made by Furimsky [40]. However, sparse information on the kinetics of HDO of bio-oil is

available; here mainly lumped kinetic expressions have been developed, due to the diversity of the feed.

Sheu et al. [75] investigated the kinetics of HDO of pine bio-oil between ca. 300-400 °C over $Pt/Al_2O_3/SiO_2$, $Co\text{-}MoS_2/Al_2O_3$, and $Ni\text{-}MoS_2/Al_2O_3$ catalysts in a packed bed reactor. These were evaluated on the basis of a kinetic expression of the type:

$$-\frac{dm_{oxy}}{dZ} = k \cdot m_{oxy}^{m} \cdot P^{n} \tag{2.13}$$

Here m_{oxy} is the mass of oxygen in the product relative to the oxygen in the raw pyrolysis oil, Z is the axial position in the reactor, k is the rate constant given by an Arrhenius expression, P is the total pressure (mainly H_2), m is the reaction order for the oxygen, and n is the reaction order for the total pressure. In the study it was assumed that all three types of catalyst could be described by a first order dependency with respect to the oxygen in the pyrolysis oil (i.e. $m = 1$). On this basis the pressure dependency and activation energy could be found, which are summarized in Table 2.6. Generally a positive effect of an increased pressure was reported as n was in the range from 0.3-1. The activation energies were found in the range from 45.5-71.4 kJ/mol, with $Pt/Al_2O_3/SiO_2$ having the lowest activation energy. The lower activation energy for the Pt catalyst was in agreement with an observed higher degree of deoxygenation compared to the two other. The results of this study are interesting, however, the rate term of Eq. 2.13 has a non-fundamental form as the use of mass related concentrations and especially using the axial position in the reactor as time dependency makes the term very specific for the system used. Thus, correlating the results to other systems could be difficult. Furthermore, the assumption of a general first order dependency for m_{oxy} is a very rough assumption when developing a kinetic model.

Table 2.6: *Kinetic parameters for the kinetic model in Eq. 2.13 of different catalysts. Experiments performed in a packed bed reactor between ca. 300-400 °C and 45-105 bar. Data are from Sheu et al. [75].*

Catalyst	m	n	E_a [kJ/mol]
$Pt/Al_2O_3/SiO_2$	1	1.0	45.5 ± 3.2
$Co\text{-}MoS_2/Al_2O_3$	1	0.3	71.4 ± 14.6
$Ni\text{-}MoS_2/Al_2O_3$	1	0.5	61.7 ± 7.1

A similar approach to that of Sheu et al. [75] was made by Su-Ping et al. [90], where $Co\text{-}MoS_2/Al_2O_3$ was investigated for HDO of bio-oil in a batch reactor between 360-390 °C. Here a general low dependency on the hydrogen partial pressure was found over a pressure interval from 15 bar to 30 bar, so it was chosen to omit the pressure dependency. This led to the expression:

$$-\frac{dC_{oxy}}{dt} = k \cdot C_{oxy}^{2.3} \tag{2.14}$$

Here C_{oxy} is the total concentration of all oxygenated molecules. A higher reaction order of 2.3 was found in this case, compared to the assumption of Sheu et al. [75]. The quite high apparent reaction order may be correlated with the activity of

the different oxygen-containing species; the very reactive species will entail a high reaction rate, but as these disappear a rapid decrease in the rate will be observed (cf. discussion in Section 2.4). The activation energy was in this study found to be 91.4 kJ/mol, which is somewhat higher than that found by Sheu et al. [75].

Massoth et al. [72] on the other hand established a kinetic model of the HDO of phenol on Co-MoS_2/Al_2O_3 in a packed bed reactor based on a Langmuir-Hinshelwood type expression:

$$-\frac{dC_{Phe}}{d\tau} = \frac{k_1 \cdot K_{Ads} \cdot C_{Phe} + k_2 \cdot K_{Ads} \cdot C_{Phe}}{(1 + C_{Phe,0} \cdot K_{Ads} \cdot C_{Phe})^2} \tag{2.15}$$

Here C_{Phe} is the phenol concentration, $C_{Phe,0}$ the initial phenol concentration, K_{Ads} the equilibrium constant for adsorption of phenol on the catalyst, τ the residence time, and k_1 and k_2 rate constants for respectively a direct deoxygenation path (cf. Eq. 2.1) and a hydrogenation path (cf. Eq. 2.2). It is apparent that in order to describe HDO in detail all contributing reaction paths have to be regarded. This is possible when a single molecule is investigated. However, expanding this analysis to a bio-oil reactant will be too comprehensive, as all reaction paths will have to be considered.

Overall it can be concluded that describing the kinetics of HDO is complex due to the nature of a real bio-oil feed.

2.4.3 Deactivation

A pronounced problem in HDO is deactivation. This can occur by poisoning with nitrogen species or water, sintering of the catalyst, metal deposition (specifically alkali metals), or coking [42, 84]. The extent of these phenomena is dependent on the catalyst, but carbon deposition has proven to be a general problem and one of the main paths of catalyst deactivation [142].

Carbon is principally formed by polymerization and polycondensation reactions on the catalytic surface, forming polyaromatic species. This results in the blockage of the active sites on the catalysts [142]. Specifically for Co-MoS_2/Al_2O_3, it has been shown that carbon builds up quickly due to strong adsorption of polyaromatic species. These fill up the pore volume of the catalyst during the start up of the system. In a study of Fonseca et al. [143, 144], it was reported that about one third of the total pore volume of a Co-MoS_2/Al_2O_3 catalyst was occupied with carbon during this initial carbon deposition stage and hereafter a steady state was observed where further carbon deposition was limited [142].

The rates of the carbon forming reactions are to a large extent controlled by the feed to the system, but process conditions also play an important role. With respect to hydrocarbon feeds, alkenes and aromatics have been reported as having the largest affinity for carbon formation, due to a significantly stronger interaction with the catalytic surface relative to saturated hydrocarbons. The stronger binding to the surface will entail that the conversion of the hydrocarbons to carbon is more likely. For oxygen containing hydrocarbons it has been identified that compounds with more than one oxygen atom appears to have a higher affinity for carbon formation by polymerization reactions on the catalysts surfaces [142].

Coking increases with increasing acidity of the catalyst; influenced by both Lewis and Brønsted acid sites. The principle function of Lewis acid sites is to bind species to

the catalyst surface. Brønsted sites function by donating protons to the compounds of relevance, forming carbocations which are believed to be responsible for coking [142]. This constitute a problem as acid sites are also required in the mechanism of HDO (cf. Figure 2.4). Furthermore, it has been found that the presence of organic acids (as acetic acid) in the feed will increase the affinity for carbon formation, as this catalyzes the thermal degradation path [125].

In order to minimize carbon formation, measures can be taken in the choice of operating parameters. Hydrogen has been identified as efficiently decreasing the carbon formation on Co-MoS_2/Al_2O_3 as it will convert carbon precursors into stable molecules by saturating surface adsorbed species, as for example alkenes [142, 145].

Temperature also affects the formation of carbon. At elevated temperatures the rate of dehydrogenation increases, which gives an increase in the rate of polycondensation. Generally an increase in the reaction temperature will lead to increased carbon formation [142].

The loss of activity due to deposition of carbon on Co-MoS_2/Al_2O_3 has been correlated with the simple model [146]:

$$k = k_0 \cdot (1 - \Theta_C) \tag{2.16}$$

Here k is the apparent rate constant, k_0 is the rate constant of an un-poisoned catalyst, and Θ_C is the fractional coverage of carbon on the catalyst's active sites. This expression describes the direct correlation between the extent of carbon blocking of the surface and the extent of catalyst deactivation and indicates an apparent proportional effect [142].

2.5 Zeolite Cracking

Catalytic upgrading by zeolite cracking is related to fluid catalytic cracking (FCC), where zeolites are also used [82]. Compared to HDO, zeolite cracking is not as well developed at present, partly because the development of HDO to a large extent has been extrapolated from HDS. It is not possible to extrapolate zeolite cracking from FCC in the same degree [57, 83, 147].

In zeolite cracking, all the reactions of Figure 2.1 take place in principle, but the cracking reactions are the primary ones. The conceptual complete deoxygenation reaction for the system can be characterized as (the reaction is inspired by Bridgwater [57, 83] and combined with the elemental composition of bio-oil specified in Table 2.3 normalized to carbon):

$$CH_{1.4}O_{0.4} \longrightarrow 0.9\text{"}CH_{1.2}\text{"} + 0.1CO_2 + 0.2H_2O \tag{2.17}$$

With "$CH_{1.2}$" being an unspecified hydrocarbon product. As for HDO, the bio-oil is converted into at least three phases in the process: oil, aqueous, and gas.

Typically, reaction temperatures in the range from 300 to 600 °C are used for the process [69, 148]. Williams et al. [80] investigated the effect of temperature on HZSM-5 catalysts for upgrading of bio-oil in a fixed bed reactor in the temperature range from 400-550 °C, illustrated in Figure 2.8. An increased temperature resulted in a decrease in the oil yield and an increase in the gas yield. This is due to an increased rate of cracking reactions at higher temperatures, resulting in the production of the

smaller volatile compounds. However, in order to decrease the oxygen content to a significant degree the high temperatures were required. In conclusion, it is crucial to control the degree of cracking. A certain amount of cracking is needed to remove oxygen, but if the rate of cracking becomes too high, at increased temperatures, degradation of the bio-oil to light gases and carbon will occur instead.

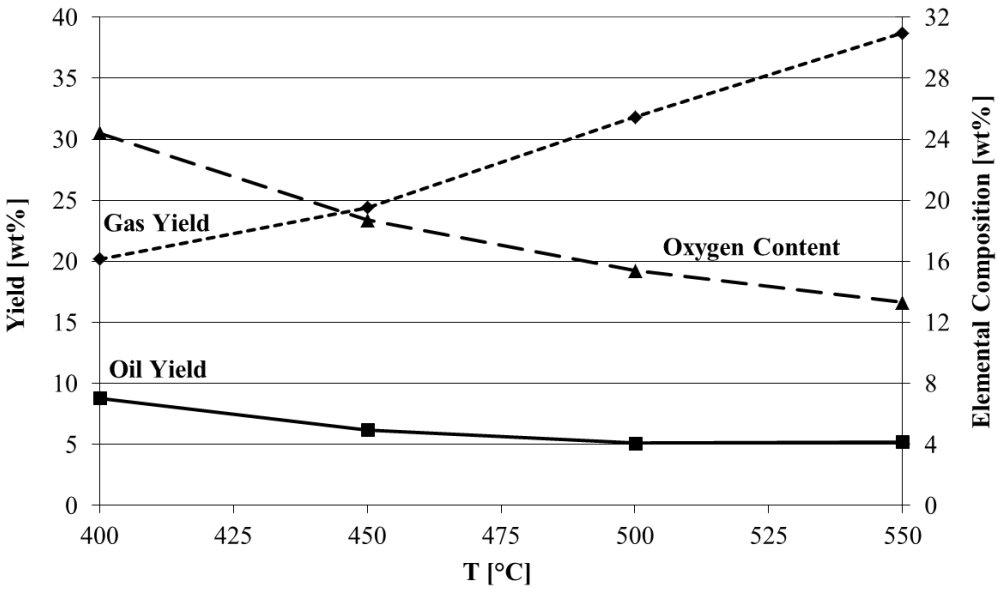

Figure 2.8: *Yields of oil and gas compared to the elemental oxygen content in the oil from a zeolite cracking process as a function of temperature. Experiments were performed with a HZSM-5 catalyst in a fixed bed reactor for bio-oil treatment. Yields are given relative to the initial biomass feed. Data are from Williams and Horne [80].*

In contrast to the HDO process, zeolite cracking does not require co-feeding of hydrogen and can therefore be operated at atmospheric pressure. The process should be carried out with a relatively high residence time to ensure a satisfying degree of deoxygenation, i.e. LHSV around 2 h^{-1} [29]. However, Vitolo et al. [149] observed that by increasing the residence time, the extent of carbon formation also increased. Once again the best compromise between deoxygenation and limited carbon formation needs to be found.

In the case of complete deoxygenation the stoichiometry of Eq. 2.17 predicts a maximum oil yield of 42 wt%, which is roughly 15 wt% lower than the equivalent product predicted for HDO [57]. The reason for this lower yield is because the low H/C ratio of the bio-oil imposes a general restriction in the hydrocarbon yield [43]. The low H/C ratio of the bio-oil also affects the quality of the product, as the effective H/C ratio ($(\mathrm{H/C})_{eff}$) of the product from a FCC unit can be calculated as [82, 150]:

$$(\mathrm{H/C})_{eff} = \frac{\mathrm{H} - 2 \cdot \mathrm{O} - 3 \cdot \mathrm{N} - 2 \cdot S}{\mathrm{C}} \tag{2.18}$$

Here the elemental fractions are given in mole%. Calculating this ratio on the basis of a representative bio-oil (35 mole% C, 50 mole% H, and 15 mole% O, cf. Table 2.3) gives a ratio of 0.55. This value indicates that a high affinity for carbon exist in the process, as an H/C ratio toward 0 implies a carbonaceous product.

The calculated $(H/C)_{eff}$ values should be compared to the H/C ratio of 1.47 obtained for HDO oil in Eq. 2.6 and the H/C ratio of 1.5-2 for crude oil [14, 15]. Some zeolite cracking studies have obtained H/C ratios of 1.2, but this has been accompanied with oxygen contents of 20 wt% [78, 80].

The low H/C ratio of the zeolite cracking oil implies that hydrocarbon products from these reactions typically are aromatics and further have a generally low HV relative to crude oil [41, 57].

Experimental zeolite cracking of bio-oil has shown yields of oil in the 14-23 wt% range [151]. This is significantly lower than the yields predicted from Eq. 2.17, with the difference being due to pronounced carbon formation in the system during operation, constituting 26-39 wt% of the product [151].

2.5.1 Catalysts & Reaction Mechanisms

Zeolites are three-dimensional porous structures. Extensive work has been conducted in elucidating their structure and catalytic properties [152–157].

The mechanism for zeolite cracking is based on a series of reactions. Hydrocarbons are converted to smaller fragments by general cracking reactions. The actual oxygen elimination is associated with dehydration, decarboxylation, and decarbonylation, with dehydration being the main route [158].

The mechanism for zeolite dehydration of ethanol was investigated by Chiang and Bhan [159] and is illustrated in Figure 2.9. The reaction is initiated by adsorption on an acid site. After adsorption, two different paths were evaluated, either a decomposition route or a bimolecular monomer dehydration (both routes are shown in Figure 2.9). Oxygen elimination by decomposition was concluded to occur with a carbenium ion acting as a transition state. On this basis a surface ethoxide is formed, which can desorb to form ethylene and regenerate the acid site. For the bimolecular monomer dehydration, two ethanol molecules should be present on the catalyst, whereby diethylether can be formed. Preference for which of the two routes is favored was concluded by Chiang and Bhan [159] to be controlled by the pore structure of the zeolite, with small pore structures favoring the less bulky ethylene product. Thus, product distribution is also seen to be controlled by the pore size, where deoxygenation of bio-oil in medium pore size zeolites (ca. 5-6 Å) gives increased production of C_6-C_9 compounds and larger pores (ca. 6-8 Å) gives increased production of C_9-C_{12} [160].

The decomposition reactions occurring in the zeolite are accompanied by oligomerisating reactions, which in the end produces a mixture of light aliphatic hydrocarbons (C_1-C_6) and larger aromatic hydrocarbons (C_6-C_{10}) [161]. The oligomerizing reaction mechanism is also based on the formation of carbenium ions as intermediates [162]. Thus, formation of carbenium ions is essential in all relevant reaction mechanisms [158, 159, 161–164].

In the choice of catalysts the availability of acid sites is important. This tendency has also been described for petroleum cracking zeolites, where a high availability of acid sites leads to extensive hydrogen transfer and thereby produces a high gasoline fraction. However, carbon forming mechanisms are also driven by the hydrogen transfer, so the presence of many acid sites will also increase this fraction. When discussing aluminosilicate zeolites the availability of acid sites is related to the Si/Al

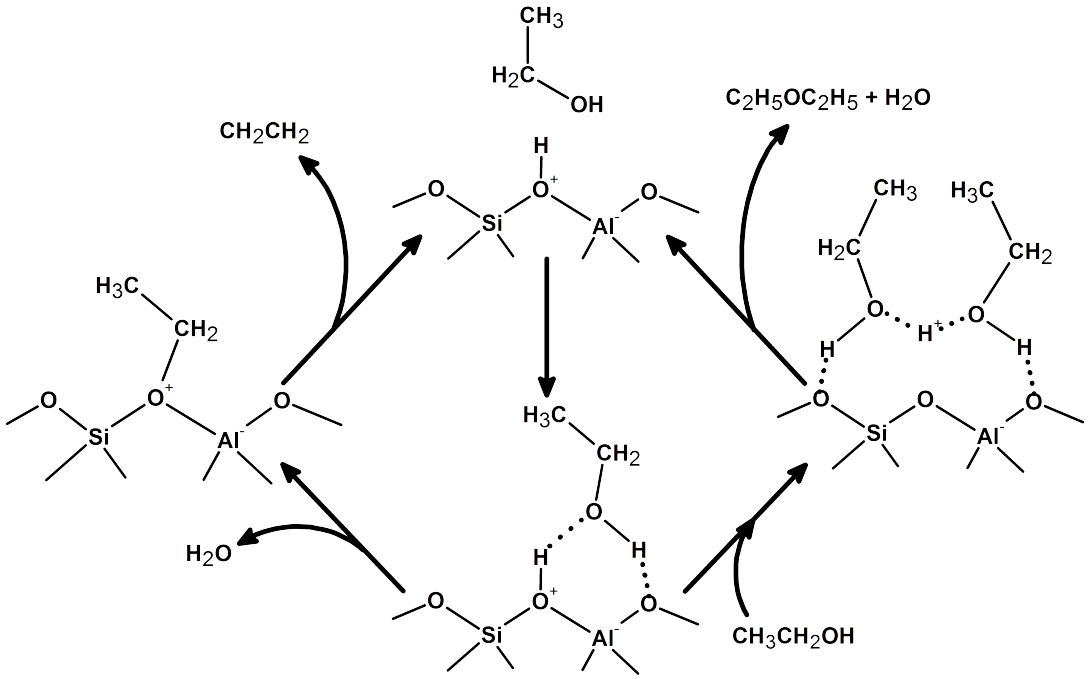

Figure 2.9: *Dehydration mechanism for ethanol over zeolites. The left route is the decomposition route and the right route is the bimolecular monomer dehydration. The mechanism is drawn on the basis of information from Chiand and Bhan [159].*

ratio, where a high ratio entails few alumina atoms in the structure leading to few acid sites, and a low Si/Al ratio entails many alumina atoms in the structure, leading to many acid sites [164].

Different types of zeolites have been investigated for the zeolite cracking process of both bio-oil and model compounds, as seen from Table 2.4, with HZSM-5 being the most frequently tested [69, 78, 79, 149, 160, 161, 163, 165–173]. Adjaye et al. [79, 160] performed some of the initial catalyst screening studies by investigating HZSM-5, H-mordenite, H-Y, silica-alumina, and silicalite in a fixed bed reactor fed with aspen bio-oil and operated between 330-410 °C. In these studies it was found that the activity of the catalysts followed the order:

$$\begin{aligned}&\text{HZSM-5 (5.4 Å)} > \text{H-mordenite (6.7 Å)} > \text{H-Y (7.4 Å)}\\&> \text{silica-alumina (31.5 Å)} > \text{silicalite (5.4 Å)}\end{aligned} \tag{2.19}$$

With the number in the parentheses being the average pore sizes of the zeolites. Practically, silicalite does not contain any acid sites as it is a polymorph structure of Si. In comparison, HZSM-5 is rich in both Lewis and Brønsted acid sites. The above correlation therefore shows that the activity of zeolite cracking catalysts are highly dependent on the availability of acid sites [160].

Overall, tuning of the acid sites availability is important in designing the catalyst, as it affects the selectivity of the system, but also the extent of carbon formation. Many acid sites give a high yield of gasoline, but this will also lead to a high affinity for carbon formation as both reactions are influenced by the extent of acid sites [164].

2.5.2 Kinetic Models

Only a few kinetic investigations have been reported for zeolite cracking systems.

On the basis of a series of model compound studies, Adjaye and Bakshi [69, 148] found that the reaction network in zeolite cracking could be described as sketched in Figure 2.10. They suggested that the bio-oil initially separates in two fractions, a volatile and a non-volatile fraction (differentiated by which molecules evaporated at 200 °C under vacuum). The non-volatile fraction can be converted into volatiles due to cracking reactions. Besides this, the non-volatiles can either polymerize to form residue or condensate/polymerize to form carbon, with residue being the fraction of the produced oil which does not evaporate during vacuum distillation at 200 °C. The volatile fraction is associated with the formation of the three fractions in the final product: the oil fraction, the aqueous fraction, and the gas fraction. Furthermore the volatiles can react by polymerization or condensation reactions to form residue or carbon.

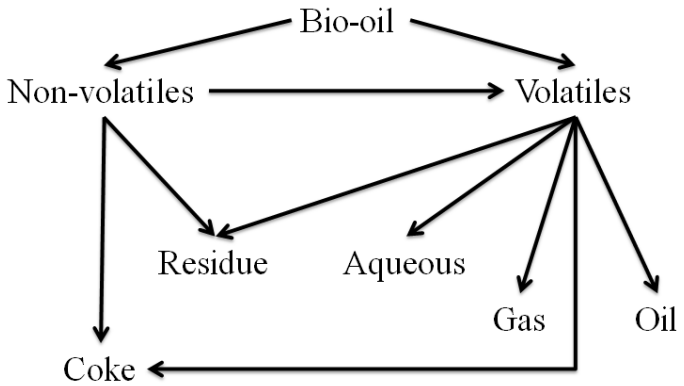

Figure 2.10: *Reaction network for the kinetic model described in Eqs. 2.20-2.26.*

This reaction network was used in the formulation of a kinetic model, which was fitted to experiments with aspen bio-oil over HZSM-5 in the temperature range from 330 to 410 °C:

Nonvolatiles:
$$\frac{dC_{NV}}{dt} = k_{NV} \cdot C_B - k_{Cr} \cdot C_{NV}^{0.9} - k_{R1} \cdot C_{NV}^{r1} - k_{C1} \cdot C_{NV}^{c1} \tag{2.20}$$

Volatiles:
$$\frac{dC_V}{dt} = k_V \cdot C_B + k_{Cr} \cdot C_{NV}^{0.9} - k_{Oil} \cdot C_V^o - k_{Gas} \cdot C_V^g - k_{Aqua} \cdot C_V^a - k_{R2} \cdot C_V^{r2} - k_{C2} \cdot C_V^{c2} \tag{2.21}$$

Oil:
$$\frac{dC_{Oil}}{dt} = k_{Oil} \cdot C_V^o \tag{2.22}$$

Aqueous:
$$\frac{dC_{Aqua}}{dt} = k_{Aqua} \cdot C_V^a \tag{2.23}$$

Gas:
$$\frac{dC_{Gas}}{dt} = k_{Gas} \cdot C_V^g \tag{2.24}$$

Carbon:
$$\frac{dC_C}{dt} = k_{C1} \cdot C_{NV}^{c1} + k_{C2} \cdot C_V^{c2} \tag{2.25}$$

Residue:
$$\frac{dC_R}{dt} = k_{R1} \cdot C_{NV}^{r1} + k_{R2} \cdot C_V^{r2} \tag{2.26}$$

Here C_i is the concentration of i, k_i is the rate constant of reaction i, index B means bio-oil, index Cr means cracking, o is the reaction order for oil formation (decreasing from 1 to 0.8 with increasing T), a is the reaction order for the aqueous phase formation (in the interval from 1.4 to 1.6), g is the reaction order for gas formation (increasing from 0.7 to 0.8 with increasing T), $c1$ is the reaction order for carbon formation from non-volatiles (increasing from 0.9 to 1.1 with T), $c2$ is the reaction order for carbon formation from volatiles (ranging from 1.1 to 1.2 with increasing T), $r1$ is the reaction order for carbon formation from non-volatiles (increasing from 1.9 to 2.5 with increasing T), and $r2$ is the reaction order for carbon formation from volatiles (decreasing from 1.5 to 0.7 with increasing T).

Figure 2.11 shows a fit between the model and representative data. Overall the model succeeded in reproducing the experimental data adequately, but this was done on the basis of variable reaction orders, as mentioned above. Thus, the model becomes insufficient to describe the rate correlation in any broad context.

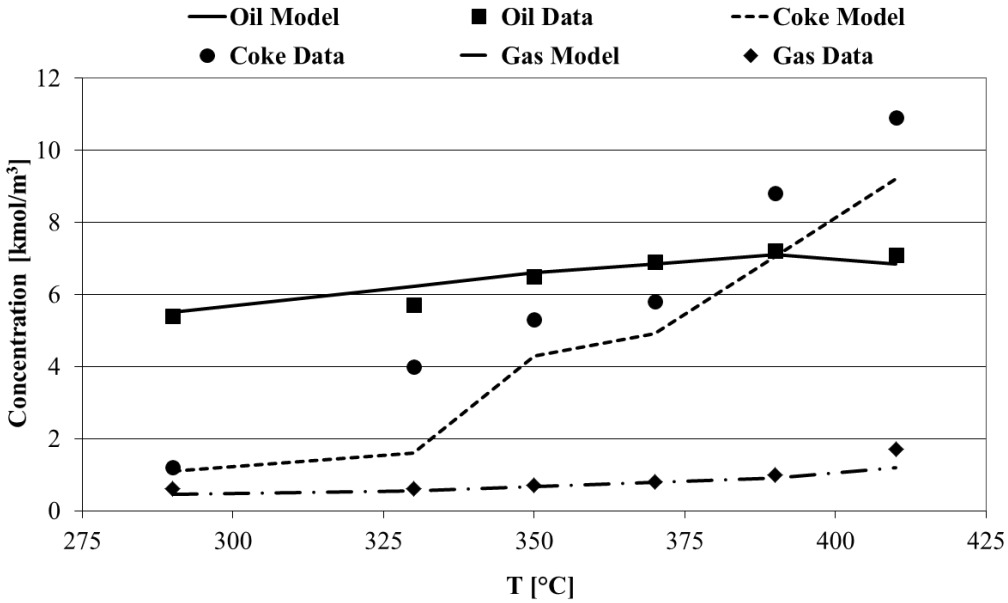

Figure 2.11: *Fit between a kinetic model for zeolite cracking of bio-oil and experimental data. Experiments were performed in a fixed bed reactor with aspen bio-oil as feed and HZSM-5 as catalyst. The figure is reproduced from Adjaye and Bakhshi [70].*

Overall the results of Adjaye and Bakshi [69, 148] display the same problems as observed in the kinetic systems discussed for HDO (Section 2.4.2); the complexity of the feed makes it difficult to create a kinetic description of the system without making a compromise.

2.5.3 Deactivation

As for HDO, carbon deposition and thereby catalyst deactivation constitute a pronounced problem in zeolite cracking.

In zeolite cracking, carbon is principally formed by polymerization and polycondensation reactions, such formation results in the blockage of the pores in the zeolites [164, 167]. Guo et al. [167] investigated the carbon precursors formed during operation of bio-oil over HZSM-5 and found that deactivation was caused by an initial

build-up of high molecular weight compounds, primarily having aromatic structures. These species formed in the inner part of the zeolites and then expanded, resulting in the deactivation of the catalyst.

Gayubo et al. [168] investigated the carbon formed on HZSM-5 during operation with synthetic bio-oil in a fixed bed reactor at 400-450 °C with temperature programmed oxidation (TPO) and found two types of carbon: thermal carbon and catalytic carbon. The thermal carbon was described as equivalent to the depositions on the reactor walls and this was only found in the macropores of the catalyst. The catalytic carbon was found in the micropores of the zeolites and was ascribed to dehydrogenation, condensation, and hydrogen transfer reactions. This was found to have a lower hydrogen content compared to the thermal carbon [168, 174]. In the TPO, the thermal carbon was removed at lower temperatures (450-480 °C) compared to the catalytic carbon, which was removed at 520-550 °C. These observations were assumed due to the catalytic carbon being steric hindered, deposited in the micropores, strongly bound to the acidic sides of the zeolite, and less reactive due to the hydrogen deficient nature. The conclusion of the study was that the catalytic carbon was the principal source of deactivation, as this resulted in blockage of the internal acidic sites of the catalyst, but thermal carbon also contributed to the deactivation.

The study of Huang et al. [164] described that acid sites played a significant role in the formation of carbon on the catalysts. Proton donation from these was reported as a source for hydrocarbon cations. These were described as stabilized on the deprotonated basic framework of the zeolite, which facilitated potential for cracking and aromatization reactions, leading to carbon.

Summarizing, it becomes apparent that carbon forming reactions are driven by the presence of acid sites on the catalyst leading to poly (aromatic) carbon species. The acid sites are therefore the essential part of the mechanism for both the deoxygenating reactions (cf. Section 2.5.1) and the deactivating mechanisms.

Trying to decrease the extent of carbon formation on the catalyst, Zhu et al. [165] investigated co-feeding of hydrogen to anisole over HZSM-5 in a fixed bed reactor at 400 °C. This showed that the presence of hydrogen only decreased the carbon formation slightly. It was suggested that the hydrogen had the affinity to react with adsorbed carbenium ions to form paraffins, but apparently the effect of this was not sufficient to increase the catalyst lifetime in any significant degree. Ausavasukhi et al. [175] reached a similar conclusion in another study of deoxygenation of benzaldehyde over HZSM-5, where it was described that the presence of hydrogen did not influence the conversion. However, a shift in selectivity was observed as an increase in toluene production was observed with H_2, which was ascribed to hydrogenation/hydrogenolysis reactions taking place.

In a study of Peralta et al. [176] co-feeding of hydrogen was investigated for cracking of benzaldehyde over NaX zeolites with and without Cs at 475 °C. The observed conversion as a function of time on stream is shown in Figure 2.12. Comparing the performance of CsNaX and NaX in hydrogen shows that the stability of the CsNaX catalyst was significantly higher as the conversion of this catalyst only decreased by ca. 10% after 8 h, compared to a drop of ca. 75% for NaX. However, as CsNaX has an initial conversion of 100% this drop might not display the actual drop in activity as an overpotential might be present in the beginning of the experiment.

Replacing H_2 with He showed a significant difference for the CsNaX catalyst, as

a much faster deactivation was observed in this case; dropping by ca. 90% over 8 h of operation. It was concluded that H_2 effectively participated in hydrogen transfer reactions over these catalysts, leading to the better stability. Ausavasukhi et al. [175] reported that when using HZSM-5 promoted with gallium for deoxygenation of benzaldehyde in the presence of H_2, the gallium served as hydrogen activating sites, which participated in hydrogenation reactions on the catalyst. Comparing these results to the work by Zhu et al. [165] shows that co-feeding of hydrogen over zeolites has a beneficial effect if a metal is present.

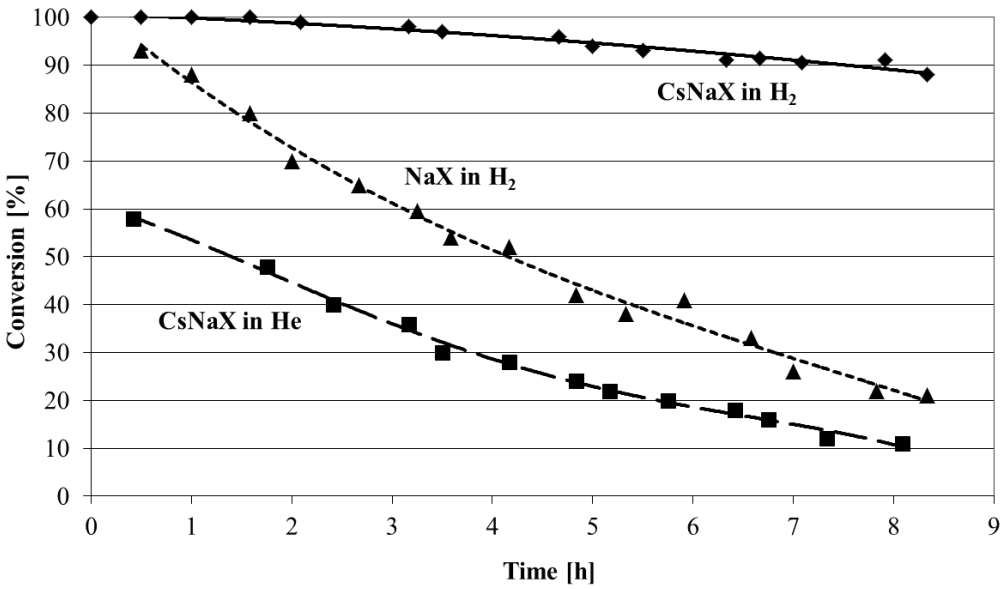

Figure 2.12: *Stability of CsNaX and NaX zeolites for cracking of benzaldehyde with either H_2 or He as carrier gas. Experiments were performed in a fixed bed reactor at 475 °C. Data are from Peralta et al. [176].*

In another approach, Zhu et al. [165] showed that if water was added to an anisole feed and treated over HZSM-5 at 400 °C, the conversion was ca. 2.5 times higher than without water. It was concluded that water actively participated in the reactions on the zeolite. A possible explanation for these observations could be that low partial pressures of steam result in the formation of so called extra-framework alumina species which give an enhanced acidity and cracking activity [177–179]. Thus, it appears that addition of water to the system can have a beneficial effect and constitute a path worth elucidating further, but it should also be kept in mind that bio-oil already has a high water content.

In summary, the results of Zhu et al. [165], Ausavasukhi et al. [175], and Peralta et al. [176] show that a hydrogen source in catalytic cracking has a positive effect on the stability of the system. Thus, it seems that a potential exist for catalysts which are combinations of metals and zeolites and are co-fed with hydrogen. Some initial work has recently been performed by Wang et al. [180] where Pt on ZSM-5 was investigated for HDO of dibenzofuran, but generally this area is unexamined.

Finally, regeneration of zeolite catalysts has been attempted. Vitolo et al. [161] investigated regeneration of a HZSM-5 catalyst which had been operated for 60-120

min in a fixed bed reactor at 450 °C fed with bio-oil. The catalyst was washed with acetone and heated in an oven at 500 °C over 12 h. Nevertheless, a lower catalyst lifetime and deoxygenation degree was found for the regenerated catalyst relative to the fresh. This effect became more pronounced as a function of regeneration cycles. This persistent deactivation was evaluated as being due to a decrease in the availability of acid sites, which decreased by 62% over 5 regeneration cycles.

Guo et al. [78] tried to regenerate HZSM-5 at 600 °C over 12 hours; the catalyst had been used in a fixed bed reactor with bio-oil as feed at 380 °C. Unfortunately the time on stream was not reported. Testing of the catalyst after regeneration showed an increasing oxygen content in the produced oil as a function of regeneration cycles, relative to the fresh catalyst. The fresh catalyst produced oil with 21 wt% oxygen, but after 5 regenerations this had increased to 30 wt%. It was concluded that this was due to a decrease in the amount of exposed active sites on the catalyst.

At elevated steam concentrations it has been found that aluminosilicates can undergo dealumination where the tetrahedral alumina in the zeolite frame is converted into so called partially distorted octahedral alumina atoms. These can diffuse to the outer surface of the zeolite where they are converted into octahedrally coordinated alumina atoms, which are not acidic. Overall this process will entail that the availability of acidic sites in the zeolite will decrease during prolonged exposure to elevated steam concentrations [178, 181]. As Vitolo et al. [161] observed a decrease in the availability of acid sites in the zeolite used for bio-oil upgrading and because bio-oil has a general high water content, it could be speculated that dealumination is inevitably occurring during zeolite cracking of bio-oil and thus regeneration cannot be done.

Overall, the work of Vitolo et al. [161] and Guo et al. [78] are in analogy with traditional FCC where air is used to remove carbon depositions on the catalyst [182], but it appears that this method can not be applied to zeolite cracking of bio-oils. Thus, new strategies are required.

2.6 General Aspects

The grade of the fuels produced from upgrading bio-oil is an important aspect to consider, but depending on the process conditions different product compositions will be achieved. Table 2.7 illustrates what can be expected for the compositions and the characteristics between raw pyrolysis oil, HDO oil, zeolite cracking oil, and crude oil (as a benchmark).

Comparing bio-oil to HDO and zeolite cracking oil, the oxygen content after HDO and zeolite cracking is decreased. In HDO a drop to < 5 wt% is seen, where zeolite cracking only decreases the oxygen content to 13-24 wt%. Therefore a larger increase in the HHV is seen using HDO compared to zeolite cracking. Furthermore, the viscosity at 50 °C ($\mu_{50°C}$) of the HDO oil is lower compared to bio-oil, which improves flow characteristics and is advantageous in further processing. The decrease in the oxygen content also affects the pH value of the oil, as this increases from ca. 3 to about 6 in HDO, i.e. making it almost neutral. Generally, the characteristics of the HDO oil approaches the characteristics of the crude oil more than those of the zeolite cracking oil.

Table 2.7: *Comparison of characteristics of bio-oil, catalytically upgraded bio-oil, and crude oil.*

		Upgraded Bio-oil		
	Bio-oil[a]	HDO[b]	Zeolite Cracking[c]	Crude Oil[d]
Y_{Oil} [wt%]	100	21-65	12-28	-
$Y_{\text{Water Phase}}$ [wt%]	-	13-49	24-28	-
Y_{Gas} [wt%]	-	3-15	6-13	-
Y_{Carbon} [wt%]	-	4-26	26-39	-
		Oil Characteristics		
Water [wt%]	15-30	1.5	-	0.1
pH	2.8-3.8	5.8	-	-
ρ [kg/l]	1.05-1.25	1.2	-	0.86
$\mu_{50°C}$ [cP]	40-100	1-5	-	180
HHV [MJ/kg]	16-19	42-45	21-36[e].	44
C [wt%]	55-65	85-89	61-79	83-86
O [wt%]	28-40	<5	13-24	<1
H [wt%]	5-7	10-14	2-8	11-14
S [wt%]	<0.05	<0.005	-	<4
N [wt%]	<0.4	-	-	<1
Ash [wt%]	<0.2	-	-	0.1
H/C	0.9-1.5	1.3-2.0	0.3-1.8	1.5-2.0
O/C	0.3-0.5	<0.1	0.1-0.3	≈ 0

[a]Data from [14, 15, 41].
[b]Data from [29, 68].
[c]Data from [78, 80].
[d]Data from [14, 15, 41].
[e]Calculated on the basis of Eq. 2.27 [183].

Table 2.7 includes a comparison between the product distribution from HDO and zeolite cracking. Obviously, yields from the two syntheses are significantly different. The principal products from HDO are liquids, especially oil. On the contrary, the main product from zeolite cracking appears to be carbon, which constitutes a significant problem. The low oil yield from zeolite cracking further contains a large elemental fraction of oxygen. For this reason the fuel characteristics of the HDO oil is significantly better, having a HHV of 42-45 MJ/kg compared to only 21-36 MJ/kg for the zeolite cracking oil. Note, however that part of the increase in the HHV of the HDO oil is due to the addition of hydrogen.

Overall, HDO oil can be produced in a larger yield and in a higher fuel grade compared to zeolite cracking oil.

A general concern in both processes is the carbon deposition. Table 2.8 summarizes observed carbon deposition on catalytic systems for both HDO and zeolite cracking after operation. Despite different experimental conditions it is apparent that the extent of carbon formation is more pronounced in zeolite cracking relative to HDO. To give an idea of the extent of the problem; lifetimes of around 100 h for

Pd/C catalysts for HDO of bio-oil in a continuous flow setup at 340 °C were reported by Elliott et al. [76] and other studies have indicated lifetimes of around 200 h for HDO of bio-oil with Co-MoS_2/Al_2O_3 catalysts [57, 184]. For zeolite cracking, Vitolo et al. [161] reported that significant deactivation of HZSM-5 occurred after only 90 min of operation in a continuous flow setup with pine bio-oil at 450 °C due to carbon deposition. Zhu et al. [165] showed that cracking of anisole with HZSM-5 in a fixed bed reactor at 400 °C caused significant deactivation over periods of 6 h. Thus, rapid deactivation is found throughout the literature, where deactivation of zeolite cracking catalysts is more pronounced than that of HDO catalysts.

Table 2.8: *Carbon deposition on different catalysts after operation, given in wt% of total catalyst mass. Data for zeolites in row 1 and 2 are from Park et al. [163], experiments performed in a packed bed reactor at 500 °C over a period of 1h with pine bio-oil. Data for HDO catalysts in row 3 and 4 are from Gutierrez et al. [77], experiments performed in a batch reactor at 300 °C over a period of 4 h with guaiacol.*

Catalyst	Carbon [wt%]
HZSM-5	13.6
Meso-MFI	21.3
Co-MoS_2/Al_2O_3	6.7
Rh/ZrO_2	1.8

Baldauf et al. [74] investigated direct distillation of HDO oil (with ca. 0.6 wt% oxygen). The produced gasoline fraction had an octane number (RON) of 62, which is low compared to 92-98 for commercial gasoline. The diesel fraction had a cetane number of 45, also being low compared to a minimum standard of 51 in Europe [185]. The overall conclusion of this study therefore was that the fuel product was not sufficient for the current infrastructure. Instead it has been found that further processing of both HDO oil and zeolite cracking is needed for production of fuel; as for conventional crude oil [147, 186].

Processing of HDO oil in fluid catalytic cracking (FCC) both with and without co-feeding crude oil has been done. In this approach the remaining oxygen in the HDO oil is converted to CO_2 and H_2O [85, 187]. Mercader et al. [85] found that if HDO oil was fed in a ratio of 20 wt% HDO oil to 80 wt% crude oil to a FCC unit, a gasoline fraction of above 40 wt% could be obtained, despite an oxygen content of up to 28 wt% in the HDO oil. The gasoline fraction proved equivalent to the gasoline from pure crude oil. Furthermore, FCC processing of pure HDO oil was found to produce gasoline fractions equivalent to conventional gasoline, with oxygen content in the HDO oil up to ca. 17 wt% [85].

Elliott et al. [39] investigated upgrading of HDO oil using conventional hydrocracking and found that by treating the HDO oil at 405 °C and 100 bar with a conventional hydrocracking catalyst the oxygen content in the oil decreased to less than 0.8 wt% (compared to 12-18 wt% in the HDO oil). In Table 2.9 the development in the oil composition through the different process steps can be seen. From bio-oil to HDO oil it is seen that the fraction of larger oxygen containing molecules decreases and the fraction of the smaller molecules increases. In the hydrocracking the smaller oxygen containing molecules is converted, in the end giving a pure hy-

drocarbon product. The process was reported to have an overall yield of 0.33-0.64 g oil per g of bio-oil.

Table 2.9: *Oil composition on a water-free basis in mol% through the bio-oil upgrading process as specified by Elliott et al. [39]. The bio-oil was a mixed wood bio-oil. HDO was performed at 340°C, 138 bar and a LHSV of 0.25 with a Pd/C catalyst. Hydrocracking was performed at 405°C, 103 bar and a LHSV of 0.2 with a conventional hydrocracking catalyst.*

	Bio-oil	HDO oil	Hydrocracked oil
Ketones/aldehydes	13.8	25.1	0
Alkanes	0	4.5	82.9
Guaiacols etc.	34.2	10.3	0
Phenolics	10.3	18.6	0
Alcohols	3.5	5.3	0
Aromatics	0	0.9	11.5
Acids/esters	19.8	25.2	0
Furans etc.	11.7	6.8	0
Unknown	6.8	3.4	5.6

2.7 Prospect of Catalytic Bio-oil Upgrading

The prospect of catalytic bio-oil upgrading should be seen not only in a laboratory perspective, but also in an industrial one. Figure 2.13 summarizes the outline of an overall production route from biomass to liquid fuels using HDO. The production is divided into two sections: flash pyrolysis and biorefining.

In the pyrolysis section the biomass is initially dried and grinded to reduce the water content and produce particle sizes in the range of 2-6 mm, which are needed to ensure sufficiently fast heating during the pyrolysis. The actual pyrolysis is here occurring as a circulating fluid bed reactor system where hot sand is used as heating source, but several other routes also exists [13, 42, 44, 45, 52, 62]. The sand is subsequently separated in a cyclone, where the biomass vapor is passed on in the system. By condensing, liquids and residual solids are separated from the incondensable gases. The oil and solid fraction is filtered and the bio-oil is stored or sent to another processing site. The hot off-gas from the condenser is passed on to a combustion chamber, where methane and potentially other hydrocarbons are combusted to heat up the sand for the pyrolysis. The off-gas from this combustion is in the end used to dry the biomass in the grinder to achieve maximum heat efficiency.

To minimize transportation costs, bio-oil production should take place at smaller plants placed close to the biomass source and these should supply a central biorefinery for the final production of the refined bio-fuel. This is illustrated in Figure 2.13 by several trucks supplying feed to the biorefinery section. In this way the bio-refinery plant is not required to be in the immediate vicinity of the biomass source (may be >170 km), as transport of bio-oil can be done at larger distances and still be economically feasible [53, 54].

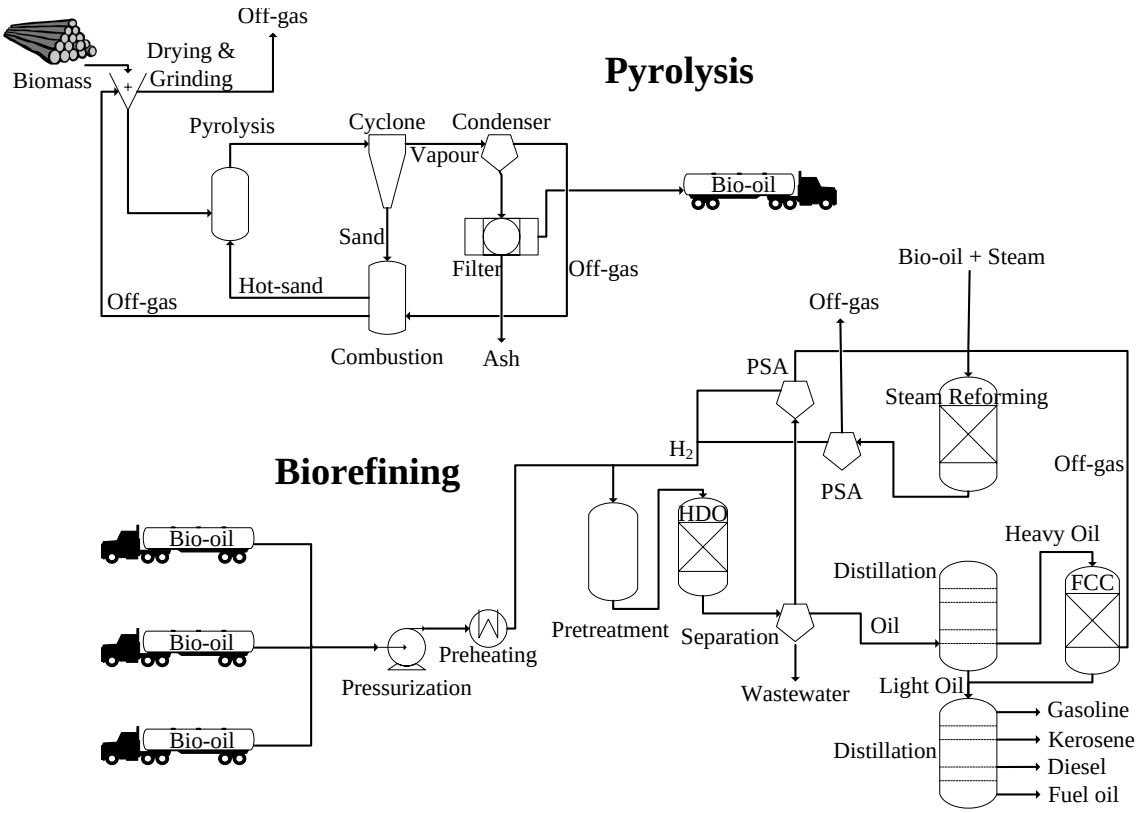

Figure 2.13: *Overall flow sheet for the production of bio-fuels on the basis of catalytic upgrading of bio-oil. The figure is based on information from Jones et al. [22].*

At the biorefinery plant the bio-oil is fed to the system and initially pressurized and heated to 150-280 °C [97, 125]. It has been proposed to incorporate a thermal treatment step without catalyst prior to the catalytic reactor with either the HDO or zeolite catalyst. This should take place between 200-300 °C and can be carried out both with and without the presence of hydrogen. This will prompt the reaction and stabilization of some of the most reactive compounds in the feed and thereby lower the affinity for carbon formation in downstream processes [15, 22, 97, 170, 186]. After the thermal treatment the actual HDO synthesis is prompted, producing oils equivalent to the descriptions of Table 2.7.

The HDO oil is processed by an initial distillation to separate light and heavy oil. The heavy oil fraction is further processed using cracking, which here is illustrated by FCC, but also could be hydrocracking. The cracked oil fraction is hereafter joined with the light oil fraction again. Finally, distillation of the light oil is performed to separate gasoline, diesel, etc.

Off-gasses from the HDO and the FCC should be utilized in the hydrogen production. However, these are not sufficient to produce the required amount of hydrogen for the synthesis, instead additional bio-oil (or another feed) should be supplied to the plant [22]. In the flow sheet of Figure 2.13, steam reforming is shown simplified as a single step followed by hydrogen separation using pressure swing adsorption (PSA). In reality this step is more complex, as heat recovery, feed pre-treatment, and water-gas-shift all would have to be incorporated in such a section, but these details are outside the scope of this study, readers should instead consult references [188–193]. If hydrogen is supplied from steam reforming of bio-oil, as indicated in

Figure 2.13, it would result in a decrease in the fuel production from a given amount of bio-oil by about one third [22]. In the future it is believed that the hydrogen could be supplied using hydrolysis with energy generation on the basis of solar or wind energy, when these technologies are mature [82, 194, 195]. This also offers a route for storage of some of the solar energy.

In between the pyrolysis and the HDO plant a potential stabilization step could be inserted due to the instability of the bio-oil. The necessity of this step depends on a series of parameters: the time the bio-oil should be stored, the time required for transport, and the apparent stability of the specific bio-oil batch. The work of Oasmaa and Kuoppala [60] indicates that utilization of the bio-oil should be done within three months if no measures are taken. Different methods have been suggested in order to achieve increased stability of bio-oil; one being mixing of the bio-oil with alcohols, which should decrease the reactivity [66, 166, 170]. Furthermore a low temperature thermal hydrotreatment (100-200 °C) has been proposed, as this will prompt the hydrodeoxygenation and cracking of some of the most reactive groups [36].

In the design of a catalytic upgrading unit it is relevant to look at the already well established HDS process, where the usual choice is a trickle bed reactor [13, 142, 196, 197]. Such a reactor is illustrated in Figure 2.14. This is essentially a packed bed reactor, but operated in a multiphase regime. In the reactor the reactions occur between the dissolved gas (hydrogen) and the liquid on the catalytic surface. The liquid flow occurs as both film and rivulet flow filling the catalyst pores with liquid [198, 199]. The advantages of using a trickle bed reactor, with respect to the current HDO process, are: the flow pattern resemblance plug flow behavior giving high conversions, low catalyst loss, low liquid/solid ratio ensuring low affinity for homogenous reactions in the oil, relatively low investment costs, and possibility to operate at high pressure and temperature [196, 198].

The HDO process has been evaluated as being a suitable choice in the production of sustainable fuels, due to a high carbon efficiency and thereby a high production potential [14, 36, 195, 200]. In an evaluation by Singh et al. [195] it was estimated that the production capacity on an arable land basis was 30-35 MJ fuel/m^2 land/year for pyrolysis of the biomass followed by HDO, combined with gasification of a portion of the biomass for hydrogen production. In comparison, gasification of biomass followed by Fischer-Tropsch synthesis was in the same study estimated as having a land utilization potential in the order of 21-26 MJ fuel/m^2 land/y. It was further found that the production of fuels by HDO could be increased by aproximately 50% if the hydrogen was supplied from solar energy instead of gasification, thus being 50 MJ fuel/m^2 land/y. However, care should be taken with these results, as they are calculated on the basis of assumed achievable process efficiencies.

A relatively new economic study has been made by the U. S. Department of Energy [22] where all process steps were taken into consideration, in analogy to Figure 2.13, but with natural gas as hydrogen source. The total cost from biomass to gasoline was calculated to be 0.54 \$/l of gasoline, compared to a price of 0.73 \$/l for crude oil derived gasoline in USA at present, excluding distribution, marketing, and taxes [26]. Thus, this work concluded that production of fuels using the HDO

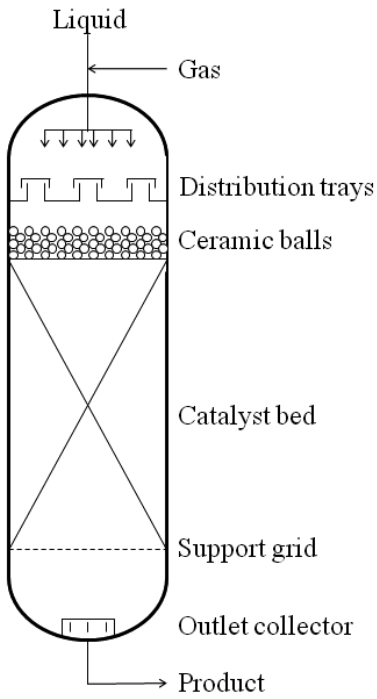

Figure 2.14: *Scheme of a trickle bed reactor. The figure is drawn on the basis of information from Mederos et al. [196].*

synthesis is economically feasible and cost-competitive with crude oil derived fuels. However, a certain uncertainty in the calculated price of the synthetic fuel must be remembered and the reported value is therefore not absolute.

The above discussion only treats the production and prices of the HDO synthesis. To the knowledge of the authors, zeolite cracking has not yet been evaluated as an industrial scale process.

Evaluating zeolite cracking in industrial scale would include some changes relative to Figure 2.13, with the exclusion of hydrogen production as the most evident. Alternatively, the zeolite cracking could be placed directly after the pyrolysis reactor, treating the pyrolysis vapors online [80, 163, 169, 201]. Hong-yu et al. [169] concluded that online upgrading was superior in liquid yield and further indicated that a better economy could be achieved this way, compared to the two separate processes. However, oxygen content was reported as being 31 wt% in the best case scenario, indicating that other aspects of zeolite cracking still should be elucidated prior to evaluating the process in industrial scale.

2.8 Discussion

Catalytic bio-oil upgrading is still a technology in its infancy regarding both HDO and zeolite cracking. Zeolite cracking is the most attractive path due to more attractive process conditions. The low pressure operation and independence of a hydrogen feed could make it easy to implement in industrial scale. However, the high proportion of carbon formed in the process deactivates the zeolites, presently giving it insufficient lifetime. Another concern is the general low grade of the fuel produced, as shown

in Table 2.7. Explicitly, the low heating value entails that the produced fuel will be of a grade too low for utilization in the current infrastructure. Increasing this low fuel grade does not seem possible, as the effective H/C ratio calculated from Eq. 2.18 at maximum can be 0.6; significantly lower than the typical value of crude oil (1.5-2). Furthermore, zeolite cracking has proven unable to give high degrees of deoxygenation, as O/C ratios of 0.6 in the product have been reported (compared to 0 of crude oil). Low H/C ratios and high O/C ratios both contribute to low heating values, as seen from Channiwala's and Parikh's correlation for calculation of the HHV in MJ/kg on the basis of the elemental composition in wt% [183]:

$$HHV = 0.349 \cdot \mathrm{C} + 1.178 \cdot \mathrm{H} - 0.103 \cdot \mathrm{O} - 0.015 \cdot \mathrm{N} + 0.101 \cdot \mathrm{S} - 0.021 \cdot \mathrm{ash} \quad (2.27)$$

Here it is seen that hydrogen contributes positively and oxygen negatively.

We conclude that zeolite cracking cannot produce fuels of sufficient quality to cope with the demands in the current infrastructure. This is in agreement with Huber et al. [29] where the usefulness of the technology was questioned due to the low hydrocarbon yields and high affinity for carbon formation. Zhang et al. [41] expressed concern about the low quality of the fuels, concluding that zeolite cracking was not a promising route for bio-oil upgrading.

The process still seems far from commercial industrial application in our point of view. To summarize, three crucial aspects still has to be improved: product selectivity (oil rather than gas and solids), catalyst lifetime, and product quality.

Overall it is concluded that a hydrogen source is a requirement in order to upgrade bio-oil to an adequate grade fuel, i.e. HDO. However, this route is also far from industrial application. A major concern of this process is the catalyst lifetime, as carbon deposition on these systems has to be solved before steady production can be achieved.

Regarding deactivation mechanisms it appears that sulfur poisoning from the bio-oil has been disregarded so far, as carbon has been a larger problem and because much effort has been focused on the sulfur tolerant Co-MoS_2 and Ni-MoS_2 systems. However, a number of interesting catalysts for hydrodeoxygenation of bio-oil not based on CoMo and NiMo hydrotreating catalysts have been reported recently. With the work by Thibodeau et al. [202], Wildschut et al. [68, 125, 203, 204], Elliott et al. [76], and Yakovlev et al. [116, 205, 206] a turn toward new catalysts such as WO_3, Ru/C, Pd/C, or NiCu/CeO_2 has been indicated. Drawing the parallel to steam reforming where some of these catalysts have been tested, it is well known that even low amounts of sulfur over e.g. a nickel catalyst will result in deactivation of the catalyst [207–209]. As bio-oil is reported to contain up to 0.05 wt% sulfur, deactivation of such catalytic systems seems likely.

Other challenges of HDO involve description of the kinetics, which so far has been limited to either lumped models or compound specific models. Neither of these approaches seems adequate for any general description of the system and therefore much benefit can still be obtained in clarifying the kinetics. Inspiration can be found when comparing to already well established hydrotreating processes, such as HDS and hydrocracking. In industry these systems are described on the basis of a pseudo component approach, where the feed is classified on the basis of either boiling range or hydrocarbon type. In this way the kinetic model treats the kinetics of the

individual fractions on the basis of detailed kinetic investigations on representative model compounds [210, 211]. In order to describe the kinetics of HDO (and zeolite cracking as well) of bio-oil an approach similar to this would probably be necessary, where the division probably should be on the basis of functional groups.

Further elucidation of HDO in industrial scale is also a request. Elaboration of why high pressure operation is a necessity and evaluation of potential transport limitations in the system are still subjects to be treated, they also have been questioned by Venderbosch et al. [15]. Both aspects affect the reactor choice, as the proposed trickle bed reactor in Section 2.7 potentially could be replaced with a better engineering solution.

2.9 Conclusion and Future Tasks

Due to the demand for fuels, the increased build-up of CO_2 in the atmosphere, and the general fact that the oil reserves are depleting, the need of renewable fuels is evident. Biomass derived fuels is in this context a promising route, being the only renewable carbon resource with a sufficiently short reproduction cycle.

Problems with biomass utilization are associated with the high cost of transport due to the low mass and energy density. To circumvent this, local production of bio-oil seems a viable option, being a more energy dense intermediate for processing of the biomass. This process is further applicable with all types of biomass. However, the bio-oil suffers from a high oxygen content, rendering it acidic, unstable, immiscible with oil, and giving it a low heating value. Utilization of bio-oil therefore requires further processing in order to use it as a fuel.

Several applications of bio-oil have been suggested. Deoxygenation seems as one of the most prospective options, which is a method to remove the oxygen containing functional groups. Two different main routes have been proposed for this: HDO and zeolite cracking.

HDO is a high pressure synthesis where oxygen is removed from the oil by hydrogen treatment. This produces oil with low oxygen content and a heating value equivalent to crude oil.

Zeolite cracking is performed at atmospheric pressure in the absence of hydrogen, removing oxygen by cracking reactions. This is attractive from a process point of view, but it has been found unfeasible since the product is a low grade fuel and because of a too high carbon formation (20-40 wt%). The latter results in rapid deactivation of the catalyst.

Overall HDO seems the most promising route for production of bio-fuels by upgrading of bio-oil and the process has further been found economically feasible with production prices equivalent to conventional fuels from crude oil, but challenges still exist within the field. So far the process has been evaluated in industrial scale to some extent, elucidating which unit operations should be performed when going from biomass to fuel. However, aspects of the transport mechanisms in the actual HDO reactor and the high pressure requirement are still untreated subjects which could help optimize the process and bring it closer to industrial utilization. Another great concern within the field is catalyst formulation. Much effort has focused around either the Co-MoS_2 system or noble metal catalysts, but due to a high affinity for carbon formation, and also due to the high raw material prices for the noble met-

als, alternatives are needed. Thus, researchers investigate to substitute the sulphide catalysts with oxide catalysts and the noble catalysts with base metal catalysts. The principal requirement to catalysts are to have a high resistance toward carbon formation and at the same time have a sufficient activity in hydrodeoxygenation.

Overall the conclusion of this review is that a series of fields still have to be investigated before HDO can be used in industrial scale. Future tasks include:

- Catalyst development; investigating new formulations, also in combination with DFT to direct the effort.
- Improved understanding of carbon formation mechanism from classes of compounds (alcohols, carboxylic acids, etc.).
- Better understanding of the kinetics of HDO of model compounds and bio-oil.
- Influence of impurities, like sulfur, in bio-oil on the performance of different catalysts.
- Decrease of reaction temperature and partial pressure of hydrogen.
- Defining the requirement for the degree of oxygen removal in the context of further refining.
- Finding (sustainable) sources for hydrogen.

Chapter 3

Experimental Work

Two different experimental setups were used during this work: a commercial batch reactor from Parr and a custom made high pressure gas and liquid continuous flow fixed bed setup. These are described in Section 3.1 and 3.2, respectively. This chapter also summarizes the general operation of the two setups, data treatment/calculations, catalyst preparation, and catalyst characterization.

3.1 Batch Reactor Setup

3.1.1 Setup Description

Batch experiments were performed in a 4566 Mini Bench Top Reactor Unit from Parr made from Hastelloy C steel and controlled by a 4840 series controller from Parr. The top of the reactor is attached to the support stand of the setup, which ensures that all attachments (as thermocouple, stirrer, feed lines, etc.) are permanently in place. In Figure 3.1(a) a picture of the assembled reactor is shown and in Figure 3.1(c) a schematic drawing is shown.

The reactor container is a 300 ml hollow cylinder. A cover clamp with a total of 6 screws is used to attach and tighten this to the fixed top. A polytetrafluoroethylene (PTFE) gasket is placed between the reactor container and the fixed top. This, combined with recesses in the top face of the cylinder ensures tight sealing of the reactor during operation. The construction of the setup and the used gasket results in a maximum operating temperature of 350 °C and a maximum operating pressure of 200 bar. The minimum volume in the container was evaluated by cold experiments with a transparent reactor to be ca. 30-40 ml to ensure proper mixing by the stirrer and maximum volume is by Parr advised as 2/3 of the maximum volume, i.e. 200 ml.

When assembled, the reactor is surrounded by a furnace, which ensures an uniform heating of the reactor. The output of the furnace is controlled from the controller on the basis of a specified temperature setpoint value (SP).

The fixed top is equipped with a T316 stainless steel Bourbon tube pressure gauge with a 0-3000 psig (0-200 bar) range and a safety rupture disc rated to 3000 psig at 22 °C. The rupture disc will rupture when stressed above 90% of its rating.

(a) Assembled batch reactor setup.

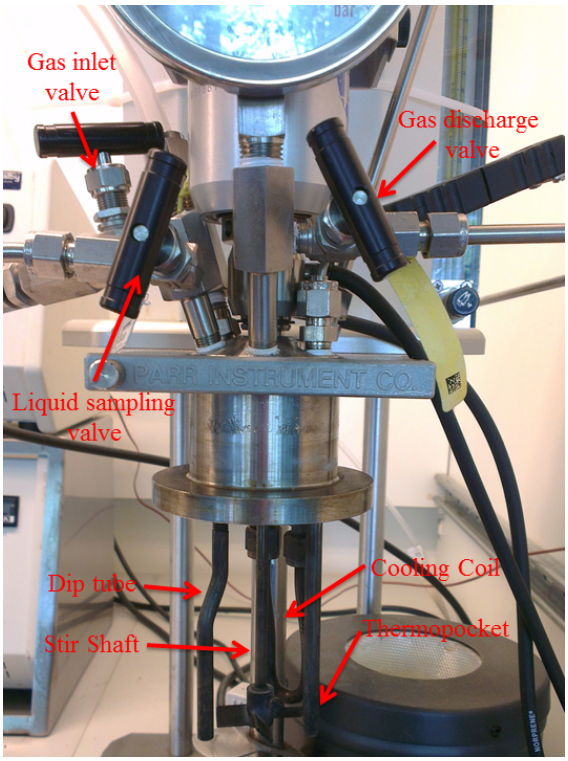

(b) Fixed top of batch reactor.

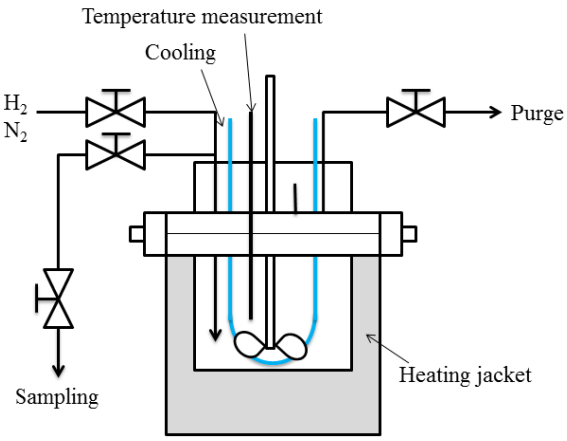

(c) Schematic drawing of batch reactor.

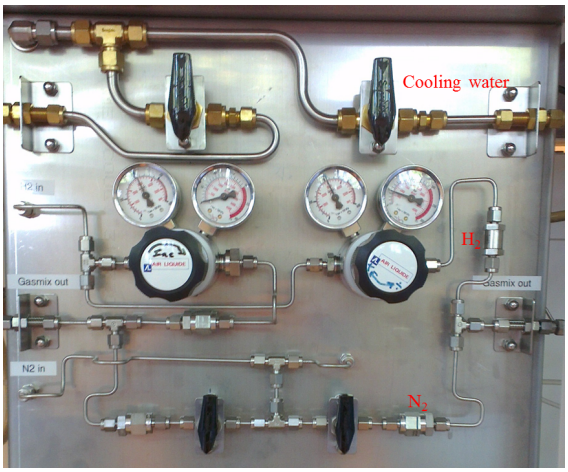

(d) Gas supply panel.

Figure 3.1: *Batch reactor setup used in the current work.*

The stir shaft protrude from the underside of the fixed top to almost the bottom of the reactor container where a propeller is placed with less than 1 cm of free height. This is magnetically driven to ensure tight sealing of the batch and can be adjusted to a speed between 0-700 rpm. Adjustment of the speed is done on a knob on the controller. A cooling sleeve surrounds the magnetic drive which ensures that the epoxy bonding of the magnetic assembly is not heated above 100 °C, where it will break. A constant flow of cooling water is thus needed in this sleeve.

A single loop cooling coil also protrude into the reactor volume, see Figure 3.1(b) and 3.1(c). This is connected to a VWR RC-10 Basic chiller which supplies cooling water of 7±2 °C. Cooling water can be led into the reactor by turning a ball valve prior to the loop. This is used in cases of temperature overshoot or when cooling down the reactor.

A thermocouple type J is inserted in a 1/4" thermopocket running in parallel with the stir shaft and ending at the same height as the bottom of the propeller (see Figure 3.1(b)). This thermocouple supplies the process value (PV) for the controller, which regulates the output to the desired SP by a set of proportional-integral-derivative (PID) parameters.

When operating with liquids in the reactor container, the thermocouple will give a very accurate measurement of the actual temperature in the reaction medium. However, in cases with only gas in the reactor a difference between the bottom of the reactor and the thermocouple will be in the order of 60-120 °C, when operating around a SV of 300 °C. The later aspect must be considered when e.g. reducing catalysts. The evaluation and quantification of this is described further in Appendix B.

Three valves are connected to the fixed top: gas inlet valve, liquid sampling valve, and gas discharge valve. The gas inlet valve is connected to a dip tube with an opening just below the bottom of the stirrer (see Figure 3.1(b)), ensuring that gas is introduced in the liquid phase during normal operation. The liquid sampling valve is also placed on the dip tube. This valve is further connected to a blind peace of 1/4" tube closed by a needle valve. This constellation can be used to withdraw a part of the liquid in the 1/4" tube during operation, which then can be withdrawn with the needle valve when cooled.

The gas discharge valve is connected to an opening on the underside of the fixed top and evacuation of gas will therefore take place from the top of the gas phase.

Gas to the reactor is supplied from a gas supply board, shown in Figure 3.1(d). Nitrogen is supplied from the in-house nitrogen supply and is available from the gas supply board at a pressure of 6 bar. A ball valve is used to control flow to the reactor. Hydrogen (AGA, 99.9%) is supplied from a high pressure hydrogen cylinder. This is regulated with a back pressure valve and can be varied between 1-200 bar.

3.1.2 Experimental Procedure

In a typical experiment, one gram of catalyst was loaded in the reactor and 50 g of phenol (Sigma-Aldrich, $\geq 99\%$) was added. The reactor was flushed three times with nitrogen to remove oxygen in the reactor and hereafter flushed with 10 bar hydrogen. Prior to the experiment, the reactor was pressurized at 50 bar and the stirring was

started at 380-390 rpm, which was kept constant throughout the experiment. The start time was noted as just before the heater was turned on. The heating rate was ~12.5 °C/min. During heating, hydrogen was added in order to reach a final pressure of 100 bar, which was kept constant by further addition of hydrogen throughout the experiment.

To stop the experiment, the reactor was placed in an ice bath and also the internal cooling was used, giving an initial cooling rate of ~50 °C/min. The end of the experiment was when the reactor was lowered into the ice bath. The reactor was cooled sufficiently to ensure condensation of all products.

The resultant product was filtered by suction filtration to separate the product liquid and catalyst. Finally the liquid volume was measured in a measuring cylinder. This final volume was corrected for loss during transferring processes, filtering, and absorption in the pore volume of the catalyst. This loss was quantified by a series of tests where 50 ml of liquid was stirred with 1 g of Ni/SiO_2 in the reactor, filtered, and measured in a measuring cylinder. Three tests with water gave an average loss of 4.1±0.2 ml and three tests with 1-octanol gave an average loss of 4.1±0.1 ml. Thus, a correction of 4.1 ml was used in all experiments.

By 3-fold repetition of a hydrodeoxygenation experiment with Ni/SiO_2, it was found that the procedure typically had an uncertainty in the measured yields of ±2 mol%, corresponding to <5% as the relative standard deviation. Overall, the repeatability of the experiments was good.

In a blank experiment without catalyst, 10 g of phenol and 40 ml of H_2O were allowed to react for 4 h at 275 °C and 100 bar. Almost no catalytic activity was seen in this case as a conversion of 0.3% was observed. Thus, the reactor was hardly catalytically active and did not influence the experiments. The blank experiment was repeated occasionally to ensure that the reactor was not contaminated over time.

3.1.2.1 Alternative Experiments

Some catalytic activity measurements were performed with a mixture of 10 g of phenol in 40 ml of deionized water as feedstock, because low levels of conversion were observed in this series of experiments. Addition of water was required as a solvent for phenol, as the reactant is solid at room temperature and therefore difficult to work with in the product separation and gas chromatography (GC) analysis.

In some cases, shorter experiments had to be performed not to reach 100% conversion. Here the batch reactor was initially heated without its contents being stirred. It was assumed that the extent of the reaction was low in the heating phase because of the mass transfer restriction of hydrogen in such systems [212]. This was supported by the observation that no hydrogen was consumed in the heating phase. Furthermore, a test with 50 ml 1-octanol and 1 g of Ni/SiO_2 gave a conversion of only 1% in the heating phase to 280 °C. When the desired temperature was reached, the stirring was started at 380-390 rpm and the experiment could be performed at close to isothermal conditions. This made it possible to measure the activity in short-term (5-30 min) experiments.

3.2 High Pressure Continuous Flow Fixed Bed Reactor Setup

As a part of this project a high pressure gas and liquid continuous flow fixed bed reactor system was developed, named the Pyrolysis Oil Converter or in short POC. Detailed documentation of operation, construction, and programming of the setup has been written and is available at DTU-KT [213], here a shorter overview is given. Figure 3.2 show pictures of the setup, Figure 3.3 shows the flow scheme of this setup, and Table 3.1 gives the specification of the individual components presented in the flowsheet. The setup is designed to operate unattended for up to 48 h.

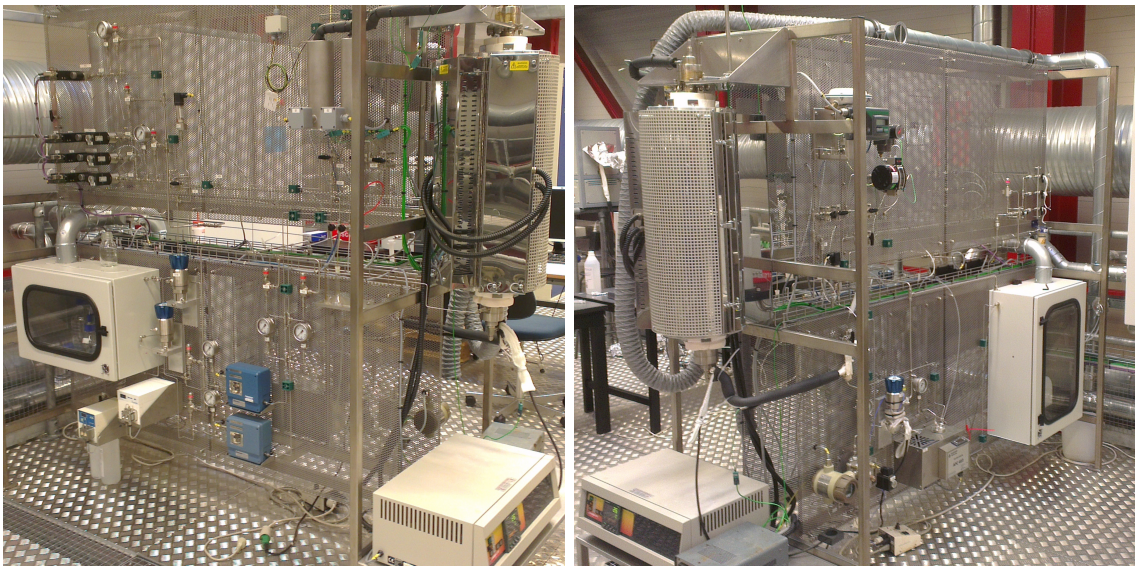

(a) Upstream section of the POC. (b) Downstream section of the POC.

Figure 3.2: *High pressure gas and liquid continuous flow fixed bed reactor system used in the current work. Pictures show (a) upstream and (b) downstream sections of the POC with the oven and reactor placed at the end of the setup in each picture.*

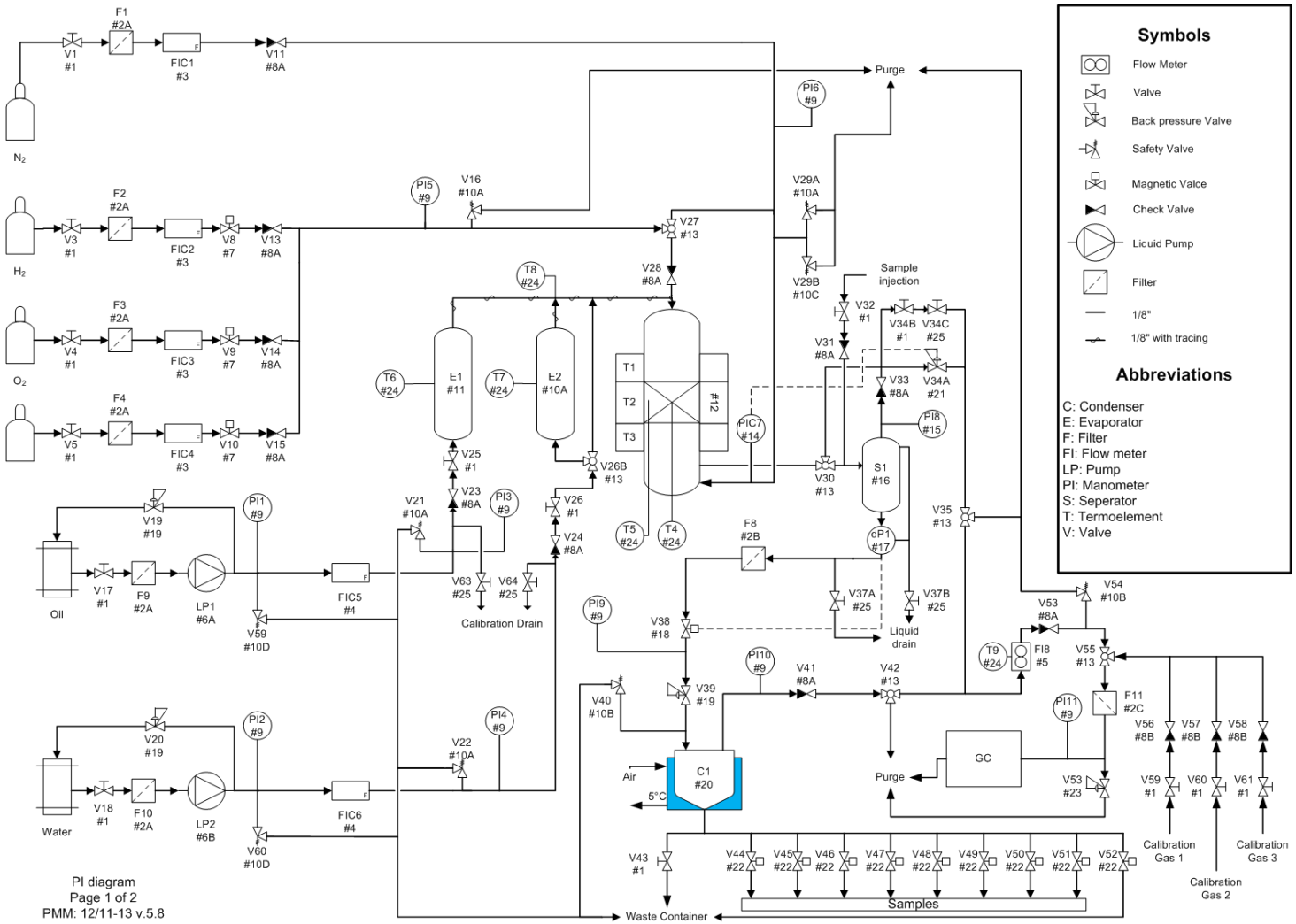

Figure 3.3: *Flowsheet for the POC setup. See Table 3.1 for specification of the individual components marked with #.*

Table 3.1: Component list related to the flowsheet in Figure 3.3.

Position	Component	Manufacturer	Type
#1	2-way valve	Swagelok	SS-83PS2
#2A	Filter	Swagelok	SS-2F-05
#2B	Filter	Swagelok	SS-2TF-2
#2C	Filter		Glass filter
#3	Gas massflow controller	Brooks	S5850
#4	Liquid massflow controller	Brooks	Flomega 5882
#5	Flowmeter	Brooks	3750
#6A	HPLC pump	Knauer	KN A50112
#6B	HPLC pump	Knauer	KN A50102
#7	Magnetic valve	Bürkert	2200
#8A	Check valve 5 psi	Swagelok	SS-CHS2-5
#8B	Check valve 10 psi	Swagelok	SS-CHS2-10
#9	Pressure gauge	WIKA	235.50.063
#10A	Safety valve 122 bar	Swagelok	SS-4R3A
#10B	Safety valve 5 bar	Swagelok	SS-4R3A
#10C	Safety valve 26 bar	Swagelok	SS-4R3A
#11A	Copper core		200 mm × 20 mm
#11B	Thermoshell		500 W
#11E	Thermoelement	Labfacility	K
#12	Oven	Carbolite	TVS12/600
#13	3-way valve	Swagelok	SS-83XPF2
#14	Pressure transmitter	Siemens	Sitrans PZ
#15	Pressure transmitter	Siemens	Sitrans PZ
#16	High pressure separator	Swagelok	1/2" tube
#17	Differential pressure cell	Honeywell	STD 924
#18	Magnetic valve	Bürkert	2200
#19	Backpressure valve	GO	BP66
#20	Condensator	APC	403
#21	Backpressure valve	Buamann	51000
#22A	Magnetic valve	Bürkert	6604
#22B	Manifold	Bürkert	
#23	Backpressure valve	Fairchild	10222BPHJ
#24	Thermoelement	Labfacility	K
#25	Needle valve	Swagelok	SS-ORS2

3.2.1 Setup Description

3.2.1.1 Gas Feed Section

All the gas is supplied from gas cylinders having a maximum supply pressure of 200 bar. In total the system has four gas feed lines. One line is dedicated to N_2 (FIC1) and one for H_2 (FIC2). The two additional lines can be used to feed an oxidizing gas (FIC3) or combustible gas (FIC4).

Each of the gas lines are constructed of a hand valve to manually switch on or off feed to the system. Hereafter a filter is placed to protect the consecutive flow controller. These are Brooks digital mass flow controllers type S5850. After the flow controllers a magnetic valve (Bürkert type 2200) is placed to ensure complete sealing of the gas line when not in use. These also help to ensure that combustible gasses (FIC2 and FIC4) and oxidizing gasses (FIC3) are not accidentally fed to the system at the same time. In the end of the general feed line a check valve is placed to ensure that backflow does not occur through the lines which are not in use.

This part of the system is protected against overpressure by safety valve V16, V29A, and V29B; V29A and V29B also protect the reactor against overpressure. V16 and V29A are set to release at 122 bar and V29B is set to release at 26 bar. V29A and V29B are not connected to the system simultaneously, but a physical connection has to be changed when switching between them. In this way, V29A should be fitted when operating above 20 bar and V29B should be used below. In the case of overpressure the safety valves will evacuate to the ventilation system of the pilot hall.

The nitrogen line is dedicated for pressurizing the reactor and is therefore always fed in the bottom of the reactor. The other gases can be fed either in the top or bottom of the reactor by turning three-way valve V27, depending on the request of the user.

3.2.1.2 Liquid Feed Section

The liquid feed section consists of two feed lines for two different types of liquids. Originally the setup has been designed for one feed line with water and one feed line with an undefined oil, but any combination of liquids feeds can be used.

A fume-hood (steel cupboard with ventilation) has been constructed for the reactants, where containers of up to 2.5 l can be placed (5 l for water). The feed containers are placed in a spilling tray with a total capacity of 10 l.

Each feed line consists of a two way valve to manually close the feed to the system. After this a Knauer KN50102 HPLC pump (LP) is placed. These pumps are used to build up a pressure against a back pressure valve (GO type BP66-1A11CJN157) and here from be recycled back to the feed tank. In this way a constant pressure can be set prior to the liquid mass flow controllers (FIC5 and FIC6), which are of the type Brooks Flomega 5882. Both controllers has been calibrated for water originally with a range setting of 0-1 ml/min and 0-5 ml/min for respectively FIC5 and FIC6. Whenever changing liquid, these has to be re-calibrated, which can be done by draining liquid through respectively needle valve V63 and V64. A small shelf is fitted beneath the two valves where appropriate measuring cylinders can be placed during the calibration process.

After the flow controller, the liquid can be evaporated in the custom build evaporators (E1 and E2). These are constructed of a copper core with a length of 200 mm and a diameter of 20 mm. Inside the copper rod a 500 W thermo cartridge is placed and on the outside of the rod, 6 m of 1/8" stainless steel pipe is curled. Two thermo elements are placed between the copper and the steel pipe, one for controlling and one for safety. The evaporator is insulated by Rockwool and fitted in a steel house to reduce heat loss and shield it. The design enables that the liquid passing in the steel pipe can be heated and evaporated in the pipes. The evaporation will cause an

expansion of the liquid, but the relative large volume of the pipe (ca. 15 ml) should reduce the shock in the system and in this way give a uniform flow.

It is possible to bypass E2 by turning three-way valve V26B. This can be used if the liquid feed is changed in an experiment, thereby bypassing the large volume in the evaporator and use less time flushing the feed line with the new feed.

After the evaporators, the connection to the reactor is heat traced in order to maintain the desired temperature of the feed. Use of the evaporator and the heat tracing is optional.

3.2.1.3 Reactor

The reactor is fitted vertical to enable trickle flow and consist of an outer pressure baring shell and an internal straight tube reactor where catalyst can be loaded, as shown in the schematic drawing in Figure 3.4.

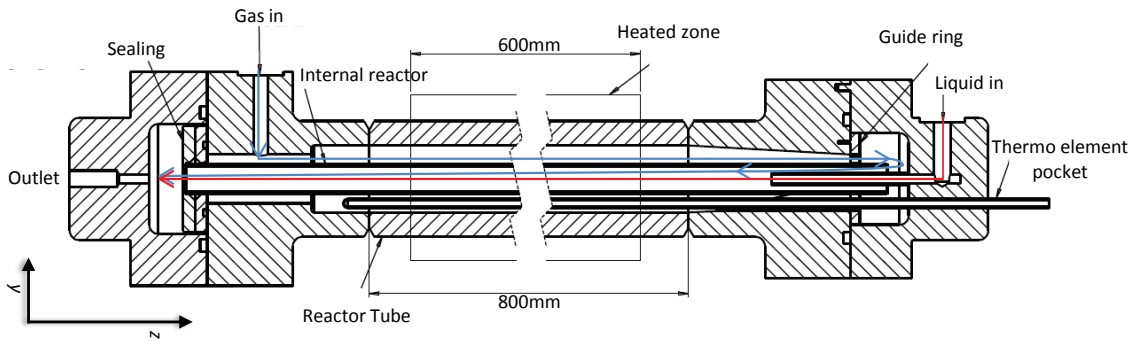

Figure 3.4: *Schematics drawing of the reactor. Blue lines indicate the flow path of the gas and red line indicate the flow path of liquid. The z-axis indicate the upward direction relative to mounting of the reactor.*

All parts of the reactor are constructed of certified SS316 steel. The total length is 996 mm, with 800 mm of these being the actual reactor tube and the rest being the flanges. The external diameter of the reactive zone is 40 mm and the internal is 20 mm, giving a wall thickness of 10 mm. The total volume of the reactor is 0.31 l. The theoretical pressure limit for the reactor is 125 bar at 500 °C. It has further been tested up to a maximum pressure of 140 bar at room temperature. The general maximum operation temperature of SS316 is 550 °C.

Two asymmetric flanges are welded on the reactor tube in each end. The top flange is the inlet of the liquid feed and potentially also some of the gas feed. This will enter in the side of the flange and flow to the internal reactor through a dip tube.

Gas will be fed in the bottom flange and travel along the outside of the internal reactor and be mixed with the liquid in the top flange. The actual flows of gas and liquids are exemplified with colors in Figure 3.4.

The internal reactor is 915 mm long with an outer diameter of 10 mm and an inner of 8 mm, the inner diameter can be changed if lower residence time is required. 425 mm from the bottom of the reactor a support pin is placed, which is used when packing catalytic material.

The reactor enables for two additional temperature measurements; one in the thermo element pocket parallel to the internal reactor (T5) and one fixed beneath the support in the internal reactor (T4, not shown in figure 3.4) inserted from the bottom flange.

The reaction temperature is ensured by a vertical Carbolite TVS12/600 oven that can be opened lengthwise. This has a heated length of 600 mm and an isothermal zone in the oven room of 500 mm, with temperature fluctuations within ±5°C. Figure 3.5 shows the measured temperature profile in the thermo element pocket at an oven setpoint of 250 °C in a case where the reactor was loaded with glassbeads. The practical isothermal zone inside the reactor is roughly 12 cm long, here a temperature of 243.6±0.4 °C is obtained over the region where the catalyst bed normally would be positioned.

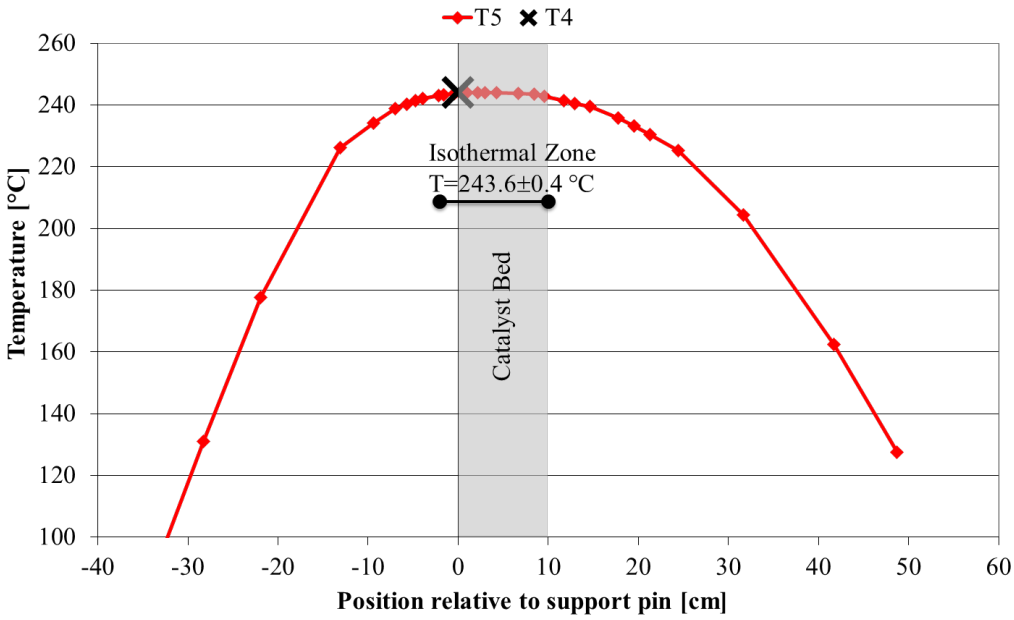

Figure 3.5: *Temperatureprofile in the reactor when loaded with glass beads and an oven setpoint of 250 °C. 0 on the x-axis refers to the position of the support pin in the internal reactor.*

3.2.1.4 Liquid Makeup Section

After the reactor the product enters a gas-liquid high pressure separator (S1). This is in practice a 490 mm 1/2" stainless steel tube where the product enters 220 mm from the top. Liquid will in this way travel downwards and gas will rise. Beneath the separator, a differential pressure (dP) cell (Honeywell type STD 924) is placed to measure the pressure difference between the bottom of the separator and the top. This pressure difference is directly dependent on the liquid height in the separator and is given by:

$$\Delta P = (h \cdot \rho \cdot g + P) - P = h \cdot \rho \cdot g \tag{3.1}$$

Here ΔP is the pressure difference, P is the pressure in the system, h the liquid height, ρ the density of the liquid, and g the gravitational acceleration.

The signal from dP1 is used to open magnetic valve V38 (Bürkert type 2200); in this way an approximately constant liquid height can be maintained in the separator. After V38 the liquid is flushed against backpressure valve V39 (GO type BP66-1A11CJN157). This valve should be set to a pressure slightly lower than the process pressure to make sure that the liquid will be removed from the separator when V38 is open.

The liquid pressure is relieved to 0-1 barg by V39 and then enters the air cooled condensator C1 (APC type 403), which is maintained at a constant temperature of 6 °C. C1 functions as a low pressure separator and here any residual gas dissolved in the liquid should be removed. From here, the liquid is transferred to a valve manifold consisting of eight magnetic two-way valves in line (V44-V52, Bürkert type 6604). The manifold can be controlled to take out samples at specific times to enable sampling without the presence of a user; at least for a certain period. Sample containers have a volume of 60 ml and are placed inside a dedicated fume-hood (steel cupboard with ventilation). The system has been designed to use medical flasks from Grathwol of type 15 1433 110. In the fume-hood a waste container of 5 l is also placed where all excess liquids are gathered. In the bottom of the fume-hood, a spilling tray with a total capacity of 10 l is placed to contain accidental overflow.

3.2.1.5 Gas Makeup Section

After liquid and gas has been separated in S1 the gas travels upward to backpressure valve V34A (Baumann type 51000). This valve is used to control the pressure in the reactor on the basis of the pressure measured before the reactor at PIC7. The valve can operate between 10-100 bar with flows from 0-200 Nml/min in the low pressure range and flows from ca. 0-5000 Nml/min in the high pressure range. Figure 3.6 shows a plot of the possible operation flow as a function of system pressure. As an alternative to this valve, a needle valve is installed parallel to V34A, which can be opened if atmospheric pressure operation is desired.

After pressure reduction, the gas is mixed with residual gas coming from C1 and hereafter the combined flow is measured in flowmeter FI8 (Brooks type 3750). It is possible to direct the gas flow from the backpressure valve or from C1 directly to the ventilation system of the pilot hall by turning respectively three-way valve V35 or V42. After the flow measurement the gas is passed to a gas chromatograph (GC, Shimadzu GC-2014) fitted with a thermal conductivity detector (TCD) for quantification, allowing analysis in 20 min intervals. This was equipped with a Restek ShinCarbon column with high surface area carbon molecular sieve as stationary phase. The GC was calibrated for H_2, N_2, CH_4, CO_2, CO, ethane and ethene. The pressure in the sampling loop of the GC is maintained at approximately 1 barg by using backpressure valve V53 (Fairchild type 10222BPHJ).

3.2.2 Experimental Procedure

In a typical experiment, 2.5 g of catalyst was mixed with 7.5 g glass beads in sieve fraction 212-245 μm to dilute the catalyst bed and thereby obtain better control of the exothermic reactions. The glass bead/catalyst mixture was suspended on a quartz wool plug in the reactor, which was supported on a crossbar in the reactor. The loading profile of the reactor from the crossbar up was: 1 cm quartz wool, 12 cm catalyst/glass beads, 1 cm quartz wool, 25 cm glass beads (1 mm diameter).

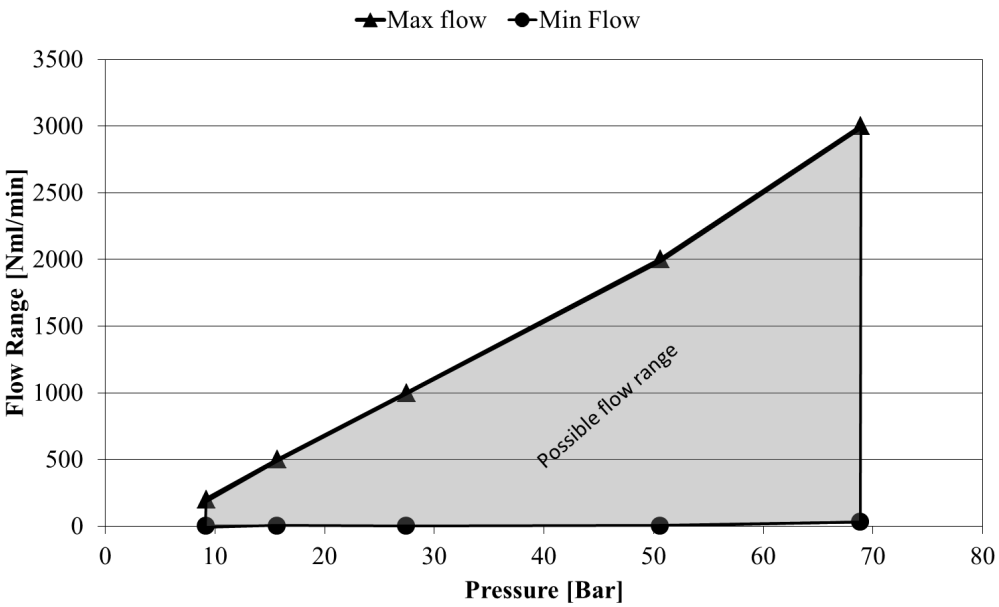

Figure 3.6: *Possible operation flow as a function of system pressure for valve V39A. The maximum flow is evaluated at 90% valve opening and minimum flow is evaluated at 10% valve opening.*

A feed mixture of either guaiacol (Sigma-Aldrich, $\geq$ 99%) or phenol (Sigma-Aldrich, $\geq$ 99%) in 1-octanol (Sigma-Aldrich, $\geq$ 99%) was used as bio-oil model compound system. 1-octanol was chosen as solvent (despite it not is an usual bio-oil component) due to its relative high boiling point (195 °C) and ability to mix with guaiacol/phenol in a homogenous phase. The feed flow was typically 0.2 ml/min of oil. This corresponds to a WHSV of 4.0 h^{-1} (relative to the mass of catalyst used) or a LHSV of 2.0 h^{-1} (relative to the volume of glass beads/catalyst mixture in the reactive zone), see Section 3.3.3 for further details.

Liquid samples were collected over 2 hours at intervals of 4-6 hours. The average between start and end time was used as reference time for the specific liquid sample. The volume of the aqueous and oil phases of the samples were measured in a measuring cylinder.

Hydrogen (AGA, 99.9%) and nitrogen (AGA, 99.9%) were fed to the reactor at a flow of respectively 200-300 Nml/min and 50-100 Nml/ml. Nitrogen was used as internal reference in the gas flow, as this was assumed inert in the reaction and therefore could be used to quantify the downstream gas flow. During the reactions the reactor was maintained at a constant pressure of 100 bar and the set point of the reactor oven was 250-380 °C.

In an experiment with HDO of 10% guaiacol in 1-octanol over a 5 wt% Ni/ZrO_2 catalyst at a set point of 250 °C, the actual temperature in the catalyst bed varied between 245 °C in the bottom of the bed and 251 °C in the top part. The slightly higher temperature in the top part of the bed was due to the exothermic reactions taking place.

A blank experiment without catalyst at 100 bar and 250 °C was made with 10% guaiacol in 1-octanol. Here a conversion of 2% for guaiacol and very close to 0% for 1-octanol were found, showing that the reactor was not catalytically active for the

reaction.

In the deactivation experiments either 1-octanethiol (Sigma-Aldrich, $\geq 98.5\%$) or 1-chlorooctane (Sigma-Aldrich, 99%) were added to the liquid feed corresponding to a concentration of 0.05 wt% S or Cl, respectively.

In experiments where either temperature or feed rate was changed during the experiment, at least 8 h for stabilization was given before taking liquid samples to ensure a representative sample.

3.3 Product Analysis

3.3.1 GC-MS/FID

Analysis of the liquid product was performed with a Shimadzu GCMS/FID-QP-2010UltraEi. A Supelco Equity-5 column with bonded 5% diphenyl/95% dimethyl siloxane stationary phase was used in the GC. This is a non-polar column suitable for general analysis of oil mixtures and with a high thermal stability. Identification of the oil products was done with a mass spectrometer (MS) scanning at a rate of 1666 m/z/s in the range from 22 to 300 m/z. A flame ionization detector (FID) was used for quantification in all experiments. MS and FID spectra were obtained simultaneously in all measurements as a split was installed after the column in the GC. All samples were analyzed as produced, but a split of 90 was used in the injection part to protect the MS detector from saturation.

External standards were prepared for phenol, cyclohexanol, cyclohexanone, and cyclohexane using ethanol as a solvent for the batch reactor experiments in Chapter 4 and 5. External standards for guaiacol, phenol, cyclohexanol, cyclohexane, methanol, 1-octanol, octane, and heptane were used as external standards for the continuous flow experiments in Chapter 6, 7, and 8. 3-5 calibrations points were used for all standards. The concentrations of the remaining peaks were calculated from the FID on the basis of the effective carbon number method [214], where the concentration of a compound is found as:

$$C_i = C_{\text{ref}} \cdot \frac{A_i}{A_{\text{ref}}} \cdot \frac{\nu_{\text{eff,ref}}}{\nu_{\text{eff},i}} \tag{3.2}$$

Here C is the concentration, A the area of the peak in the FID spectrum, and ν_{eff} the effective carbon number. Index i refers to the compound with the unknown concentration and index ref refers to a reference compound where the concentration is known. Table 3.2 summarizes the effective carbon number of relevant compound groups. Cyclohexanol was generally used as reference in the batch experiments with phenol as feed and in the continuous flow experiments, all having 1-octanol in the feed, octane or heptane were used as reference.

3.3.2 CHN-S

Liquid product from experiments with real bio-oil as feed was analyzed using an EA3000 CHN-S from EuroVector. In this analysis the samples were burned at 900 °C

Table 3.2: *Effective carbon number of different types of chemical groups. ν_{eff} is the effective carbon number and ν_C is the number of carbon atoms in the given molecule. Data are from Schofield [214].*

Chemical Group	ν_{eff}	Non-contributing carbon
Alkanes	ν_{C}	0
Ketones	ν_{C} - 1	1
Aldehydes	ν_{C} - 1	1
Ethers	ν_{C} - 1	1
Alcohols	ν_{C} - 0.5	0.5
Acids	ν_{C} - 1	1
Esters	ν_{C} - 1.5	1.5

in the elemental analysis equipment and the combustion product was then analyzed by GC-TCD. The quantities of carbon, hydrogen, nitrogen, and sulfur was quantified by measuring the product of CO_2, H_2O, N_2, and SO_2, respectively. The oxygen content was assumed as balance.

Sulphanilamide was used as reference in the calibration.

The liquid samples were prepared for analysis by using a 1 μl micro syringe to inject the sample on a Carbosorb ® adsorbent packed in a tin capsule. Hereafter the capsule was folded and transferred to the apparatus for analysis.

3.3.3 Calculations

The weight hourly space velocity (WHSV) was calculated as:

$$WHSV = \frac{v_0 \cdot \rho_{feed}}{m_{cat}} \tag{3.3}$$

Here v_0 is the volumetric feed flow, ρ_{feed} the density of the liquid feed, and m_{cat} the mass of catalyst used.

The liquid hourly space velocity (LHSV) was calculated as:

$$LHSV = \frac{v_0}{V_{cat}} \tag{3.4}$$

Here V_{cat} is the volume of the catalyst/glass beads mixture in the reactor. This was correlated directly with the retention time (τ), which was calculated as:

$$\tau = \frac{1}{LHSV} \tag{3.5}$$

The conversion (X) was calculated by Eq. 3.6 or 3.7, respectively for batch or continuous flow experiments:

$$X = \left(1 - \frac{C_i \cdot V_{\text{final}}}{C_{0,i} \cdot V_0}\right) \cdot 100\% \tag{3.6}$$

$$X = \left(1 - \frac{C_{out,i} \cdot v_{out}}{C_{0,i} \cdot v_0}\right) \cdot 100\% \tag{3.7}$$

Here C_i is the concentration of compound i, V the liquid volume, and v is the volumetric flow. Index *out* refers to the conditions after the reactor, index final refers to after a batch experiment, index 0 refers to the initial conditions, and i refers to the compound of relevance. The conversions of all feed components were evaluated.

The yields (Y_i) of relevant products were calculated for the batch (Eq. 3.8) and the continuous flow experiments (Eq. 3.9) as:

$$Y_i = \frac{C_{out,i} \cdot V_{\text{final}}}{C_{0,j} \cdot V_0} \cdot 100\% \tag{3.8}$$

$$Y_i = \frac{C_{out,i} \cdot v_{out}}{C_{0,j} \cdot v_0} \cdot 100\% \tag{3.9}$$

Index i is here referring to the compound of relevance and index j is referring to the initial reactant.

The selectivity (S_i) of a compound (i) was calculated as:

$$S_i = \frac{Y_i}{X} \cdot 100\% \tag{3.10}$$

The degree of deoxygenation (DOD) was calculated as:

$$\text{DOD} = \left(1 - \frac{F_{\text{O},out}}{F_{\text{O},in}}\right) \cdot 100\% \tag{3.11}$$

Here F_{O} is the molar flow of oxygen in oxygen containing species except water either in or out of the reactor. To give further emphasis on the HDO of guaiacol in some of the experiments, which only constituted 10% of the feed, also the degree of deoxygenation for the guaiacol related compounds (DOD^{GUA}) was calculated:

$$\text{DOD}^{\text{GUA}} = \left(1 - \frac{\sum_i F_{\text{O in } i,out}}{2 \cdot F_{\text{Guaiacol},in}}\right) \cdot 100\% \tag{3.12}$$

Here index i refers to the oxygen containing guaiacol related compounds, which were defined as: guaiacol, methanol, cyclohexanol, and 2-methoxy-cyclohexanol.

To make an additional quantification of the activity of the catalyst in some experiments, the first order rate constants were calculated on the basis of a plug flow reactor design equation [199]:

$$X_i = 1 - \exp\left(-k_i \cdot \frac{W}{v}\right) \tag{3.13}$$

$$\tag{3.14}$$

Here k_i is the rate constant of reaction i and W the mass of catalyst.

The carbon balance was evaluated in all batch experiments by comparing the carbon initially in the reactor to the carbon measured in the product:

$$\Delta\text{C} = \left(\frac{\sum_i \nu_i \cdot n_i - 6 \cdot n_{0,\text{Phenol}}}{6 \cdot n_{0,\text{Phenol}}}\right) \cdot 100\% \tag{3.15}$$

Here ΔC is the carbon deviation in percent and n_i the moles of compound i. All compounds identified in the GC analysis were included in the carbon balance. Generally, the carbon balance was closed within 10%, but in many experiments almost complete closure was achieved.

The carbon balance was evaluated similar in the continuous flow experiments, using data from both the GC-MS/FID and GC-TCD measurements:

$$\Delta \mathrm{C} = \left(\frac{\sum_i \nu_i \cdot F_{out,i} - \sum_j \nu_j \cdot F_{0,j}}{\sum_j \nu_j \cdot F_{0,j}} \right) \cdot 100\% \tag{3.16}$$

Here F_i is the molar flow of compound i. All compounds identified in the GC-MS/FID and GC-TCD analysis were included in the carbon balance. Generally the carbon balance was closed to within 5%.

3.4 Catalyst Synthesis and Preparation

Almost all catalysts used in the current work has been synthesized in house by incipient wetness impregnation on a support. A range of different active phases were synthesized using a variety of precursors, as summarized in Table 3.3.

The supports were obtained from different suppliers and their properties are summarized in Table 3.4. All supports were initially crushed and sieved.

In the synthesis, the amount of precursor corresponding to the desired metal loading was dissolved in deionized water equivalent to the pore volume of the amount of support intended for impregnation (the pore volume of the supports are summarized in Table 3.4). In cases were the precursor was not easily dissolved the flask with the solution was heated in a water bath at 70-80 °C, which in all instances was sufficient to get everything in solution. This solution was then mixed with the weighed support to form a slurry. After impregnation, the samples were dried at 70-110 °C for at least 12 h.

Some catalysts were calcined after drying, which was done by heating the samples in an oven with atmospheric air at a rate of 10 °C/min to 400 °C where it was held for 4 h.

Table 3.3: *Precursors used for the preparation of the different catalysts. All precursors were supplied by Sigma-Aldrich.*

Active phase	Precursor salt	Precursor Purity [%]
MnO	$Mn(C_2H_3O_2)_2 \cdot 4\,H_2O$	≥ 99.0
WO_3	$(NH_4)_6H_2W_{12}O_{40} \cdot xH_2O$	≥ 99.0
MoO_3	$(NH_4)_6Mo_7O_{24} \cdot 4\,H_2O$	≥ 99.0
V_2O_5	NH_4VO_3	≥ 99.0
ZnO	$Zn(NO_3)_2 \cdot 6\,H_2O$	≥ 99.0
Cu	$Cu(NO_3)_2 \cdot 3\,H_2O$	≥ 99.0
Fe	$Fe(NO_3)_3 \cdot 9\,H_2O$	≥ 98.0
Co	$Co(NO_3)_2 \cdot 6\,H_2O$	98.0%
Ni	$Ni(NO_3)_2 \cdot 6\,H_2O$	98.0%

Table 3.4: Overview of the supports used in the current work. Data specified by supplier.

Support	Supplier	Product code	Surface Area [m^2/g]	Pore Volume [ml/g]	Significant Impurities
SiO_2	Saint-Gobain	SS61138	250	1	-
ZrO_2	Saint-Gobain	SZ61152	160	0.32	4.6% SiO_2
TiO_2	Saint-Gobain	ST61120	150	0.38	<0.3% S
CeO_2	AMR Ltd.	2-02-13-01	140	0.55-0.60[a]	-
CeO_2-ZrO_2[b]	AMR Ltd.	5020	140	1.0-1.1[a]	-
Al_2O_3	Sasol	TH100/150	150	0.8-1.0	-
$MgAl_2O_4$[bc]	Sasol		90	0.7[a]	-
C	Daihope	C-008	1100	0.85	-

[a]Determined by drop test.
[b]Confirmed by XRD to be a mixed oxide.
[c]Produced by mixing stoichiometric amounts of MgO with Puralox Al_2O_3 and calcining at 900 °C.

3.4.1 Catalyst Screening

A screening of suitable catalyst for HDO was performed in the batch reactor setup, as described in Chapter 4. Here 23 catalysts were tested. Table 3.5 summarizes the theoretical loadings, particle sizes, specific surface areas, and pretreatment conditions of these.

The Ni-V_2O_5 catalysts were made by initially impregnating the support with vanadium, drying the catalyst, and then impregnating it with nickel nitrate. NH_4VO_3 was dissolved by using additionally oxalic acid (Sigma-Aldrich, $\geq$ 99.0%) in a molar ratio of 1:2 (V:oxalic acid).

Cu/ZnO/Al_2O_3 was prepared according to the method of Baltes et al. [215]. An aqueous solution of $Cu(NO_3)_2 \cdot 3\,H_2O$ (0.6 mol/l,), $Zn(NO_3)_2 \cdot 6\,H_2O$ (0.3 mol/l), and $Al(NO_3)_3 \cdot 9\,H_2O$ (0.1 mol/l, Sigma-Aldrich, $\geq$ 98%) was co-precipitated with a solution of Na_2CO_3 (1 mol/l, Sigma-Aldrich, $\geq$ 99%) for 1 h. During the precipitation process, the pH was maintained at 7$\pm$0.1, and the temperature was kept at 60 °C. Afterward, the precipitate was filtered and washed with demineralized water followed by drying overnight at 80 °C and calcining at 300 °C under air for 3 h.

NiO-MoO_3/Al_2O_3 and CoO-MoO_3/Al_2O_3 catalysts were obtained from Haldor Topsøe A/S. Ru/C, Pd/C, and Pt/C were obtained from Sigma-Aldrich.

The catalysts requiring initial reduction in Table 3.5 were reduced in the continuous flow setup at the indicated temperature by heating in a flow of 250 Nml/min N_2 and 250 Nml/min H_2 at 1 bar and keeping the sample at the given temperature for the specified time. After reduction the samples were transferred directly to the batch setup for testing.

Table 3.5: *Summary of properties of catalysts used in the screening work, i.e. the theoretical loading of active component, particle size of support (sieve fraction), specific surface area, and reduction conditions for the tested catalysts.*

Catalyst	Loading [wt%]	Particle Size [μm]	Surface Area [m^2/g]	Reduction T [°C]/t [h]
MnO/C	15	710-1400	680	None
WO_3/C	15	710-1400	790	None
MoO_3/C	15	710-1400	660	None
V_2O_5/C	15	710-1400	310	None
NiO-MoO_3/Al_2O_3[a]	-	300-600	-	None
CoO-MoO_3/Al_2O_3[a]	-	300-600	-	None
Cu/ZnO/Al_2O_3	45%Cu/5%Zn	$\approx$ 900	60	300/7
NiCu/SiO_2	10%Ni/10%Cu	$\approx$ 900	180	350/19
Cu/SiO_2	15	300-600	170	380/19
Ru/C	5	$\approx$ 15	1160	400/2
Pd/C	5	$\approx$ 15	1100	400/2
Pt/C	5	$\approx$ 15	1140	400/2
Co/SiO_2	5	300-600	210	550/2
Fe/SiO_2	5	300-600	200	550/2
Ni/SiO_2	5	63-125	210	400/2
Ni/Al_2O_3	5	63-125	140	550/2
Ni/CeO_2	5	63-125	130	400/2
Ni/ZrO_2	5	63-125	130	550/2
Ni/CeO_2-ZrO_2	5	63-125	120	550/2
Ni/$MgAl_2O_4$	5	63-125	80	550/2
Ni/C	5	63-125	1020	550/2
Ni-V_2O_5/SiO_2	5%Ni/5%V	300-600	210	550/2
Ni-V_2O_5/ZrO_2	5%Ni/5%V	300-600	120	550/2

[a] Commercial catalyst by Haldor Topsøe A/S without detailed characterization data.

3.4.2 Nickel Catalysts

Experiments investigating the structure sensitivity of 5 wt% Ni/SiO_2, described in Chapter 5, were all performed from a batch of 63-125 μm catalyst. Calculation of the Mears' and Weisz-Prater criteria (cf. Table C.1) indicated that this system was not limited by neither external nor internal transport, this is further explained in Appendix C.

Prior to the activity test, the catalyst was reduced by four different reduction methods to achieve different nickel particle sizes:

- Red. 1: Reduction of calcined Ni/SiO_2 in a batch reactor at 395 °C and 7 bar of H_2 in a stagnant gas atmosphere. This method is expected to yield large nickel particles due to the high pressure and the presence of water [216–218].

- Red. 2: Reduction of calcined Ni/SiO_2 in a batch reactor with a flow of 1 Nl/min H_2 at 395 °C and 5 bar of hydrogen. This method is expected to yield

intermediate size nickel particles since water is continuously removed.

- Red. 3: Reduction of calcined Ni/SiO_2 in a continuous flow reactor with a flow of 250 Nml/min H_2 and 250 Nml/min N_2 at 400 °C and 1 bar of hydrogen. This method is expected to yield smaller nickel particles than Red. 2 due to the milder conditions and more controlled removal of water.

- Red. 4: Reduction of un-calcined $Ni(NO_3)_2/SiO_2$ in a continuous flow reactor with a flow of 250 Nml/min H_2 and 250 Nml/min N_2 at 400 °C and 1 bar. This method is expected to yield small nickel particles, due to the direct reduction of the nickel nitrate catalyst precursor [219].

From TPR analyses of Ni/SiO_2, 400 °C was found sufficient for complete reduction of the nickel. This is elaborated in Section 4.5.

In the investigation of the stability of nickel based catalysts in Chapter 6 a batch of 300-600 μm 5 wt% Ni/ZrO_2 catalyst was used. A part of this catalyst was left un-calcined and the other calcined.

Reduction of the catalysts was done in the continuous flow setup prior to testing of the catalysts by heating at a rate of 10 °C/min to 500 °C in a flow of 250 Nml/min H_2 and 250 Nml/min N_2 at atmospheric pressure. 500 °C was sufficient for complete reduction of Ni/ZrO_2 as found by in situ X-ray absorption spectroscopy (XAS). This is further discussed in Section 6.3.

The high rates of reaction found for this system was by evaluation of the Mears' and Weisz-Prater criteria (cf. Table C.1) found to cause slight internal transport limitations in the system. The effectiveness factor of the catalyst pellets was estimated to be in the order of 85-97%, being lowest for the largest particles. However, as this catalyst was used to evaluate stability and because all experiments were performed similar, this did not affect the conclusions made in Chapter 6, but it does mean that the kinetic constants derived in Section 6.8 are not intrinsic. Further information on the calculations on transport limitations can be found in Appendix C.

To test the effect of potassium, KCl or KNO_3 were impregnated to separate portions of the catalyst by incipient wetness impregnation. A portion of the un-calcined Ni/ZrO_2 catalyst was weighed off and a solution (corresponding to the pore volume of the given fraction of catalyst) with KCl or KNO_3 in H_2O was prepared. KCl and KNO_3 were impregnated in amounts corresponding to the molar content of nickel. After mixing the solution and the catalyst, it was dried for 12 h at 70 °C.

3.4.3 Molybdenum Carbide Catalysts

To produce Mo_2C/ZrO_2, 15 wt% of Mo was initially impregnated on ZrO_2 in a sieve fraction of 125-180 μm.

The carbide was produced in the setup from the 15 wt% MoO_3/ZrO_2 prior to testing. The sample was heated to 200 °C in N_2 at atmospheric pressure, and hereafter ramped to 550 °C at 0.5 °C/min in 50 Nml/min 20% CH_4 in H_2, and finally held at this temperature for 4 h. 550 °C was verified by in situ X-ray diffraction (XRD) and X-ray absorption spectroscopy (XAS) to be sufficient for carburization of MoO_3/ZrO_2. This is further described in Section 7.2.

These catalysts was indicated not to be limited by neither external nor internal transport. This is evidenced in Appendix C.

3.4.4 Sulfided Catalysts

Ni-MoO_3/ZrO_2 (3 wt% Ni, 15 wt% Mo) was prepared by sequential incipient wetness impregnation. 15 wt% Mo was initially impregnated from $(NH_4)_6Mo_7O_{24} \cdot 4\,H_2O$ dissolved in water on ZrO_2 in sieve fraction 300-600 μm and then dried overnight at 70 °C. On the dry catalyst, $Ni(NO_3) \cdot 3\,H_2O$ was dissolved in water and impregnated on the catalyst corresponding to 3 wt% Ni and then dried at 70 °C overnight. Impregnation of the promoter (Co or Ni) after molybdenum has previously been established to give the best interaction between Mo and the promoter [220]. Finally the catalyst was calcined by heating to 400 °C at a rate of 10 °C/min and held there for 4 h.

A commercial Ni-Mo/Al_2O_3 catalyst was supplied by Haldor Topsøe A/S. This was crushed to a particle size of 300-600 μm. This catalyst was used in the experiments with real bio-oil described in Section 9.

The catalysts were sulfided in the continuous flow reactor prior to testing by initially heating a portion of the catalyst to 200 °C in N_2 and then heating at a rate of 5 °C/min to 350 °C in a flow of 800 Nml/min H_2 and 0.2 ml/min dimethyldisulfid (DMDS) at atmospheric pressure. Sulfidation was done for 2.5 h at 350 °C. Assuming complete decomposition of DMDS to H_2S, the feed concentration of the gas would be: 12% H_2S, 12% CH_4, and 76% H_2.

Calculations of the Mears' and Weisz-Prater criteria (cf. Table C.1) revealed that the Ni-MoS_2/ZrO_2 catalyst was slightly inhibited by internal mass transport. However, as discussed for the Ni/ZrO_2 catalyst above (Section 3.4.2), it was evaluated that the catalyst was only slightly limited and as the experiments cover stability it did not influence the conclusions. Further details can be found in Appendix C.

3.5 Catalyst Characterization

3.5.1 Ammonia Temperature Programmed Desorption

NH_3 temperature programmed desorption (NH_3-TPD) was performed with an Autochem II 2920 apparatus. Here ~0.1 g portions of the samples were initially heated to 500 °C in a 50 Nml/min He flow and then cooled to 100 °C. At this point, the samples were saturated in a 50 Nml/min NH_3 flow for 120 min. Desorption of NH_3 was hereafter measured by flushing with a 50 Nml/min He flow while heating the samples at a rate of 5 °C/min to 500 °C. Quantification of the NH_3 was done with a TCD. The quantity of adsorbed NH_3 was directly correlated to the acidity of the catalyst.

3.5.2 Brunauer-Emmett-Teller Surface Area

A Quantachrome iQ2 was used for measurement of the specific surface area on the basis of BET theory [221]. Nitrogen at its boiling point was used in the p/p_0 range from 0.05-0.3 to construct a seven point BET plot.

3.5.3 Energy Dispersive X-Ray Spectroscopy

The elemental composition of the catalysts was analyzed by means of Energy Dispersive X-Ray Spectroscopy (EDX) in a FEI Quanta 200 ESEM FEG Scanning Electron

Microscope (SEM) operated at 10kV and equipped with an Oxford Instruments 80 mm^2 X-Max silicon drift detector. Few particles of 300-600 μm sieved fractions of catalyst were fixed to standard SEM aluminium stubs with Vishay Micro-Measurements M-Bond epoxy resin and then mechanically polished in order to reach a flat geometry configuration.

EDX elemental maps were acquired using a FEI Osiris Transmission Electron Microscope (TEM) operated at 200kV in scanning mode (STEM). Catalysts were crushed in a mortar and dry dispersed on a copper TEM grid coated with lacey carbon. Maps were smoothed using a 7x7 pixels kernel smoothing algorithm implemented in the Bruker Esprit software.

3.5.4 Environmental Transmission Electron Microscopy

Environmental transmission electron microscopy (ETEM) was performed using a Titan E-Cell 80-300ST TEM where images were obtained at reducing conditions. The samples were crushed, slurried with ethanol, and deposited on a copper grid covered with lacey carbon film.

In the case of Ni/SiO_2 where the nickel particle size was investigated, the samples were heated to 450 °C and reduced in a flow of 5 Nml/min H_2 at a pressure of 2.5 mbar. The average nickel particle size was determined by measuring the size of > 200 particles on the images and subsequently calculating the number based average.

3.5.5 Plasma Emission Spectroscopy

Elemental analysis of the catalysts was performed using inductively coupled plasma atomic emission spectroscopy (ICP-OES). In the analysis, the samples were crushed and melted together with potassium pyrosulfate. This was dissolved in a solution of water and HCl and then analyzed by plasma emission spectroscopy. The instrument was calibrated with certified standards for the elements analyzed for.

3.5.6 Temperature Programmed Oxidation

Temperature programmed oxidation (TPO) was performed in a tubular furnace. 50-100 mg of the spent catalyst was placed in a ceramic boat and placed in the center of the oven and heated at a ramp of 11 °C/min in a flow of 1100 Nml/min gas (10% oxygen in nitrogen). Online CO and CO_2 measurements were performed with an ABB automation GmbH AO2020 Uras26 IR detector in order to quantify the amount of carbon on the catalyst. Carbon determination was done on the basis of the integration of the CO/CO_2 signal relative to flow and time.

All catalyst samples were washed and filtered with ethanol and then dried at 50 °C for 2-3 h prior to the analysis, to wash out excess oil in the catalysts' pores.

3.5.7 Temperature Programmed Reduction

Temperature programmed reduction (TPR) by hydrogen was performed for selected catalysts on a Netzsch STA 449 F1 Jupiter ASC thermogravimetric analyzer (TGA) to identify the required temperature for complete reduction of the supported metal. The analysis was performed on the basis of changes in mass, and the total mass

applied was on the order of 20-40 mg. Five volume percent hydrogen in nitrogen was added at a flow of 100 Nml/min and the samples were heated at a rate of 5 °C/min to 300 °C, at a rate of 1 °C/min from 300 to 500 °C, and at a rate of 5 °C/min from 500 to 700 °C.

3.5.8 X-Ray Absorption Spectroscopy

The local structure of the Ni/ZrO_2 catalyst was characterized by XAS in terms of X-ray absorption near edge structure (XANES) and extended X-ray absorption fine structure (EXAFS) at the Ni-K edge at the XAS beamline at the synchrotron radiation source ANKA (Karlsruhe, Germany). The reduction of the Ni/ZrO_2 was followed in situ, whereas the structure of the poisoned catalysts were analyzed ex-situ after the corresponding reactions.

In situ characterization of catalysts was followed by Quick-XAS in fluorescence detection mode [222]. For this purpose, a 63-125 μm sieved fraction of the catalyst was filled into the quartz capillary micro reactor (1 mm internal diameter) resulting in plug flow-like conditions [223]. The reaction mixture was supplied by a gas delivery system. The microreactor was heated with a gas blower (FMB Oxford), similar to the setup in reference [224]. Spectra were recorded every 12.5 °C.

Catalyst characterized ex-situ, were pressed to pellets and then measured in transmission mode.

The carburization and deactivation of Mo_2C were followed by alternated in situ XAS and XRD. The measurements were carried out at the BM01B (Swiss-Norwegian beamlines) at the ESRF (Grenoble, France). An in situ cell based on a quartz capillary and heated by a gas blower, was employed resulting in plug-flow like conditions [223, 225]. The sample, around 5 mg of 15 wt% MoO_3/ZrO_2 (sieved), was filled in a 0.5 mm diameter quartz capillary between two glass wool plugs. The gases, 50 ml/min, were delivered by mass flow controllers. The outlet gas composition was monitored by mass spectrometry.

XRD patterns were acquired using wavelength of 0.504 Å delivered by a Si (111) channel-cut monochromator. The diffracted photons were recorded by 2 dimensional CCD detector located at 408.534 mm of the sample. The XRD patterns used as standards were downloaded from the Inorganic Structure Crystal Database of the Leibniz-Institut für Informationsinfrastruktur [226].

XAS spectra were recorded by continuous scanning at the Mo K-edge in transmission mode, and a Mo foil was used for calibration. The X-ray beam was monochromatized by a Si(111) double crystal monochromator and high harmonics rejected by a Au-coated mirror. The beam size on the samples was 0.3 mm vertical by 3.0 mm horizontal.

XAS data analysis was carried out using Athena and Arthemis software of the IFEFFIT package [227]. The spectra were energy calibrated from a reference metal foil, the background was extracted and then normalized. The structural parameters were obtained by adjusting theoretical backscatteing phases and amplitudes (ab initio calculated by FEEF6) [228].

During in situ analysis, the relative proportions between the starting and formed species were estimated by linear combinations carried out using the Athena IFEFFIT

software [227]. The linear combination fitting was performed in the spectral range of -20 and 90 eV, relative to the investigated edge. This procedure allowed tracking the proportion of species consumed and formed during the in situ reactions. The references for the linear combinations were the first spectrum, at room temperature, and the last spectrum at the final temperature.

3.5.9 X-Ray Diffraction

Powder X-Ray Diffraction (XRD) measurements were carried out using a PANalytical X'Pert PRO diffractometer in a Bragg-Brentano Theta-Theta geometry. The catalysts were analyzed in a $25° < 2\theta < 100°$ range using a monochromatic Cu-Kα radiation ($\lambda \approx 1.5418$ Å). XRD data treatment was carried out using PANalytical HighScore Plus 3.0.5 software and the average crystallite size was estimated using the Scherrer equation:

$$\tau = \frac{K\lambda}{\beta cos\theta} \tag{3.17}$$

Here K is a dimensionless shape factor, λ is the X-ray wavelength, β is the peak broadening measured at half the maximum intensity after subtracting the instrumental peak broadening and θ is the Bragg angle. The crystallite size analysis was carried out neglecting lattice strain effects.

Chapter 4

Screening of Catalysts for Hydrodeoxygenation of Phenol as Model Compound for Bio-oil

Abstract

Four groups of catalysts have been tested for hydrodeoxygenation (HDO) of phenol as a model compound of bio-oil, including oxide catalysts, methanol synthesis catalysts, reduced noble metal catalysts, and reduced non-noble metal catalysts. In total, 23 different catalysts were tested at 100 bar H_2 and 275 °C in a batch reactor. The experiments showed that none of the tested oxides or methanol synthesis catalysts had any significant activity for phenol HDO under the given conditions, which were linked to their inability to hydrogenate the aromatic ring of phenol. HDO of phenol over reduced metal catalysts could effectively be described by a kinetic model involving a two-step reaction in which phenol initially was hydrogenated to cyclohexanol and then subsequently deoxygenated to cyclohexane. Among reduced noble metal catalysts, ruthenium, palladium, and platinum were all found to be active, with activity decreasing in that order. Nickel was the only active non-noble metal catalyst. For nickel, the effect of support was also investigated and ZrO_2 was found to perform best. Pt/C, Ni/CeO_2, and Ni/CeO_2-ZrO_2 were the most active catalysts for the initial hydrogenation of phenol to cyclohexanol, but were not very active for the subsequent deoxygenation step. Overall, the order of activity of the best performing HDO catalysts was as follows: Ni/ZrO_2 > Ni-V_2O_5/ZrO_2 > Ni-V_2O_5/SiO_2 > Ru/C > Ni/Al_2O_3 > Ni/SiO_2 $\gg$ Pd/C > Pt/C. The choice of support influenced the activity significantly. Nickel was found to be practically inactive for HDO of phenol on a carbon support, but more active than the carbon-supported noble metal catalysts when supported on ZrO_2. This observation indicates that the nickel-based catalysts require a metal oxide as a carrier on which the activation of the phenol for the hydrogenation can take place by heterolytic dissociation of the O-H bond to facilitate the reaction.

4.1 Introduction

As discussed in Chapter 2, one of the major challenges in HDO is to find a catalyst with a high activity for the deoxygenation reaction and at the same time obtain a sufficient lifetime, as deposition of carbonaceous species has proven to be a severe problem [229]. Preferably, HDO catalysts should be relatively inexpensive and function at low temperatures (<300 °C) and low pressures (<100 bar). In particular, low temperatures are desirable to prevent coking [142] and therefore focus has in the current screening study been on catalysts operating at 275 °C. Four categories of catalysts were tested as catalysts for HDO of phenol:

1. Oxide catalysts
2. Methanol synthesis catalysts
3. Reduced noble metal catalysts
4. Reduced non-noble metal catalysts

Phenol was chosen as model compound of bio-oil, as phenols have been identified among the most persistent [40, 230], yet fairly abundant [231], compounds in the bio-oil.

As discussed in Section 2.4.1.1, oxide catalysts have been proposed to catalyze the reaction by roughly three steps as shown in Figure 4.1(a): chemisorption via the oxygen atom on a coordinatively unsaturated metal site, donation of a proton from a hydroxyl group, and desorption [111]. In this mechanism, the generation of vacancy sites (the dotted circle in the figure) is responsible for the activation of both the oxy-compound and hydrogen on the catalytic surface [111].

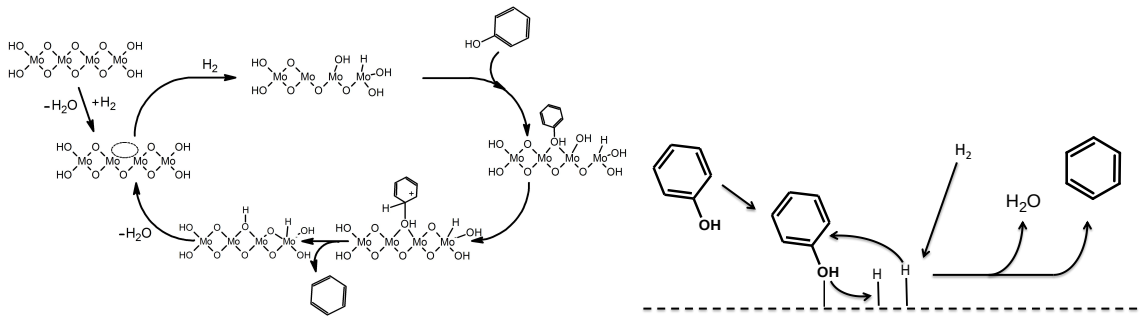

(a) Oxide catalysts reaction mechanism

(b) Reduced metal catalysts reaction mechanism

Figure 4.1: *Proposed reaction mechanisms of oxide catalysts (a) [111] and reduced metal catalysts (b) [116, 120].*

Methanol synthesis catalysts have proven to be able to activate CO/CO_2 by adsorption at the oxygen atom [232–235]. Thus, these catalysts could potentially activate oxy-compounds at their oxygen group and in this way permit reaction.

Figure 4.1(b) shows the key concepts of the reaction mechanism for reduced metal catalysts, as discussed in Section 2.4.1.2. The reaction is initiated by adsorption of the oxy-compound on the catalyst surface. Adsorbed hydrogen on the active

metal clusters reacts with the oxy-compound to facilitate the deoxygenation. This is followed by desorption of the final product. The oxy-compound adsorption step can take place either on the support or directly on the active metal, depending on which type of metal is used (cf. Section 2.4.1.2).

Hence, these four different classes of catalysts were screened in this work using the batch reactor setup described in Section 3.1. Table 3.5 in Section 3.4.1 summarizes the theoretical loading of active component, particle size of support (sieve fraction), specific surface area, and reduction conditions for the tested catalysts.

4.2 Kinetics of Phenol Hydrodeoxygenation

To determine the activity of the catalysts on a quantitative basis, a kinetic model was developed. In the following, this model is presented as a basis for the later discussion.

The time dependent development of the conversion of phenol and the yields of cyclohexanone, cyclohexanol, and cyclohexane in an experiment with a Ni-V_2O_5/SiO_2 catalyst at 250 °C and 100 bar in the batch reactor is shown in Figure 4.2. At first, phenol was converted to primarily cyclohexanol. This yield was maximal at approximately 3.5 h of reaction. The cyclohexane yield, on the other hand, increased continuously throughout the experiment, and with an increasing rate toward the end.

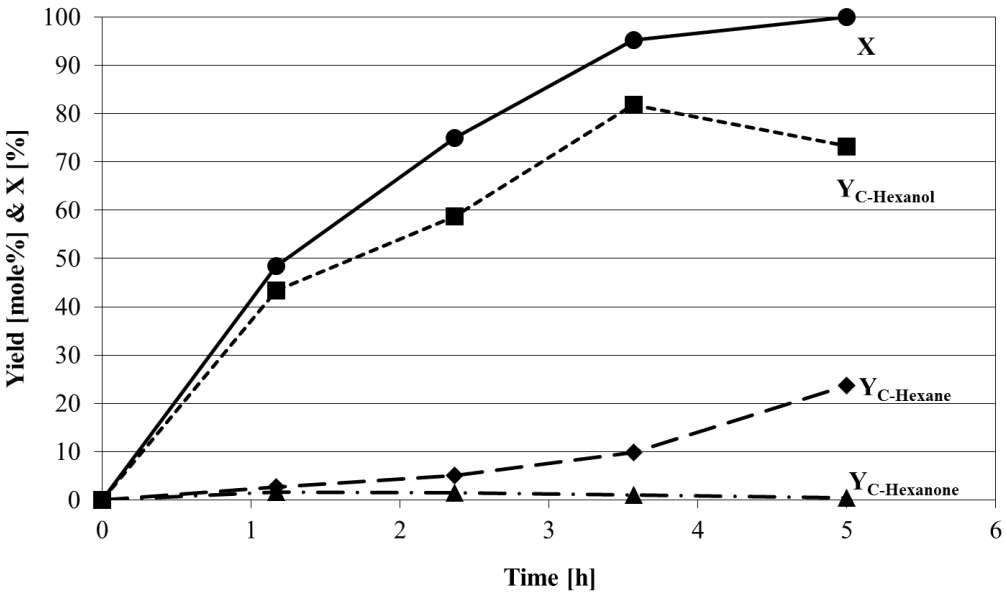

Figure 4.2: *Conversion of phenol (X) and yields of cyclohexanone, cyclohexanol and cyclohexane as a function of time over a Ni-V_2O_5/SiO_2 catalyst. The experiments were conducted with 1 g of catalyst in 50 g of phenol. $T = 250°C$, $P = 100$ bar.*

The data in Figure 4.2 indicate a reaction mechanism at 250 °C in which hydrogenation of the aromatic ring occurs as a first step followed by deoxygenation, with cyclohexanol as the intermediate product and cyclohexane as the final product. Also, cyclohexanone and cyclohexene were observed in small amounts. The cyclohexanone yield reached a maximum of 1.7% after 1 h and then steadily decreased (cf. Figure 4.2). The cyclohexene yield was even less and on the order of 0.01%.

Shuikin and Erivanskaya [236] suggested that hydrogenation of phenol over Ni catalysts produces cyclohexanone as the primary product; however the subsequent hydrogenation of cyclohexanone to cyclohexanol proceeds at a much higher rate, and therefore, cyclohexanone is seen in only low yields. Similarly, cyclohexene is formed by dehydration of cyclohexanol followed by quick hydrogenation to cyclohexane. Overall, the observations from Figure 4.2 and previous literature for nickel catalysts [236–238], Pd/C [129, 131], Pt/C [239], Ni/HZSM-5 [240], and Ni-MoS_2/Al_2O_3 [98] suggest the reaction scheme depicted in Figure 4.3 with solid arrows, specifically for supported metal catalysts.

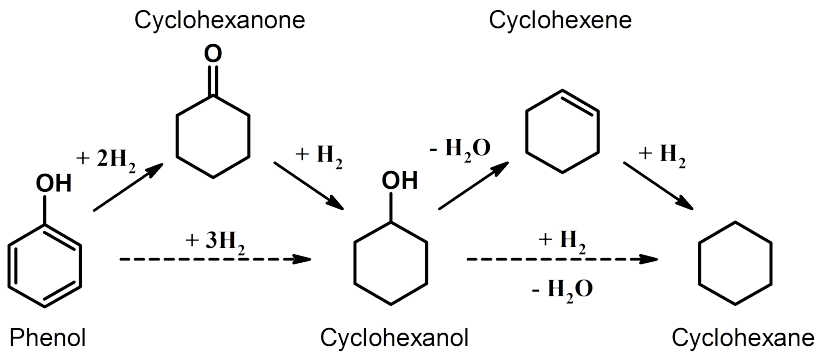

Figure 4.3: *Observed reaction path for HDO of phenol. Solid arrows indicate main pathways while dashed arrows show the effective conversion steps in the kinetic model.*

To verify this, the individual steps of Figure 4.3 were investigated in separate experiments to quantify the relative rates in one example with a Ni/ZrO_2 catalyst. Initially a 15 min short term isothermal experiment (see Section 3.1.2) was performed with 50 g of phenol, giving a phenol conversion of 26%.

Cyclohexanone was loaded in the reactor in another short term isothermal experiment and over 4 min of reaction a conversion of 44% was observed.

Cyclohexanol dehydration was quantified from the standard 5 h experiment where 99.8% conversion of phenol and a yield of 83% cyclohexane was found.

Hydrogenation of cyclohexene was quantified from a 5 min short term isothermal experiment with cyclohexene, giving a conversion of 98.7%.

Table 4.1 summarizes first order rate constants and turnover frequencies for the respective reactions from these experiments. This analysis confirmed that the rates of hydrogenation of cyclohexanone and cyclohexene were significantly higher than the hydrogenation of phenol and dehydration of cyclohexanol.

From the data in Figure 4.2 and 4.3, deoxygenation appears to take place more readily from a saturated ring than from an unsaturated ring, which has also been shown elsewhere [15, 40]. This is related to the dissociation energy of the C-O bond in alcohols [242], which decreases in the following order:

$$\begin{aligned}&\text{Aromatic alcohol } (469kJ/mol) >> \text{Secondary alcohol } (385kJ/mol)\\&\approx \text{Primary alcohol } (383kJ/mol) \approx \text{Tertiary alcohol } (379kJ/mol)\end{aligned} \tag{4.1}$$

The data clearly show that the aromatic alcohol (i.e. phenol) has a ~100 kJ/mol higher bond dissociation energy than the secondary alcohol (as cyclohexanol) and the

Table 4.1: *Experimetal data for quantifying individual reaction steps in Figure 4.3 over a 5 wt% Ni/ZrO_2 catalyst. Turnover frequency (TOF) is calculated from a nickel crystallite size of 7 nm, a dispersion of 0.20 and normalized to a standard concentration of 1 mol/l as recommended by Kozuch and Martin [241]. The experiments were made with 1 g of catalyst and 50 g of feed. T=275 °C, P=100 bar.*

Reaction	1st order k [ml/(kg_{cat} min)]	TOF [s^{-1}]
Phenol hydrogenation	1010	0.10
Cyclohexanone hydrogenation	7200	0.69
Cyclohexanol dehydration	330	0.03
Cyclohexene hydrogenation	43140	>4.1

deoxygenation can therefore more readily take place from the cyclohexanol compared to the phenol as the C-O bond is markedly weakened.

Because the rates of hydrogenation of both cyclohexanone and cyclohexene are relative fast and the yields of these compounds are low, the effective reaction scheme can be described by the dotted arrows in Figure 4.3, which gives the two following main reactions:

Reaction 1: $\text{Phenol} + 3H_2 \longrightarrow \text{Cyclohexanol}$

Reaction 2: $\text{Cyclohexanol} + H_2 \longrightarrow \text{Cyclohexane} + H_2O$

Assuming first-order dependency of the hydrocarbon compounds leads to the following rate expressions:

$$r_1 = k_1 \cdot C_{\text{Phenol}} \cdot P_{H_2}^n \tag{4.2}$$

$$r_2 = k_2 \cdot C_{\text{C-hexanol}} \cdot P_{H_2}^m \tag{4.3}$$

Here r_i is the rate of reaction i, k_i is the rate constant of reaction i, C_i is the concentration of either phenol or cyclohexanol, and n and m are the reaction orders of hydrogen in reaction 1 and 2, respectively. Previous work has shown that 1st order reactions of guaiacol, anisole, and phenol HDO sufficiently describes these systems for simple interpretations [243, 244].

As all the experiments were performed with the same and constant pressure of hydrogen, the hydrogen pressure can in the current case be included in the rate constant and thereby give the following lumped rate expressions:

$$r_1 = k_1' \cdot C_{\text{Phenol}} \tag{4.4}$$

$$r_2 = k_2' \cdot C_{\text{C-hexanol}} \tag{4.5}$$

Here k_1' is the rate constant for the hydrogenation reaction and k_2' is the rate constant for the deoxygenation reaction. By defining X_1 as the degree of conversion in reaction 1 relative to the initial phenol concentration and X_2 as the degree of conversion in reaction 2 relative to the initial phenol concentration a stoichiometric table can be set up as shown in Table 4.2.

Using the expressions for the molar amounts of phenol and cyclohexanol established in Table 4.2, the concentrations can be found as:

$$C_{\text{Phenol}} = C_{0,\text{Phenol}} \cdot (1 - X_1) \tag{4.6}$$

$$C_{\text{C-hexanol}} = C_{0,\text{Phenol}} \cdot (X_1 - X_2) \tag{4.7}$$

Table 4.2: Stoichiometric table for effective reaction scheme shown in Figure 4.3.

Compound	Phenol	Cyclohexanol	Cyclohexane
In	$n_{0,\text{Phenol}}$	0	0
Change	$-n_{0,\text{Phenol}} \cdot X_1$	$n_{0,\text{Phenol}} \cdot X_1 - n_{0,\text{Phenol}} \cdot X_2$	$n_{0,\text{Phenol}} \cdot X_2$
Out	$n_{0,\text{Phenol}} \cdot (1 - X_1)$	$n_{0,\text{Phenol}} \cdot (X_1 - X_2)$	$n_{0,\text{Phenol}} \cdot X_2$

Here $C_{0,\text{Phenol}}$ is the initial concentration of phenol.

The reaction takes place in a batch reactor, for which the mole balances are [199]:

$$\frac{dX_1}{dt} = k_1' \cdot (1 - X_1) \cdot \frac{W}{V} \tag{4.8}$$

$$\frac{dX_2}{dt} = k_2' \cdot (X_1 - X_2) \cdot \frac{W}{V} \tag{4.9}$$

Here W is the mass of catalyst and V is the volume of liquid in the reactor, which were assumed constant in the derivation and equal to the initial values. On this basis, the algebraic solution to Eq. 4.8 and 4.9 is:

$$X_1 = 1 - \exp\left(-k_1' \cdot \frac{W}{V} \cdot t\right) \tag{4.10}$$

$$X_2 = 1 - \frac{k_1' \cdot \exp\left(-k_2' \cdot \frac{W}{V} \cdot t\right) - k_2' \cdot \exp\left(-k_1' \cdot \frac{W}{V} \cdot t\right)}{k_1' - k_2'} \tag{4.11}$$

X_1 is identical to the conversion of phenol and from Table 4.2 it can be seen that X_2 is equivalent to the yield of cyclohexane.

The assumption of constant volume induces an uncertainty in the calculations since the liquid volume expands as phenol is converted into cyclohexanol/cyclohexane and water is evolved, while on the other hand some of the liquid evaporates into the gas phase. Based on stoichiometry and the specific volumes of the pure compounds, the liquid volume can be estimated to increase by 18% when phenol is completely converted to cyclohexanol and by 43% when phenol is completely converted to cyclohexane and water. Thus, the expansion of the liquid volume can be described as:

$$V = V_0 \cdot (1 + 0.18 \cdot (X_1 - X_2) + 0.43 \cdot X_2) \tag{4.12}$$

This does not take evaporation into account. By substituting this expression into Eq. 4.6-4.9 the equation system can be solved numerically. On average this increased the values of k_1' and k_2' in the order of 5%.

However, by a flash calculation using Specs v. 5.62 using the Soave-Redlich-Kwong equation of state combined with the association equation of state (CPA model [245, 246]), the equilibrium between the gas phase and the liquid phase at 275 °C and 100 bar was calculated for a mixture of 45 mole% H_2, 22 mole% phenol, and 11 mole% of cyclohexane, cyclohexanol, and water (corresponding to a case with $X_1 = 50\%$ and $X_2 = 25\%$ in the current setup). This showed that 45% of the phenol, 45% of the cyclohexanol, 60% of the cyclohexane, and 90% of the water was in the gas phase at the specified conditions.

Overall, the two phenomena induce changes in the liquid volume during the reaction, but with opposite effect. The low degree of change observed when using the expanding volume in Eq. 4.12 in the model indicates that the effect of the changing volume is limited and therefore the assumption of constant volume does not appear to cause a marked error. Thus, for all calculations of the kinetic parameters in the batch reactor experiments, the algebraic expressions of Eq. 4.10 and 4.11 have been used.

Finally the kinetic model was fitted to the data of Figure 4.2, as shown in Figure 4.4. The dotted lines indicate the fit of the kinetic model to the experimental data. The calculated values of X_1 and X_2 were within ±6% and ±2%, respectively, of the experimental data, which is acceptable considering the simplicity of the model and the incorporated assumptions. The good correlation between model and experiments further supports the validity of the implemented assumptions.

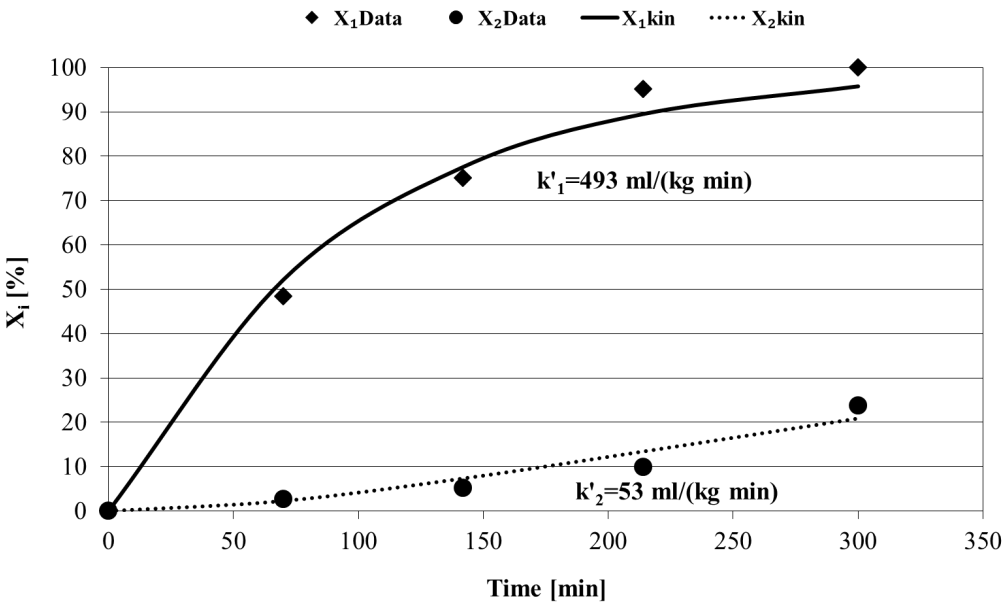

Figure 4.4: *Fit of the kinetic model to the experimental data from a test with Ni-V_2O_5/SiO_2. The experiments were made with 1 g of catalyst in 50 g phenol. T=250 °C, P=100 bar.*

4.3 Oxide and Methanol Synthesis Catalysts

The results from testing the oxide catalysts at 275 °C and 100 bar are shown in Figure 4.5 in terms of the yields of cyclohexanone, cyclohexanol, and cyclohexane, and the conversion of phenol. None of the catalysts achieved a conversion >10%. The NiO-MoO_3/Al_2O_3 catalyst showed some hydrogenation activity with a yield of 4% oxygenated cyclohexanes. However, the activity for HDO over this catalyst was low, with a yield of cyclohexane of only 0.9%.

Table 4.3 gives a summary of the performance of the catalysts. The carbon balances of the experiments were reasonably well closed and in most cases were on the order of -2%. Only the CoO-MoO_3/Al_2O_3 catalyst had a larger carbon deviation

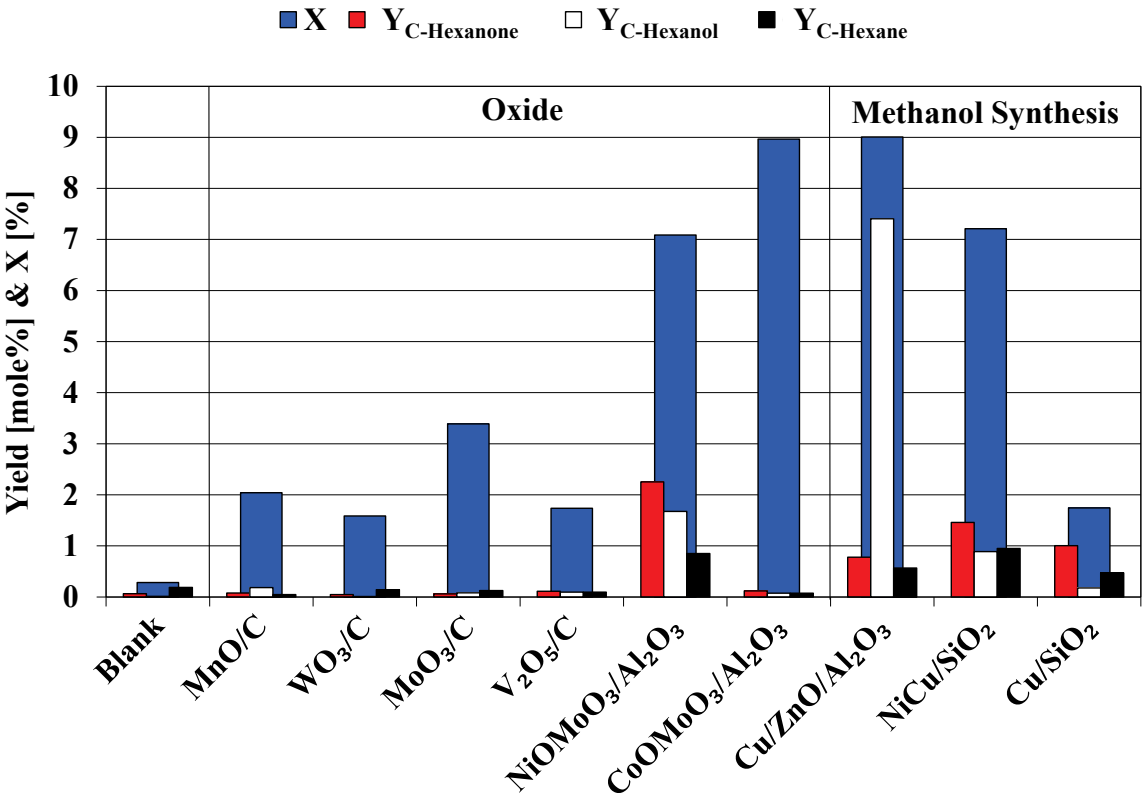

Figure 4.5: *Conversion of phenol (X) and yields of cyclohexanone, cyclohexanol, and cyclohexane from experiments with different types of oxide catalysts ("Oxide") and methanol synthesis catalysts ("Methanol Synthesis") and for the blank experiment. The experiments were conducted with 0.5 g of catalyst in 10 g of phenol and 40 ml of water.* $T = 275°C$, $P = 100$ *bar. The reaction time was 4 h.*

of -8.5%. As the conversion of phenol was 9% on this catalyst, it could indicate that this catalyst mainly was active for cracking.

Prasomsri et al. [247] did observe HDO activity of bulk V_2O_5, Fe_2O_3, CuO, WO_3, and MoO_3 catalysts in a continuous flow reactor for acetone and anisole deoxygenation in the gas phase at atmospheric pressure and 400 °C, with MoO_3 performing the best. In contrast to their study for which temperatures of 400 °C were required to deoxygenate anisole, much lower temperatures were used in the current screening. The higher temperature requirement is probably linked to the inability of the catalyst to hydrogenate the anisole and instead being forced to break the stronger C-O bond of the aromatic alcohol compared to the saturated form, as discussed in Section 4.2 (see Eq. 4.1).

Figure 4.5 also shows the results of the screening of the methanol synthesis catalysts (Cu/SiO_2, $NiCu/SiO_2$, and $Cu/ZnO/Al_2O_3$). This group of catalysts also had a low activity. $Cu/ZnO/Al_2O_3$ had a conversion of ~9%, but primarily was selective toward hydrogenation, with cyclohexanol and cyclohexanone constituting 91% of the product. $NiCu/SiO_2$ had a conversion of 7%, but according to the carbon balance (cf. Table 4.3) half of the measured conversion was not accounted for.

Among these catalysts, $Cu/ZnO/Al_2O_3$ was the best performing, with the highest conversion and a good closure of the carbon balance (ΔC = -0.2%). However, as the

Table 4.3: *Overview of results from different oxide catalysts and methanol synthesis catalysts.* k_1' *is the rate constant for hydrogenation,* k_2' *is the rate constant for deoxygenation, and* ΔC *is the deviation in the carbon balance. The experiments were conducted with 0.5 g of catalyst in 10 g of phenol and 40 ml of water.* $T = 275°C$, $P = 100$ *bar. The reaction time was 4 h.*

Catalyst	k_1' [ml/(kg$_{cat}$ min)]	k_2' [ml/(kg$_{cat}$ min)]	ΔC [%]
Blank	-	-	0.0
MnO/C	1	7	-1.1
WO_3/C	1	10	-1.4
MoO_3/C	2	4	-3.1
V_2O_5/C	1	3	-1.4
NiO-MoO_3/Al_2O_3	5	20	-2.2
CoO-MoO_3/Al_2O_3	6	0	-8.5
Cu/ZnO/Al_2O_3	8	10	-0.2
NiCu/SiO_2	7	28	-3.9
Cu/SiO_2	1	50	-0.1

product primarily was cyclohexanol the potential of this catalyst seems limited in the context of HDO.

Ardiyanti et al. [248] previously investigated Cu/Al_2O_3 and NiCu/Al_2O_3 catalysts at varying Ni/Cu ratios for HDO of anisole at 300 °C and 10 bar in a continuous flow reactor. In these studies, it was observed that the pure Cu catalyst was unable to perform HDO of the anisole, as the only product was phenol. For NiCu/Al_2O_3, the best catalyst was obtained with a 8:1 Ni:Cu weight ratio. In agreement with this, we also observed improved activity of the NiCu/SiO_2 (with a Ni:Cu ratio of 1) catalyst relative to that of Cu/SiO_2, but the activity of NiCu/SiO_2 was not optimized as in the work of Ardiyanti et al. [248]. The results indicate that the Ni loading has to be markedly higher than the Cu loading to achieve good HDO activity.

Summarizing, the apparent order of activity for the tested oxide and methanol catalysts was:

$$\begin{aligned}\text{Cu/ZnO/Al}_2\text{O}_3 \approx \text{NiO-MoO}_3\text{/Al}_2\text{O}_3 \approx \text{NiCu/SiO}_2 > \text{Cu/SiO}_2 \\ > \text{MnO/C}, \text{WO}_3\text{/C}, \text{V}_2\text{O}_5\text{/C}, \text{CoO-MoO}_3\text{/Al}_2\text{O}_3\end{aligned}$$

Commonly, none of the catalysts achieved high conversion under these conditions because of their inability to hydrogenate the aromatic ring of phenol (cf. hydrogenation rate constants in Table 4.3).

4.4 Reduced Noble Metal Catalysts

In the experiments with reduced noble metal catalysts, higher conversions were observed compared to the oxide and methanol synthesis catalysts. Thus, pure phenol was used for these experiments, as this gave consistency. The reaction temperature and pressure were kept the same.

Figure 4.6 summarizes the conversion of phenol and the yields of cyclohexanol, cyclohexane, and dicyclohexyl ether from the experiments with noble metal catalysts. All the catalysts gave complete conversion of the phenol by a relatively fast hydrogenation reaction to cyclohexanol. The subsequent HDO more favorably took place on the ruthenium catalyst than on the platinum and palladium catalysts. The ruthenium catalyst provided a yield of 52% cyclohexane relative to 1% and 11% on the platinum and palladium catalysts, respectively. The palladium catalyst furthermore had a high yield of dicyclohexyl ether of 21%, i.e. higher than the cyclohexane yield.

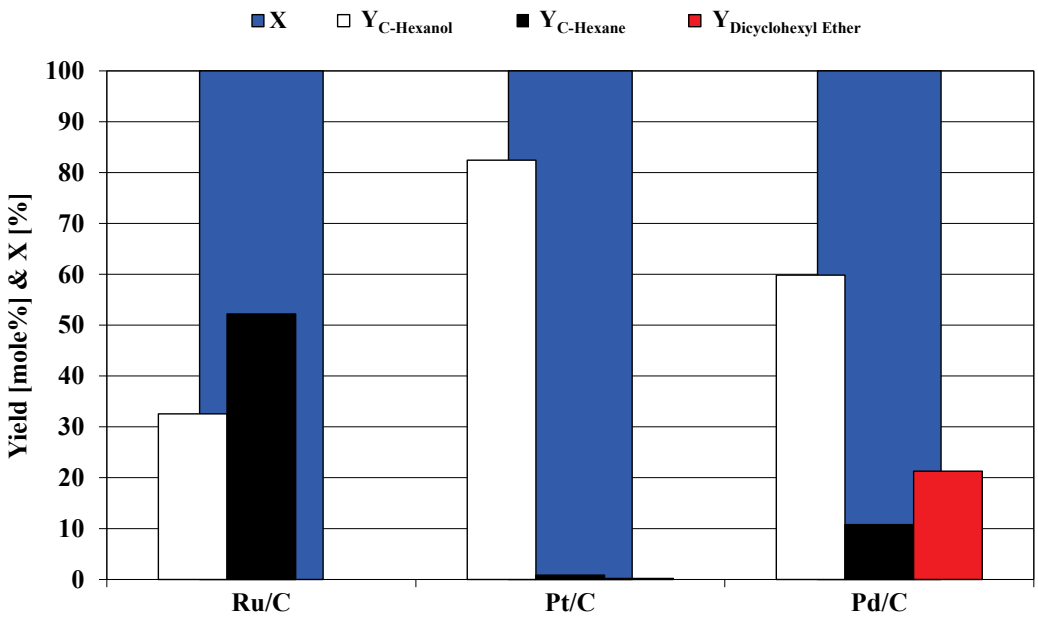

Figure 4.6: *Conversion of phenol (X) and yields of cyclohexanol, cyclohexane, and dicyclohexyl ether from experiments with different types of reduced noble metal catalysts. The experiments were conducted with 1 g of catalyst in 50 g of phenol.* $T = 275°C$, $P = 100$ *bar. The reaction time was 5 h.*

Table 4.4 summarizes the kinetic parameters of the reactions. The hydrogenation rate constants (k_1') were on the same order of magnitude for Ru/C and Pd/C, but Pt/C had a rate of hydrogenation ~1 order of magnitude higher. In general, all three catalysts, however, were good hydrogenation catalysts, achieving 100% conversion of the phenol in the 5 h experiments.

With regard to the hydrodeoxygenation step (k_2') the catalytic activity of Ru/C was 1 order of magnitude higher than that of Pd/C, and 2 orders of magnitude higher than that of Pt/C. This analysis does not take into account that the primary part of the deoxygenation for the Pd/C catalyst was taking place by the ether-forming reaction, and k_2' is therefore not completely descriptive of the affinity for deoxygenation on Pd/C. Nevertheless, the trend is clear.

The carbon balance in Table 4.4 shows that all the tested catalysts lacked on the order of 5-10% carbon. Analysis of the gas phase from the Ru/C experiment by sampling in a gas bag and then analyzing on a GC-TCD instrument showed the presence of CO_2, CH_4, and CO. Furthermore, traces of pentane, hexane, ethanol, methanol, and acetone could be identified in the oil phase. This shows that cracking

Table 4.4: *Overview of results from the reduced noble metal catalysts. d_M is the metal particle size measured by XRD, k_1' is the rate constant for hydrogenation, k_2' is the rate constant for deoxygenation, and ΔC is the deviation in the carbon balance. The experiments were conducted with 1 g of catalyst in 50 g of phenol. $T = 275°C$, $P = 100$ bar. The reaction time was 5 h.*

Catalyst	d_M [nm]	k_1' [ml/(kg$_{cat}$ min)]	k_2' [ml/(kg$_{cat}$ min)]	ΔC [%]
Ru/C	7	1950[a]	115	-10.8
Pt/C	4	31200[b]	1	-11.8
Pd/C	6	1840[c]	19	-6.1

[a]Determined from an 18 min isothermal experiment at 275 °C with 50% phenol conversion.
[b]Determined from a 10 min isothermal experiment at 275 °C with 99.8% phenol conversion.
[c]Determined from a 16 min isothermal experiment at 275 °C with 44% phenol conversion.

reactions take place on the Ru/C catalyst. It has previously been shown that Ru/C can produce CH_4 and CO_2 from guaiacol at temperatures above 250 °C [134]. Elliott and Hart [134] linked the production of these gases to aqueous phase reforming, which for Ru/C has been shown to occur under similar conditions [249].

Overall, the apparent order of activity for deoxygenation for the tested noble metal catalysts for HDO of phenol was found to be:

$$\text{Ru/C} > \text{Pd/C} > \text{Pt/C}$$

In agreement with this, Elliott and Hart [134] found Ru/C to be a better catalyst than Pd/C for the conversion of guaiacol in a batch reactor. Wildschut et al. [68] identified Ru/C and Pd/C as better performing catalysts compared to Pt/C for bio-oil HDO in a batch reactor. Lee et al. [250] identified Ru/SiO_2-Al_2O_3 as the best performing catalyst for guaiacol HDO in comparison to platinum and palladium. Adriyanti et al. [251] found Pd/ZrO_2 to be a better catalyst for bio-oil HDO in a batch reactor compared to Pt/ZrO_2. Thus, the current results for HDO over noble metal catalysts are in good agreement with the literature, which all point toward ruthenium being one of the best performing noble metals for HDO and with Pd being more efficient than Pt. The kinetic model revealed that the reason for this is that Pt is a relatively poor deoxygenation catalyst but a very good hydrogenation catalyst.

The reason for ruthenium being the best performing noble metal could be correlated to the affinity of the metals to bind oxygen. Nørskov et al. [252] showed by density functional theory (DFT) calculations that the binding energies of oxygen relative to water (ΔE_O) were -0.01 eV, 1.53 eV, and 1.57 eV on Ru, Pd, and Pt, respectively. Thus, ruthenium has the strongest binding energy with respect to oxygen, and platinum the weakest, which correlates with the affinity for performing deoxygenation.

In this work the effect of support was not investigated, but previous work has shown that the type of support can significantly increase the activity of noble metal catalysts. Lee et al. [250] tested noble metal catalysts on C, Al_2O_3, and SiO_2-Al_2O_3 for guaiacol HDO at 250 °C and 40-70 bar in a batch reactor. Their work showed

that the activity of all the supported noble metal catalysts was improved in the order of increasing support acidity, i.e. an apparent order of activity of: NM/SiO_2-Al_2O_3 > NM/Al_2O_3 > NM/C, where NM is a noble metal. Similar, Foster et al. [253] also observed increasing catalytic activity for HDO of m-cresol over platinum catalysts with increasing acidity of the support at 260 °C and 1 atm in a packed bed reactor setup. Both studies point toward an acidic support possibly can increase the activity of the noble metal catalysts. The role of support is discussed further in Section 4.5.1.

4.5 Reduced Non-noble Metal Catalysts

Prior to the activity tests of the non-noble metal catalysts, the required reduction temperatures were determined by H_2-TPR. Table 4.5 summarizes the results of these measurements, showing the temperature intervals where the reduction took place. Detailed TPR profiles can be found in Appendix D.

Table 4.5: *Results from H_2-TPR of the reduced non-noble metal catalysts. Start and end indicate the temperature interval where reduction was observed. TPR profiles can be found in Appendix D. Gas: 5% H_2 in N_2, Flow: 100 Nml/min, Heating ramp: 5 °C/min up to 300 °C, 1 °C/min from 300 °C to 500 °C, and 5 °C/min from 500 °C to 700 °C, Sample amount: 20-40 mg.*

Catalyst	Start [°C]	End [°C]	Mass loss [wt%]	Theoretical mass loss
Co/SiO_2	260	520	1.0	1.4
Ni/SiO_2	305	365	1.4	1.4
Ni/Al_2O_3	310	505	0.9	1.4
Ni/CeO_2	280	335	1.3	1.4
Ni/CeO_2-ZrO_2	295	500	1.2	1.4
Ni/ZrO_2	310	485	1.4	1.4
Ni/$MgAl_2O_4$	305	500	0.6	1.4
Ni/C	360	505	1.1	1.4
Ni-V_2O_5/SiO_2	300	390	3.1	5

For the nickel-based catalysts, the theoretical mass loss is 1.4 wt% for a nickel loading of 5 wt%, assuming that all nickel is reduced from NiO to Ni. Generally, the measured mass loss was close to the theoretical mass loss. The largest deviation was seen in the case of Ni/Al_2O_3 and Ni/$MgAl_2O_4$ with measured mass losses of 0.9 wt% and 0.6 wt%, respectively. For these catalysts, the XRD analysis of the used catalysts revealed that the nickel to some extent was interacting with the supports, forming a mixed oxide with the alumina or spinel. These oxides have been shown to retard reduction, resulting in the observed lower degree of reduction [254].

For Ni-V_2O_5/SiO_2, complete reduction of the nickel and vanadium into NiV/SiO_2 would result in a theoretical mass loss of 5 wt%. However, only 3.1 wt% weight loss was observed, showing that the catalyst was not completely reduced and probably still contained vanadium in the form of oxides even at 700 °C.

Overall, the identified end temperatures from the TPR analysis are judged to be sufficient for complete reduction. The actual reduction temperature, which is given in Table 3.5, was set higher for the individual samples to ensure complete reduction.

Three reduced non-noble metals were tested: Ni/SiO_2, Co/SiO_2, and Fe/SiO_2. These were chosen on the basis of their known hydrogenation activity in other processes [208, 255–257]. Figure 4.7 shows the comparison between the activities of these three catalysts. Ni/SiO_2 was the most active catalyst with a conversion of 80%, compared to 3.2% and 0.8% for Co/SiO_2 and Fe/SiO_2, respectively.

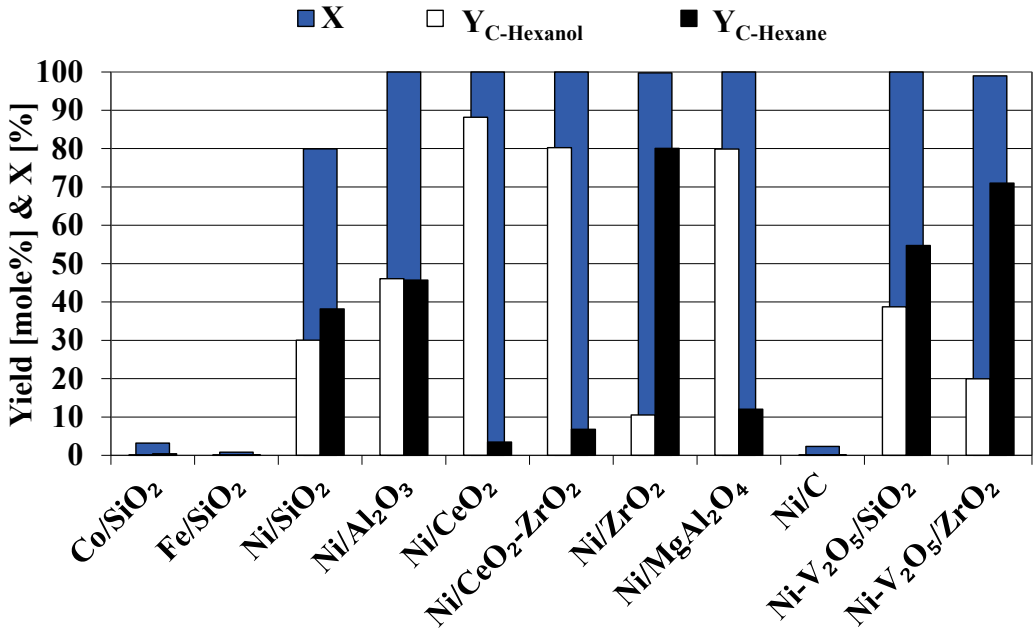

Figure 4.7: *Conversion of phenol (X) and yields of cyclohexanol and cyclohexane from experiments with different types of reduced non-noble metal catalysts. The experiments were conducted with 1 g of catalyst in 50 g of phenol. $T = 275°C$, $P = 100$ bar. The reaction time was 5 h.*

The kinetic data for the three catalysts are listed in Table 4.6. The k_1' rate constants of Co/SiO_2 and Fe/SiO_2 were 5 ml/(kg_{cat} min) and 1 ml/(kg_{cat} min), respectively, showing that Co/SiO_2 was the better hydrogenation catalyst of the two. However, k_1' was two orders of magnitude larger for Ni/SiO_2 in comparison. k_2' was on the same order of magnitude for Co/SiO_2 and Fe/SiO_2, but significantly larger for Ni/SiO_2, as seen from Table 4.6.

XRD of the spent Ni/SiO_2, Co/SiO_2, and Fe/SiO_2 showed the active metals to be reduced and to have similar metal particle sizes.

In summary, the apparent order of activity for the three non-noble metal catalysts is:

$$Ni/SiO_2 \gg Co/SiO_2 > Fe/SiO_2 \tag{4.13}$$

The better performance of Co/SiO_2 compared to that of Fe/SiO_2 is due to a better activity for hydrogenation on this catalyst. Finding similar results, Filley and Roth [258] investigated cobalt and iron supported on alumina for HDO of guaiacol at atmospheric pressure and 350 °C and did not find any notable activity. Yakovlev et al. [116] investigated both cobalt and nickel catalysts for HDO of anisole at 300 °C and 10 bar of hydrogen and found that Co/SiO_2 was practically inactive compared to Ni/SiO_2, which is similar to the results of this work.

Table 4.6: *Overview of results from reduced non-noble metal catalysts. d_M is the metal particle size measured by XRD, k_1' is the rate constant for hydrogenation, k_2' is the rate constant for deoxygenation, and ΔC is the deviation in the carbon balance. NH_3 ads. (adsorption) is the ammonia saturation measured by NH_3-TPD, the data is distinguished in weak and strong adsorption with weak being the signal recorded for desorption peaks below 200 ° and strong being above. The experiments were conducted with 1 g of catalyst in 50 g of phenol. $T = 275°C$, $P = 100$ bar. The reaction time was 5 h.*

Catalyst	d_M [nm]	k_1' [ml/(kg$_{cat}$ min)]	k_2'	ΔC [%]	NH_3 ads. [μmol/g$_{cat}$] Weak	Strong
Co/SiO_2	12	5	52	-2.6	-	-
Fe/SiO_2	12	1	64	-0.3	-	-
Ni/SiO_2	9	230	159	-4.2	40	-
Ni/Al_2O_3	7	3200[a]	100	-0.5	210	220
Ni/CeO_2	8	21800[b]	6	-8.0	-	400
Ni/CeO_2-ZrO_2	6	10500[c]	13	-6.3	-	250
Ni/ZrO_2	7	1010[d]	361	-1.1	210	210
$Ni/MgAl_2O_4$	10	6580[e]	25	-4.4	140	150
Ni/C	14	3	121[f]	-2.0	30	-
Ni-V_2O_5/SiO_2	-	1160	136	-0.8	60	-
Ni-V_2O_5/ZrO_2	-	701	256	-1.5	130	230

[a]Determined from a 13 min isothermal experiment at 275 °C with 54% phenol conversion.
[b]Determined from a 10 min isothermal experiment at 275 °C with 98.7% phenol conversion.
[c]Determined from a 15 min isothermal experiment at 275 °C with 95% phenol conversion.
[d]Determined from a 15 min isothermal experiment at 275 °C with 26% phenol conversion.
[e]Determined from a 10 min isothermal experiment at 275 °C with 74% phenol conversion.
[f]Determined from a 4 h experiment at 275 °C with cyclohexanol as the feed instead of phenol.

4.5.1 Support Effect on Nickel Catalysts

With nickel identified as the best performing of the tested non-noble metal catalysts, this was chosen for further investigation with respect to the influence of support.

Seven different types of supports of comparable specific surface areas (cf. Table 3.5) were tested and very different activities were observed, as summarized in Figure 4.7. Ni/C was the only catalyst with practically no activity and a conversion of only 2%. On the other hand, Ni/CeO_2, Ni/CeO_2-ZrO_2, and $Ni/MgAl_2O_4$ were very active for hydrogenation with conversions of 100%, but less active for deoxygenation with yields of cyclohexane of 4%, 8%, and 12%, respectively. Ni/Al_2O_3 had a high activity for both hydrogenation and deoxygenation with a conversion of 100% and a yield of 46% cyclohexane. Ni/SiO_2 gave a yield of cyclohexane on the same order of magnitude (38%), but was significantly less active for hydrogenation with a conversion of 80%. Ni/ZrO_2 was the overall best performing catalyst under these conditions with complete conversion of phenol and a high selectivity toward cyclohexane ($Y_{\text{C-hexane}} = 83\%$).

The kinetic data in Table 4.6 show that Ni/CeO_2 had the highest hydrogenation rate constant (k_1') followed by Ni/CeO_2-ZrO_2. Both catalysts showed hydrogenation

rate constants one order of magnitude higher than those of $Ni/MgAl_2O_4$, Ni/Al_2O_3, and Ni/ZrO_2, decreasing in that order. Ni/SiO_2 had a hydrogenation rate constant two orders of magnitude lower than that of Ni/CeO_2.

In contrast, the Ni/CeO_2 catalyst had practically no activity for deoxygenation. The deoxygenation activity of Ni/CeO_2-ZrO_2 and $Ni/MgAl_2O_4$ was 2-5 times larger than for Ni/CeO_2, but still low yields of cyclohexane were produced. Only Ni/ZrO_2, Ni/SiO_2, and Ni/Al_2O_3 had relatively high rates of deoxygenation, decreasing in that order. An interesting aspect of this is that Ni/SiO_2 had a higher rate constant for deoxygenation than Ni/Al_2O_3, but because Ni/Al_2O_3 had a higher rate of hydrogenation, the cyclohexane yield with the Ni/Al_2O_3 catalyst was higher than that with the Ni/SiO_2 catalyst.

Ni/SiO_2 and Ni/ZrO_2 were additionally tested as catalysts where the support had initially been promoted by vanadium before impregnation with nickel. The results of these experiments are also shown in Figure 4.7, while kinetic data are listed in Table 4.6. For Ni-V_2O_5/SiO_2 the rate of hydrogenation was significantly increased compared to that of the pure Ni/SiO_2 catalyst. The cyclohexane yield also increased, which was primarily caused by the increased rate of hydrogenation, as the rate of deoxygenation did not change between the Ni-V_2O_5/SiO_2 and Ni/SiO_2 catalysts (cf. Table 4.6). The Ni-V_2O_5/ZrO_2 catalyst performed slightly worse than the non-vanadium-doped catalyst, as both the yield of cyclohexane and the rate constants were lower. Overall, it was observed that addition of vanadium primarily influenced the hydrogenation rate of the catalysts.

The carbon balances listed in Table 4.6 show an adequate closure in most cases. The largest deviation was found for the Ce-containing supports, where 6-8% of the carbon was unrecovered. This indicates that either cracking or coke deposition could take place on these catalysts. On the other hand, for the two best performing catalysts, Ni/ZrO_2 and Ni/Al_2O_3, the carbon balance deviation was on the order of 1% indicating that these catalysts were less prone to coke deposition. In general, better closure of the carbon balance was found for the nickel-based catalysts than for the noble metal catalyst (cf. Table 4.4 and 4.6) showing that these catalysts had a weaker tendency to cause cracking.

NH_3-TPD was performed, giving information about the total amount of available acid sites on the catalysts (see Table 4.6). The total acidity of the supports decreases in the following order:

$$\begin{aligned} &Ni/Al_2O_3 \geq Ni/ZrO_2 \geq Ni/CeO_2 > Ni\text{-}V_2O_5/ZrO_2 > Ni/MgAl_2O_4 \\ &> Ni/CeO_2\text{-}ZrO_2 \gg Ni\text{-}V_2O_5/SiO_2 > Ni/SiO_2 > Ni/C \end{aligned}$$

Via comparison of this to the apparent order of activity discussed above (or see Table 4.6), it follows that the amount of available acid sites (as measured by NH_3-TPD) and the HDO activity are not directly correlated. Most notable is Ni/SiO_2, which practically contains no acid sites but is found to be one of the three best HDO catalysts (of the investigated nickel catalysts). However, comparing only the rate constant for hydrogenation to the acidity gives some consistency as the poor hydrogenation catalysts (Ni/SiO_2 and Ni/C) have very little acidity, while the catalysts with better hydrogenation affinity all have higher acidity. However, the acidity measurements do not reveal the true acidic nature of the catalyst under experimental conditions,

as the reducing atmosphere in the experiments will result in an increased level of formation of oxygen vacancy sites and thereby acid sites [259–262].

A better understanding of this is gained by plotting the hydrogenation activity relative to the metal-oxygen bond strength ($E_{(\text{M-O})}$) of the support, as shown in Figure 4.8. This reveals that oxide supports with low metal-oxygen bond energy had the highest activity for hydrogenation. Low M-O bond energies can be linked to the tendency for oxygen vacancy site generation in the oxide [263, 264], and these vacancy sites will function as Lewis acid sites [262, 264]. Thus, the best performing hydrogenation catalyst is therefore the catalyst with the strongest tendency to form Lewis acid sites in the oxide structure and that is most likely on the supports with the lowest metal-oxygen bond energy. Because of this effect, introducing V_2O_5 to a SiO_2 support causes formation of more vacancy sites because of the lower metal-oxygen bond energy of V_2O_5 (12.3 eV) compared to that of SiO_2 (34.2 eV) and thereby increases the hydrogenation activity (cf. Table 4.6). In contrast, doping ZrO_2 with V_2O_5 does not induce any large changes as the metal-oxygen bond energies are relatively close (14.2 eV compared to 12.3 eV, respectively).

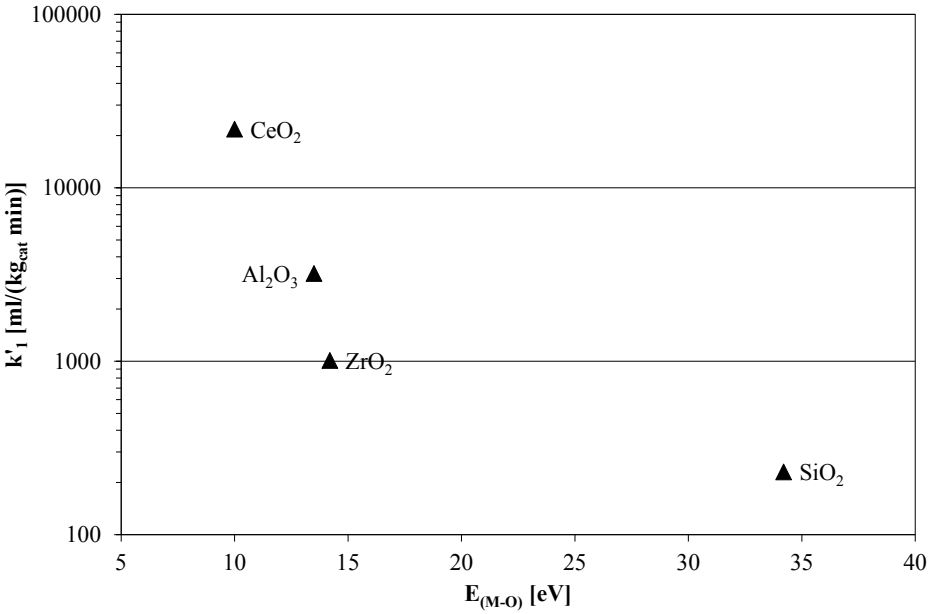

Figure 4.8: *Hydrogenation activity as a function of the metal-oxygen bond strength ($E_{(M\text{-}O)}$) of the pure support. Only hydrogenation rate constants for nickel catalysts supported on pure oxides from Table 4.6 are plotted. $E_{(M\text{-}O)}$ data from Idriss and Barteau [264].*

A similar correlation to the metal-oxygen bond energy could not be made with respect to the deoxygenation affinity, which indicates that this reaction does not rely on the activation on oxygen vacancies in the support.

Taking the yield of cyclohexane as the primary parameter for the ranking, the apparent order of activity for HDO of phenol with nickel on different supports can be summarized as:

$$\text{Ni/ZrO}_2 > \text{Ni-V}_2\text{O}_5\text{/ZrO}_2 > \text{Ni-V}_2\text{O}_5\text{/SiO}_2 > \text{Ni/Al}_2\text{O}_3 > \text{Ni/SiO}_2$$
$$\gg \text{Ni/MgAl}_2\text{O}_4 > \text{Ni/CeO}_2\text{-ZrO}_2 \approx \text{Ni/CeO}_2 \gg \text{Ni/C}$$

It may be expected that the nickel particle size will influence the kinetics of the reactions, so it is important to note that the ranking presented here was made for catalysts with roughly the same nickel particle size (cf. Table 4.6).

Comparing k_2' values for the most active nickel catalyst: Ni/ZrO_2, $Ni\text{-}V_2O_5/ZrO_2$, $Ni\text{-}V_2O_5/SiO_2$, Ni/Al_2O_3, and Ni/SiO_2 shows that all values are on the same order of magnitude (ranging from 100-361 ml/(kg_{cat} min)). The differences are probably related to support-metal interaction.

On the other hand, $Ni/MgAl_2O_4$, $Ni/CeO_2\text{-}ZrO_2$, and Ni/CeO_2 all have lower k_2' values. For the $Ni/MgAl_2O_4$ catalyst, TPR showed that it was hard to reduce (cf. Table 4.5), indicating that part of the nickel is interacting with the support, as also indicated by XRD (cf. Section 4.5). This could be the reason for the poor performance of this catalyst.

For the catalysts with Ce-containing supports the carbon balance indicated a tendency toward cracking/coke formation, and therefore the poor deoxygenation performance of these catalysts could be related to potential deactivation of the deoxygenating sites by carbon deposition. However, no further investigations into these issues have been performed.

Obviously, Ni/C exhibited behavior markedly different from that of the other supports. Hence, this catalyst was tested in an experiment in which 50 g of cyclohexanol was used as feed with 1 g of catalyst at 100 bar and 275 °C for 4 h. In this experiment, a conversion of 47% was observed with a yield of 42% cyclohexane, the remaining product being primarily dicyclohexyl ether (4% yield). Thus, despite not being active for hydrogenation of the aromatic ring of phenol, this catalyst was found to be active for deoxygenation. Calculating the kinetic rate constant for this reaction (corresponding to k_2') further showed that the deoxygenation capability of this catalyst was on the same order of magnitude as those of the other nickel catalysts, as shown in Table 4.6.

Hence, all catalysts supported on oxides are active for both hydrogenation and deoxygenation, but with different rates. In contrast, the carbon-supported catalyst is active for only the deoxygenation reaction. In a continuation of the discussion in Section 2.4.1.2, it follows that the dual action of the catalyst primarily is required in the hydrogenation of complex molecules as phenol. On the other hand, the deoxygenation can take place on the nickel surfaces. Thus, we suggest a mechanism as sketched in Figure 4.9 for the HDO of phenol over nickel catalysts. The coordinatively unsaturated metal sites in the oxide surface often behave like Lewis acids, and the surface oxygen behaves like Lewis bases [262]. Thus, the activation of phenol on the oxide can take place by heterolytic dissociation of the O-H bond on the oxide where the hydrogen from the phenol is adsorbed on an oxygen site in the oxide surface layer and a metal vacancy site stabilizes the phenoxide ion. Generally, alcohols have been found to almost always adsorb by heterolytic dissociation on metal oxides [262]. Supporting this, Popov et al. [137] observed phenoxide formation on Al_2O_3 when studying adsorption of phenol via IR spectroscopy. Liu et al. [265] concluded that when phenol is adsorbed at a Lewis acid site, one of the carbons in the aromatic ring becomes highly nucleophilic and thereby receptive to electrophiles, such as H^+. Thus, the phenoxide will interact with a nickel particle where hydrogen has been adsorbed, thereby facilitating the saturation of the double bounds and producing

cyclohexanone. These steps are all illustrated in Figure 4.9. The cooperative effect of the support and active metal has also been found for the phenol hydrogenation on palladium catalysts where the activity for hydrogenation can be significantly increased by the introduction of a Lewis acid because of the activation of the phenol on the Lewis sites [265–267].

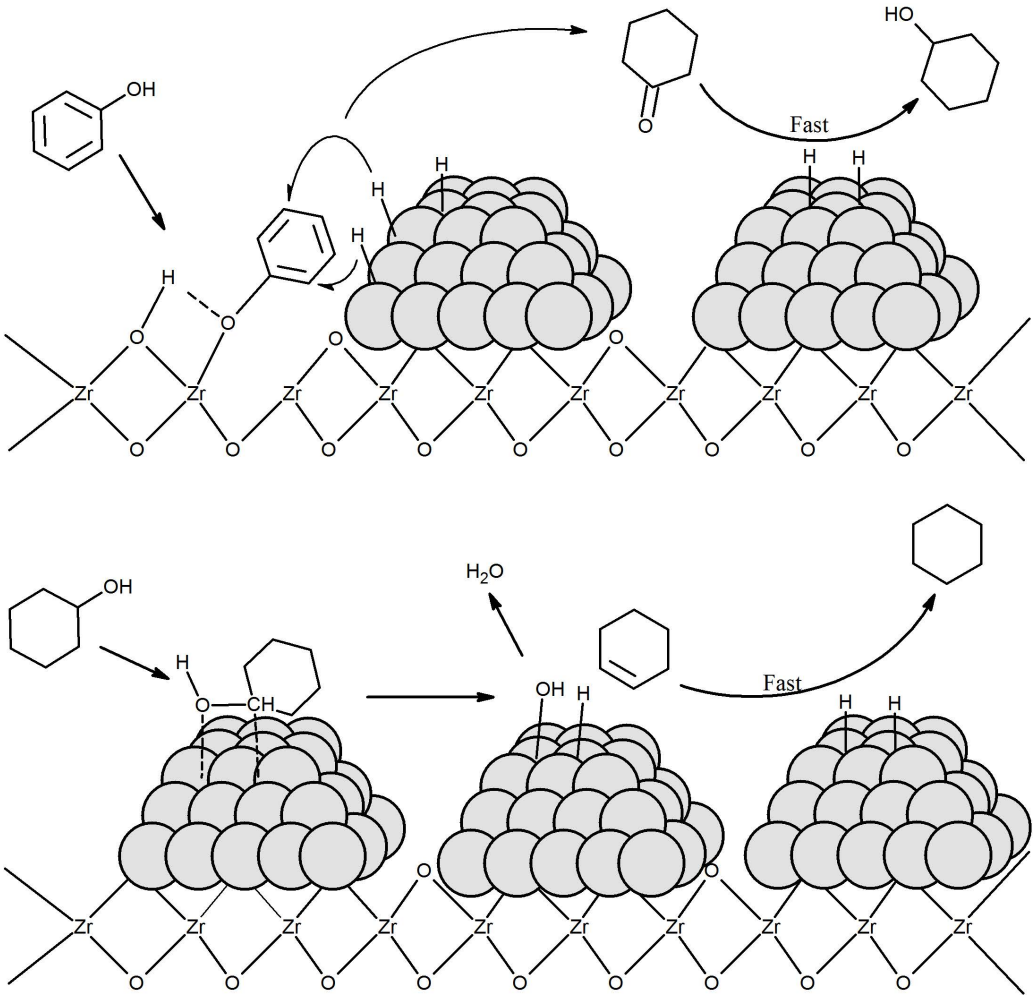

Figure 4.9: *Proposed reaction mechanism for HDO of phenol over an oxide-supported nickel catalyst (here Ni/ZrO_2). Gray spheres represent nickel atoms.*

The formed cyclohexanol can directly react with the exposed metallic nickel surfaces as shown in Figure 4.9 by adsorption at the OH-group. The actual deoxygenation step probably takes place by a dehydration reaction, forming cyclohexene, as proposed in the reaction scheme of Figure 4.3. The cyclohexene can subsequently be hydrogenated into cyclohexane as the final product. This reaction mechanism is more complex than that described in Figure 4.1(b).

In summary, among all tested catalysts, only those catalysts that showed both good hydrogenation and deoxygenation capabilities performed well, as a key step in the HDO of phenol under the tested conditions is the weakening of the C-O bond obtained by hydrogenation of the aromatic ring, as described in Section 4.2. Hydrogenation of an aromatic hydrocarbon is, however, not trivial as these are considered

to bind weakly to metal catalysts compared to conventional alkenes [268, 269], but adsorption on Lewis acid sites on the support appears to aid in this task.

4.6 Conclusion

Screening experiments have been performed to identify efficient catalysts for HDO of phenol at intermediate temperature and pressure (275 °C and 100 bar) in a batch reactor. Four groups of catalysts were investigated: oxide catalysts, methanol synthesis catalysts, reduced noble metal catalysts, and reduced non-noble metal catalysts, totaling 23 catalytic systems.

Across the series of investigated catalysts distinct differences were observed in the catalytic activity. Listing the apparent order of activity for all the tested catalysts, the following was found:

$$\begin{gathered}\mathrm{Ni/ZrO_2} > \mathrm{Ni\text{-}V_2O_5/ZrO_2} > \mathrm{Ni\text{-}V_2O_5/SiO_2} > \mathrm{Ru/C} > \mathrm{Ni/Al_2O_3} > \mathrm{Ni/SiO_2} \\ \gg \mathrm{Pd/C} > \mathrm{Ni/MgAl_2O_4} > \mathrm{Ni/CeO_2\text{-}ZrO_2} \approx \mathrm{Ni/CeO_2} > \mathrm{Pt/C} \\ \gg \mathrm{Cu/ZnO/Al_2O_3} \approx \mathrm{NiO\text{-}MoO_3/Al_2O_3} \approx \mathrm{NiCu/SiO_2} > \mathrm{Cu/SiO_2} \\ > \mathrm{Co/SiO_2} > \mathrm{Ni/C} > \mathrm{Fe/SiO_2}, \mathrm{MnO/C}, \mathrm{WO_3/C}, \mathrm{V_2O_5/C}, \mathrm{CoO\text{-}MoO_3/Al_2O_3}\end{gathered}$$

The tested oxide and methanol synthesis catalysts had a low activity for the HDO of phenol under the given conditions, which was linked to their inability to hydrogenate the phenol ring. Reduced metal catalysts of both noble and non-noble metals were significantly more active. On these catalysts, HDO of phenol proceeds by an initial hydrogenation to cyclohexanone, which is rapidly hydrogenated to cyclohexanol. This can then in a second step be dehydrated to cyclohexene, which is rapidly hydrogenated to cyclohexane. The hydrogenation of the aromatic ring causes a weakening of the C-O bond, making the deoxygenation more favorable from cyclohexanol than from phenol.

A kinetic model revealed that the best hydrogenation catalyst not necessarily was the best deoxygenation catalyst. Pt/C, Ni/CeO_2, and Ni/CeO_2-ZrO_2 were found to be the best performing hydrogenation catalysts, with their effectiveness decreasing in that order, but were all found to have low activity for deoxygenation.

Nickel was the best performing reduced non-noble metal catalyst and was therefore tested on different supports. Oxide supports showed good activity, while a non-oxide support (as carbon) showed no activity for phenol HDO. However, Ni/C was active for HDO of cyclohexanol showing that the activation of the phenol prior to the hydrogenation takes place on an oxygen vacancy site on the oxidic support, but the subsequent deoxygenation likely takes place directly on the nickel particles.

Noble metal catalysts, in contrast to nickel, performed well on carbon supports, showing that these metals on their own have the required affinity for phenol activation probably by direct interaction with the aromatic ring. Ruthenium was found to be the most active catalyst of the carbon-supported transitions metals, but overall, Ni/ZrO_2 was the best performing catalyst, with balanced rates of both hydrogenation and deoxygenation. Thus, nickel appears to be a promising catalyst for HDO with a prospective activity and an appealing price.

Chapter 5

Structure Sensitivity of Nickel Based Catalysts for the Hydrodeoxygenation of Phenol

Abstract

Hydrodeoxygenation (HDO) of phenol over different sizes of nickel nano-particles (5-22 nm) supported on SiO_2 has been investigated in a batch reactor at 275 °C and 100 bar. Deoxygenation was only observed as a consecutive step of the hydrogenation of phenol. Rapid hydrogenation of phenol was achieved on the large particles, while the rate of deoxygenation of cyclohexanol was slow. For hydrogenation, the turn over frequency (TOF) was 85 times slower for 5 nm particles than for 22 nm particles. Contrary, the TOF of cyclohexanol deoxygenation increased by a factor of 20 with decreasing particle size. A kinetic model showed that the rate limiting step for phenol HDO shifted from deoxygenation to hydrogenation when the particle size was below 9-10 nm. Surface site population theory and a simple Langmuir-Hinshelwood kinetic model evidenced that the deoxygenation reactions were favored on step/corner sites, giving higher deoxygenation rates at small particles. For hydrogenation, the influence of particle size may be caused by a certain minimum size of the surface facets or by competitive adsorption on hydrogenation sites.

5.1 Introduction

From the screening work in Chapter 4, supported reduced nickel was identified as a prospective catalytic system for HDO of phenol. For metal supported catalysts, it is known that the activity of the catalyst can be altered by changing the metal particle size as this will induce a change in the fraction of available surface sites (facet sites, step sites, and corner sites) [270, 271]. Such structure-performance relations have been observed in: steam reforming over supported noble metal and nickel catalysts [272–274], methanation reaction over nickel catalysts [275, 276], Fischer-Tropsch synthesis on cobalt and ruthenium catalysts [277–280], CO oxidation over supported gold catalysts [281–284], CO and NO oxidation over Pt based catalysts [285], and oxygen reduction on Pt based catalysts [286, 287]. However, no similar work has yet been done in the area of HDO.

In the current work the kinetics over a 5 wt% Ni/SiO_2 catalyst has been investigated in the batch reactor setup described in Section 3.1 with special emphasis on understanding the influence of metal particle size and the relationship between the hydrogenation and deoxygenation reactions taking place for HDO of phenol.

5.2 Results

Ni/SiO_2 was prepared using four different reduction methods (Red. 1-4, as described in Section 3.4.2) to investigate the effect of the metal particle size on the catalytic performance. The particle sizes were measured on the basis of ETEM images at 450 °C and 2.5 mbar H_2. Figure 5.1 shows sample images from each of the four catalysts and the particle size distribution. The number based average particle size of the four samples was 22±3 nm, 14±3 nm, 10±3 nm, and 5±2 nm for respectively Red. 1, Red. 2, Red. 3, and Red. 4. The sub-figure to each picture show the Gaussian function fitted to the size distribution. Overall the four samples represent very different average particle sizes and relatively narrow particle size distributions.

The different catalysts were tested in the batch reactor setup with 50 g of phenol as reactant at 275 °C and 100 bar for 5 h. Figure 5.2 shows the conversion of phenol and the yields of cyclohexane and cyclohexanol for these experiments. The conversion of phenol increased as a function of the particle size. A conversion of phenol of 41% was obtained for the 5 nm particles, but ca. 100% for both the 14 nm and 22 nm cases. This is intuitively a somewhat surprising result since decreasing particle size, i.e. increasing dispersion, is normally expected to increase the rate of catalytic reactions, and not the opposite. It can further be seen that the yield of cyclohexanol increased with increasing particle size, while the cyclohexane yield had a maximum for the 10 nm particle size and was lowest in the case of the largest particles. However, the case with the lowest particle size had the highest selectivity toward cyclohexane, with practically no cyclohexanol in the products.

Generally, cyclohexane and cyclohexanol constituted the primary products from the reaction with a combined selectivity in the order of 80-90%. Besides these, cyclohexanone (up to 10% selectivity), cyclohexene (up to 5% selectivity), and bicyclic compounds such as dicyclohexyl ether and bicyclohexyl (up to 5% selectivity) were identified as the major byproducts. Overall supporting the reaction scheme in Figure 4.3.

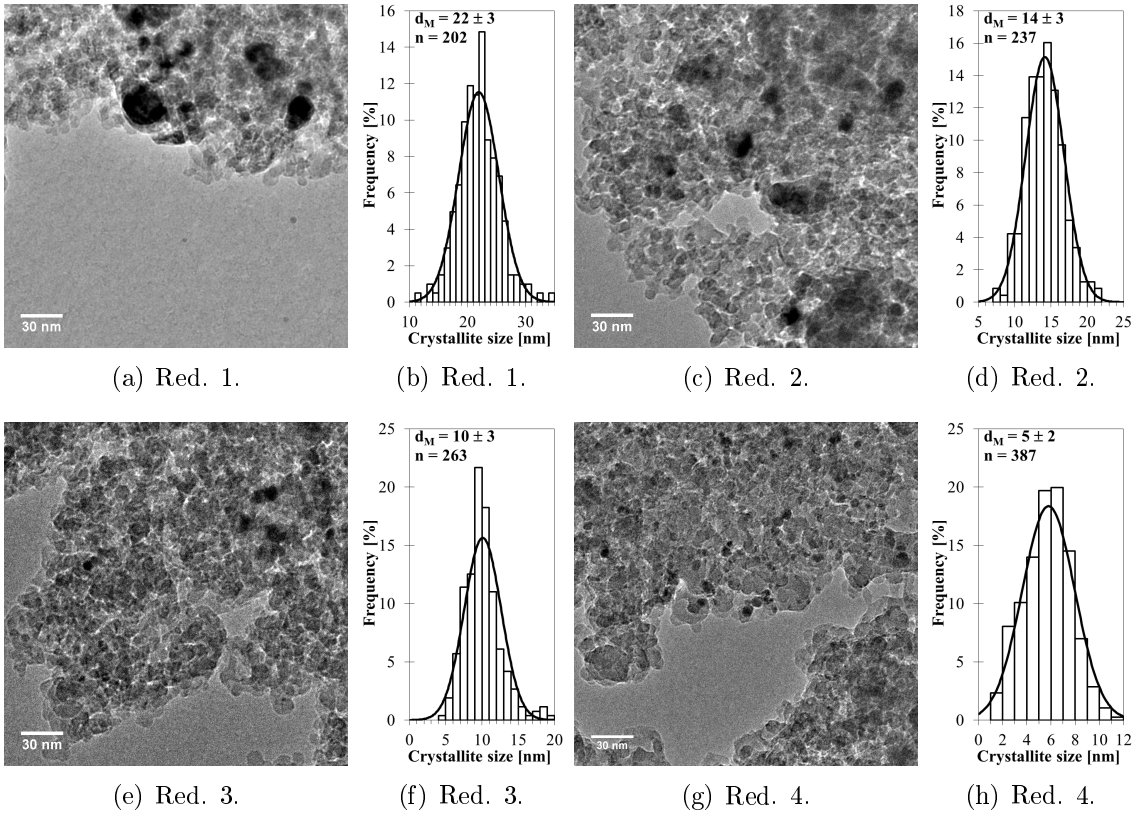

(a) Red. 1. (b) Red. 1. (c) Red. 2. (d) Red. 2.

(e) Red. 3. (f) Red. 3. (g) Red. 4. (h) Red. 4.

Figure 5.1: *ETEM images of the Ni/SiO_2 catalysts showing particle sizes and particle size distribution and Gaussian fit of Red. 1 (a,b), Red. 2 (c,d), Red. 3 (e,f), and Red. 4 (g,h).*

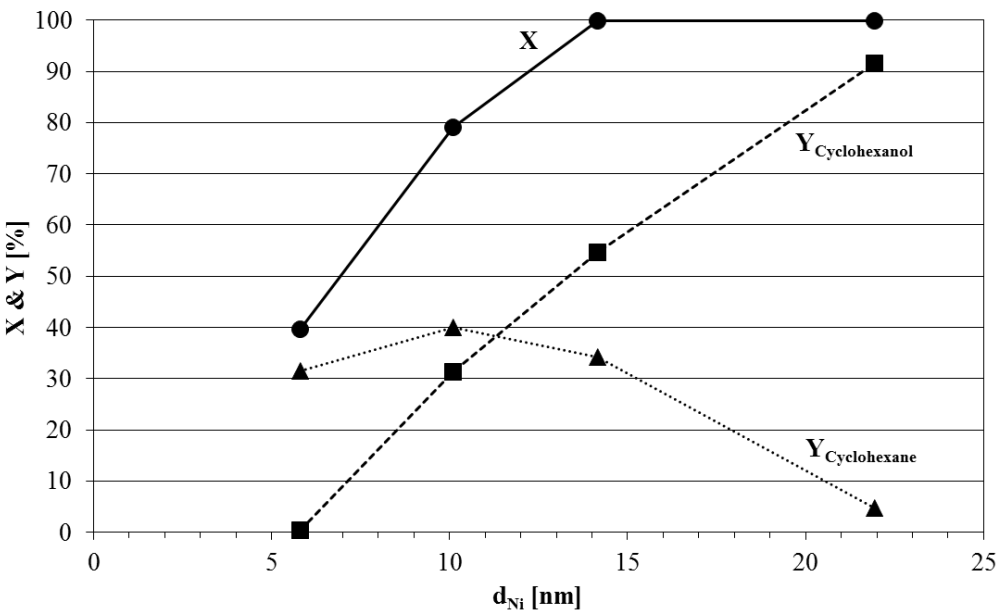

Figure 5.2: *Conversion of phenol (X) and yields of cyclohexanol and cyclohexane as a function of the nickel particle sizes on Ni/SiO_2 catalysts. The experiments were made with 1 g of catalyst in 50 g phenol. T=275 °C, P=100 bar, reaction time=5 h.*

As presented in Table 5.1, the carbon balance closed well in all experiments. Only Red. 5 had a loss of more than 6% carbon, but the other experiments were closed within 2%.

Table 5.1: *Overview of results from the Ni/SiO_2 catalysts with different particle sizes. d_{Ni} is the nickel crystallite size measured by ETEM, k_1' is the rate constant for hydrogenation, k_2' is the rate constant for deoxygenation, and ΔC is the deviation in the carbon balance. The experiments were made with 1 g of catalyst in 50 g phenol. T=275 °C, P=100 bar, reaction time=5 h.*

Sample	d_{Ni} [nm]	k_1' [ml/(kg$_{cat}$ min)]	k_2' [ml/(kg$_{cat}$ min)]	ΔC [%]
Red. 1	22 ± 3	1830[a]	8	-0.7
Red. 2	14 ± 3	900[b]	70	-5.5
Red. 3	10 ± 3	220	180	-0.2
Red. 4	5 ± 2	80	650	-1.6

[a]Determined from a 15 min isothermal experiment at 275 °C with 40% phenol conversion.
[b]Determined from a 15 min isothermal experiment at 275 °C with 21% phenol conversion.

The data in Figure 5.2 were used to fit values of k_1' and k_2' in the kinetic model introduced in Section 4.2. For Red. 1 and Red. 2 (where 100% conversion was achieved during the 5 h experiments presented in Figure 5.2), additional 15 min experiments were performed to determine k_1'. The kinetic data is shown as a function of the nickel particle size in Figure 5.3. The rate of hydrogenation (k_1') increased as a function of particle size with about two orders of magnitude from the highest to the lowest value. On the contrary, the rate of deoxygenation (k_2') decreased with increasing particle size. Linking these observations to Figure 5.2, it follows that the low conversion for Red. 4 was accompanied by a very rapid deoxygenation, explaining the high selectivity toward cyclohexane. For this catalyst the rate constant for deoxygenation was higher than the rate constant for hydrogenation. Thus, a shift in the rate determining step occurs for Ni/SiO_2 catalysts with nickel particles around ca. 9-10 nm, as seen from the intersect in Figure 5.3. When the particle size is above 9-10 nm the rate limiting step is the deoxygenation, but below this range the rate limiting step becomes the hydrogenation.

5.3 Theoretical Distribution of Nickel Sites

Further interpretation of the results in Figure 5.2 and 5.3 required analysis of the crystal structure and the availability of different surface sites. Three types of sites are generally considered: facet sites, step sites, and corner sites, as visualized in Figure 5.4. The overall (measured) rate constant is the result of the contribution from each

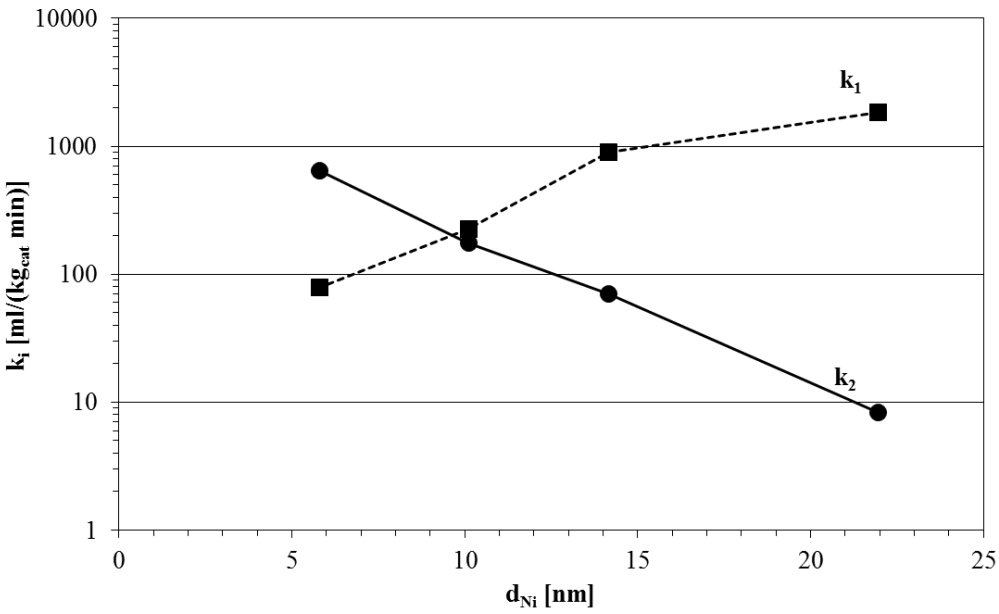

Figure 5.3: *k_1' and k_2' as a function of the nickel particle sizes on Ni/SiO_2 catalysts. k_1' in the two cases with 100% conversion (cf. Figure 5.2) was determined by additional shorter 15 min isothermal experiments. k_1' represents the rate constant for hydrogenation and k_2' represents the rate constant for deoxygenation. The experiments were made with 1 g of catalyst in 50 g phenol. Typical conditions: T=275 °C, P=100 bar, reaction time=5 h.*

of these sites, leading to the following equation:

$$k = k_{facet} \cdot N_{facet} + k_{step} \cdot N_{step} + k_{corner} \cdot N_{corner} \quad \Leftrightarrow \tag{5.1}$$

$$\frac{k}{N_S} = k_{facet} \cdot \frac{N_{facet}}{N_S} + k_{step} \cdot \frac{N_{step}}{N_S} + k_{corner} \cdot \frac{N_{corner}}{N_S} \quad \Leftrightarrow \tag{5.2}$$

$$\frac{k}{N_S} = k_{facet} \cdot x_{facet} + k_{step} \cdot x_{step} + k_{corner} \cdot x_{corner} \tag{5.3}$$

Here k is the overall rate constant in ml/(kg$_{\text{cat}}$ min), k_i is the rate constant at the specific site in ml/(site min), N_i is the number of sites of type i in sites/kg$_{\text{cat}}$, N_S is the total number of exposed surface atoms in sites/kg$_{\text{cat}}$, and x_i is the fraction of the different sites. This can be linked to the turn over frequency (TOF):

$$TOF = C^\circ \cdot N_A \cdot \frac{k}{N_S} \tag{5.4}$$

$$= C^\circ \cdot N_A \cdot (k_{facet} \cdot x_{facet} + k_{step} \cdot x_{step} + k_{corner} \cdot x_{corner}) \tag{5.5}$$

Here TOF is the turn over frequency in 1/min, C° is the standard concentration of 1 mol/l (as recommended by Kozuch and Martin [241]), and N_A is the Avogadro constant in mol^{-1}. As both a rate constant for the hydrogenation reaction (k_1') and the deoxygenation reaction (k_2') has been defined, the TOF for hydrogenation (TOF$_{\text{Hyd}}$) and the TOF for deoxygenation (TOF$_{\text{Deox}}$) can now be defined on the basis of Eq. 5.4 by calculating the surface sites (in sites sites/kg$_{\text{cat}}$) as:

$$N_T = \frac{w_{\text{Ni}}}{M_{\text{Ni}}} \tag{5.6}$$

$$N_S = D \cdot N_T \tag{5.7}$$

Here D is the dispersion, w_{Ni} is the weight fraction of nickel on the catalyst, and M_{Ni} is the molar mass of nickel.

On the basis of the ETEM determination of the average particle size, the dispersion (D) was calculated as [288]:

$$D = \frac{5.01 \cdot d_{\mathrm{M},at}}{d_{\mathrm{M}}}, \qquad 6\ nm < d_{\mathrm{M}} \tag{5.8}$$

$$D = \left(\frac{3.32 \cdot d_{\mathrm{M},at}}{d_{\mathrm{M}}}\right)^{0.81}, \quad 1\ nm < d_{\mathrm{M}} < 6\ nm \tag{5.9}$$

Here $d_{\mathrm{M},at}$ is the atomic diameter of the relevant metal ($d_{\mathrm{Ni},at} = 2.48$ Å) and d_{M} is the particle size of the metal.

Icosahedrons are one of the preferred crystal shapes for nickel nanoparticles, as shown by Cleveland and Landman with the embedded atom method [289] and as expected from an inert support like silica where no strong metal-support interaction is expected. The surface site population model by Benfield [290] states that the fraction of the three different surface sites on icosahedrons can be calculated as:

$$x_{corner} = \frac{N'_{corner}}{N'_S} = \frac{12}{N'_S} \tag{5.10}$$

$$x_{step} = \frac{N'_{step}}{N'_S} = \frac{24 \cdot (m-2)}{N'_S} \tag{5.11}$$

$$x_{facet} = \frac{N'_{facet}}{N'_S} = \frac{6 \cdot (m-2)^2 + 4 \cdot (m-3) \cdot (m-2)}{N'_S} \tag{5.12}$$

$$N'_S = 10 \cdot m^2 - 20 \cdot m + 12 \tag{5.13}$$

$$N'_T = \frac{1}{3} \cdot (2 \cdot m - 1) \cdot (5 \cdot m^2 - 5 \cdot m + 3) \tag{5.14}$$

$$D = \frac{N'_S}{N'_T} = \frac{N_S}{N_T} \tag{5.15}$$

Here m is the cluster edge length, D the dispersion, and N'_i is atoms of type i in a single crystal. N'_i relates to N_i by a factor of how many crystals are present per kg of catalyst.

Based on Eq. 5.10-5.15 the fraction of the different surface sites can be plotted as a function of dispersion, as shown in Figure 5.4. The fraction of facet sites decreases with dispersion (approximately linearly), the fraction of step sites increases with dispersion (approximately linearly), and the fraction of corner sites slowly increases with dispersion (approximately with the square of the dispersion).

Coupling this to the TOF defined in Eq. 5.5, this will decrease as a function of the dispersion if the reaction primarily is taking place at the facet sites. Contrary, the TOF will increase approximately linearly as a function of dispersion if the reaction preferentially takes place on the step sites and if the reaction preferably is taking place on the corner sites it will increase with the square of the dispersion.

Additionally, the total amount of surface sites available per mass of catalyst is plotted in Figure 5.4 to clearly show that the amount of available sites scales with the dispersion; at high dispersions more sites are available.

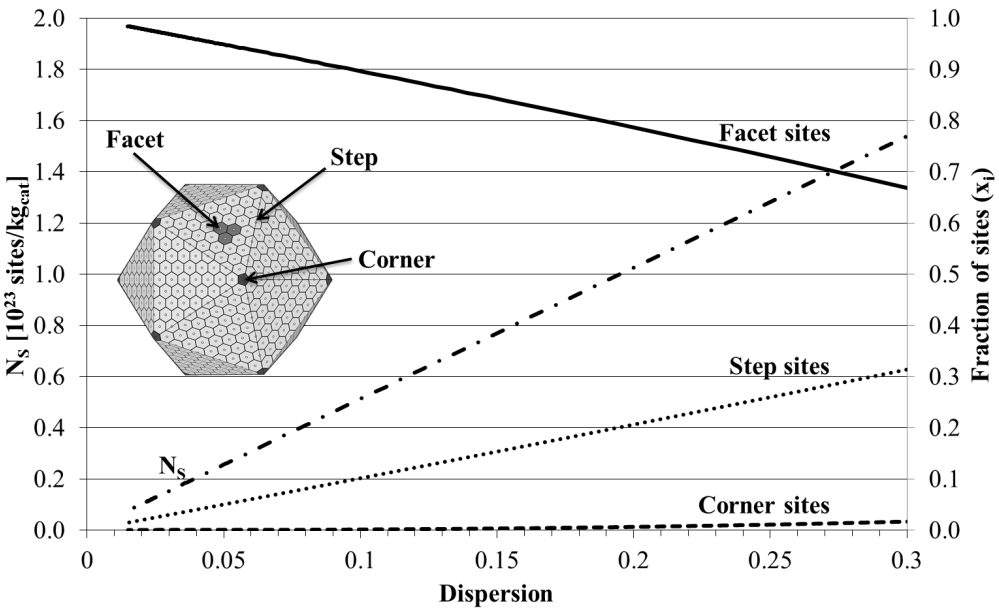

Figure 5.4: *Fraction of different surface sites (x_i) and the total amount of surface sites (N_S) as a function of dispersion of icosahedron crystals. Calculations were made on the basis of the relations derived by Benfield [290].*

5.4 Discussion

By combining Eq. 5.4 with the kinetic data in Figure 5.3, TOF_{Hyd} and TOF_{Deox} was plotted as a function of dispersion, as shown in Figure 5.5. TOF_{Deox} increased almost linearly as a function of dispersion. This is similar to the observed trend of the fraction of step sites in Figure 5.4. As the development in the fraction of corner sites is limited in the relevant dispersion range (cf. Figure 5.4), the contribution from this type of site is difficult to deduce, but most likely both step and corner sites could catalyze the reaction as both are low coordinated sites leading to the observed structure-sensitivity of the reaction.

In Section 4.5.1, it was evidenced that the deoxygenation of cyclohexanol takes place by direct adsorption of the alcohol on the nickel particle, and from Figure 5.5 it therefore follows that the low coordinated nickel sites facilitate this adsorption.

A number of studies have been reported on site dependency or structure sensitivity for other combinations of catalytic systems/reactions. For example, Jones et al. [272] showed that the TOF of methane steam reforming over supported Ru, Rh, Ni, Ir, Pt, and Pd catalysts scaled linearly with dispersion, linking this to the step sites exhibiting the highest activity for the reaction. Bengaard et al. [291] showed by DFT calculations on different nickel sites that the activation energy for methane dissociation was ca. 80 kJ/mol on a step site compared to ca. 100 kJ/mol on a facet site, indicating a significantly higher activity on the step sites relative to the facet sites. Overall, it has therefore been established that low coordinated sites are the most active ones for steam reforming over supported metal catalysts [272–274].

Similarly, DFT unraveled that the low coordinated Ni sites lead to the lowest activation energy for CO dissociation on nickel catalysts [276]. Elaborating on this, Engbæk et al. [275] showed that by selective poisoning the step sites of a nickel catalyst with sulfur, the rate of CO dissociation decreased by a factor of more than

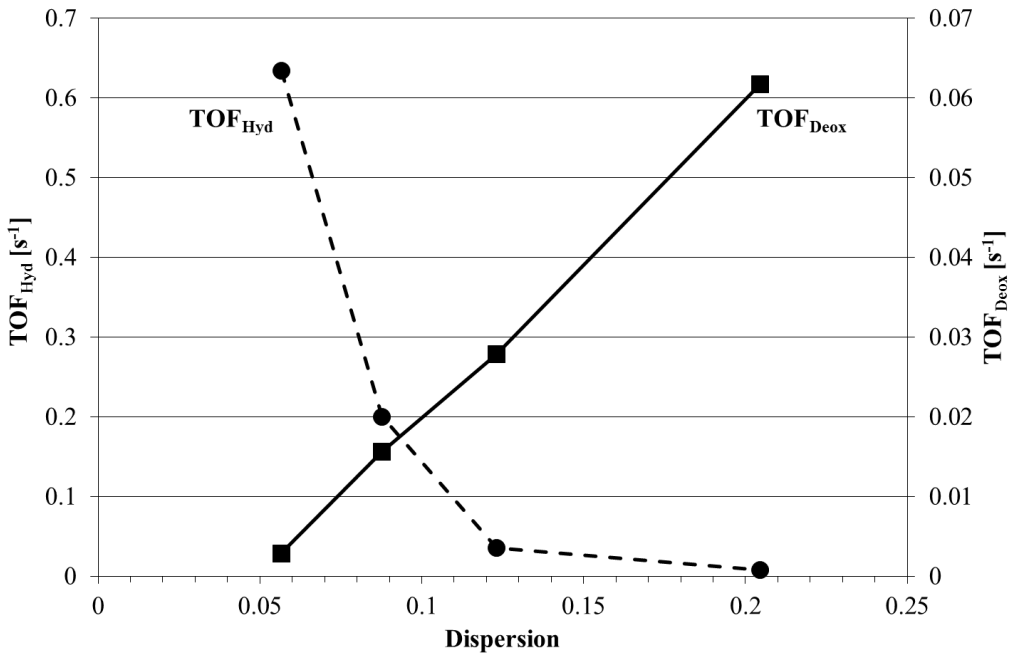

Figure 5.5: *TOF_{Hyd} and TOF_{Deox} over Ni/SiO_2 catalysts plotted as a function of dispersion. TOF_{Hyd} represents the TOF for hydrogenation and TOF_{Deox} represents the TOF for deoxygenation. The experiments were made with 1 g of catalyst in 50 g phenol. T=275 °C, P=100 bar, reaction time=5 h.*

50. Thus, step sites are the most active in the methanation reaction on this type of catalyst [275, 276].

In addition, Grunwaldt et al. [281] found that low coordinated sites were essential for low temperature CO oxidation on gold catalysts. This is because the affinity to adsorb CO and O_2 is much higher on low-coordinated Au-atoms relative to the higher coordinated facet atoms, as shown by DFT calculations [282, 284, 292]. Generally, adsorbates form stronger bonds at low coordinated sites [271].

Based on the experimental results and by analogy to the observations from other catalytic systems discussed above, we conclude that in the HDO process on nickel catalysts, the low-coordinated step and corner site atoms interact more readily with the oxygen group of the oxy-compound to facilitate the deoxygenation. Thus, the C-O bond breaking reaction will more readily take place on this type of site.

TOF_{Hyd} decreased as a function of dispersion, but not linearly (cf. Figure 5.5). At higher dispersions the TOF_{Hyd} was below 0.05 s^{-1}, but below a dispersion of 0.1 it increased sharply by an order of magnitude. None of the surface site distributions follow a similar trend (cf. Figure 5.4), indicating that this reaction is probably not linked to a specific type of site. At most, some similarity to the behavior of the fraction of facet sites can be drawn as this decreases linearly with dispersion.

In Section 4.5.1, it was shown that hydrogenation of phenol over oxide supported Ni catalysts at temperatures below 300 °C probably occurs by an initial heterolytic dissociation of the phenol on an oxide support vacancy site followed by hydrogenation with hydrogen adsorbed on the nickel surface, as depicted in Figure 4.9. Thus, the hydrogenation reaction is influenced by the availability of vacancy/Lewis acid sites in the oxide and the hydrogen availability on the nickel particle. In the comparison

of Figure 5.4 and 5.5 a clear link to a specific type of site can therefore not be found.

In the work of Chary et al. [293] the hydrogenation of gas phase phenol over a Pd/C catalyst was investigated. Similar to the present observations, they found that TOF_{Hyd} had a sharp increase upon the transition from high to low dispersions. The observed change occurred around a dispersion of 0.25. Further decrease of the dispersion did not lead to a further increase of the TOF, which was linked to that the hydrogenation reaction required Pd crystals of a certain size (>5 nm) to take place. Additionally, Martin and Dalmon [294] observed that the rate of hydrogenation of benzene over Ni/SiO_2 had a maximum in hydrogenation rate at around 6 nm and concluded that the size was the limiting factor for the reaction, but that the reaction otherwise was unaffected by available fractions of specific surface sites. In the current work a somewhat higher limiting nickel particle size is found compared to the work of Chary et al. [293] and Martin and Dalmon [294]. This could be related to that the hydrogenation of phenol by Ni/SiO_2 does not take place by a direct adsorption on the nickel particle, but on a vacancy site in the oxide from where it interacts with the nickel particle.

Alternatively, in a series of catalytic reactions, low coordinated sites are readily blocked by one of the reactants or products due to a too strong adsorption on these sites. For example, Co and Ru catalysts for Fischer-Tropsch bind CO strongly on low coordinated sites, resulting in low activity of the smaller metal particles due to the concomitant blocking of the active sites [278–280]. Similar, CO oxidation over Pt catalysts is blocked by non-reactive oxygen adsorbed on the low coordinated sites [295]. Common for these cases is that small nano-particles generally display a low activity due to low availability of active sites and therefore the TOF increases as a function of particle size (or decreases with dispersion).

To evaluate whether a similar mechanism caused the development in the hydrogenation rate of phenol in the present work, a Langmuir-Hinshelwood kinetic model was set up. The approach recently described by Murzin [296–299] was applied for the incorporation of the effect of dispersion on the TOF. Additionally, the model was setup considering two types of sites: metal sites (*) for adsorption of hydrogen, water, cyclohexanol, etc. and oxide vacancy sites (#) for adsorption of phenol. Appendix E describes the derivation of the model in detail. The TOF for hydrogenation of phenol over Ni/SiO_2 can on the basis of this be described as:

$$TOF = k_3 \cdot K_{\mathrm{Ph}} \cdot \sqrt{K_{\mathrm{H_2}}} \cdot C^{\circ 3/2} \cdot \Theta_* \cdot \Theta_\# \cdot \frac{N_A}{D \cdot N_{S,s} + N_{S,0}} \tag{5.16}$$

$$\Theta_* = \frac{1}{1 + \sqrt{K_{\mathrm{H_2}} \cdot C^\circ} + K_{\mathrm{Ch}} \cdot e^{-\chi_{\mathrm{Ch}} \cdot D} \cdot C^\circ + \frac{K_{\mathrm{H_2O}} \cdot e^{-\chi_{\mathrm{H_2O}} \cdot D} \cdot C^\circ}{\sqrt{K_{\mathrm{H_2}} \cdot C^\circ}}}$$

$$\Theta_\# = \frac{1}{1 + K_{\mathrm{Ph}} \cdot C^\circ}$$

Here k_3 is the forward rate constant of the rate determining reaction, K_{Ph} is the equilibrium constant for the phenol coverage, $K_{\mathrm{H_2}}$ is the equilibrium constant for the hydrogen coverage, Θ_* the fraction of free * sites, $\Theta_\#$ the fraction of free # sites, $N_{S,s}$ and $N_{S,0}$ are scaling parameters of N_S with dispersion, K_{Ch} is the equilibrium constant for the cyclohexanol coverage, χ_{Ch} is the difference in free energy of adsorption of cyclohexanol at step sites relative to facet sites, $K_{\mathrm{H_2O}}$ is the equilibrium

constant for the H_2O coverage, and χ_{H_2O} is the difference in free energy of adsorption of water at step sites relative to facet sites. All concentrations are set to the standard concentration (C°) to normalize the TOF.

Figure 5.6 shows a fit between eq. 5.16 and the TOF_{Hyd} data found in this work, fitting k_3, the K_{Ch} and K_{H_2} ratio, and χ_{Ch} by minimizing the sum of squares (SSQ). In the fitting the influence of H_2O was neglected at this point, i.e. the water concentration was set to zero.

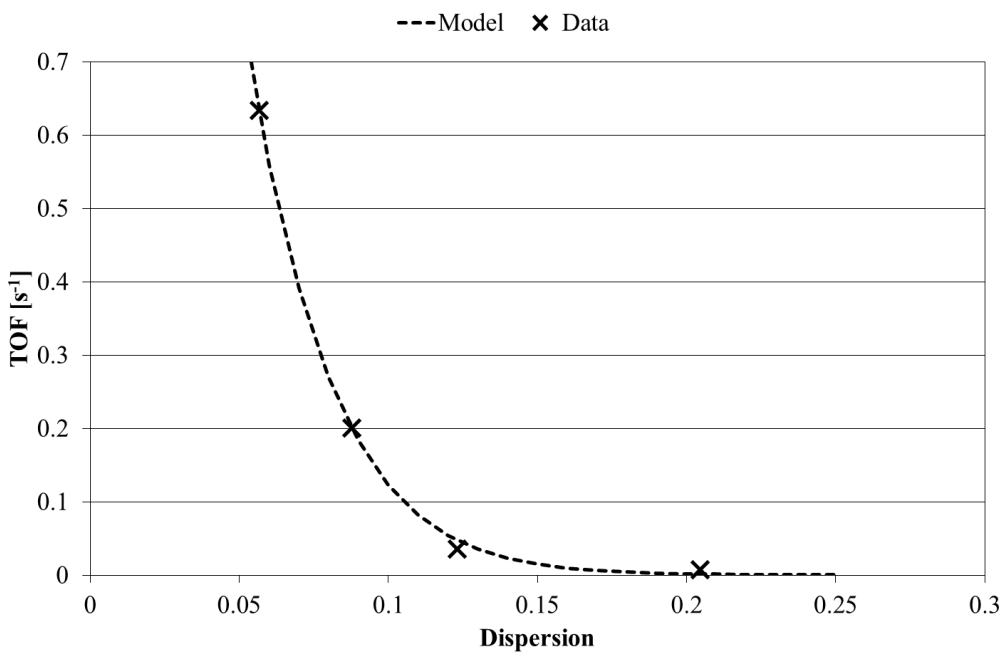

Figure 5.6: *TOF of hydrogenation in Eq. 5.16 fitted to the data of TOF_{Hyd}. SSQ =* $1.9 \cdot 10^{-4}$ s^{-2}.

Comparing the experimental data and the model in Figure 5.6 shows a good fit using a k_3 of 0.014, a K_{Ch}/K_{H_2} ratio of 0.21, and χ_{Ch} of 37.4, giving a relative low SSQ of $1.9 \cdot 10^{-4}$ s^{-2}. In the analysis the effect from adsorption of OH groups was neglected, but it is easily realized that the mathematical difference between fitting with K_{Ch} or K_{H_2O} is indifferent. The low SSQ gives credibility to the model and indicates that site blocking could be the reason for the observed development in the TOF_{Hyd} as a function of dispersion observed in Figure 5.5. Plotting the fractional coverage of cyclohexanol and hydrogen further clarifies this blocking effect (cf. Figure 5.7), showing that the coverage of cyclohexanol completely depletes the hydrogen availability when the dispersion increases. Figure 5.7 further shows that cyclohexanol adsorption is not limited to a specific type of site as a significant coverage is present already at low dispersions, but the cyclohexanol coverage dominates at high dispersions.

Analyzing the parameters found in the data fitting, a χ_{Ch} of 37.4 would correspond to a difference between $\Delta G^\circ_{ads,step}$ and $\Delta G^\circ_{ads,facet}$ of 93 kJ/mol. In other systems, this difference has been reported up to 116 kJ/mol [296], which makes the found value plausible.

Xiang et al. [300] found that the hydrogenation rate of phenol over Raney Ni in a batch reactor at 90 °C and 20 bar was severely suppressed when using methanol

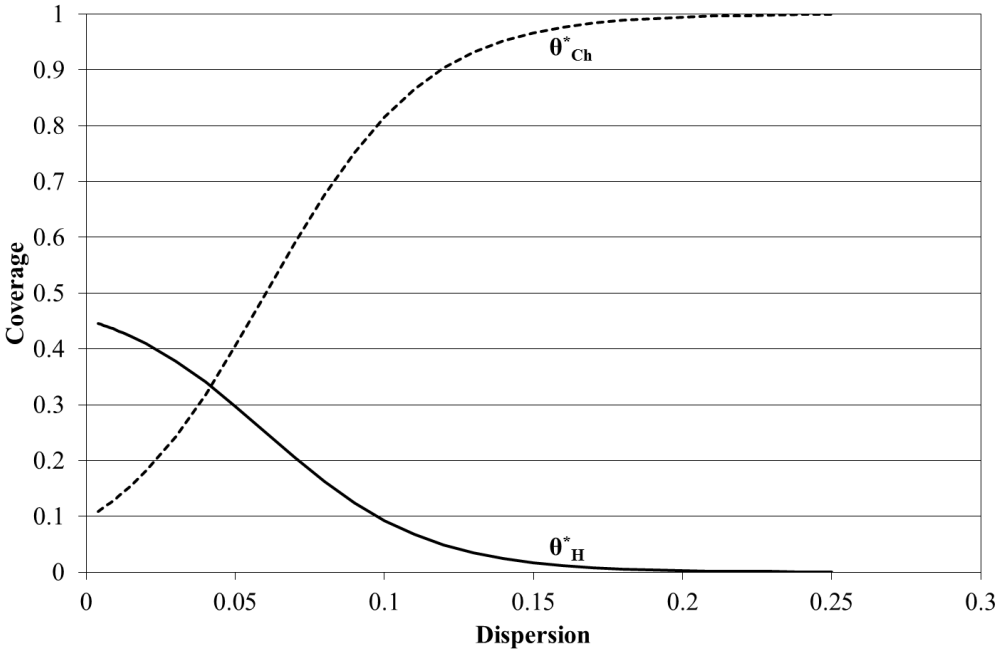

Figure 5.7: *Fractional coverage of Θ^*_{Ch} and Θ^*_H as a function of dispersion for the parameters used in the data fitting in Figure 5.6.*

as solvent compared to water; the conversion of phenol dropped from 95.8% (5 h reaction) in water to 6.8% (6 h reaction) in methanol. This was explained by competitive adsorption of the alcohol on the catalyst. It was found that the hydrogen and phenol uptake on the catalyst was 117 μmol/g and 283 μmol/g, respectively, when using water as solvent, but only 69 μmol/g and 117 μmol/g, respectively, when using methanol as solvent. Analogously, Velu et al. [266] observed that the conversion of phenol dropped from 93.7% in cyclohexane as solvent to 28% in ethanol as solvent for hydrogenation of phenol over a Pd/CeO_2 catalyst in continuous flow at 180 °C and atmospheric pressure, probably due to competitive adsorption of ethanol. In general, alcohols tend to block the active sites for hydrogenation of phenol. Thus, the formation of cyclohexanol from hydrogenation of phenol could also potentially lead to blocking of the nickel surface. Considering the size of cyclohexanol, it may further be expected that this molecule potentially could block several sites.

The work of Garcia-Dieguez and Iglesia [295] showed that inactive oxygen atoms adsorbed on low vacancy sites on Pt blocked the surface and hindered the oxidation of CO. Similarly, OH groups formed during HDO of phenol might block the nickel surface. Thus, these groups also appear as candidates for site blocking.

Overall, the good fit in Figure 5.6 indicates that a site blocking mechanism could explain why larger nickel particles are more favorable for the hydrogenation reaction. However, the analysis cannot deduce whether cyclohexanol, OH groups, both cyclohexanol and OH groups, or a third type of molecule is the source of the low hydrogenation activity of small nickel particles.

From the current discussion in literature, two feasible explanations for the observed particle size dependence in the hydrogenation rate can be given: a sufficient size may be required for the reaction to take place. In addition, smaller nickel particles could have a tendency to strongly adsorb alcohols (such as cyclohexanol) or OH groups on low coordinated sites, leading to competitive blocking of the active

sites. In both cases, higher hydrogenation rates will be favored on larger nickel particles. Maybe, the smallest particles would then have low hydrogenation rate due to a simple size effect of the nickel particles, but at larger nickel particles a blocking mechanism might explain the increasing hydrogenation rate with increasing particle size.

However, comparing the hydrogenation rate constants of nickel catalysts on different support in Table 4.6 to the the hydrogenation rate constants with of Ni/SiO_2 catalysts with different nickel particle sizes (cf. Table 5.1) reveal that the hydrogenation rate is significantly more influenced by the choice of support than the size of the nickel particle. Ultimately, it therefore appears that a good HDO nickel catalyst should have a small nickel particle size in combination with a good hydrogenation support, as ZrO_2 (cf. Table 4.6).

5.5 Conclusion

The influence of nickel particle size for a Ni/SiO_2 catalyst on the catalytic HDO of phenol has been investigated for particle sizes varying from 5 nm to 22 nm. A strong structure and particle-size sensitivity was observed. Hydrogenation of the aromatic ring to form cyclohexanol was required before deoxygenation could take place. Hydrogenation as first step is probably necessary because the O-C bond energy in phenol is higher than in cyclohexanol. The large particles were very active for hydrogenation of phenol, giving 100% conversion of phenol into primarily cyclohexanol in 5 h reaction time at 275 °C. By decreasing the particle size the conversion of phenol decreased and the yield of cyclohexane increased, reaching a maximum yield of 38% for a catalyst with a nickel particle size of 10 nm.

A simple kinetic model was set up to analyze the observations from the experiments quantitatively in terms of hydrogenation and deoxygenation rate constants. The model showed that the rate of hydrogenation increased with increasing particle size (decreasing dispersion) while the opposite trend was observed for the deoxygenation step. The rate determining step thus changed at about 9-10 nm, where hydrogenation was rate-limiting for particles below 9-10 nm while the deoxygenation step was rate-limiting above this size. Thus, to achieve a high yield of the deoxygenated product cyclohexane, good control of the particle size is needed and a size of 9-10 nm seems optimal.

Comparison of the TOF for the deoxygenation reaction with that calculated from surface site population theory for the nickel particles led to the conclusion that the rate of deoxygenation was linked to the fraction of available step sites on the nickel particles. This reaction therefore more readily took place on small nickel particles. Probably, both the adsorption of the oxy-compound and the C-O bond dissociation more readily take place on a low coordinated nickel atom.

The hydrogenation reaction over nickel based catalysts requires activation of the phenol by interaction with an oxidic support, but it is not clear which type of sites on the nickel is required for the reaction. The influence of particle size on the hydrogenation rate may be caused by size limitation on the nickel particles or a blocking of active sites by strong adsorption of cyclohexanol or OH groups on low coordinated sites. Both could favor large nickel particles for hydrogenation as observed experimentally.

Overall it is concluded that a compromise in nickel particle size is needed for phenol HDO over Ni/SiO_2. Relatively small particles are required to facilitate deoxygenation, but too small particles will have low activity for hydrogenation which will hinder the overall degree of deoxygenation.

Chapter 6

Stability and Resistance of Nickel Catalysts for Hydrodeoxygenation: Effects of Sulfur, Potassium, and Chlorine in the Feed

Abstract

The long term stability and resistance toward sulfur, chlorine, and potassium of Ni/ZrO_2 as catalyst for hydrodeoxygeantion (HDO) of guaiacol in 1-octanol (as model compound system for bio-oil) has been investigated at 250 °C and 100 bar in a trickle bed reactor setup. A small nickel particle size (9 nm) gave both better stability and higher catalytic activity, compared to a larger nickel particle size (18 nm), and without impurities in the feed good stability of the former catalyst could be achieved over more than 100 h of operation. Exposing the catalyst to 0.05 wt% sulfur in the feed resulted in a rapid deactivation of both hydrogenation and deoxygenation reactions, with complete loss of activity do to formation of nickel sulfide, as evidenced by XAS. Exposing the Ni/ZrO_2 to chlorine containing compounds (at a concentration of 0.05 wt% Cl) on-stream led to a steady decrease in activity over 40 h of exposure. Deoxygenation reactions were most severely deactivated, while the hydrogenation of guaiacol was less affected. Removal of the chlorine species from the feed led to regain of activity. Analysis of the spent catalyst by EDX revealed that the adsorption of chlorine on the catalyst was completely reversible, but XRD revealed that the chlorine had caused sintering of the nickel particles. In two experiments, potassium was impregnated on the catalyst prior to testing as either KCl and KNO_3. In both cases deactivation was persistent through more than 20 h of testing, and severely decreased the deoxygenation activity while the hydrogenation of guaiacol was unaffected. The results indicate that both chlorine and potassium species preferentially adsorb on and block low coordinated nickel metal sites, which are the active sites for deoxygenation. In the presence of sulfur, chlorine, or potassium containing species, the durability of Ni/ZrO_2 catalysts for HDO has been found to be poor, as all cause pronounced deactivation with sulfur being worst, followed by potassium and then chlorine. Thus, removal/limitation of these species from the bio-oil is a requirement to achieve long term operation with this catalyst.

6.1 Introduction

As shown in Chapter 4 and 5 and previous literature [116, 141, 244, 301], nickel based catalysts are very interesting due to their relatively low price combined with good activity. However, little work on these catalytic systems has been devoted to evaluating long term stability during HDO [139, 302]. Particularly, formation of carbon species on the catalysts or poisoning of impurities in the feed are potential challenges [139, 230, 302–304].

Carbon on the catalyst is formed because many of the oxy-compounds present in bio-oil can undergo polymerization and polycondensation reactions on the catalyst surface, forming polyaromatic species which can lead to blocking of both the pore structure and the active sites of the catalyst [142], as discussed more thoroughly in Section 2.4.3.

As the bio-oil is derived from biomass, it will contain traces of a range of inorganic compounds like alkali metals, transition metals, chlorine, sulfur, and phosphorus [29]. Especially potassium, chlorine, and sulfur can be found in relative high amounts in the bio-oil with concentrations up to 0.3 wt%, 0.6 wt%, and 0.8 wt%, respectively [305]. These are therefore of significant concern.

As Ni/ZrO_2 was found as an attractive catalyst in Chapter 6, this has been investigated in a continuous flow setup, using a bio-oil model compound system consisting of guaiacol in 1-octanol. Guaiacol was chosen as bio-oil model compound representing the phenolic fraction, as these are present in significant quantities in the bio-oil [231, 306], are among the most persistent molecules of the bio-oil [40, 302], and are partly responsible for carbon formation [302, 307]. 1-octanol was chosen as solvent for the guaiacol due to its ideal phase-characteristics under the given experimental conditions and furthermore to serve as a simple alcohol model compound.

6.2 Kinetic Model

For a more quantitative description of the catalyst activity a kinetic model was developed for the HDO of guaiacol and 1-octanol.

For guaiacol the sequential reaction scheme shown in Figure 6.1 was observed as the primary reaction. Guaiacol was initially hydrogenated to 2-methoxy-cyclohexanol, followed by hydrogenolysis of the ether bond to form cyclohexanol and methanol. Both alcohols can subsequently undergo hydrodeoxygenation to produce respectively cyclohexane and methane. The same reaction scheme has been observed for HDO of guaiacol over noble metal catalysts [131, 250, 308], indicating that this is a general reaction path over transition metal catalysts.

Heptane was the primary product from 1-octanol (as shown in Figure 6.1), and therefore a cracking type reaction was the primary path for this compound. Previous work on Pt catalysts with C_3 alcohols [309, 310] has shown that these undergo an initial dehydrogenation to form the aldehyde, which can then undergo decarbonylation producing ethane and CO. Probably, the same reaction pathway occurs for octanol over nickel catalysts. However, at the conditions used in our experiments, the CO produced will be readily hydrogenated into CH_4. Note that, the Gibbs free energy of the reaction: $CO + 3\,H_2 \rightleftharpoons H_2O + CH_4$ is -96.4 kJ/mol at 500 K (calculated with data from [71]), and the equilibrium is completely displaced toward CH_4 formation. Thus, in the experiments only CH_4 was detected in the gas phase.

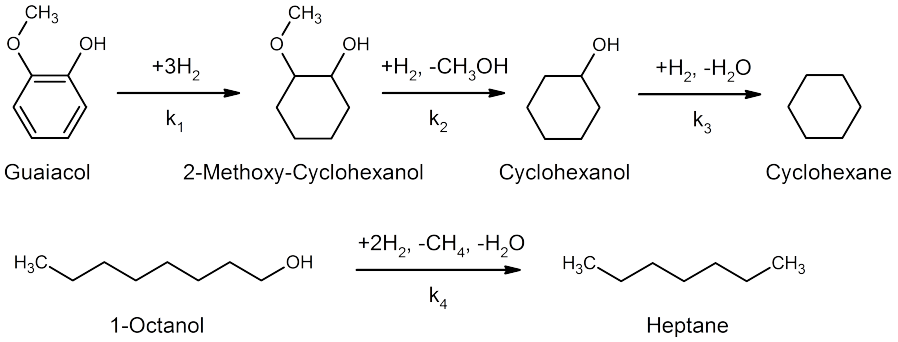

Figure 6.1: *Observed reaction path of guaiacol and 1-octanol.*

Based on the experimental observations summarized in Figure 6.1, the reaction rates of the four identified main reactions were assumed to be:

$$r_1 = k_1 \cdot C_{\text{Guaiacol}} \cdot P_{\text{H}_2}^n \tag{6.1}$$

$$r_2 = k_2 \cdot C_{\text{2-Methoxy-cyclohexanol}} \cdot P_{\text{H}_2}^m \tag{6.2}$$

$$r_3 = k_3 \cdot C_{\text{Cyclohexanol}} \cdot P_{\text{H}_2}^l \tag{6.3}$$

$$r_4 = k_4 \cdot C_{\text{1-Octanol}} \cdot P_{\text{H}_2}^k \tag{6.4}$$

Here r_i is the rate of reaction i, k_i is the rate constant for reaction i, C_i is the concentration of compound i in the liquid phase, P_{H_2} is the partial pressure of H_2, and n-k are the unknown reaction orders of hydrogen. All hydrocarbon reaction orders were assumed 1st order. Previous work has shown that 1st order reactions of guaiacol, anisole, and phenol HDO sufficiently describes these systems for simple interpretations [2, 243, 244, 311].

As a significant excess of hydrogen was used in all experiments the partial pressure of hydrogen was assumed constant and therefore the kinetic expressions reduces to:

$$r_1 = k_1' \cdot C_{\text{Guaiacol}} \tag{6.5}$$

$$r_2 = k_2' \cdot C_{\text{2-Methoxy-cyclohexanol}} \tag{6.6}$$

$$r_3 = k_3' \cdot C_{\text{Cyclohexanol}} \tag{6.7}$$

$$r_4 = k_4' \cdot C_{\text{1-Octanol}} \tag{6.8}$$

Based on these rate terms a kinetic model was derived for a plug flow reactor system. The derivation of this model can be found in Appendix F.

6.3 Reduction Temperature of Ni/ZrO_2

To evaluate the required reduction temperature, reduction of the calcined NiO/ZrO_2 was monitored by in-situ XAS. Figure 6.2(a) shows the evolution of the Ni-K near edge region as function of the temperature. The decrease in the absorption threshold intensity during the activation step show that Ni was being reduced. Furthermore, all spectra shown in Figure 6.2(a) are superposed at the same isosbestic points indicating that conversion of calcined Ni species to the reduced Ni phase took place in a single step. The fraction of oxidized and reduced phase was estimated by linear combination analysis and is presented in Figure 6.2(b). The reduction rate strongly

increased from 264 °C and was completed at 450 °C. Thus, in all experiments a reduction temperature of 500 °C was used to ensure complete reduction of the catalysts. Additional information on the EXAFS analysis of the calcined and reduced sample is found in Section 6.7.

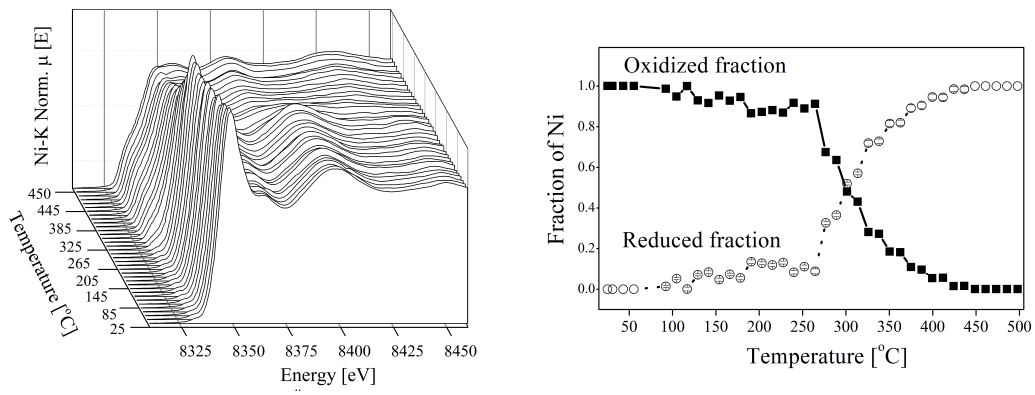

(a) Ni-K near edge spectra.

(b) Fraction of oxidized and reduced Ni.

Figure 6.2: *Ni-K near edge spectra recorded as function of the temperature during the reduction of the catalyst (a) and linear combination results estimating the fraction of oxidized and reduced Ni phases during the reduction of the catalyst (b).*

6.4 Long Term stability

Two batches of 5 wt% Ni/ZrO_2 were prepared: one where the batch was calcined at 400 °C for 4 h and one where the batch was not calcined. Both samples were reduced at 500 °C as found from the analysis in Section 6.3. In this way two different nickel particle sizes could be obtained, as described by Louis et al. [219]. In the following Ni/ZrO_2-CR will refer to the calcined and reduced sample and Ni/ZrO_2-DR will refer to the directly reduced sample.

Representative STEM-EDX elemental maps for both Ni/ZrO_2-CR and Ni/ZrO_2-DR are shown in Figure 6.3(a) and 6.3(b), respectively. From these and other acquired maps it was possible to estimate the Ni particle size being in average 9 nm for Ni/ZrO_2-DR and 18 nm for Ni/ZrO_2-CR, based on size measurements of more than 80 particles for each catalyst (size distributions are shown in Figure 6.4). Although the number of analyzed particles cannot be considered fully statistically representative, the size distribution for Ni/ZrO_2-DR was noticed to be more homogenous than Ni/ZrO_2-CR. For the calcined sample, a tail toward larger particle sizes and the presence of very big ones (>100 nm) were observed (cf. Figure 6.4(a)), indicating agglomeration of some nickel during the preparation procedure. It is worth mentioning that using the Ni signal to estimate the average particle size does not take into account any oxidation effect that could occur by exposure of the sample to air. However, XRD measurements did not reveal any evident oxidation of the Ni nanoparticles.

The two catalysts were tested at 250 °C and 100 bar with a feed of 0.2 ml/min 10 vol% guaiacol in 1-octanol corresponding to a WHSV of 4.0 h^{-1}. In Figure 6.5(a) and 6.5(b) the development in the conversion of guaiacol and 1-octanol and the degree

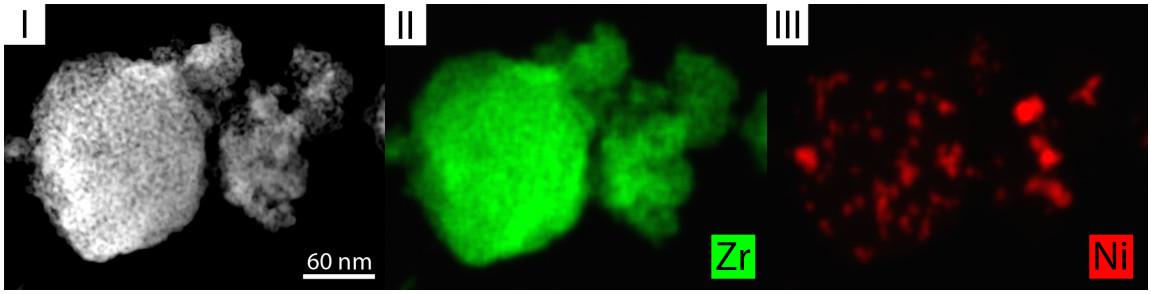

(a) STEM-HAADF micrograph of Ni/ZrO_2-CR

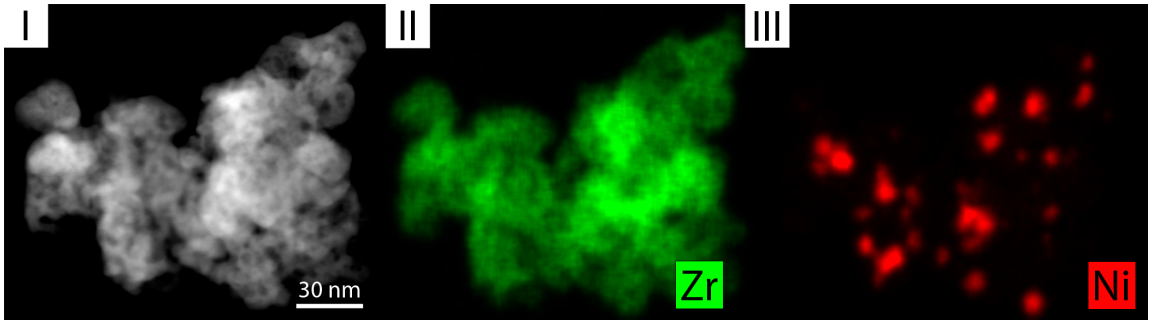

(b) STEM-HAADF micrograph of Ni/ZrO_2-DR

Figure 6.3: *STEM-HAADF micrograph of Ni/ZrO_2-CR (a) and Ni/ZrO_2-DR (b). Sub images I: STEM-HAADF micrograph. Sub-images II: Zirconium EDX elemental distributions. Sub-images III: Nickel EDX elemental distributions.*

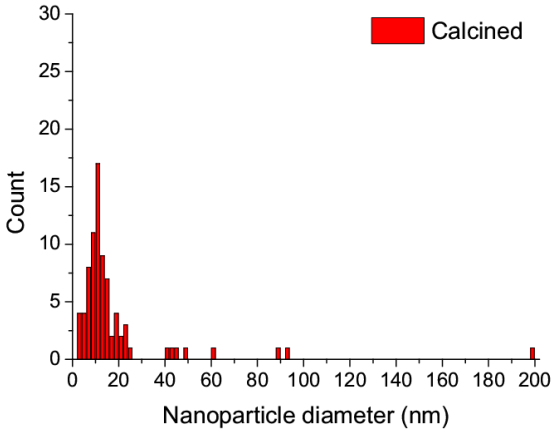

(a) Ni/ZrO_2-CR size distribution

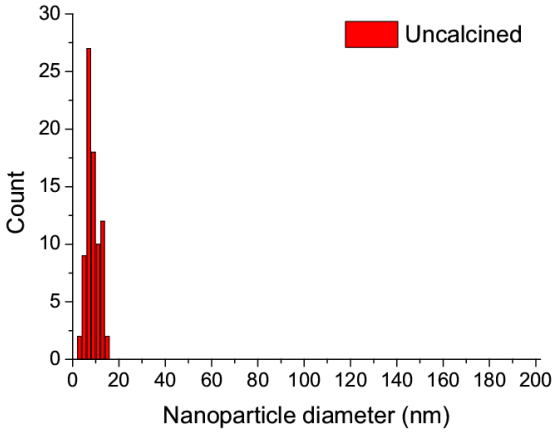

(b) Ni/ZrO_2-DR size distribution

Figure 6.4: *Size distribution of Ni/ZrO_2-CR (a) and Ni/ZrO_2-DR (b) based on the STEM-HAADF images.*

of deoxygenation (DOD) is shown as a function of time on stream (TOS) for both catalysts.

For the Ni/ZrO_2-CR (cf. Figure 6.5(a)) a maximum DOD of 40% was achieved after 3.5 h of TOS and hereafter the activity decreased throughout the 80 h of TOS, ending at 23% DOD. The relative decrease of the DOD^{GUA} was more pronounced, from a value 17% to only 4% after 80 h TOS. Thus, little deoxygenation of the guiaicol was found at the end of the experiment.

For Ni/ZrO_2-DR (cf. Figure 6.5(b)) the DOD was significantly higher; in the order of 90%. Also the stability of this catalyst was better, as the DOD^{GUA} only decreased from a value of 71% to 61% after 104 h TOS.

Both catalysts converted all guaiacol into 2-methoxy-cyclohexanol as a first step. However, the selectivities toward subsequently formed cyclohexanol and cyclohexane were only ca. 30% and ca. 1% on Ni/ZrO_2-CR, respectively, but ca. 50% and ca. 25% on Ni/ZrO_2-DR, respectively (detailed development in the yield of 2-methoxy-cyclohexanol, cyclohexanol, cyclohexane, and heptane can be found in Appendix G). Similarly, the conversion of the 1-octanol was around 30% on Ni/ZrO_2-CR, but 100% on Ni/ZrO_2-DR. In both cases >90% selectivity toward heptane was observed.

Using the simple kinetic model in Section 6.2, the catalytic activity of the catalysts was quantified, as summarized in Table 6.1. The rate of hydrogenation (k_1') could not be distinguished on the two catalysts, as both had 100% conversion. However, the rate of the three deoxygenation reactions (k_2', k_3', and k_4') were a factor of respectively 2.4, 6.9, and approximately 10 times higher for Ni/ZrO_2-DR compared to Ni/ZrO_2-CR.

Table 6.1: *Comparison between Ni/ZrO_2-CR and Ni/ZrO_2-DR, summarizing kinetic parameters, nickel particle size, and carbon buildup on the spent catalysts. Ni/ZrO_2-CR was calcined and then reduced and Ni/ZrO_2-DR was not calcined but reduced directly from the nickel nitrate. Kinetic parameters evaluated at TOS = 4.5 h for Ni/ZrO_2-CR and TOS = 10 h for Ni/ZrO_2-DR. Carbon content measured on the basis of temperature programmed oxidation (TPO).*

Catalyst	Ni/ZrO_2-CR	Ni/ZrO_2-DR
Total TOS [h]	79	106
Crystallite size [nm]	18	9
Carbon content [wt%]	3.7	1.5
Carbon content [mol C/mol Ni]	3.6	1.5
Carbon deposition rate [$\mu g_C/g_{cat}/h$]	463	144
k_1' [$ml/kg_{cat}/min$]	>500	>500
k_2' [$ml/kg_{cat}/min$]	51	126
k_3' [$ml/kg_{cat}/min$]	11	76
k_4' [$ml/kg_{cat}/min$]	52	>500

The large difference in activity can be linked to the difference in nickel particle size on the catalysts. As smaller nickel nano-particles has higher activity for deoxygenation, as discussed in Chapter 5. Thus, Ni/ZrO_2-DR would also be expected to have the highest activity. Comparing the individual rate constants, the decarbonylation reaction and the deoxygenation reaction were most dependent on the type of

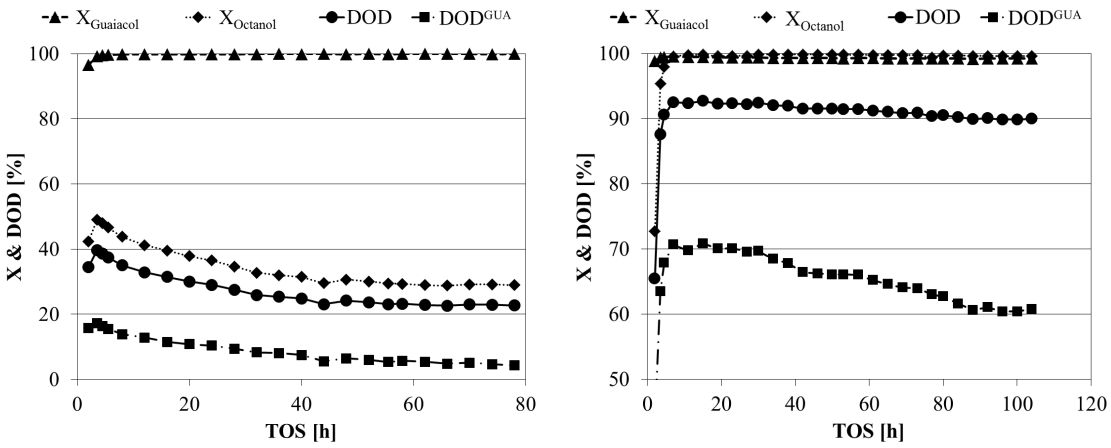

(a) Stability of Ni/ZrO_2-CR

(b) Stability of Ni/ZrO_2-DR

Figure 6.5: *Development of the conversions of guaiacol and 1-octanol and DOD for Ni/ZrO_2-CR (a) and Ni/ZrO_2-DR (b) as a function of TOS. DOD^{GUA} is the degree of deoxygenation of the guaiacol feed. Ni/ZrO_2-CR was calcined and then reduced and Ni/ZrO_2-DR was not calcined but reduced directly from the nickel nitrate. $T = 250\,°C$, $P = 100$ bar, $F_{oil} = 0.2$ ml/min, $WHSV = 4.0\ h^{-1}$.*

nickel sites available, as k_3' and k_4' had the largest relative increase. Contrary, the hydrogenolysis reaction (k_2') was less structure sensitive, which may be linked to a lower bond dissociation energy of the methoxy group (343 kJ/mol [242]) compared to the alcohol group (385 kJ/mol [242]).

Detailed analysis of the GC-MS/FID data revealed that the side products included methanol, cyclopentane, cyclopentanol, octane, methoxy-cyclohexane, cyclohexanone, dicyclohexyl ether, and dioctyl ether. A complete carbon analysis from the experiment with Ni/ZrO_2-DR (cf. Figure 6.5(b)) showed that 91% of the carbon fed to the reactor was recovered in the oil phase, 1% in the aqueous phase, and 6% in the gas phase, the remaining 2% was unaccounted for. The aqueous phase contained methanol, cyclohexanol, and 2-methoxy-cyclohexanol as primary carbon containing species. Loss of carbon to the gas phase was through formation of CH_4, which was linked to reduction of the methanol formed from guaiacol and hydrogenation of CO from 1-octanol (see discussion in Section 6.2).

In order to quantify the carbon on the spent catalyst, the used catalysts were subjected to TPO, (cf. results in Table 6.1). For both catalysts the deposited carbon was ozidized in the temperature range from 200-500 °C, with a peak in the CO/CO_2 evolution just below 400 °C. Comparing Ni/ZrO_2-DR to Ni/ZrO_2-CR, Ni/ZrO_2-CR had 3 times higher carbon deposition rate. This correlates with a more pronounced deactivation on Ni/ZrO_2-CR as a function of TOS (cf. Figure 6.5(a)).

Borowiecki [312] showed that the carbon deposition rate during steam reforming of butane at 500 °C was highly dependent on the nickel crystallite size; increasing by more than an order of magnitude when increasing the nickel crystallite size from 6.5 nm to 35.7 nm. Bengaard et al. [291] later described that carbon nucleation takes place on the step sites on the nickel crystals and builds carbon layers from here. These layers are however only thermodynamic stable when the carbon layer is larger

than ≈25 Å and therefore the associated nickel facet, on which the carbon layer is build, should be larger than this. Increasing the carbon layer size further decreases the total energy and therefore stabilizes the carbon formation further. Thus, large nickel particles are in other contexts also found more prone to carbon formation [291, 312, 313].

Another potential source of deactivation is loss of active metal by leaching. Therefore, the nickel content was investigated for Ni/ZrO_2-DR by ICP-OES. Prior to reduction, this catalyst had a nickel content of 4.5-4.9 wt%; the span is indicated because Ni/ZrO_2-DR contained some fraction of NO_3 which should be corrected for in the comparison. After 104 h of operation the nickel content was again measured, now being 4.7 wt%. Hence, the extent of nickel leaching from the catalyst is negligible.

In conclusion, carbon deposition appears to be the most probable cause for the observed loss of activity in Figure 6.5. This is supported by the observation that the rate of deactivation is faster on Ni/ZrO_2-CR compared to Ni/ZrO_2-DR, which correlates with the threefold higher carbon build-up rate on Ni/ZrO_2-CR compared to Ni/ZrO_2-DR.

6.5 Effect of Impurities in the Feed

To understand other potential deactivation mechanisms during HDO of bio-oil, exposure to sulfur, chlorine, and potassium was simulated, as described in the following. Ni/ZrO_2-DR was used for all of these measurements due to the higher activity of this sample.

6.5.1 Effect of Sulfur

In an experiment similar to those discussed in Section 6.4, 0.3 vol% 1-octanethiol (corresponding to 0.05 wt% S in the feed) was added to the feed of 10% guaiacol in 1-octanol after 8 h of TOS. This impurity of sulfur is representative of what can be present in bio-oil [305]. Figure 6.6(a) shows the development in the conversion of guaiacol and 1-octanol and the DOD as a function of TOS. Initially, when sulfur was not present, the conversion of both 1-octanol and guaiacol were 100% and the DOD in the order of 90-92%, similar to the experiment with no impurities present (cf. Figure 6.5(b)). After introduction of the sulfur, the activity rapidly decreased. After only 12 h exposure to sulfur the conversions of both guaiacol and 1-octanol were almost 0%. The conversion of both compounds and the DOD decreased in a similar way, indicating that the deactivation was taking place as a progressive front in the catalyst bed, inhibiting all types of reactions as the sulfur front progressed. The relative exposure to sulfur over the entire experiment was 1.1 mol S/mol Ni, showing an effective deactivation by sulfur.

1-octanethiol was effectively converted to heptane or octane and H_2S throughout the experiment. Only in the final two liquid samples, where the activity had severely decreased, traces of of 1-octanethiol could be found.

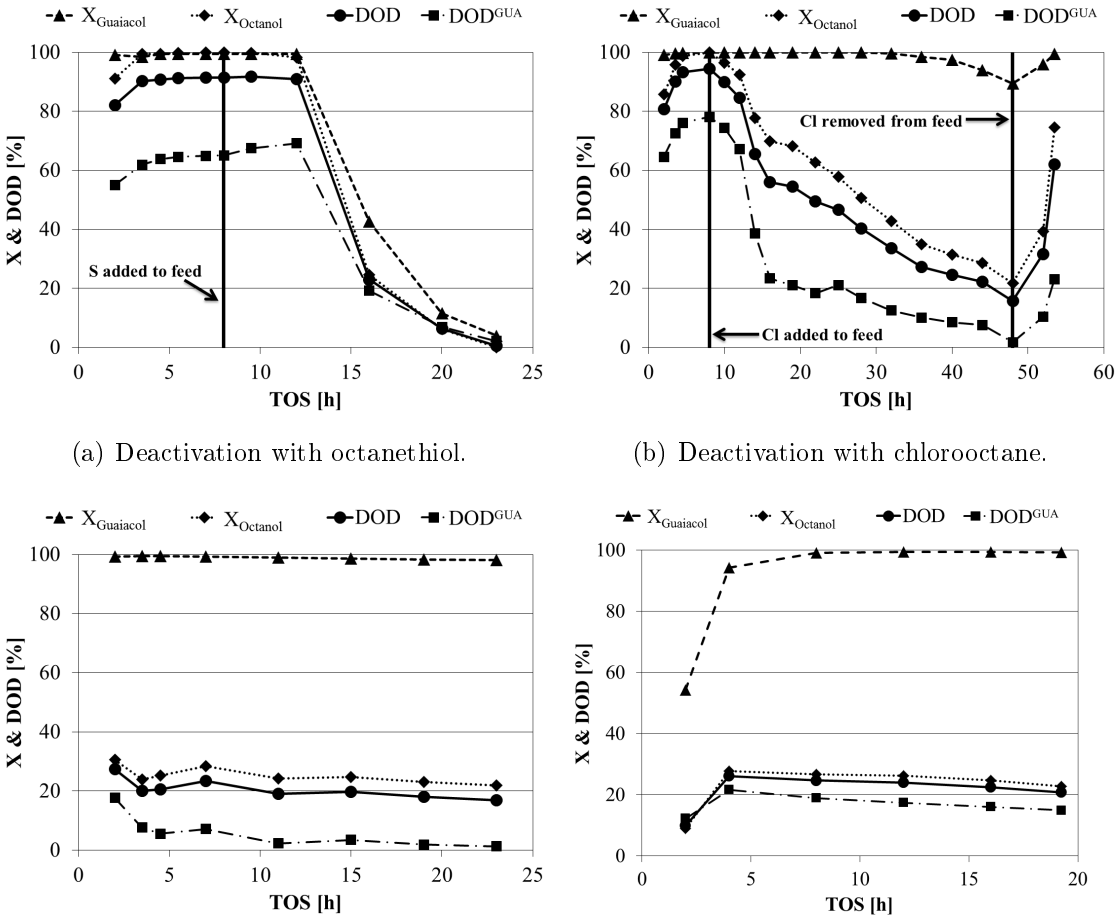

(a) Deactivation with octanethiol.

(b) Deactivation with chlorooctane.

(c) Deactivation by impregnation with KCl.

(d) Deactivation by impregnation with KNO_3.

Figure 6.6: *Development in the conversion of guaiacol and 1-octanol and the DOD over the Ni/ZrO_2-DR catalyst as a function of time when deactivated with 1-octanethiol (a), 1-chlorooctane (b), KCl (c), and KNO_3 (d). 1-octanethiol and 1-chlorooctane were added to the feed in concentrations of 0.05 wt% S and 0.05 wt% Cl, respectively, after 8 h of TOS as indicated in the respective figures. 1-chlorooctane was removed from the feed again after 48 h of TOS, as shown in Figure 6.6(b). KCl or KNO_3 were impregnated in stoichiometric amounts relative to nickel on a fresh batch of catalyst prior to testing. DOD^{GUA} is the degree of deoxygenation isolated for the guaiacol feed. $T = 250\ °C$, $P = 100$ bar, $F_{oil} = 0.2$ ml/min, $WHSV = 4.0\ h^{-1}$.*

6.5.2 Effect of Chlorine

In a similar experiment to the one described above, a new batch of catalyst was loaded and started up with the standard feed of 10 vol% guaiacol in 1-octanol. After 8 hours of operation the feed was changed to 10 vol% guaiacol and 0.3 vol% chlorooctane (corresponding to 0.05 wt% Cl in the feed) in 1-octanol. This corresponds to the quantity of organic bound chlorine, which can be found in bio-oil [305]. In Figure 6.6(b) the development in the conversion of guaiacol and 1-octanol and the DOD is seen as a function of TOS. Initially, the activity was similar to the reference case (cf. Figure 6.4) with no impurities in the feed, but after introduction of the chlorine to the feed the activity for deoxygenation steadily decreased; the DOD decreased from a level of 90-95% to 16% after 40 h exposure to the chlorine containing feed. However, the DOD^{GUA} decreased even faster and dropped to below 25% after only 8 h of exposure .

The conversion of the 1-octanol followed the development in the DOD. In contrast, the conversion of guaiacol was only slightly affected, dropping a few percent points only after 30 h of exposure. With respect to the product composition, the yield of cyclohexane decreased from 40% prior to deactivation to only a few percent after ca. 10 h exposure to the chlorine. The cyclohexanol yield was not affected to the same extent and only dropped from a yield of 32% to 17% after 40 h of exposure. 2-methoxy-cyclohexanol ended up being the primary product with a yield of more than 70% when highest (cf. Appendix G). Thus, chlorine deactivation is primarily associated with the deoxygenation activity of the catalyst.

Throughout the chlorine exposure period there was complete conversion of 1-chlorooctane to heptane and HCl. Nickel has also previously been reported as effective in the hydrodechlorination (HDCl) reaction [314–317]. The exposure to chlorine atoms has therefore been high throughout the exposure period.

After 48 h of TOS the feed was changed back to the chlorine free feed (10 vol% guaiacol in 1-octanol). At this point the activity increased (cf. Figure 6.6(b)) toward the initial activity level, before terminating the experiment. Thus, the deactivation by chlorine appears to be at least partly reversible indicating that the Cl species blocking the surface sites required for HDO can desorb. The desorbtion of chlorine from the catalyst was further proven by verification of Cl^- in the liquid product collected at TOS 51-52 h by precipitation with $AgNO_3$.

In the 40 h where chlorine was fed to the reactor the relative exposure was 3.2 mol Cl/mol Ni. All of this shows that the deactivation by chlorine was not as persistent as with sulfur, which is probably linked to reversible adsorption.

6.5.3 Effect of Potassium

In a third type of deactivation experiment, KCl was impregnated on a batch of Ni/ZrO_2-DR in stoichiometric amount relative to the nickel on the catalyst. Figure 6.6(c) shows the conversions of guaiacol and 1-octanol and the DOD as a function of TOS for this catalyst. In this experiment the DOD was in the order of 20%, the conversion of guaiacol was 100% throughout the 24 h of TOS, while the conversion of 1-octanol was in the order of 25%. The primary part of the deoxygenation was from the 1-octanol, as the DOD^{GUA} was only around 5%, with the 2-methoxy-cyclohexanol yield being 76% (cf. Appendix G). Thus, similar to the Cl deactivated catalyst, KCl deactivated mainly the deoxygenation reactions. However, in contrast to the Cl

deactivated case this catalyst was persistently deactivated as the DOD was constantly low throughout the 24 h experiment.

The isolated effect of potassium was tested by impregnation of a batch of Ni/ZrO_2-DR with stoichiometric amounts of KNO_3 relative to nickel. In Figure 6.6(d) the conversions of guaiacol and 1-octanol and the DOD are shown as a function of TOS in a 20 h experiment. Comparing to Figure 6.6(c), with KCl deactivation, similar trends are seen: the conversion of guaiacol was high (100%) throughout the test, 2-methoxy-cyclohexanol was the primary product (56% selectivity) from guaiacol, and the deactivation was persistent as the activity was stable throughout the 20 h of TOS. However, the DOD^{GUA} was around 10-15% for the KNO_3 deactivated sample compared to 5% in the KCl case, and therefore the interaction with the guaiacol molecule was more hampered in the latter case.

6.6 XRD and TEM Characterization of Poisoned Catalysts

6.6.1 Sulfur Poisoning

The presence of sulfur in the spent catalyst was confirmed by STEM-EDX elemental maps, showing a very similar spatial distribution of sulfur and nickel signals (cf. Figure 6.7). Thus, it appears that sulfur preferentially adsorbed on the nickel.

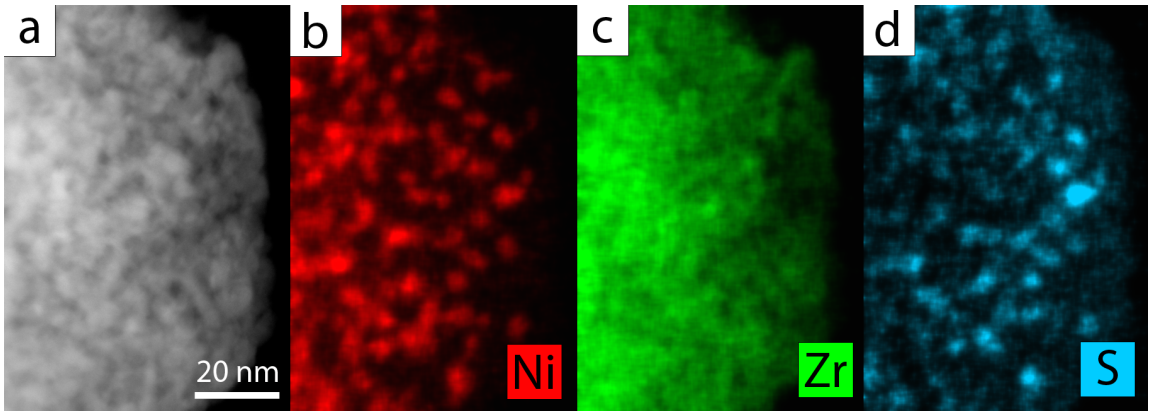

Figure 6.7: *(a) STEM-HAADF micrograph of the sulfur poisoned catalyst with (b) nickel, (c) zirconium and (d) sulfur EDX elemental distributions.*

XRD measurements (cf. Figure 6.8(a)) revealed the presence of zirconia and a reflection at $2\theta \approx 45.2°$ could be identified as NiS, confirming the permanent deactivation of the catalyst by formation of a non-active nickel sulfide phase. XRD analysis was carried out on the same specimen used for XAS measurements, thus the presence of cellulose can be ascribed to the XAS sample preparation procedure. Three reflections at $2\theta \approx 41°$, 37.9° and 36.8° belong to the sample stage. Cellulose peak labelling was carried out according to Park et al. [318].

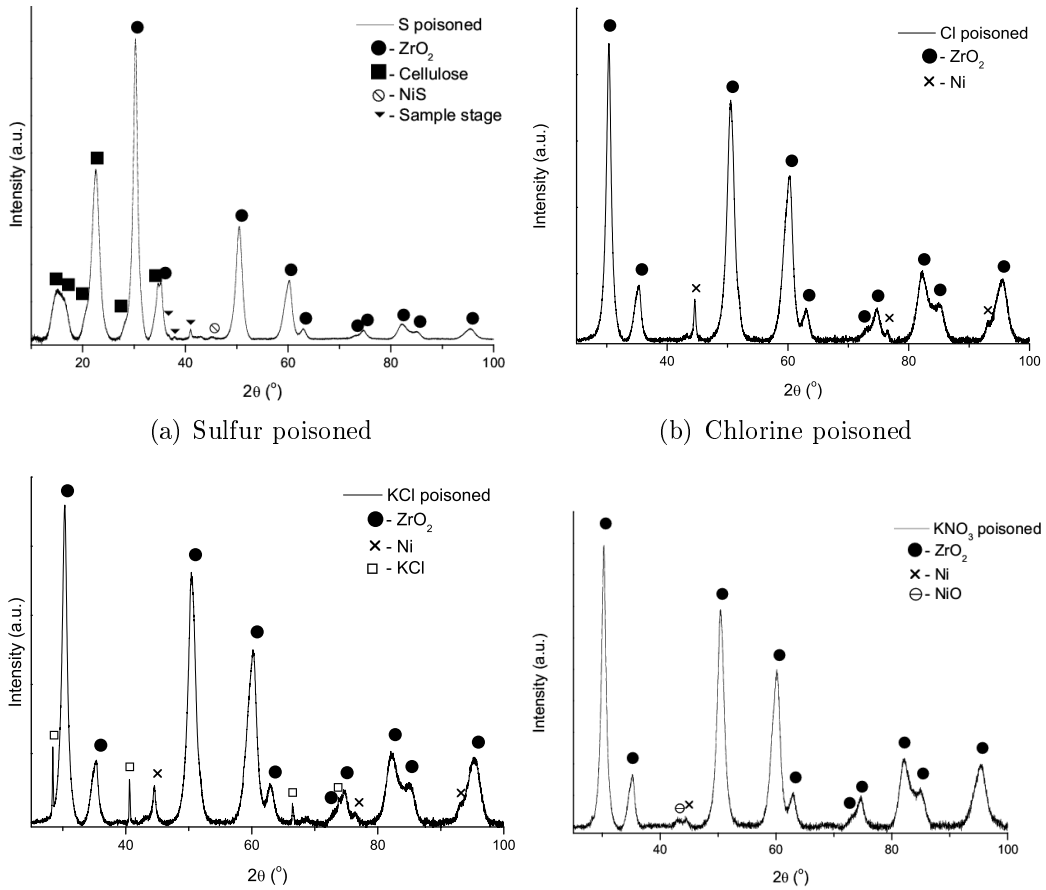

(a) Sulfur poisoned (b) Chlorine poisoned

(c) KCl poisoned (d) KNO_3 poisoned

Figure 6.8: *X-ray diffraction patterns of the poisoned catalysts.*

6.6.2 Chlorine Poisoning

XRD analysis of the chlorine poisoned catalyst after reaction showed reflections belonging exclusively to zirconia and nickel (cf. Figure 6.8(b)). The absence of chlorine species was further confirmed by EDX measurements carried out in the SEM (cf. Figure 6.9(a)). This supports the non-persistent nature of chlorine indicated in the catalytic experiment described in Section 6.5.2.

The nickel crystallite size was estimated from XRD patterns by applying the Scherrer equation on the $2\theta \approx 44.5°$ reflection. The nickel particle was estimated to be approximately 39 nm for the chlorine exposed sample, indicating a growth of the nickel particles during exposure to chlorine. The growth of nickel nanoparticles could be explained by the formation of mobile Ni-Cl species upon reaction of HCl with surface oxides [319].

In order to investigate in more detail the extent of chlorine poisoning, the deactivation experiment was repeated with a new batch of catalyst and without restoring the chlorine-free feed. XRD and SEM-EDX analysis of the sample after 48 h of TOS did not reveal the presence of chlorine species either. Thus, it appears that chlorine species readily will leave nickel when exposed to air and/or hydrogen (during cool down of the experiment).

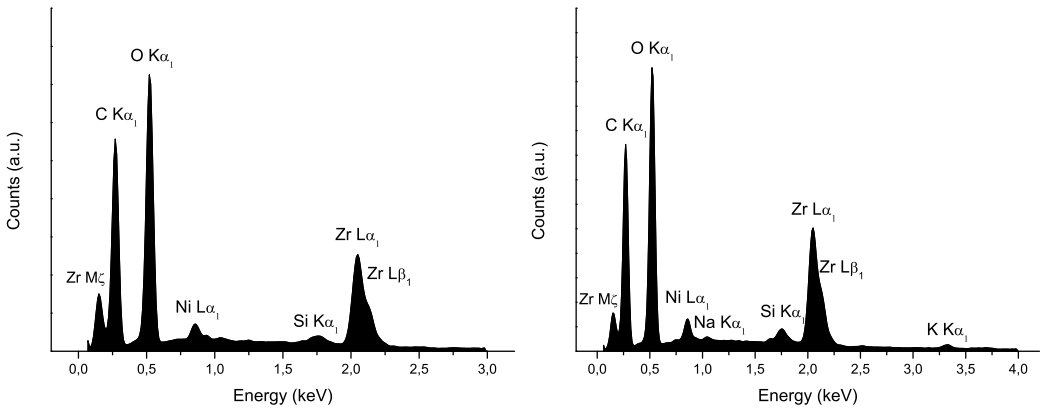

(a) Chlorine poisoned (b) KNO_3 poisoned

Figure 6.9: *SEM-EDX spectra of the poisoned catalysts.*

6.6.3 Potassium Poisoning

Impregnation of KCl on the catalyst resulted in deposition of KCl crystals on the catalyst surface, as visualized by both STEM-EDX (Figure 6.10) and XRD (Figure 6.8(c)) measurements on the spent sample. The XRD measurements indicate an average crystallite size >100 nm, approximately the size limit after which the reflection peak width is dominated by the instrumental broadening. KCl particle sizes up to 600 nm were reported as shown by STEM-EDX maps in Figure 6.10.

The nickel crystallite size was estimated to be approximately 24 nm for the KCl impregnated catalyst after 25 h TOS, indicating growth of the nickel particle size. This was however less pronounced, when compared to the chlorine poisoned samples, but could be explained once more by the presence of HCl during reaction.

Analyzing the spent KNO_3 impregnated catalyst by SEM-EDX confirmed the presence of potassium, as shown in Figure 6.9(b). However, XRD analysis did not reveal any potassium-containing crystalline phase (cf. Figure 6.8(d)). This indicates a more homogeneous deposition of the potassium compared to the KCl impregnated catalyst.

In an attempt to visualize the potassium deposition, STEM-EDX mapping of this catalyst resulted in the redistribution of potassium all over the scanned area. This is due to the high mobility of potassium ions under the effect of the electron beam [320, 321].

6.7 XAS Analysis of Poisoned Catalysts

To further understand the deactivation mechanism of the Ni/ZrO_2 catalyst caused by the impurities in the feed, the local structures of the poisoned samples were analyzed by XAS. Table 6.2 presents the respective refined structural parameters of the investigated samples. Additional information can be found in Appendix H.

Initially, the local structure of the fresh calcined Ni/ZrO_2 and the in-situ reduction of this catalyst (as discussed in Section 6.3) was studied by refining the extended X-ray absorption fine structure (EXAFS) spectra. Figure 6.11 presents the experimental and refined Fourier Transformed k_3 and k_2 weighted, respectively, EXAFS spectra of the calcined (Figure 6.11(a)) and reduced (Figure 6.11(b)) catalysts. Table

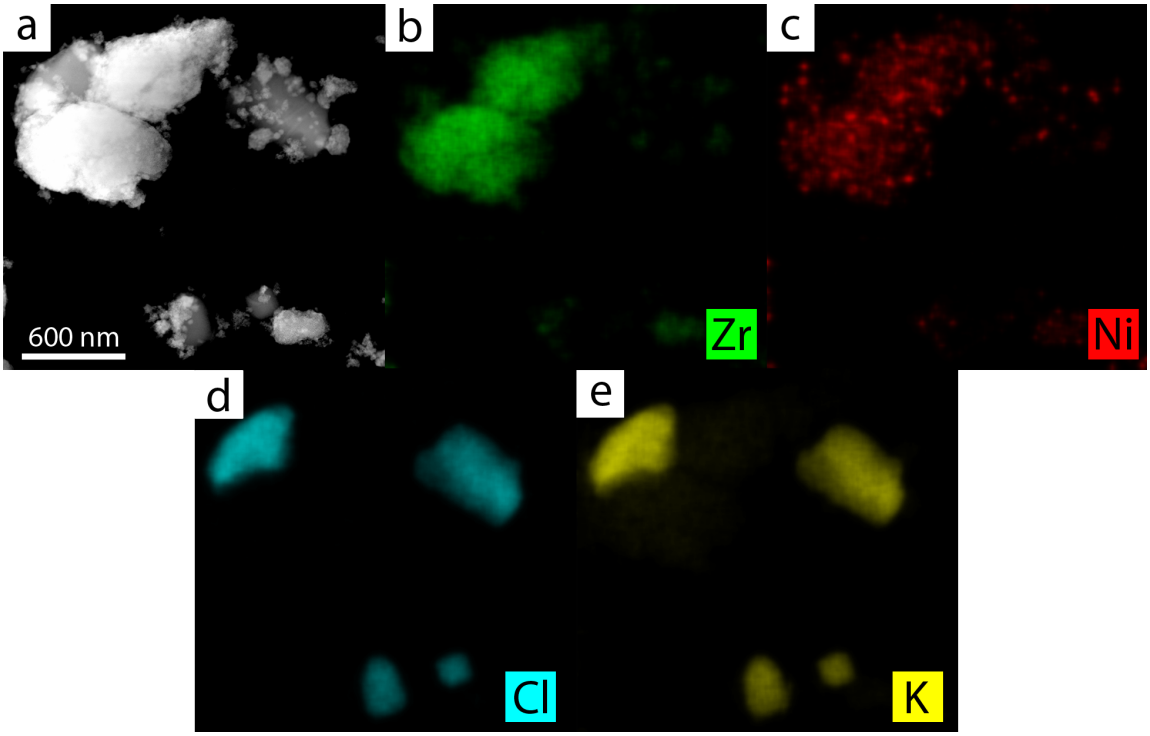

Figure 6.10: *(a) STEM-HAADF micrograph of the potassium chloride poisoned catalyst with (b) zirconium, (c) nickel, (d) chlorine and (e) potassium EDX elemental distributions.*

6.2 presents the respective refined structural parameters. The Fourier Transformed spectra, besides being a filter, give an intuitive and immediate idea of the radial atomic distribution around the absorber atom, in this case nickel.

For the calcined catalyst, nickel was coordinated by 6 oxygen atoms at 2.06 Å, and the second coordination shell was constituted of 8.6 ± 0.9 nickel atoms at 2.96 Å. This local order was similar to NiO as expected, however the number of nickel atom at the second coordination shell was lower than the one found for NiO (12 nickel atoms [322]), which indicates a small particle size of the NiO like structure after calcination.

The local chemical environment of the reduced catalyst was similar to a metallic nickel phase, nevertheless the refined 9.2 ± 1.0 coordination number of the first shell showed that the reduced phase of the catalyst was structured as small particles.

Analyzing the poisoned catalyst samples, the local nickel surrounding in the KNO_3, KCl, chlorine, and carbon (catalyst exposed to feed for 106 h TOS) poisoned catalysts remained similar to the reduced catalyst as seen from the refined structural parameters in Table 6.2, with the exception of a slight oxidation after reaction. This was evidenced by a peak shoulder around 2 Å at the Fourier Transformed EXAFS spectra (additional information is available in Appendix H). These oxygen atoms were most likely at the surface of the nickel metallic particle since the refined bond distances, varying between 1.96-2.00 Å, were shorter than the expected Ni-O distance in the NiO reference (2.08 Å) [322]. The oxidation was probably a consequence of exposure to air in between the experiment and XAS measurements, as confirmed in the XRD pattern of potassium and chlorine poisoned catalysts (cf.

Table 6.2: *Structural parameters around the Ni absorber atom refined from the EXAFS spectra of the Ni/ZrO$_2$ catalysts, comparing calcined, freshly reduced, and poisoned samples. Calcined is the fresh catalyst prior to reduction and reduced is the same catalyst after in-situ reduction, as discussed in Section 6.3. N is the number of neighboring atoms, r the distance, σ^2 the mean-square disorder in the atomic distances, and ρ the misfitting between the experimental data and the theory. $S_0^2 = 0.78$, calcined: $\Delta E_0 = -3.5 \pm 0.5$, reduced: $\Delta E_0 = 6.5 \pm 0.6$, carbon: $\Delta E_0 = 5.8 \pm 0.9$, chlorine: $\Delta E_0 = 6.6 \pm 1.4$, KCl: $\Delta E_0 = 7.1 \pm 0.7$, KNO$_3$: $\Delta E_0 = 6.6 \pm 1.0$ and $C_3 = 4.9 \cdot 10^{-4}$ Å^3, sulfur: $\Delta E_0 = -8.4 \pm 0.5$.*

Sample	Shell	Atom	N	r [Å]	$\sigma^2 \cdot 10^{-3}$ [Å^2]	ρ [%]
Calcined	1st	O	6.0^c	2.06$^{f\ a}$	6.2±0.5^f	0.7
	2nd	Ni	8.6±0.9^f	2.96$^{f\ a}$	9.6±1.0^f	
Reduced	1st	Ni	9.2±1.0^f	2.48±0.01^f	5.5±0.8^f	3.2
	2nd	Ni	6.9±3.4^f	3.46±0.02^f	14.0±0.5^f	
	3rd	Ni	21.6±7.8^f	4.33±0.01^f	10.2±3.3^f	
Carbon	1st	O	0.8±0.3^f	1.98±0.05^f	7.1±0.1$^{f\ d}$	0.5
poisoned^b	2nd	Ni	8.7±0.9^f	2.48±0.01^f	6.3±1.0^f	
Chlorine	1st	O	0.8±0.2^f	2.00±0.04^f	7.2±0.1$^{f\ a}$	0.9
poisoned	2nd	Ni	8.5±0.6^f	2.48$^{f\ a}$		
KCl	1st	O	0.6±0.1^f	2.00±0.04^f	7.2±0.1$^{f\ a}$	0.9
poisoned	2nd	Ni	9.9±0.4^f	2.48$^{f\ a}$	6.8±0.5^f	
KNO$_3$	1st	O	1.1±0.3^f	1.96±0.01^f	7.9±4.5$^{f\ a}$	1.3
poisoned	2nd	Ni	8.3±0.9^f	2.48±0.01^f	9.2±1.0^f	
Sulfur	1st	S	5.0^c	2.22±0.01^f	7.6±0.4^f	2.5
poisoned						

^{a}Fitted uncertainty less than 1%
^{b}Ni/ZrO$_2$-DR used in the long term testing in Section 6.4 analyzed after 106 h TOS.
^{c}Constrained
^{d}Ni-O σ^2 was constrained and fitted together with NiCO$_3$ reference
^{f}Fitted

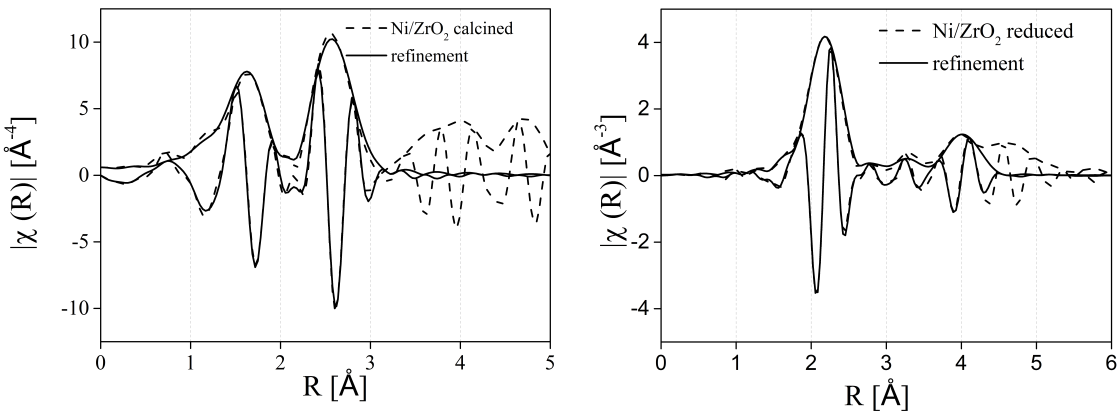

(a) EXAFS of calcined Ni/ZrO$_2$ (b) EXAFS of reduced Ni/ZrO$_2$

Figure 6.11: *Experimental (full line) and refinements (dotted line) Fourier Transformed EXAFS spectra of Ni/ZrO$_2$ catalysts (a) calcined and (b) reduced.*

Figure 6.8) by the presence of a weak peak at $2\theta \approx 43$ °, corresponding to a NiO phase.

The Fourier transformed EXAFS spectra of the carbon and KCl poisoned catalysts presented a significant amplitude reduction (Figure 6.12(b)). The structural refinements showed that this amplitude reduction was mainly caused by the increase of the structural disorder, expressed by the mean-square disorder in the atomic distances.

The KNO_3 poisoned catalyst showed the strongest amplitude reduction as a result of the high structural disorder. The refinement of its EXAFS spectrum required an additional structural parameter (the third cumulant of disorder, C_3), which measures the asymmetry of the atomic vibrations. A reduction in the magnitude of the Ni signal was also observed in the XRD pattern of this catalyst (cf. Figure 6.8). Note that both in the Fourier transformed EXAFS spectra (Figure 6.12(b)) and the EXAFS-fit (cf. Table 6.2) there was a stronger contribution for backscattering at low R-values. This evidences a stronger oxidation.

Overall, these XAS measurements support the observations in Section 6.6, that chlorine and alkali metals did not induce a phase change of the nickel crystals. Thus, the deactivation caused by these species was probably related to deposition on the nickel surface.

The Ni-K-edge XANES of the sulfur poisoned catalyst sample showed the presence of a completely different Ni-species, as shown in Figure 6.12. The refinements suggested the conversion of the metallic Ni phase to a NiS-like phase, which explains the total loss of the catalytic activity in this case. This is supported by the STEM-EDX map in Figure 6.7, also showing sulfur to be distributed similar to Ni, confirming the tight interaction and the reflection of NiS in the XRD pattern (cf. Figure 6.8(a)).

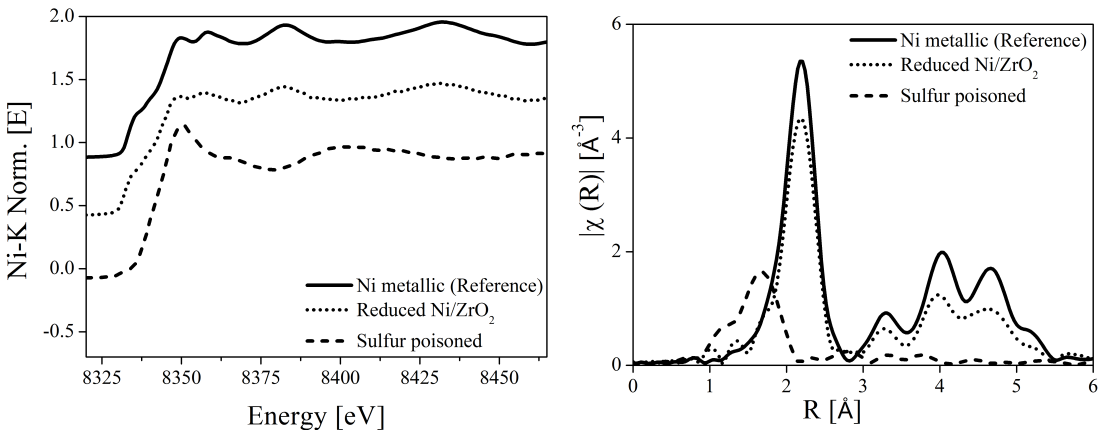

(a) X-ray absorption spectra (b) Fourier transformed EXAFS spectra

Figure 6.12: *Ni-K X-ray absorption spectra of the poisoned catalyst (a) and respective k^2-weighted Fourier transformed EXAFS spectra (b).*

6.8 Comparison of Deactivation Mechanisms

For a quantitative comparison of the different deactivation phenomena, the kinetic constants for the four reactions were calculated, as summarized in Table 6.3. Sulfur was the worst poison as this catalyst was completely inactive both with respect to hydrogenation and deoxygenation after a relatively short exposure time.

Table 6.3: *Rate constants for HDO of guaiacol and 1-octanol deactivated with different poisons relative to the case shown in Figure 6.5(b) with Ni/ZrO$_2$-DR and no poison. TOS refers to when the kinetic parameters are evaluated in comparison to Figure 6.5 and 6.6. T = 250 °C, P = 100 bar, F$_{oil}$ = 0.2 ml/min, WHSV = 4.0 h^{-1}.*

Poison	TOS [h]	Exposure [mol$_{poison}$/mol$_{Ni}$]	k_1'	k_2'	k_3'	k_4'
			[ml/kg$_{cat}$/min]			
None[a]	-	-	607	124	80	602
Carbon[b]	104	$3{\cdot}10^4$	> 500	108	52	>500
Sulfur	23	1.1	0	0	0	0
Chlorine	48	3.2	181	25	6.1	20
KCl	11	1	> 500	26	0.6	22
KNO$_3$	12	1	> 500	53	0	24

[a]Determined from an intrinsic activity measurement with 1.5 g of 5 wt% Ni/ZrO$_2$ in sieve fraction 125-180 μm, but otherwise similar experimental conditions. In this experiment the conversions of guaiacol and 1-octanol were respectively 99.0% and 98.9%.

[b]Ni/ZrO$_2$-DR used in the long term testing in Section 6.4.

The XRD, STEM-EDX, and EXAFS analysis revealed that the sulfur deactivated catalyst was a bulk deactivation (cf. Figure 6.12), which explains the distinct deactivation profile (cf. Figure 6.6(a)). It has previously been shown that sulfur forms a saturated surface layer on nickel at p_{H_2S}/p_{H_2} ratios above $5 \cdot 10^{-6}$ [323]. The p_{H_2S}/p_{H_2} threshold for formation of bulk sulfides is decreasing with decreasing temperatures and is in the order of 10^{-4} at 400 °C [324], but even lower at 250 °C. In the current experiment the p_{H_2S}/p_{H_2} ratio was $2 \cdot 10^{-4}$, assuming all 1-octanethiol decomposed to H_2S, which is in the range where bulk nickel sulfides can be expected to form.

Sulfur deactivation of nickel catalysts has previously been established to be severely persistent and hardly reversible in hydrogen alone [325, 326]. Removal of the sulfur can be achieved to some extent by steaming of the catalyst, but this requires temperatures above 600-650 °C [327, 328]. Thus, the catalyst appears to have little chance to avoid deactivation or to regain activity in the presence of sulfur species during HDO.

Exposure to either Cl, KCl, or KNO$_3$ caused deactivation in the same order of magnitude. Hydrogenation was only slightly deactivated by the chlorine, and unaffected by the KCl or KNO$_3$. The hydrogenolysis (k_2') was most severely deactivated in the case with Cl and KCl, where the second and the deep deoxygenation step of the alcohol group (k_3') was most deactivated in the case with the potassium salts. The deoxygenation of 1-octanol was affected in the same order of magnitude for both chlorine and KCl/KNO$_3$.

In steam reforming, where nickel catalysts have been extensively used, alkali metals are known to readily deactivate the catalyst [208, 209, 313, 329]. Bengaard et al. [291] showed that deactivation of nickel catalysts for steam reforming by alkali metals was due to adsorption at the step sites on the nickel crystallites.

In this study, doping with potassium hindered the deoxygenation reactions (k_2', k_3', and k_4' in Table 6.3), while the hydrogenation reaction was less affected. This correlates with the Ni/ZrO_2 catalyst has two different types of active sites: vacancy sites in the oxide support where the phenolic compounds can adsorb prior to hydrogenation and exposed low coordinated metal sites facilitating the deoxygenation reactions (cf. Section 4.5.1 and Figure 4.9). Thus, it appears that potassium (and maybe also chlorine) preferentially interacts with low coordinated nickel sites, as primarily the deoxygenation reactions were affected.

The most striking difference in the deactivation by chlorine and potassium was the reversibility of the chlorine poisoning. This reversibility of chlorine adsorption has also been observed previously [330–333]. During methane steam reforming over Ni/Al_2O_3, Ortego et al. [332] observed that the reforming activity decreased when co-feeding CH_3Cl. However, the activity was regained when removing the chlorine source from the feed. Richardson et al. [331] also found that the presence of chlorocarbons in the feed led to a decrease in the methane steam reforming activity of a Ni/Al_2O_3 catalyst. They concluded that chlorine formed an equilibrium surface layer on the nickel, which at high coverage could deplete the availability of hydrogen. Similarly, Kiskinova and Goodman [330] found that the poisoning effect on CO and H_2 adsorption on a Ni (100) surface increased in the order: $P < S < Cl$. However, despite Cl was the worst poison, it easily reacted with H_2 to form HCl. Thus, if the chlorine surface layer was not maintained, chlorine was found to not effect the catalytic activity for methanation.

In summary, the current and previous work show that chlorine primarily affects the catalytic activity when fed to the reactor as the coverage appears to be determined by a fast adapting equilibrium with hydrogen and HCl. This is supported by the identification of Cl^- in the liquid product after ending the exposure to chlorooctane. However, investigation of the particle size by XRD did indicate that chlorine also causes sintering of the nickel particles on the catalyst.

Comparing the effect of impregnation with KCl and KNO_3 shows many of the same trends. Deactivation by KCl, however, was slightly worse, especially considering the hydrogenolysis reaction (k_2'). This may be linked to the sintering induced by the presence of chlorine.

6.9 Conclusion

In this work, the stability and resistance of Ni/ZrO_2 has been investigated during long term operation in a continuous flow setup for HDO of a mixture of 10% guaiacol in 1-octanol as a model system for bio-oil.

The stability and activity of the catalyst was dependent on the nickel particle size. Small nickel particles (9 nm) gave higher activity for HDO and produced less coke on the catalyst, compared to larger particles (18 nm). Over a period of more than 100 h of operation a carbon build-up of only 1.5 wt% relative to the catalyst mass occurred

for the 9 nm Ni/ZrO_2 catalyst and therefore the activity only decreased slightly; from a DOD of 92% of the fresh catalyst to a DOD of 90% after 104 h TOS.The higher activity of the small crystallites was linked to their higher fraction of low coordinated sites which are efficient in the deoxygenation reaction. The smaller particle size was also responsible for the lower carbon deposition since it is more difficult for carbon to form on these.

The catalyst stability was very sensitive to sulfur, chlorine, and potassium exposure. Addition of sulfur to the feed resulted in a fast deactivation of the catalyst, leading to complete loss of activity over a period of only 12 h, which was roughly the time required to feed the stoichiometric amount of sulfur relative to the available nickel. In line with this, STEM-EDX, XRD, and XAS measurements unraveled the formation of a NiS like phase, which was the reason for the complete loss of activity for this catalyst.

Chlorine did not deactivate the catalyst to the same extent as sulfur, as primarily the deoxygenation activity was decreased after exposure to chlorine over a period 40 h, corresponding to addition of 3.2 mol Cl/mol Ni. Furthermore, the deactivation by chlorine was reversible as the activity could be partly regained when removing the chlorine from the feed. Neither XRD, XAS, nor EDX could identify chlorine on the spent catalyst, supporting the reversibility of the deactivation mechanism. It is suggested that chlorine binds to the nickel surface sites (preferentially low coordinated sites) and forms an equilibrium surface layer, but when not co-feeding Cl this layer is easily removed. However, chlorine also appeared to cause sintering of the nickel particles on the catalyst, providing a more persistent deactivation/activity loss.

KCl and KNO_3 were impregnated on two different batches of catalyst to test the effect of potassium. The hydrogenation activity was not affected in any significant degree in the two cases, but the deoxygenation activity was markedly decreased and was persistent over more than 20 h of operation. Probably, potassium blocked low coordinated sites leading to loss of deoxygenation activity, as these are considered crucial for this reaction.

Comparing the different poisons, sulfur was the most severe, while potassium and chlorine were in the same order of magnitude when looking at the activity. However, as potassium is a persistent poisoning this must be considered more severe than chlorine.

Overall, it is concluded that it is difficult to obtain long term stability for nickel based catalysts for bio-oil HDO as any of the three types of poisons tested will lead to deactivation. From an application point of view it would be crucial to remove specifically sulfur from the feed beforehand and to minimize the potassium and chlorine impurities. The present work shows the importance of studying the stability of catalysts for HDO of bio-oil.

Chapter 7

Activity and Stability of Mo_2C as Catalyst for Hydrodeoxygenation of Bio-oil

Abstract

In the search for a stable and active hydrodeoxygenation (HDO) catalyst, Mo_2C was investigated in a high pressure continuous flow gas and liquid reactor system with a bio-oil model system of phenol in 1-octanol. The catalyst was very selective for direct deoxygenation of the phenol to benzene at temperatures higher than 320 °C and 100 bar, below this temperature only the 1-octanol was deoxygenated. During long term stability testing of the catalyst at 300 °C, poor stability was found, with the conversion of 1-octanol decreasing from 70% to 34% over 74 h of operation. An additional experiment co-feeding water verified that the loss of activity was due to oxidation by the water, as complete loss of activity took place over ca. 12 h of operation when co-feeding water. Additionally, thermodynamic calculations and in situ XRD analysis supported that Mo_2C is oxidized to MoO_2 in the presence of water at the given conditions. Thus, the potential for using Mo_2C as HDO catalyst for HDO of bio-oil seems challenged, as bio-oil always contains large amounts of water.

7.1 Introduction

As it was realized in Chapter 6 that the nickel based catalysts was readily deactivated by many of the impurities conventionally found in bio-oil, alternative HDO catalysts was investigated. A less investigated group of catalysts for HDO is carbides [139, 302]. This group of catalysts has received increasing attention in many different reactions as their properties has been compared to noble metal catalysts [334–336]. Additionally, Mo_2C has been used as hydrodesulfurization catalyst and is therefore also tolerant to at least sulfur [337–340], which makes it an interesting catalyst for HDO as well. So far, the use of this catalyst as a HDO catalyst has been demonstrated with propanol [341], fatty acids and vegetable oils [342–346], and guaiacol type molecules [347–350]. However, little is known about its stability during prolonged operation.

To evaluate the potential of Mo_2C as catalyst for HDO, the activity and stability of Mo_2C/ZrO_2 was investigated in the continuous flow setup (cf. Section 3.2) with a bio-oil model system of phenol in 1-octanol. The ZrO_2 support was maintained as this from the work in Chapter 4 and other groups [116, 138, 139, 351, 352] is indicated as a prospective support for HDO. Further details on preparation and carburization of the catalyst can be found in Section 3.4.3.

7.2 Carburization Procedure

Initially the carburization method was followed in situ by XRD and XAS. The combination of XRD and XAS provides a more complete description of the structure of the catalyst, because XRD mainly supplies information related to long range order, whereas XAS captures the local structure around the absorber atom (short-range order).

Figure 7.1 shows the XRD patterns recorded during the in situ carburization. At room temperature, under carburizing atmosphere, the diffraction pattern only showed reflections related to the ZrO_2 support phase. The reflections related to the ZrO_2 support did not change during the carburization and deactivation. None of the signals of the as-prepared samples could be associated with MoO_3, which may be consequence of the high dispersion of this phase on the support.

After increasing the temperature to 250 °C, a small reflection at a 2Θ of 25.6° appeared. This reflection can be attributed to the formation MoO_2. After reaching 550 °C the reflection at 25.6° shifted to 25.9°, which is closer to the value of the reference pattern of MoO_2, which is 26.0° [353]. The referred reflection was also sharper at 550 °C than at 250 °C. These results indicate crystal growth of the MoO_2 phase as function of temperature under reducing/carburizing atmosphere. Another reflection, at a 2Θ of 40.5°, also appeared at 550 °C however it could not be attributed to any of the reference compounds. After thermal treatment for two hours this reflection shifted to 39.4° which corresponds to a Mo_2C phase [354]. At this point the reflection related to MoO_2 disappeared.

The transformation of the local structure of Mo was followed in parallel on the same sample by XAS during the carburization process. The analysis of the Mo K-edge XANES spectra showed three major components, during the carburization. Figure 7.2(a) shows the XANES spectra of these together with reference compounds

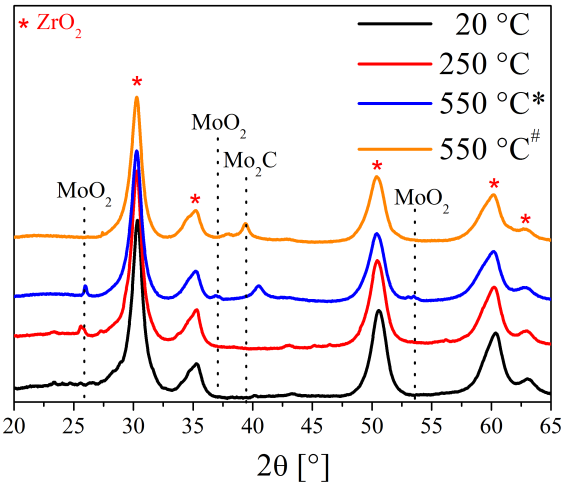

Figure 7.1: *In situ XRD patterns recorded during the carburization of 15 wt% MoO_3/ZrO_2. §: Recorded at the beginning of the annealing at 500 °C. #: Recorded after 2 hours of annealing at 500 °C. Feed gas: 1 vol% CH_4 and 4 vol% H_2 diluted in He. The sample was heated at 5 °C/min from room temperature up to 250 °C, at 2 °C/min up to 550 °C, and held at 550 °C for 2 h.*

for MoO_3, MoO_2, and Mo_2C. The three observed phases were related to MoO_3, MoO_2, and Mo_2C; the two latter were also corroborated by the XRD results (cf. Figure 7.1). Although the in situ recorded spectra share many features with the reference compounds, they are not exactly the same. It is most likely the result of the high dispersion, and therefore small particle size, of the Mo species dispersed on ZrO_2. Moreover, note that the X-ray absorption was very strong despite only a 0.5 mm capillary was used which led to less pronounced whitelines.

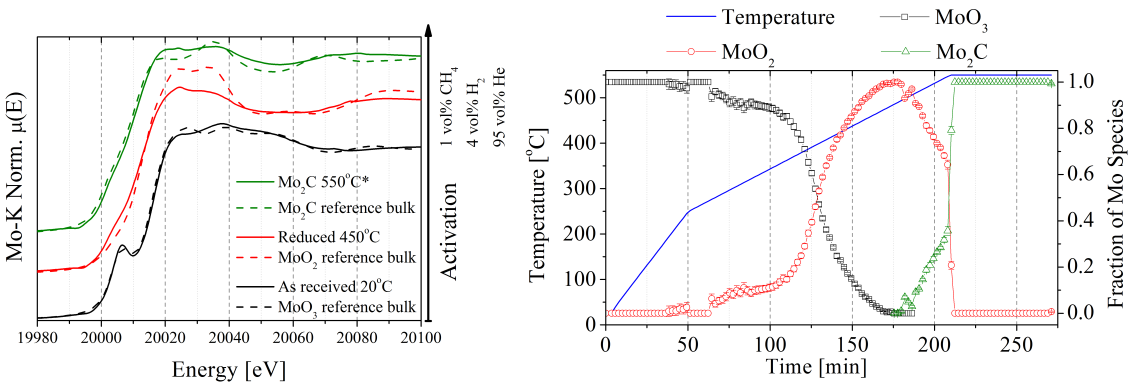

(a) XANES spectra of Mo species

(b) Fraction of Mo species

Figure 7.2: *(a) XANES spectra of Mo reference compounds and in situ recorded spectra during the carburization process, and (b) fraction of Mo phases formed during the carburization. Feed gas: 1 vol% CH_4 and 4 vol% H_2 diluted in He. The sample was heated at 5 °C/min from room temperature up to 250 °C, at 2 °C/min up to 550 °C, and held at 550 °C for 2 h.*

In Appendix I it is shown that the data cannot be properly described as a linear combination of bulk references. Instead, the three observed phases related to MoO_3, MoO_2, and Mo_2C were used as reference compounds for linear combination and were

chosen based on the isosbestic points presented during the evolution of the spectra. This approach allowed tracing the composition of Mo species during the carburization of the catalyst, as shown in Figure 7.2(b). Based on this approach it is clear that the MoO_3-like phase is not directly converted to Mo_2C, as already shown by XRD. The MoO_3-like phase was reduced forming an intermediate MoO_2-like phase in the temperature region 350-475 °C. This phase, did not change from ca. 475-500 °C, reinforcing the assumption of nearly complete transformation of MoO_3 to MoO_2. This phase was then carburized forming Mo_2C from 500-550 °C.

Overall, the combined in situ XRD and XAS analysis revealed that carburization of MoO_3/ZrO_2 proceeds by an initial reduction of MoO_2/ZrO_2 at ca. 350 °C and a subsequent carburization to Mo_2C/ZrO_2 during longer treatment at 550 °C. This verifies that the carburization procedure used in in the experimental work did produce the desired carbide.

7.3 Catalyst Activity

The activity of the Mo_2C/ZrO_2 catalyst was evaluated in the temperature range from 280 to 380 °C in increments of 20 °C, and the results are summarized in Figure 7.3. As expected, conversions of both 1-octanol and phenol increased as a function temperature, but the conversion of 1-octanol was always higher than phenol showing the more persistent nature of phenol.

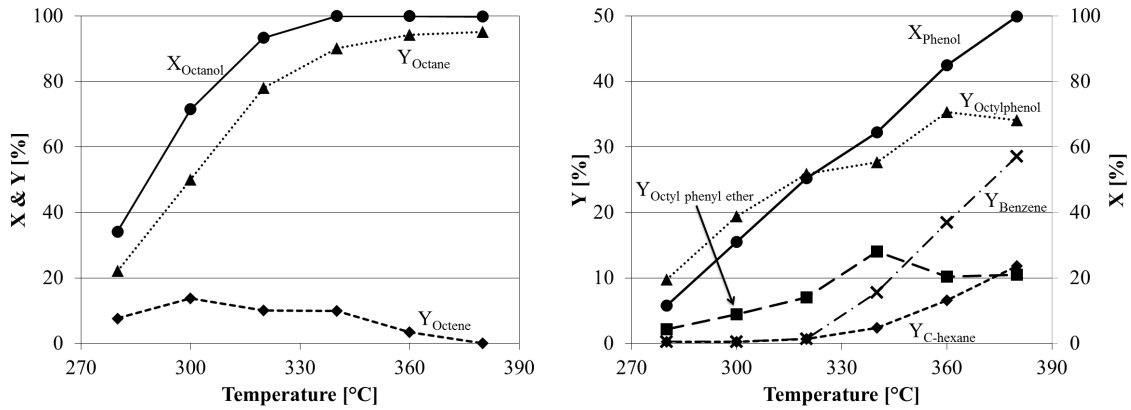

(a) Conversion and yields of 1-octanol related compounds

(b) Conversion and yields of phenol related compounds

Figure 7.3: *Activity of Mo_2C/ZrO_2 for HDO of phenol and 1-octanol as a function of temperature. (a) conversion and yields of 1-octanol related compounds and (b) conversion and yields of phenol related compounds. Note that in figure (a), the yield is based on 1-octanol while in figure (b) it is based on phenol. The graphs are combined from two experiments in the temperature range from 280-320 °C and 340-380 °C, both experiments roughly took 24 h. $P = 100$ bar, $F_{oil} = 0.2$ ml/min, $WHSV = 4.0\ h^{-1}$.*

1-octanol was primarily converted to octane, but with octenes (both 1-octene and 2-octene) as major byproduct. At 280 °C the octene/octane ratio was 0.34, but at 380 °C the octene/octane ratio had decreased to 0.001. The high yield of octene at the lower temperatures indicate a reaction scheme where 1-octanol is dehydrated to

octene and then hydrogenated to octane, as shown in Figure 7.4. Similar, Ren et al. [341] observed propylene as the primary product from HDO of vapor phase propanol at 300 °C in a continuous flow reactor at atmospheric pressure. The lower hydrogen pressure used in that study, compared to the current, probably explains the lower selectivity toward propane.

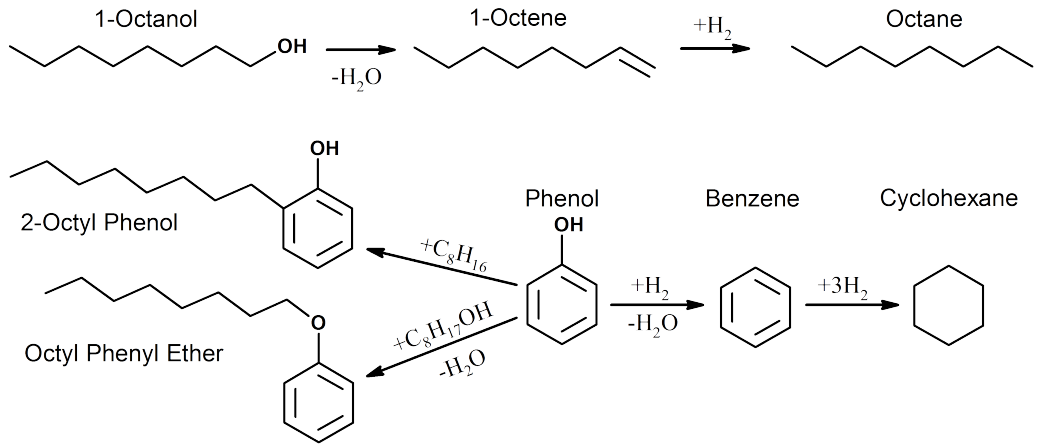

Figure 7.4: *Reaction scheme of 1-octanol and phenol over Mo_2C/ZrO_2.*

Besides octene, also dioctyl ether, octyl phenyl ether, and octyl phenol were observed as significant byproducts. However, testing the activity of the ZrO_2 alone, revealed that this readily catalyzed the ether forming reactions, as shown in Figure 7.5. Additionally, the support also catalyzed the dehydration of 1-octanol to octene, with a 30% yield at 380 °C compared to 95% yield octane at the same temperature with the Mo_2C/ZrO_2 (cf. Figure 7.3(a)). This relative high tendency for octene formation is probably catalyzed by the acid sites on the support.

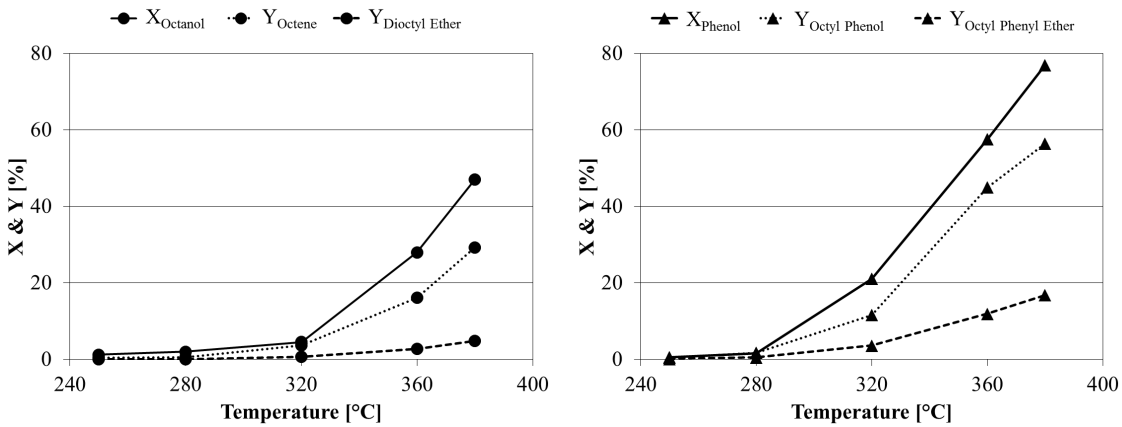

(a) Conversion and yields of 1-octanol related compounds

(b) Conversion and yields of phenol related compounds

Figure 7.5: *Catalytic performance of ZrO_2 support alone with respect to HDO of phenol and 1-octanol as a function of temperature. (a) conversion and yields of 1-octanol related compounds and (b) conversion and yields of phenol related compounds. Note that in figure (a), the yield is based on 1-octanol while in figure (b) it is based on phenol. $P = 100$ bar, $F_{oil} = 0.2$ ml/min, $WHSV = 4.0\ h^{-1}$.*

For phenol, the conversion increased with temperature as seen from Figure 7.4. However, up to 320 °C the only products were octyl phenol (ca. 85% selectivity) and octyl phenyl ether (ca. 15% selectivity), formed in reactions with phenol and octene and 1-octanol, respectively, as shown in Figure 7.4. In particular, no benzene was formed. As evidenced by the experiment with pure ZrO_2 the ether like compounds were to a large extent formed on the acid sites of the support (cf. Figure 7.5).

From Figure 7.4 it can be seen that temperatures higher than 320 °C were needed for deoxygenation of phenol. Benzene and cyclohexane were formed in a benzene/cyclohexane ratio of roughly 2.8, i.e. with benzene as the primary product in the investigated temperature range. The combined selectivity to benzene and cyclohexane was roughly 50% at 380 °C, with octyl phenol and octyl phenyl ether constituting roughly the remaining product from phenol.

HDO of phenol can proceed either by a direct deoxygenation to benzene followed by hydrogenation to cyclohexane or an initial hydrogenation to cyclohexanol followed by deoxygenation to cyclohexane. The actual route is dependent on the type of catalyst used and process conditions [72, 98, 230, 355–358]. As roughly 70% of the deoxygenated product was benzene, the direct deoxygenation path was favored with this catalyst. With increasing temperature, the selectivity toward cyclohexane increased, as the benzene/cyclohexane ratio decreased from 3.3 at 340 °C to 2.4 at 380 °C. Thus, as for 1-octanol, the hydrogenation activity increased with temperature, but generally the catalyst has a relatively low activity for hydrogenation. Similarly, Jongerius et al. [349] also found low tendency for ring hydrogenation of guaiacol over Mo_2C/CNF (CNF: carbon nanofiber) in a series of batch experiments at 300-375 °C and 55 bar. This supports our observations that over molybdenum carbides cleavage of the C-O bond occurs easier than ring hydrogenation.

The higher temperature required for the deoxygenation of phenol over Mo_2C, compared to e.g. nickel based catalysts (about 250-275 °C) [2, 116, 141], is probably linked to inability of Mo_2C to hydrogenate the aromatic ring, as the C-O bond energy of phenol is 469 kJ/mol compared to 385 kJ/mol for cyclohexanol [242]. In addition, in the latter case acid catalyzed deoxygenation may further promote this route. Thus, catalysts able to hydrogenate the phenol ring prior to deoxygenation tend to deoxygenate at a lower temperature [2]. However, as in the case of Mo_2C, where direct deoxygenation takes place, a higher temperature is required to break the strong C-O bond and aromatic deoxygenation products are obtained.

7.4 Stability

The stability of the Mo_2C/ZrO_2 catalyst for HDO of the 70 g/l phenol in 1-octanol solution was tested at 300 °C and 100 bar. Figure 7.6 summarizes the conversions of phenol and 1-octanol and the yields of octane, octene, octyl phenyl ether, and octyl phenol as a function of time on stream (TOS). Similar to the activity found at 300 °C in the investigation on temperature effect (cf. Figure 7.3), the initial conversion of 1-octanol was ca. 70 %. However, the activity decreased steadily throughout the 76 h experiment, with the conversion dropping to 37% in the end, i.e. roughly half the initial conversion. For conversion of 1-octanol, the octene/octane ratio started at 0.38, but shifted to 0.58 at the end of the experiment, showing that the hydrogenation activity decreased more rapidly than the activity for deoxygenation by dehydration.

A major byproduct from 1-octanol was dioctyl ether, with an increasing selectivity from 11% to 18% throughout the experiment.

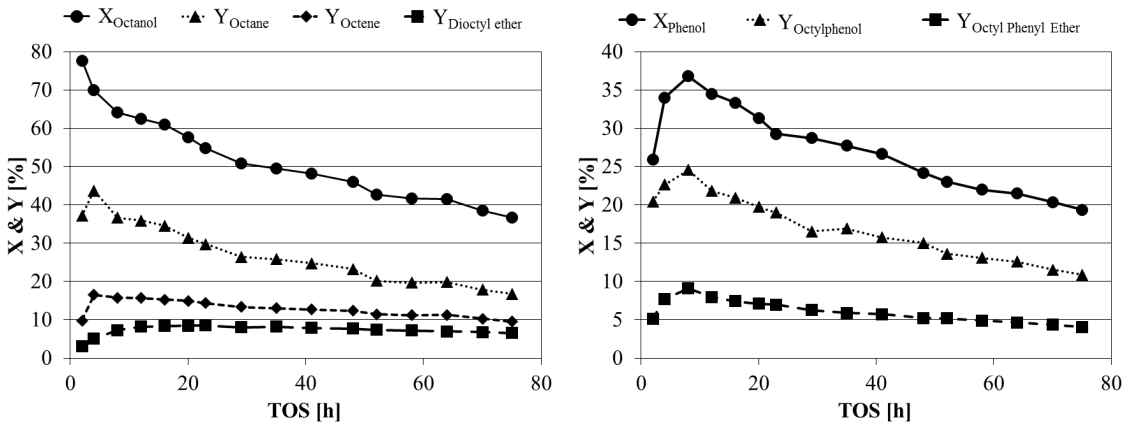

(a) Conversion and yields of 1-octanol related compounds

(b) Conversion and yields of phenol related compounds

Figure 7.6: *Stability of Mo_2C/ZrO_2 during HDO of phenol and 1-octanol, (a) shows conversion and yields of 1-octanol related compounds and (b) shows conversion and yields of phenol related compounds. Note that in figure (a), the yield is based on 1-octanol while in figure (b) it is based on phenol. $T = 300\,°C$, $P = 100$ bar, $F_{oil} = 0.2$ ml/min, $WHSV = 4.0\ h^{-1}$.*

The conversion of phenol also decreased as a function of TOS, from ca. 38% to 21% after 76 h of TOS. However, as discussed in Section 7.3, only octyl phenol and octyl phenyl ether were produced at the given conditions. The ratio between octyl phenol and octyl phenyl ether was almost constant, as it only decreased from ca. 2.9 to 2.7 throughout the experiment. The slight change was probably associated with less octene available for formation of octyl phenol, as the concentration of octene decreased as a function of TOS (cf. Figure 7.6(a)). In general the results show an overall loss of activity for all reactions.

Water is formed during deoxygenation and is a typical constituent of bio-oil. This was co-fed to the 70 g/l phenol in 1-octanol solution corresponding to 33% by volume in another stability experiment. The development in the conversions of phenol and 1-octanol can be seen in Figure 7.7. Evidently, a rapid deactivation of the catalyst occurred as the conversion of 1-octanol decreased from ca. 64% to 11% within the first 12 h of TOS. Similar, also the phenol conversion rapidly decreased, from 24% to 4% in the first 12 h of TOS.

In comparison to the stability profile in Figure 7.6, where no water was co-fed, it is obvious that the presence of water resulted in a faster deactivation of the catalyst. During the experiment, a constant signal of ca. 0.02 vol% CO_2 was measured in the off-gas, indicating oxidation of Mo_2C by H_2O to MoO_2/MoO_3. A rough calculation shows, that at this concentration of CO_2 and at a gas flow of 250 Nml/min, all carbon would be removed from 2.5 g of Mo_2C/ZrO_2 with 15 wt% Mo during 14-15 h of operation. This and the fact that mixed Mo-oxy-carbides may also be active correlates well with almost complete loss of activity of the catalyst over 12 h of operation. It is emphasized that a complete shift in the water gas shift reaction

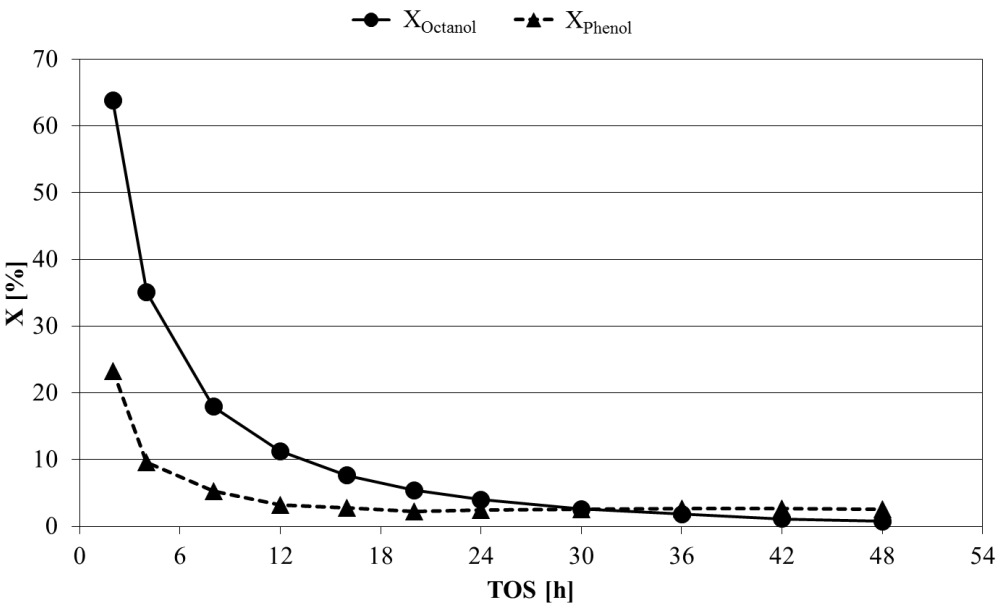

Figure 7.7: *Stability of Mo_2C/ZrO_2 during HDO of phenol and 1-octanol co-fed with water. $T = 300\ °C$, $P = 100$ bar, $F_{oil} = 0.2$ ml/min, $F_{water} = 0.1$ ml/min, WHSV = 6.4 h^{-1}.*

toward CO_2 is expected at the given conditions from thermodynamic calculations [71] and CO could therefore also have been a primary product from the oxidation.

In view of these results, the deactivation observed in the experiment not co-feeding water (cf. Figure 7.6) could also be due to water, as this is formed as a byproduct from the deoxygenation reactions. However, with limited formation of water (0.02-1 μl/min as estimated from the production of octane/octene), the oxidation of the catalyst is slow. In this experiment, traces (<0.01%) of CO_2 and CH_4 was seen in the gas phase, indicating that oxidation took place.

Similar to the current results, Chang et al. [348] observed a close to linearly decreasing activity of a Mo_2C/C catalyst for HDO of guaiacol at 400 °C and 40 bar in a continuous flow setup over 6 h of TOS. The reason for the deactivation was not identified, but in the view of the present results, it seems likely that water was a contributing factor. Claridge et al. [359] observed that molybdenum carbide deactivated as catalyst in reforming of methane due to formation of MoO_2, and that the level of deactivation increased with the strength of the oxidizing agent as: $O_2 > H_2O \approx CO_2$.

7.5 Thermodynamic Evaluation of the Stability of Mo_2C

To further analyze the potential for oxidation of Mo_2C, the Gibbs free energies of a series of oxidation reactions were calculated, as shown in Table 7.1. Assuming CO_2 as the product from the oxidation of Mo_2C to MoO_2 with water (reaction 1 and 2 in Table 7.1), ΔG is -138 kJ/mol at 300 °C, meaning that the reaction is thermodynamically favorable. It is emphasized that all molybdenum compounds

were calculated as unsupported bulk materials. The stability of supported nanoparticles may even be lower.

Table 7.1: *Gibbs free energy of reaction for a series of oxidizing reaction of Mo_2C. Data for bulk molybdenum compounds was used in the calculations. Calculations done on the basis of thermodynamic data from Barin [71, 360] and NIST [361].*

#	Reaction Temperature [°C]	ΔG [kJ/mol] 200	 300	 400
1	$Mo_2C(s) + 6\,H_2O(g) \rightleftharpoons 2\,MoO_2(s) + CO_2(g) + 6\,H_2(g)$	-26	-19	-14
2	$Mo_2C(s) + 6\,H_2O(l) \rightleftharpoons 2\,MoO_2(s) + CO_2(g) + 6\,H_2(g)$	-88	-138	-
3	$Mo_2C(s) + 5\,H_2O(l) \rightleftharpoons 2\,MoO_2(s) + CO(g) + 5\,H_2(g)$	-56	-100	-
4	$2\,MoO_2(s) + CH_4(g) + 2\,H_2(g) \rightleftharpoons Mo_2C(s) + 4\,H_2O(g)$	107	81	54
5	$Mo_2C(s) + 8\,H_2O(l) \rightleftharpoons 2\,MoO_3(s) + CO_2(g) + 8\,H_2(g)$	86	22	-
6	$Mo_2C(s) + 7\,H_2O(l) \rightleftharpoons 2\,MoO_3(s) + CO(g) + 7\,H_2(g)$	118	59	-
7	$Mo_2C(s) + 5\,CO_2(g) \rightleftharpoons 2\,MoO_2(s) + 6\,CO(g)$	103	87	70
8	$Mo_2C(s) + 3\,O_2(g) \rightleftharpoons 2\,MoO_2(s) + CO_2(g)$	-1348	-1312	-1275

As the boiling point of water is 340 °C at 100 bar [362], both liquid and gaseous water may be present at the current experimental conditions and therefore the potential for oxidation was evaluated with water in both phases (reaction 1 and 2). Comparing the two cases, the driving force for oxidation was largest when water was in the liquid phase, but in both cases the reaction readily takes place. The higher Gibbs free energy for oxidation with water in the gas phase compared to the liquid phase may correlate with the slower deactivation/oxidation in the case where water was not co-fed (cf. Figure 7.6), since in this case the formed water to a large extent will be in the gas phase.

Using the thermodynamic calculations to predict which other reactions could take, showed that when CO was the oxidation product (cf. reaction 3 in Table 7.1) a ΔG below zero was also found, indicating a spontaneous oxidation.

Co-feeding methane is not expected to prevent the oxidation, as the Gibbs free energy for the carburization reaction (cf. reaction 4 in Table 7.1) is positive in the temperature range of relevance and the reaction is therefore not thermodynamically favored.

Comparing reactions 1-3 with reactions 5 and 6, MoO_2 will be the preferred product from the oxidation, as no driving force exist for formation of MoO_3. Similar, MoO_3 reduces to MoO_2 at temperatures above 300 °C, as discussed in Section 7.2.

The Gibbs free energy for oxidation with CO_2 was calculated in Table 7.1 (reaction 7). However, there was no driving force for this reaction, excluding that the formed CO_2 aided in the oxidation of the catalyst. From a thermodynamic point of view, the strength of the oxidizer for Mo_2C oxidation therefore follows the trend $O_2 > H_2O > CO_2$ (cf. reaction 2, 7, and 8), which is similar to the observations of Claridge et al. [359].

7.6 In situ XRD During Water Deactivation

To analyze the effect of water further, an experiment was made measuring in situ XRD on the Mo_2C/ZrO_2 during exposure to water. At 300 °C the initial XRD pattern showed the carbide phase, as seen in Figure 7.1. However, after 2 hour aging in a feed of 5 vol% H_2 in He saturated with water, the Mo_2C reflection strongly decreased whereas the MoO_2 appeared, cf. Figure 7.8. This supports the observations from the activity experiments.

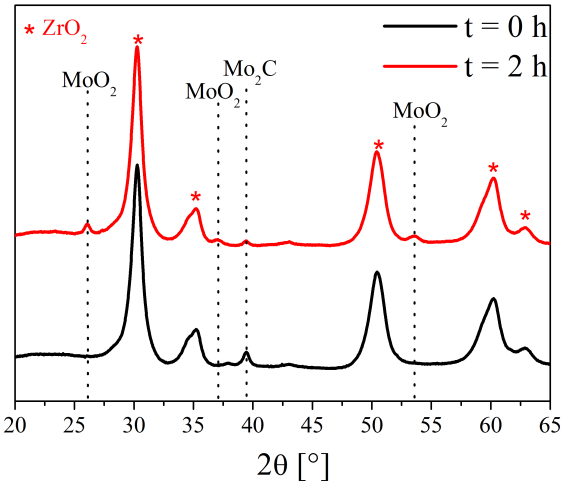

Figure 7.8: *XRD patterns recorded during aging of Mo_2C/ZrO_2. Feed gas: 5 vol% H_2 in He saturated with water. The sample was exposed to water for 2 h at 300 °C. t = 0 h is the pattern prior to water exposure and t = 2 h is after exposure.*

Overall, the combination of experiments, thermodynamic calculations, and XRD shows that deactivation of the catalyst is due to the conversion of molybdenum carbide into molybdenum (IV) oxide, which is inactive at the given conditions. Bio-oils will contain from 10 to 30 % water, depending on the biomass feed [59, 61, 305]. This water can not easily be separated from the oil [42, 45]. Additionally, water is produced as a byproduct from the HDO reaction. Thus, the upgrading of bio-oil over Mo_2C type catalysts seems challenging.

7.7 Conclusion

Molybdenum carbide has been investigated as a potential catalyst for bio-oil HDO, using phenol in 1-octanol as a simple model compound system to evaluate both activity and stability. By in situ XRD and XAS under carburization conditions, it was found that MoO_3/ZrO_2 reduced to MoO_2/ZrO_2 above 350 °C and was then carburized to Mo_2C at 550 °C.

Mo_2C/ZrO_2 effectively converted 1-octanol to octene and octane at temperatures above 280 °C. The selectivity towards octene was up to 25 % due to the low hydrogenation activity of the catalyst. Also due to the low activity for hydrogenation, phenol was directly deoxygenated to benzene which, however, required temperatures above 320 °C to break the strong C-O bond in phenol. Benzene could be hydrogenated further to cyclohexane, which increased with temperature. At 340 °C the benzene/cyclohexane ratio was 3.3, but only 2.4 at 380 °C.

During long term testing of Mo_2C/ZrO_2 for HDO of phenol in 1-octanol at 300 °C, the catalyst deactivated, and the conversion of 1-octanol decreased from 70% to 37% over 76 h of operation. Even faster deactivation was observed when co-feeding water in levels typical of bio-oil, and the catalyst was completely deactivated over 12 h of TOS.

Based on the experimental evidence, and supported by thermodynamic calculations and in situ XRD analysis, we conclude that the catalyst is deactivated by reaction of Mo_2C with water to MoO_2, which is inactive. In the absence of co-fed water, the catalyst deactivated slower as only the water formed in the HDO reaction is present to cause deactivation. In conclusion, the potential of molybdenum carbide as catalyst for HDO of bio-oil seems challenging, as water is a major part of bio-oil and further is produced in the HDO reaction. This is in general an important issue to be considered for carbide catalysts used in hydrodeoxygenation, reforming, or water-gas-shift reactions.

Chapter 8

Inhibition and Deactivation of Ni-MoS_2 by Bio-oil Impurities During Hydrodeoxygenation

Abstract

The stability and resistance of Ni-MoS_2/ZrO_2 toward water, potassium, and chlorine during hydrodeoxygenation (HDO) of phenol and 1-octanol as bio-oil model compounds has been investigated in a high pressure gas and liquid continuous flow fixed bed setup at 280 °C and 100 bar. To maintain stability of the catalyst, a sufficient co-feed of a sulfur source was necessary. Feeding insufficient sulfur resulted in oxidation of the sulfide phase, by replacement of the framework sulfur atoms. However, addition of sulfur resulted in formation of sulfur containing compounds in the oil product if the residence time was insufficient. At the given conditions a residence time of >1.4 h was needed to maintain the sulfur content of the liquid product below 30 ppm_w. An additional co-feed of sulfur was needed when water was present in the feed and the H_2O/H_2S ratio should be below ca. 10 to maintain a decent stability of the catalyst. The loss of activity when co-feeding water was linked to loss of edge sulfur atoms. Potassium was a severe poison and deactivated the catalyst completely (<5% degree of deoxygenation) when impregnated on the catalyst in a stoichiometric ratio relative to the active metal. This deactivation was linked to saturation of the edge vacancy sites on the MoS_2 slabs by potassium. Chlorine caused an inhibition of the catalyst when co-fed to the reactor, but the activity could be completely regained when removing it from the feed again. Commonly HCl, H_2O, and H_2S all inhibited the activity of the catalyst by competing for the active sites, with HCl being by far the strongest inhibitor and H_2S and H_2O of roughly the same strength. Overall potassium was however found as the worst poison causing complete and persistent loss of activity.

8.1 Introduction

Traditional hydrotreating catalysts, as Co-MoS_2 and Ni-MoS_2, have been among the most tested catalysts for HDO [39, 302, 363]. This group of catalysts is already industrially established in hydrodesulfurization (HDS) [107, 110, 364–366]. On these catalyst, HDO takes place by a Max-Van-Krevelen type reaction mechanism, as discussed in Section 2.4.1.1. In HDS, the activity of the catalyst has been linked to the availability of edge sites on the MoS_2 slabs [364, 366–370]. As the mechanism for HDS and HDO is similar, this type of sites are also believed to be the active sites for HDO [104, 371]. Promotion with either Co or Ni is believed to increase the availability of vacancy sites by lowering the Mo-S bond energy [364, 365, 368, 372, 373].

Long term stability of MoS_2 based catalysts during HDO has not been thoroughly investigated. One of the concerns raised, is their requirement for co-feeding sulfur in order to retain the catalyst in its active sulfide form, but this could potentially contaminate the otherwise sulfur scant bio-oil [108, 109, 373]. Furthermore, little is known about the influence of bio-oil impurities on the catalyst stability.

In the search for stable HDO catalysts, this group of catalysts was investigated in the continuous flow setup with a bio-oil model system of phenol in 1-octanol, as alternative to the Ni/ZrO_2 and Mo_2C/ZrO_2 catalysts investigated in Chapter 6 and 7, respectively, which suffered from deactivation by the impurities found in bio-oil. Ni-MoS_2/ZrO_2 was chosen as catalyst, as promotion by nickel previous has been indicated to be slightly superior to cobalt promotion [39, 373] and ZrO_2 has been indicated as a prospective support for HDO [116, 138, 139, 351, 352] and does apparently not suffer from the instability in high concentration of water, as reported for the conventionally used γ-Al_2O_3 support for hydrotreating catalysts [39, 132, 374] (cf. Section 2.4.1.3 for further details).

8.2 The effect of H_2S

The stability of the Ni-MoS_2/ZrO_2 catalyst and the influence of the sulfur source was investigated in two experiments: one with 0.3 vol % 1-octanethiol in the feed and one with 2 vol% DMDS in the feed, corresponding to respectively 283 ppm and 8172 ppm H_2S in the gas feed, assuming complete decomposition of the feed sulfur compounds. The first case is representative to the type of sulfur containing components and concentration that could be expected in bio-oil [305]. The second case was an attempt to improve the catalyst stability. The conversion of phenol and 1-octanol of these experiments are summarized in Figure 8.1.

In the case with 0.3 vol% 1-octanethiol in the feed, the activity steadily decreased throughout the 110 h of testing. The 1-octanol conversion decreased from 78% to 49% and the phenol conversion decreased from 56% to 21% (cf. Figure 8.1(a)). In comparison, adding 2 vol% DMDS to the feed resulted in a significantly better stability, as the 1-octanol conversion only dropped from 95% to 88% over 96 h of testing and the phenol conversion dropped from 36% to 19% in the same time frame (cf. Figure 8.1(b)).

Analysis of sulfur on the spent catalyst with ICP-OES revealed that the sulfur content in the case co-fed with 0.3 vol% 1-octanethiol had decreased to 7.5 wt%, compared to 10.9 wt% on a freshly sulfided catalyst (cf. Table 8.1). In comparison,

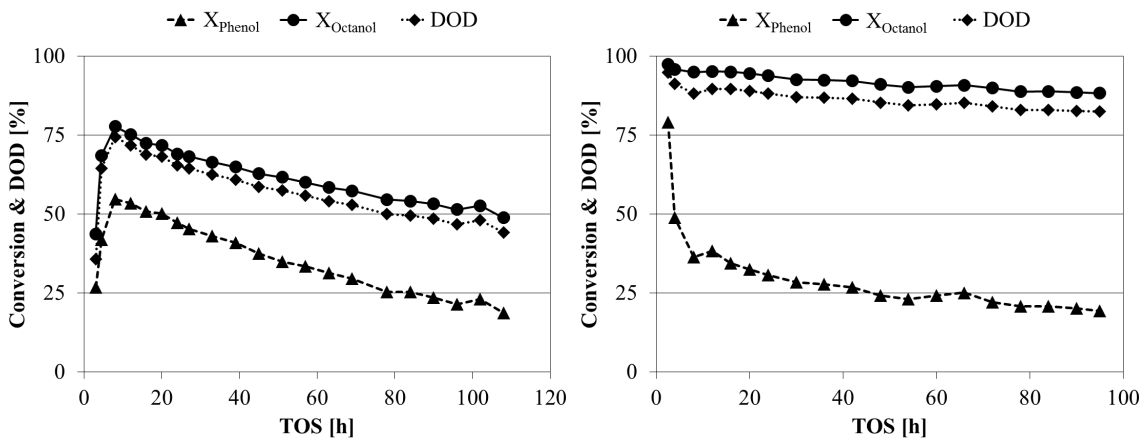

(a) 0.3% 1-octanethiol in the feed.

(b) 2% DMDS in the feed.

Figure 8.1: *Stability of Ni-MoS_2/ZrO_2 during HDO of phenol and 1-octanol. (a) shows conversions of 1-octanol and phenol in a case with 0.3 vol% 1-octanethiol in the feed and (b) shows conversions of 1-octanol and phenol in a case with 2 vol% DMDS in the feed. Feed: 50 g/l phenol in 1-octanol, T = 280 °C, P = 100 bar, F_{oil} = 0.2 ml/min, WHSV = 4.0 h^{-1}.*

the catalyst co-fed with 2 vol% DMDS had a content of 8.4 wt% sulfur after operation. Thus, both catalysts appear to loose sulfur during operation, but the case co-feeding 1-octanethiol lost significantly more sulfur.

Table 8.1: *Elemental content of sulfur and carbon on spent catalyst tested with different sources of sulfur in the feed and varying H_2O/H_2S feed ratios. Fresh catalyst is a catalyst analyzed directly after sulfidation.*

Sulfur in feed	TOS_{Total} [h]	H_2O/H_2S feed ratio	S [wt%]	C [wt%]
Fresh catalyst	-	-	10.9	1.9
0.3 vol% 1-octanethiol	110	0	7.5	3.7
2 vol% DMDS	95	0	8.4	2.0
2 vol% DMDS	96	46	8.9	2.1
5 vol% DMDS	100	16	8.2	1.7
5 vol% DMDS	92	9.7	8.3	3.1

Additionally, the ICP-OES analysis revealed that the tendency for carbon formation was low on both catalysts with less than 4 wt% carbon on both catalysts. Roughly half of this could be deposited already during sulfidation, as 2 wt% carbon was found on a freshly sulfided catalyst (cf. Table 8.1).

Figure 8.2 compares the TEM image from a freshly sulfided Ni-MoS_2/ZrO_2 and the catalyst from the experiment co-feeding 0.3 vol% 1-octanthiol. The freshly sulfided catalyst clearly displayed the presence of several slab structures on the catalytic surface as the furrows. Measuring the interplanar distance confirmed this to be MoS_2 slabs. In comparison, this structure was less apparent on the spent catalyst (cf. Figure 8.2(b)). This indicates that the slab structure had partly disappeared during the experiment co-feeding the low concentration of sulfur. However, in the comparison

it should be stressed that the analysis is very local and the results are therefore only indications.

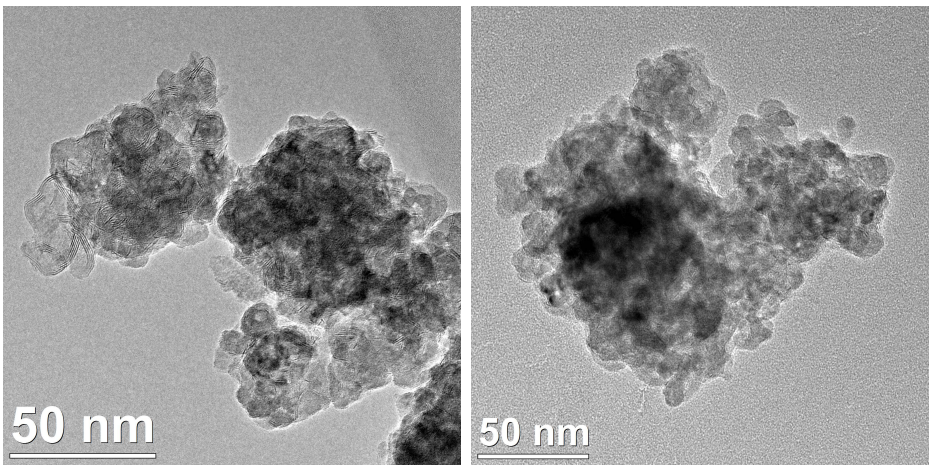

(a) Freshly sulfided Ni-MoS_2/ZrO_2. (b) Ni-MoS_2/ZrO_2 operated for 110 h.

Figure 8.2: *TEM images of freshly sulfided Ni-MoS_2/ZrO_2 catalysts and catalyst operated for 110 h with 50g/l phenol and 0.3 vol% 1-octanethiol in 1-octanol.*

Analyzing further on the results from the TEM images in Figure 8.2, the spent catalysts were analyzed by XRD. This revealed formation of MoO_3 in the case with 1-octanethiol in the feed (cf. Figure 8.3). In the case with 2 vol% DMDS in the feed, oxide formation was not detected. The XRD analysis additionally revealed Ni_3S_2 and an elemental Ni phase.

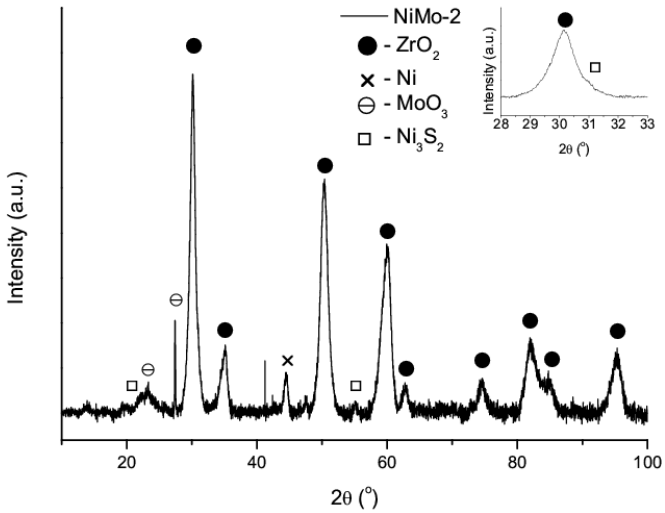

Figure 8.3: *XRD of a Ni-MoS_2/ZrO_2 catalyst operated for 110 h with 50g/l phenol and 0.3 vol% 1-octanethiol in 1-octanol.*

The combination of XRD (cf. Figure 8.3), elemental analysis (cf. Table 8.1), and TEM images (cf. Figure 8.2), indicates that feeding insufficient sulfur will result in a depletion of the sulfide phase. Previous work has also shown that not co-feeding a sulfur source will result in a replacement of the framework S-atoms in the

MoS_2 with oxygen atoms from the HDO reaction [94, 100, 105, 357, 375]. Thus, the concentration of H_2S in the gas should be sufficient and the sulfur source should be readily decomposed. The natural content of thiols in bio-oil does not appear sufficient for sustaining the catalyst in the active form during operation and addition of DMDS/H_2S is recommended during HDO of a real bio-oil feed.

Comparing the initial activity in the two cases in Figure 8.1, increasing the H_2S concentration resulted in an increase in the 1-octanol conversion from 77% to 95%, but a decrease in the initial phenol conversion from 55% to 36%. It has previously been described that co-feeding H_2S during HDO on MoS_2 type catalysts results in a competitive adsorption between H_2S and the oxy-compound [94, 356, 371, 376]. Badawi et al. [371] described on the basis of density functional theory (DFT) calculations that the adsorption of H_2S and H_2O was stronger on CoMoS sites compared to phenol and these species therefore have an inhibiting effect on this reaction. This explains why the phenol conversion decreased when increasing the H_2S concentration. In this analogy it could be thought that 1-octanol is adsorbing at a similar strength as H_2S and is therefore not affected to the same extent. The promotional effect may be understood by availability of more active sites, as phenol is not competing for these sites in the same extent anymore.

A drawback of increasing the sulfur concentration as discussed above was an increased concentration of thiols in the liquid product, which increased from 13 ppm_w sulfur in the case co-feeding 0.3 vol% 1-octanethiol to 381 ppm_w in the case co-feeding 2 vol% DMDS. Similar, Senol et al. [108, 109] also observed formation of thiols when co-feeding a sulfur source. These observations indicate that incorporation of sulfur in the liquid product is a general problem for this type of catalyst in HDO, as well as in other reactions such as higher alcohols synthesis [32]. The formation of sulfur containing compounds was linked to the reaction scheme of HDO of 1-octanol and phenol. Thus, to investigate this further, the effect of residence time on the sulfur content of the product oil was investigated, as summarized in Figure 8.4.

For 1-octanol, increasing the residence time increased the conversion, always with octane as the primary product. However, 1-octene was also found as an important byproduct with a selectivity of 12% at the lowest residence time and decreasing to 0% at the highest residence time. Thus, HDO of 1-octanol over this catalyst proceeds by a dehydration reaction scheme, producing 1-octene. This subsequently reacts with hydrogen to form octane as the final product, as shown in Figure 8.5.

For phenol, cyclohexane was observed as the primary product at all residence times, but also benzene (up to 5% selectivity), cylohexanol (up to 18% selectivity), and cyclohexene (up to 41% selectivity) were detected. HDO of phenol can take place by two paths as summarized in Figure 8.5: a direct deoxygenation of phenol to benzene, followed by hydrogenation to cyclohexane, or an initial hydrogenation of phenol to cyclohexanol followed by dehydration to cylohexene and then hydrogenation to cyclohexane. The actual reaction path will be dependent on catalyst and reaction conditions [72, 98, 230, 355–357]. Apparently, the hydrogenation path is preferred under the given conditions, as evidenced by the high fraction of cyclohexanol and cyclohexene at especially the low residence times.

1-octanethiol and cyclohexanethiol were the primary sulfur containing products formed. The selectivity toward 1-octanethiol and cyclohexanethiol dropped from re-

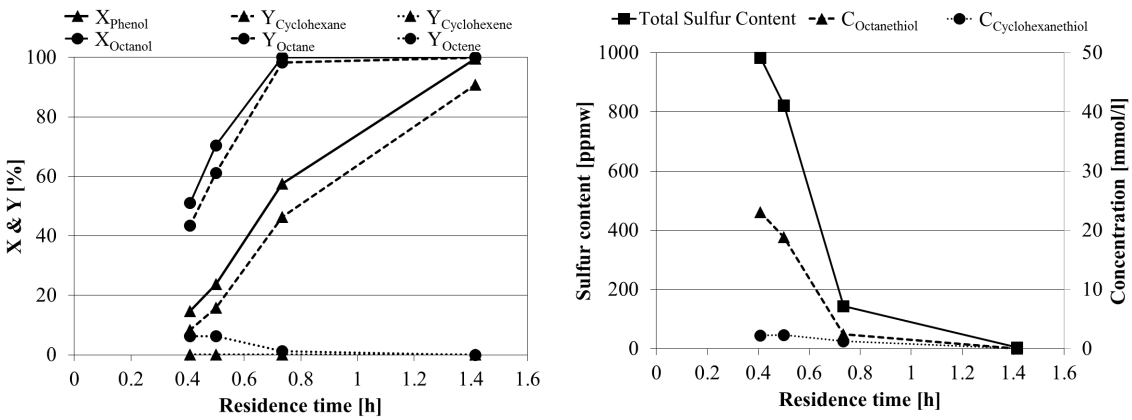

(a) Oil product distribution.

(b) Sulfur content in oil.

Figure 8.4: *Effect of the residence for HDO of 50g/l phenol and 2 vol% DMDS in 1-octanol over Ni-MoS_2/ZrO_2. (a) conversions of 1-octanol and phenol and yields of octane, octene, cyclohexane, and cyclohexene and (b) sulfur content in the liquid product. Feed: 50 g/l phenol and 2 vol% DMDS in 1-octanol, T = 280 °C, P = 100 bar.*

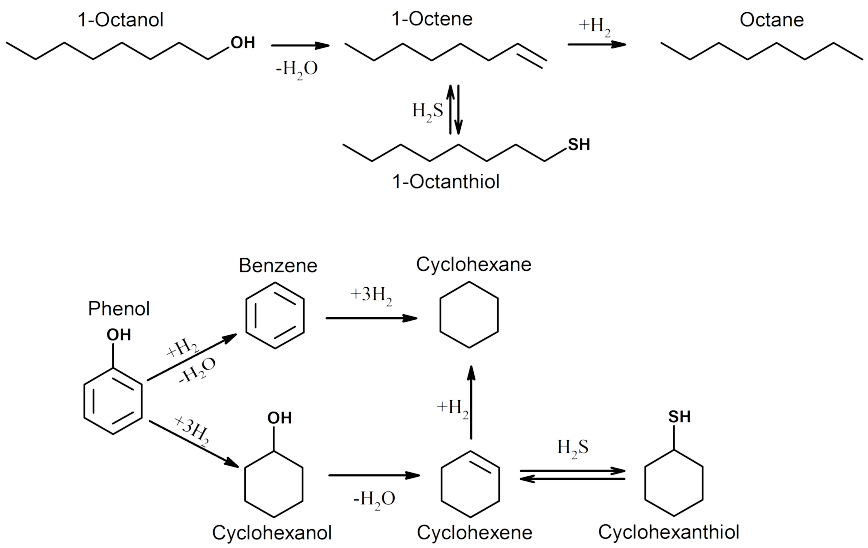

Figure 8.5: *Reaction scheme of 1-octanol and phenol over Ni-MoS_2/ZrO_2.*

spectively 3.1% and 0.8% at 0.4 h to < 0.1% at 1.4 h, as shown in Figure 8.4(b). These compounds are most likely formed by saturation of the doublebonds in 1-octene and cyclohexene with H_2S (cf. Figure 8.5), as both are present in high concentrations at the lower residence times. However, as the catalyst is widely used as HDS catalyst [107, 110, 364, 365], it also posses desulfurization capabilities and can therefore remove these thiols again. Thus, the sulfur content of the product oil ends below 5 ppm_w at the highest residence time tested in Figure 8.4(b).

In conclusion, the tendency of Ni-MoS_2 to form sulfur containing compounds can be circumvented by increasing the residence time.

8.3 The Effect of H_2O

To test the stability of the Ni-MoS_2/ZrO_2 catalyst in the presence of water, a series of experiments were carried out co-feeding water with a separate feed line. The H_2O/H_2S ratio has previously been indicated as crucial in determining the stability of sulfide catalyst in the presence of water [104, 105]. Thus, this was varied between 9.7 and 46 by changing the oil/water feed ratio and the concentration of DMDS in the oil.

Figure 8.6 shows the development in the DOD as a function of TOS for three experiments with varying H_2O/H_2S ratios; calculated in the gas phase, assuming complete conversion of DMDS to H_2S, and complete vaporization of H_2O. The highest H_2O/H_2S ratio of 46 was achieved with 33 vol% H_2O in the feed, which corresponds to a bio-oil with a high content of water (the typical water content is ca. 25 wt% [42, 63]). 2 vol% DMDS was added to the feed oil, as this was found sufficient to maintained a decent activity of the catalyst in the stability experiments in Section 8.2. In the experiment, the DOD started at 58%, but during the 96 h of TOS the catalyst lost most of its activity, ending at a DOD of 16%, i.e. a relative decrease of 74% in the DOD.

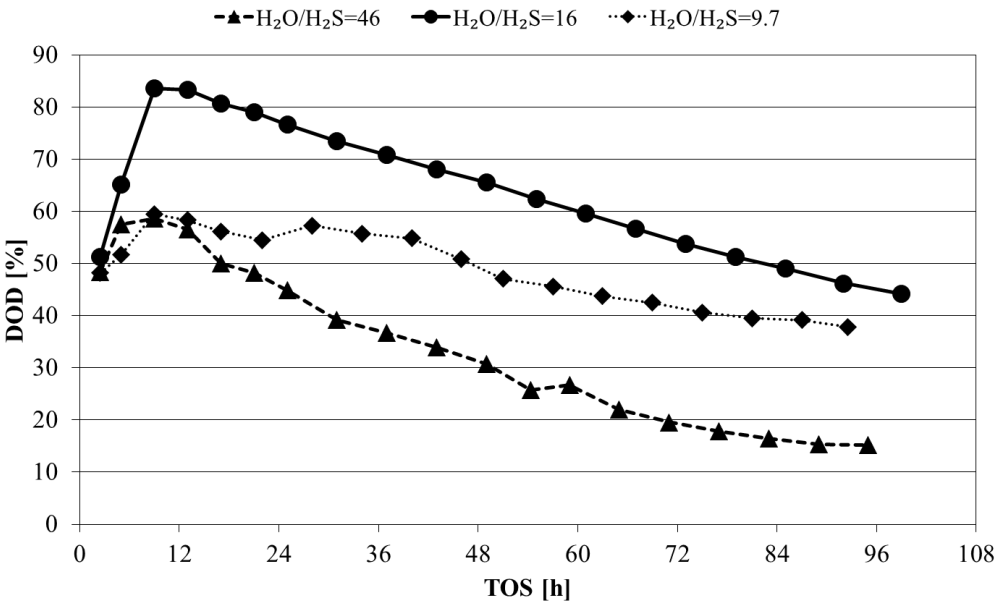

Figure 8.6: *DOD of a pheno/1-octanol feed over a Ni-MoS_2/ZrO_2 catalyst when co-feeding water. H_2O/H_2S ratio of 46: 2 vol% DMDS in feed oil, F_{oil} = 0.2 ml/min, F_{H_2O} = 0.07 ml/min, WHSV = 5.8 h^{-1}. H_2O/H_2S ratio of 16: 5 vol% DMDS in feed oil, F_{oil} = 0.2 ml/min, F_{H_2O} = 0.07 ml/min, WHSV = 3.5 h^{-1}. H_2O/H_2S ratio of 9.7: 5 vol% DMDS in feed oil, F_{oil} = 0.33 ml/min, F_{H_2O} = 0.07 ml/min, WHSV = 5.1 h^{-1}. Feed: 50 g/l phenol in 1-octanol, T = 280 °C, P = 100 bar.*

To improve the stability of the catalyst, the content of DMDS in the feed oil was increased to 5 vol% and the catalyst loading was increased, but the feed water concentration was maintained at 33 vol%, giving a H_2O/H_2S ratio of 16. This increased the stability of the catalyst somewhat, with the relative drop in the DOD now being 48%. The general higher DOD in this case compared to the H_2O/H_2S ratio of 46 case was due to the lower WHSV in this experiment.

Trying to increase the stability even further, the oil/water feed ratio was increased by increasing the oil feed rate, giving an effective water concentration of 20 vol% and H_2O/H_2S ratio of 9.7. In this case, the DOD decreased from 58% to 38% (a relative decrease of 36%) throughout the 92 h of testing. This experiment therefore displayed the best stability of the investigated cases and also indicated stabilization, as the curve seemed to level off at the end of the experiment. The increased stability is underlined by noting that the exposure of the catalyst to water was almost identical in the case with the H_2O/H_2S ratio of 16, compared to the case with 9.7.

Overall, the case with the H_2O/H_2S ratio of 9.7 had the best stability of the investigated cases, underlining the importance of controlling the H_2O/H_2S ratio. However, some concern is raised, as this case resulted in 2 mol% H_2S in the feed gas, showing the massive need of feed sulfur.

Comparing the activity in the case of co-feeding water (to simulate a real bio-oil) in Figure 8.6 to the case not co-feeding water in Figure 8.1(b), the activity decreased significantly when co-feeding water. This is consistent with previous work, where it has been shown that H_2O competes for the active sites on the MoS_2 [371]. This inhibiting effect is elaborated on in Section 8.6.

Calculating the Gibbs free energy for reactions between bulk MoS_2 and water at the given conditions (see Appendix J for elaboration), showed that ΔG is positive for all relevant reactions, indicating that oxidation of the sulfur by water should not readily take place. This was supported by quantification of the sulfur on the used catalysts, as this was similar comparing cases with H_2O/H_2S ratios varying from 0 to 46, cf. Table 8.1. Badawi et al. [104] showed by DFT calculations that it is the stability of the sulfur atoms located along the edges of the MoS_2 slabs which is important in this system. In their calculations, they found that a H_2O/H_2S ratio above 40 resulted in exchange of sulfur with oxygen (S-O exchange) along the slab edges. Comparing this to the results in Figure 8.6, revealed that this threshold appears to be even lower.

We see two paths to achieve stability in the presence of water: either addition of sufficient DMDS or recirculation of part of the hydrocarbon product to decrease the water concentration in the feed. Recirculation is probably needed for bio-oils with high water content, as 5 vol% DMDS was insufficient to maintain stability of an oil with 33 vol% water. Addition of such high levels of DMDS seems questionable.

8.4 The Effect of Potassium

To test the effect of potassium, Ni-MoS_2/ZrO_2 was impregnated with KNO_3 to a molar a ratio of K/(Ni + Mo) of 1. This catalyst was tested with a feed of 50 g/l phenol and 2 vol% DMDS in 1-octanol, i.e. similar to the experiment presented in Figure 8.1(b). The development in the DOD and the conversion of phenol and 1-octanol in this experiment are shown in Figure 8.7. The DOD rapidly stabilized at ca. 5% and remained there for the duration of the 46 h experiment. The deoxygenation only took place by converting some of the 1-octanol, with a conversion in the order of 5%. The affinity for phenol deoxygenation was practically not existing, with a conversion of <1.5%, with the primary product being octyl phenol. These reactions

probably were facilitated by the acid sites on ZrO_2, as discussed in Section 7.3 (cf. Figure 7.5).

Comparing these results to the reference case in Figure 8.1(b), the difference in the DOD was on the order of 80% lower, showing severe loss of activity of the catalyst when poisoned by potassium.

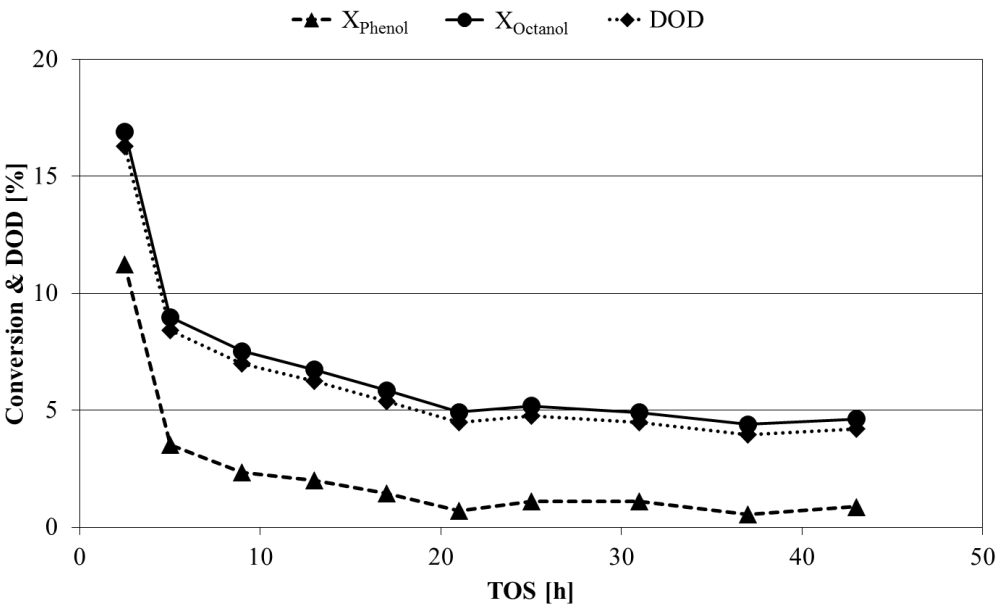

Figure 8.7: *DOD and conversions of phenol and 1-octanol during HDO over a potassium doped Ni-MoS_2/ZrO_2 catalyst. Feed: 50 g/l phenol and 2 vol% DMDS in 1-octanol, T = 280 °C, P = 100 bar, F_{oil} = 0.2 ml/min, WHSV = 4.0 h^{-1}.*

Similar, Kubicka and Horacek [375] found that the primary deactivation source of Co-MoS_2/γ-Al_2O_3 for HDO of waste rapeseed oil was deposition of alkali metals on the active sites. Andersen et al. [377] made first principle DFT calculations of potassium doped MoS_2 for CO hydrogenation. Their results showed that potassium readily binds to the edges of the MoS_2 slabs, blocking both Mo and S sites. This means that CO dissociation could not take place on the catalyst and H_2 dissociation was limited at the edges as well. Comparing this to the mechanism for HDO on MoS_2 type catalysts, the vacancy sites on the slab edges are readily blocked by potassium. Based on the DFT calculations by Andersen et al. [377], it is expected that the HDO activity will be similarly suppressed by addition of potassium.

With the experience from the nickel catalysts (cf. Chapter 6) and other combination of catalyst and reaction [378, 379], it seems difficult to find alkali tolerant catalysts. Thus, removal of this prior to HDO catalyst will probably be needed. A guard bed prior to the hydrotreating reactor has been proposed to prevent metal deposition [142, 380]. Here metals would be trapped in a porous material like alumina, bauxite, magnesium silicate, clays or similar. This will however not trap organic bound metals. Alternatively, Bridgwater [42] indicated that nearly all alkali metals can be captured in the ash fraction in the flash pyrolysis plant. Both approaches point toward preventing alkali metals reaching the catalyst.

8.5 The Effect of Chlorine

To test the effect of chlorine on the stability of the catalyst, 0.3 vol% 1-chlorooctane (corresponding to 0.05 wt% Cl) was added to a feed of 50 g/l and 2 vol% DMDS in 1-octanol, simulating a typical chlorine concentration in bio-oil [305]. Figure 8.8 shows the development in the conversion of phenol and 1-octanol and the yields of the primary products as a function of TOS. Comparing the activity in the current case to the similar case without chlorine in the feed (cf. Figure 8.1(b)), the conversion of 1-octanol dropped from ca. 91% in the chlorine free case to ca. 74% with 1-chlorooctane in the feed. However, this conversion was stable throughout the 52 h of exposure to chlorine. This indicates that chlorine is not deactivating the catalyst, but rather inhibiting the active sites. Probably, HCl will compete with the oxy-compounds for the active sites, similar to H_2O and H_2S.

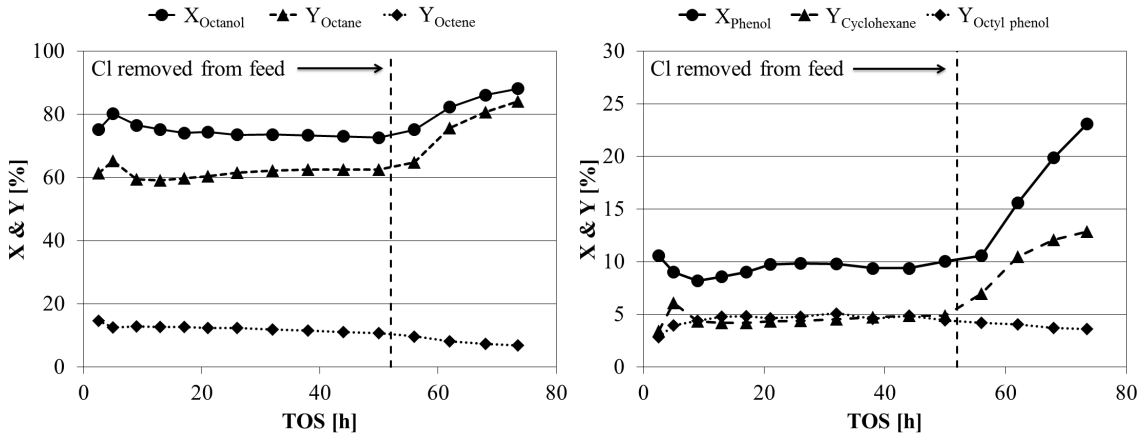

(a) Conversion and yields of 1-octanol related compounds.

(b) Conversion and yields of phenol related compounds.

Figure 8.8: *Stability of $NiMoS_2/ZrO_2$ during HDO of phenol and 1-octanol when co-feeding 1-chlorooctane, (a) shows conversion and yields of 1-octanol related compounds and (b) shows conversion and yields of phenol related compounds. The concentration of 1-chlorooctane in the feed was 0.3 vol%, corresponding to 0.05 wt% Cl. At 52 h TOS the 1-chlorooctane was removed from the feed. Feed: 50 g/l phenol and 2 vol% DMDS in 1-octanol, $T = 280\,°C$, $P = 100$ bar, $F_{oil} = 0.2$ ml/min, $WHSV = 4.0\ h^{-1}$.*

The octene/octane ratio in the oil product increased from ca. 0.06 in the chlorine free case to 0.2 when co-feeding chlorine. Thus, it appears that the chlorine inhibits hydrogenation sites more pronounced than the dehydration sites. Similar to 1-octanol, also the phenol conversion dropped when exposed to chlorine. Comparing to the chlorine free case, the conversion of phenol dropped from ca. 25% to ca. 10 % when feeding 1-chlorooctane. The drop in the phenol conversion is therefore more pronounced than that of 1-octanol. The conversion of phenol was stable throughout the exposed time frame. The higher drop in the phenol conversion compared to 1-octanol is related to the inhibiting effect on the hydrogenation sites, as the HDO of phenol partly is dependent on the hydrogenation of the aromatic ring before deoxygenation (cf. Figure 8.5).

In the experiment, the conversion of 1-chlorooctane to octene/octane and HCl was ca. 40%. Cl^- was verified in the aqueous phase product by deposition of AgCl with $AgNO_3$. 40% conversion of 1-chlorooctane in the feed containing 0.3 vol% 1-chlorooctane corresponds to a release of Cl atoms relative to Mo atoms on the catalyst in a ratio of 1.1 mol_{Cl}/mol_{Mo} after 52 h TOS. Thus, a constant exposure of Cl/HCl was present on the catalyst and sufficient to cause a potential deactivation. However, in general the exposure to chlorine for this type of catalyst appears to be limited by the activity of the HDCl reaction.

After 52 h of TOS the 1-chlorooctane was removed from the feed. At this point the activity immediately started to increase (cf. Figure 8.8), slowly rising toward the activity level of the unpoisoned catalyst (cf. Figure 8.1(b)). This proves that the chlorine is only inhibiting and not deactivating the HDO reaction on Ni-MoS_2. In the start of the experiment the chlorine inhibition was established within the first 9 h of TOS, however re-establishing the activity after removing the chlorine from the feed was a slow process in comparison, taking more than 20 h.

In summary, it appears that the presence of chlorine in the feed will cause an inhibition of the catalyst, probably by competing for the active sites. This inhibition appears to be determined by an equilibrium between the gas phase and adsorbed chlorine species. However, the chlorine inhibition appears fully reversible and is not expected to cause any major challenges for this type of catalysts, and a higher residence time would probably solve this issue.

8.6 Inhibition Strength of H_2S, H_2O, and HCl

From Section 8.2, 8.3 and 8.5, it follows that the presence of H_2S, H_2O, and/or HCl will inhibit the activity of the catalyst and especially the activity for HDO of phenol. To quantify this effect, 1st order rate constants were calculated for all experiments, as described in Eq. 3.14.

Considering the different species as inhibitors competing for the active sites on the catalyst, the 1st order rate constants can be expressed by the availability of free sites, in a Langmuir-Hinshelwood kinetic model [232, 381]:

$$k_{eff,i} = k_{0,i} \cdot \Theta_* \tag{8.1}$$

Here $k_{eff,i}$ is the effective rate constant for reaction i measured in the experiment, $k_{0,i}$ is the rate constant for reaction i of a catalyst with no inhibiting/deactivating species, and Θ_* is the fraction of free sites. If it is assumed that Θ_* only varies with the concentration of the impurity (i.e. nearly empty surface with respect to oxygenates), but otherwise is similar across the experiments, this is given by:

$$\Theta_* = 1 - \Theta_{\mathrm{H}} - \Theta_{\mathrm{SH}} - \Theta_{\mathrm{OH}} - \Theta_{\mathrm{Cl}} \tag{8.2}$$

Here Θ_H, Θ_{OH}, Θ_{SH}, and Θ_{SH} are the fractional coverage of respectively H, OH, SH and Cl on the catalyst. These coverages are determined from the reactions:

$$H_2S + 2* \rightleftharpoons H* + SH* \tag{8.3}$$
$$H_2O + 2* \rightleftharpoons H* + OH* \tag{8.4}$$
$$HCl + 2* \rightleftharpoons H* + Cl* \tag{8.5}$$
$$H_2 + 2* \rightleftharpoons 2\,H* \tag{8.6}$$

Assuming these reactions are in quasi equilibrium, the coverages of the species can be found as:

$$\Theta_i = \frac{K_i \cdot P_i}{\sqrt{K_{H_2} \cdot P_{H_2}}} \tag{8.7}$$

Here K_i is the equilibrium constant for the coverage of species i and P_i the partial pressure of i. Index i represent either H_2O, H_2S, or HCl species. Thus, Θ_* becomes:

$$\Theta_* = \frac{1}{1 + \sqrt{K_{H_2} \cdot P_{H_2}} + \frac{K_{H_2S} \cdot P_{H_2S}}{\sqrt{K_{H_2} \cdot P_{H_2}}} + \frac{K_{H_2O} \cdot P_{H_2O}}{\sqrt{K_{H_2} \cdot P_{H_2}}} + \frac{K_{HCl} \cdot P_{HCl}}{\sqrt{K_{H_2} \cdot P_{H_2}}}} \tag{8.8}$$

$K_{H_2} \cdot P_{H_2}$ was assumed constant and equal in all experiments in these calculations.

Using the two experiments with different concentrations of feed sulfur presented in Section 8.2 (see also Figure 8.1), k_0 and $K_{H_2S}/K_{H_2}^{1/2}$ were calculated. Using these two parameters for the experiment with water and chlorine, also $K_{H_2O}/K_{H_2}^{1/2}$ and $K_{HCl}/K_{H_2}^{1/2}$ were calculated, as summarized in Table 8.2. K_{H_2S} and K_{H_2O} were almost identical, differing by less than a factor of 1.5. Contrary, K_{HCl} was two orders of magnitude higher than both K_{H_2S} and K_{H_2O}. Thus, HCl was by far the worst inhibitor of the investigated species. From the analysis of Cl inhibition in Section 8.5 this strong effect of chlorine was not immediately apparent, but this was because only a limited release of chlorine was taking place due to the low affinity for HDCl, resulting in a low partial pressure of HCl in this experiment (cf. Table 8.2).

A similar analysis was not possible for the 1-octanol HDO reaction, because H_2S did not inhibit this reaction but rather promoted it, as already discussed in Section 8.2. However, comparing the rate constant in Table 8.2 for k_{Oc} shows that water and HCl both caused a significant decrease in the activity, as both were of roughly the same order of magnitude. However, considering that the partial pressure of H_2O was 3-4 orders of magnitude higher than the HCl partial pressure, it is clear that HCl is also the strongest inhibitor for this reaction.

In conclusion, the results show that the strength of inhibition of the investigated species qualitative is given as:

$$HCl > H_2O \approx H_2S \tag{8.9}$$

In a broader context, H_2S, H_2O, CO, and NH_3 are all inhibitors of sulfide catalysts as they compete for the active sites [142, 356, 371, 376]. Badawi et al. [371] found the following order of inhibition for HDO of guaiacol on MoS_2 based on DFT calculations:

$$CO > H_2S \approx H_2O \tag{8.10}$$

Table 8.2: *Kinetic data and tendency for inhibition by H_2S, H_2S, and/or HCl on a Ni-MoS_2/ZrO_2 catalyst. TOS refers to the point of evaluation in the respective experiment. k_{Ph} is the rate constant for phenol conversion k_{Oc} is the rate constant for 1-octanol conversion.*

Impurity	TOS	P_{H_2S}	P_{H_2O}	P_{HCl}	k_{Ph}	k_{Oc}	$k_{0,Ph}$	$\frac{K_{H_2S}}{K_{H_2}^{1/2}}$	$\frac{K_{H_2O}}{K_{H_2}^{1/2}}$	$\frac{K_{HCl}}{K_{H_2}^{1/2}}$
	[h]		[bar]		[ml/kg$_{cat}$/min]				[bar$^{-1/2}$]	
H_2S^a	8	0.02	0	0	65	123	67	14	-	-
H_2S^b	8	0.5	0	0	36	239	67	14	-	-
H_2O^c	9	1.9	18	0	12	91	67	14	19	-
HCl^d	26	0.5	0	0.009	8	109	67	14	-	6500

[a]See Figure 8.1(a) for further details.
[b]See Figure 8.1(b) for further details.
[c]See Figure 8.6 for further details, the experiment with the H_2O/H_2S ratio of 9.7.
[d]See Figure 8.8 for further details.

Their results also indicates H_2S and H_2O as roughly equally strong inhibitors. Laurent and Delmon [356] evaluated first order rate constants for a Ni-MoS_2/γ-Al_2O_3 catalyst and found the following order of inhibition of the hydrotreating reaction:

$$NH_3 > H_2S > H_2O \tag{8.11}$$

As a general remark, additional catalyst in the reactor would be required to treat a real bio-oil considering the many potential inhibiting species which are present during HDO, while poisons such as alkali metals should be completely avoided.

8.7 Conclusion

The stability of Ni-MoS_2/ZrO_2 has been investigated during HDO of phenol in 1-octanol, as a bio-oil model compound system. Constant addition of sulfur is essential to obtain prolonged stable operation of the catalyst and it was found that adding thiols to the feed in a concentration comparable to what can be found in bio-oil is insufficient. Instead, DMDS was found as a good sulfur source during the process, which should be added to the feed in a concentration of >1 vol%. By XRD it was found that adding insufficient sulfur resulted in a slow oxidation of the sulfide phase.

The downside of adding sulfur is that this enables incorporation of sulfur in the product, especially to unsaturated double bonds (formed from dehydration reactions) were found to willingly react with H_2S to form thiols. However, operating at sufficiently high residence times reduced the presence of thiols in the oil product as the catalyst also is effective in HDS.

Water was also capable of oxidizing the MoS_2. The results show that the H_2O/H_2S ratio is essential in determining the catalyst stability and this ratio should be <10 to obtain reasonable stability. Even lower ratios may be needed to obtained sufficient stability during prolonged operation (>100 h). While bulk MoS_2 is thermodynamically stable towards oxidation by H_2O, it is oxidation of the edge sulfur atoms which is critical in the presence of water.

Impregnation of Ni-MoS_2/ZrO_2 with KNO_3 to a molar a ratio of K/(Ni + Mo) of 1 was found to effectively decrease the activity of the catalyst. Without potassium a DOD of ca. 90% could be achieved, but adding potassium the DOD was only ca. 5%. The deactivation was caused by occupation of vacancy sites along the MoS_2 edges by potassium, blocking the active sites for HDO.

Simulating the presence of organically bound chlorine in bio-oil, it was found that Ni-MoS_2/ZrO_2 was inhibited by the presence of 1-chlorooctane in the feed. This effect was explained by competitive adsorption of the formed HCl with the oxy-compounds for the active sites. However, removing 1-chlorooctane from the feed restored the activity of the catalyst to a level similar to the un-poisoned case, showing that chlorine only inhibited the reaction.

Commonly, both H_2S, H_2O, and HCl were found to inhibit HDO of especially phenol. Competitive adsorption described by a Langmuir-Hinshelwood approach was applied to quantify the inhibition of these species. This analysis showed that HCl was by far the strongest inhibitor followed by H_2O and H_2S of roughly the same strength. However, potassium was the strongest poison, leading to complete and persistent loss of activity.

Overall, Ni-MoS_2/ZrO_2 is a prospective catalyst for HDO of phenol with promising stability, as long as sufficient sulfur is supplied. Of the investigated bio-oil impurities potassium was the worst, and prolonged operation most likely requires the removal of this compound from the feed. H_2S, H_2O, and HCl was found to primarily inhibit the catalyst. Thus, when using this catalyst high residence time is recommended to manage the inhibitors and furthermore to remove potentially formed thiols.

Chapter 9

Perspective on Real Bio-oil Upgrading

To get a final evaluation on the progress of this project in a more realistic context, a series of experiments were made with a real bio-oil feed. These experiments are described in detail in Appendix K and the results make the foundation for the following discussion. The results were not included in this main part of the thesis as they were used to evaluate and put the current work into perspective, but did not have sufficient quantitative value.

Upgrading of real bio-oil compared to model compounds is markedly more difficult. In contrast to the model compound studies in Chapter 6-8, during real bio-oil HDO the catalyst is exposed to many deactivation sources simultaneously. Among these, carbon deposition is a severe problem when working with real bio-oil, in contrast to the model compounds. This carbon deposition additionally appears to be closely linked to the overall activity of the catalyst and the operating temperature. High temperature (>150 °C) alone will result in a polymerization of the bio-oil to tar/coke, which results in reactor plugging. Thus, if a catalyst is severely deactivated (or not sufficiently active), this is the only reaction which will take place. This was observed in experiments with both Ni/ZrO_2 and $Ni\text{-}MoS_2/ZrO_2$ (cf. Appendix K). Additionally, it should be considered that carbon deposition alone will also lead to deactivation and this phenomenon is therefore self-accelerating.

From the work described in Appendix K it was found that treating the bio-oil directly at high temperatures is difficult due to the coke forming reactions. A potential solution could be to have a graduated temperature profile in the reactive zone, meaning that catalyst should be present in the entire length of the reactor and therefore also present during heating. This should convert some of the most reactive components in the initial part of the reactor where the temperature is low, and these would then be less prone for coke formation (in line with the discussion in Section 2.4). The results in Appendix K indicated that a graduated temperature profile can increase the lifetime of the catalytic bed.

In line with the analysis in Chapter 6 and 8 for Ni/ZrO_2 and $Ni\text{-}MoS_2/ZrO_2$, respectively, neither of these catalysts were efficient for HDO of real bio-oil, as they were readily deactivated. The carbon formation adds additional issues to this, which has received little attention in the current work.

Using Haldor Topsøe A/S's commercial HDS catalyst ($Ni\text{-}MoS_2/Al_2O_3$) as reference, revealed that this was a much better catalyst for HDO of real bio-oil. The better activity of the commercial catalyst gave better stability. However, also this

catalyst deactivated over time, with the DOD decreasing from 100% to 69% over 12 h of operation. Figure 9.1 shows the appearance of the oil product from the experiment with this catalyst and the DOD as a function of TOS. The initial oil product was a clear and free flowing liquid, which by analysis by CHN-S and GC-MS was found to have a DOD of 100 % and H/C ratio of 2.1 and primarily consisting of naphtenes (in the order of 65%) and linear/branched hydrocarbons (in the order of 25%). Thus, this oil product was very similar to crude oil (cf. Table 2.7).

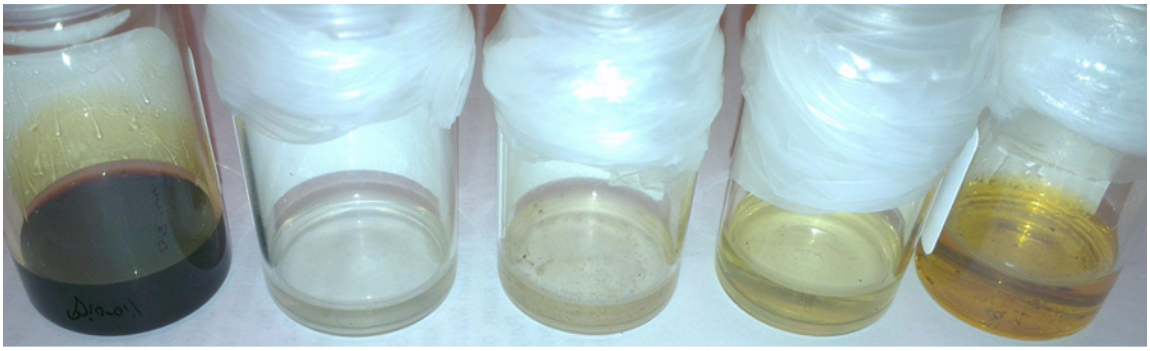

Bio-oil feed	TOS = 4-6 h DOD = 100% H/C = 2.1	TOS = 6-8 h DOD = 90% H/C = 2.1	TOS = 8-10 h DOD = 88% H/C = 2.0	TOS = 10-12 h DOD = 69% H/C = 1.9

Figure 9.1: *Oil product from HDO of 50% bio-oil in 2-butanol over a commercial Ni-MoS_2/Al_2O_3 catalyst as a function of TOS. T = 300 °C, P = 100 bar, F_{oil} = 0.2 ml/min, $WHSV_{total}$ = 0.9 h^{-1}.*

It is possible to upgrade bio-oil to fuel grade standard (cf. Figure 9.1), however, deactivation is fast. Which deactivation mechanism is the primary, cannot be deduced from the few experiment made so far, but probably a combination of several are occurring. Activity and stability additionally appears to be closely related, at least it is indicated that low activity results in accelerated deactivation. Thus, a lot can be gained by directing efforts in developing a single catalytic system, like optimizing loading, particle size, application of additives, etc.

Overall, it is apparent that deactivation is a major problem and a lot of work will be needed in catalyst development to find active and stable HDO catalysts. Achieving stable and long living HDO systems will require development of catalysts but also reactor design. It appears that a lot can be gained by having a graduated temperature profile of the reactive zone and this is suggested to be addressed in future work.

Chapter 10

Conclusions & Outlook

The combination of flash pyrolysis and catalytic upgrading to engine fuels is a prospective route to biofuels in the future. By densification of the biomass in the pyrolysis process, transport economy is significantly improved over conventional biomass when the flash pyrolysis unit is placed close to the biomass source. The subsequent upgrading can be facilitated by either zeolite cracking or HDO. Of these HDO appears as the most feasible approach, as zeolite cracking is stoichiometrically limited in hydrogen availability and therefore will produce a poor fuel in low yields. In addition, HDO of bio-oil can produce high quality fuels applicable in the current infrastructure, at a price which could be competitive to conventional petrochemical fuels. This process has been the main focus of the research work in this project. Major challenges in this field are to find an active catalyst which also has sufficient stability during operation, since coke deposition and deactivation by impurities in the bio-oil are problematic.

In an attempt to find a new HDO catalyst, screening of 23 catalytic systems for HDO of phenol was performed in a batch reactor at 275 °C and 100 bar of H_2. Four groups of catalysts were tested: oxide catalysts, methanol synthesis catalysts, reduced noble metal catalysts, and non-noble reduced metal catalysts. The investigated oxide catalysts and methanol synthesis catalysts were inactive at the applied conditions. Of the noble metals, Ru/C performed the best, but Pd/C and Pt/C also displayed activity for HDO. Among the non-noble metal catalysts only nickel had good activity. Nickel was also tested in combination with different supports, elucidating that the hydrogenation activity of this type of catalyst was closely linked to the supports affinity for generation of oxygen vacancy sites. These sites function as Lewis acid sites facilitating the adsorption of phenol. Overall Ru/C and Ni/ZrO_2 were the best performing catalysts, with Ni/ZrO_2 being most attractive due to the lower cost of this catalyst.

Another important aspect for the reduced metal catalysts was the metal particle size. Increasing the nickel particle size of Ni/SiO_2 increased the hydrogenation rate of phenol, but decreased the deoxygenation rate. Applying surface site population theory revealed that the deoxygenation TOF scaled with the availability of step and corner sites and these low coordinated sites were therefore facilitating the deoxygenation reaction. On the other hand, the hydrogenation reaction appeared hindered at small nickel particles by competitive adsorption, where hydrogen was partly depleted from the nickel surface due to species such as cyclohexanol, water, etc. However, the

support was found to influence the hydrogenation rate stronger than this size effect. Thus, a good nickel catalyst should have small (<10 nm) nickel particles to facilitate deoxygenation and an oxidic support that promotes hydrogenation (high availability of Lewis acid sites).

Ultimately, the catalyst development work pointed toward Ni/ZrO_2 prepared with small (<10 nm) nickel particles as a good catalyst for HDO, which should display both good hydrogenation and deoxygenation activity. This catalyst was tested in a high pressure liquid and gas continuous flow fixed bed setup at 250 °C and 100 bar of H_2 with a bio-oil model system of guaiacol in 1-octanol. The catalyst had good stability when treating the pure bio-oil model system, where only minor deactivation was observed over more than 100 h of operation due to buildup of coke. However, exposing the catalyst to sulfur, chlorine, or potassium all led to severe deactivation. Sulfur was the worst case, as exposure to this resulted in complete loss of activity due to formation of NiS_x as realized through XRD, XAS, and STEM-EDX. Chlorine caused reversible deactivation which decreased the deoxygenation activity as long as the chlorine source was present in the feed. Potassium caused persistent deactivation of the low coordinated sites, and thereby hampered the deoxygenation activity. Overall it was identified that nickel based catalysts readily could be deactivated by many of the impurities found in real bio-oil.

In an attempt to find a more stable HDO catalyst, Mo_2C/ZrO_2 was investigated in the continuous flow setup at 300 °C and 100 bar with a bio-oil model feed of phenol in 1-octanol. In contrast to the reduced metal catalysts, this catalyst was very selective in the direct deoxygenation reaction, selectively producing benzene from phenol. Thus, this catalyst was not dependent on initial hydrogenation of phenol, as observed for the nickel based catalysts. However, co-feeding water, which is inevitably present in bio-oil, resulted in effective oxidation of the carbide phase, completely deactivating the catalyst over 14 h of operation. Without water in the feed the catalyst deactivated slower, but the water formed from HDO was still sufficient to oxidize the carbide phase. The oxidation potential of water towards this catalyst was additionally confirmed by thermodynamic calculations and in situ XRD measurements. Overall Mo_2C/ZrO_2 was not found suitable for HDO as water must be considered unavoidable during HDO of bio-oil.

Realizing that good stability of HDO catalysts was difficult to achieve due to deactivation by impurities, the conventional hydrotreating catalyst, $Ni\text{-}MoS_2$, was investigated. This catalyst relied on a co-feed of sulfur to maintain the active phase. The presence of sulfur unfortunately also resulted in formation of sulfur compounds in the product if the residence time was not kept sufficiently high. This catalyst was more tolerant toward both water and chlorine than the nickel and Mo_2C catalysts. However, co-feeding sufficient sulfur was required to avoid oxidation of the edge sulfur atoms by water. Despite not causing deactivation, HCl, H_2O, and H_2S were all inhibiting the HDO reaction by competing for the active sites, with the strength of inhibition decreasing in that order. Contrary, potassium completely deactivated the catalyst, probably by blocking of the edge sites of the MoS_2 and was concluded as the worst of the investigated bio-oil impurities.

Comparing the investigated catalytic systems, $Ni\text{-}MoS_2/ZrO_2$ showed the best resistance toward impurities, but Ni/ZrO_2 was an attractive reduced metal catalyst

due to its high activity (active at only 250 °C) and low price (compared to noble metals). Some general trends were identified for the different types of impurities. Potassium appears as a general cause for deactivation, which will block active sites on many, if not all, types of catalysts relevant for this reaction. Thus, in a larger view potassium should probably be removed from the bio-oil either through proper removal in the ash fraction in the pyrolysis or adsorption prior to the catalyst bed.

Chlorine appears only to be an inhibitor, for both reduced metals and sulfides. It is desirable to keep the concentration of this low, but if it enters the catalytic reactor it is less detrimental to the catalyst than most other impurities.

The high concentrations of water present in bio-oil result in a problematic oxidizing potential. Thermodynamics was found to be an important tool in evaluating the stability of the catalysts, but the lower stability of nano-particles will in many instances require the use of DFT calculations to get a good estimate of the stability of single particles or surfaces.

Comparing the two best performing catalysts of the investigated, Ni-MoS_2/ZrO_2 and Ni/ZrO_2, Ni-MoS_2/ZrO_2 appears as the best performing catalyst, when considering stability in the presence of potential impurities from bio-oil. However, use of this catalyst was not straightforward and severe deactivation/inhibition did occur if not operated properly.

However, testing a real bio-oil did indicate that the higher temperature requirement of Ni-MoS_2/ZrO_2 compared to Ni/ZrO_2 resulted in increased formation of carbon and a tendency for plugging of the catalyst bed. These tests additionally showed the importance of finding stable catalysts, as the tendency for carbon formation, and thereby reactor plugging, appeared to increase with decreasing activity. When the activity of the catalyst decreases below a certain level, it appears that the carbon formation is accelerated due to a larger potential for polymerizing like reactions in the bio-oil.

As overall conclusion on this project, it appears that finding a sufficiently stable catalyst for HDO of bio-oil is the biggest challenge of the process. This task is challenged by the many sources of deactivation in the bio-oil. Impurities as sulfur, chlorine, alkali metals, and similar can cause loss of the catalyst's active sites. Additionally carbon is also a source of deactivation, but even more pronounced as a source of reactor plugging. Carbon formation appears closely linked to the activity of the catalysts, as it is indicated that this phenomenon is accelerated as a function of catalyst deactivation, probably parallel to a decrease in the hydrogenating sites.

10.1 Future Work

Looking ahead a lot of work is still needed to find a suitable catalyst for HDO. So far catalyst development has been with origin in already established knowledge from conventional hydrotreating technology and simple trial an error screening studies, as done in Chapter 4, as example. To direct the effort further, the field could benefit from DFT calculations, where screening of larger amounts of catalysts in less time is possible. The group of Studt and Nørskov has already started some work in this field with transition metal catalysts. However, as realized from this work, the use of catalysts are limited due to deactivation by impurities. More novel catalytic systems might be needed for the HDO process as already indicated with the phosphide

catalysts which have received increasing attention in the recent years [128, 382, 383] and the oxide catalysts as investigated in Chapter 4 and by Prasomsri et al. [247]. Such catalysts are however much more difficult to screen through DFT methods, indicating that this is an area requiring substantial work. Additionally, much work is also needed in more detailed development of single catalytic systems, like optimizing loading, preparation method, particle size, application of additives, etc., which has not been the focus of the work in this project. In comparison, industrial HDS catalysts have been refined over many decades.

Aspects of coke deposition have only vaguely been investigated in this work, but is a major problem for this process as discussed in Section 2.4.3. Model compound studies can help to investigate which classes of molecules are prone to coking and may also give indications of which initiatives are needed to circumvent it. However, to get the full understanding of carbon deposition, use of real bio-oil appears necessary to provide safe answers. HDO pretreatment at less severe conditions appears necessary for the real bio-oil, as heating of the bio-oil to a temperature of 300 °C (as required for Ni-MoS_2/ZrO_2) can be a problem on its own. The dual bed approach could be a solution [15, 22, 170, 384] or a graduated temperature profile in the reactive zone, as discussed in Chapter 9 and Appendix K. This also points toward a general need for understanding how to work with real bio-oil in different scales. With a maximum operation time of a single catalyst bed for HDO of real bio-oil still reported in the order of 100-200 h [57, 76, 184], this should serve as the benchmark for further improvement. Engineering tasks such as evaluating the proper design of (pilot) plants and optimal operating conditions are therefore needed, where plugging of both up- and down-stream sections due to oil/tars and reactor plugging due to coke are problems to be solved. It appears that part of the solution could be development of a low temperature catalyst, and in this context Ni/ZrO_2 appears more suitable than Ni-MoS_2/ZrO_2.

Besides deactivation by coke, also the field of bio-oil impurities is an area requiring significant work, as highlighted in this thesis. It appears that every catalytic system considered for HDO of bio-oil should be investigated for stability in the presence of sulfur, alkali metals, chlorine, and water, at least. Additionally, also phosphorous and nitrogen species could be thought to interfere with the catalysts. Alternatively, it could be beneficial to investigate how these compounds can be (partly) removed from the bio-oil. Trapping of the inorganic part in the ash in the pyrolysis section or pretreatment prior to the HDO reactor could be paths worth elucidating.

Summarizing, future work on HDO catalyst development should aim at a catalyst sufficiently active for the HDO reaction, but simultaneously resistant toward impurities and coke formation. This should ideally be solved in a combination of DFT calculations to direct the effort in catalyst development, chemical formulation of suitable catalysts, and chemical engineering research to ensure the most smooth upgrading of the bio-oil.

Bibliography

[1] P. M. Mortensen, J.-D. Grunwaldt, P. A. Jensen, K. G. Knudsen, and A. D. Jensen. A review of catalytic upgrading of bio-oil to engine fuels. *Appl. Catal. A: Gen.*, 407:1–19, 2011.

[2] P. M. Mortensen, J.-D. Grunwaldt, P. A. Jensen, and A. D. Jensen. Screening of catalysts for hydrodeoxygenation of phenol as a model compound for bio-oil. *ACS Catal.*, 3:1774–1785, 2013.

[3] U. S. energy information administration independent statistics and analysis, February 2010. `http://www.eia.doe.gov/`.

[4] United nations department of economic and social affairs, February 2010. `http://www.un.org/esa/population/`.

[5] B. van Ruijven and D. P. van Vuuren. Oil and natural gas prices and greenhouse gas emision mitigration. *Energ. Policy*, 37:4797–4808, 2009.

[6] M. Balat. Production of bioethanol from lignocellulosic materials via the biochemical pathway: A review. *Energ. Convers. Manage.*, 52:858–875, 2011.

[7] T. Werpy, G. Petersen, A. Aden, J. Bozell, J. E. Holladay, J. White, A. Manheim, D. C. Elliott, L. Lasure, and S. Jones. Top value added chemicals from biomass. volume 1- results of screening for potential candidates from sugar and synthesis gas. Technical report, Department of Energy, 2004.

[8] S. Sorrell, J. Speirs, R. Bentley, A. Brandt, and R. Miller. Global oil depletion: a review of the evidence. *Energ. Policy*, 38:5290–5295, 2010.

[9] R.K. Pachauri and A. Reisinger, (Eds.). Climate change 2007: Synthesis report. Contribution of working groups I, II and III to the fourth assessment report of the intergovernmental panel on climate change. Technical report, Intergovernmental Panel on Climate Change, 2007.

[10] S. Joussaume, J. Penner, and F. Tangang. Working group contribution to the IPCC fifth assessment report climate change 2013: The physical science basis. Technical report, Intergovernmental Panel on Climate Change, 2013.

[11] A. Roedl. Production and energetic utilization of wood from short rotation coppice - a life cycle assessment. *Int. J. Life Cycle Assess.*, 15:567–578, 2010.

[12] BP statistical review of World energy, October 2010.

[13] M. F. Demirbas. Competitive liquid biofuels from biomass. *Appl. Energ.*, 88:17–28, 2011.

[14] J. Holmgren, R. Marinageli, P. Nair, D. C. Elliott, and R. Bain. Consider upgrading pyrolysis oils into renewable fuels. *Hydrocarb. Process.*, pages 95–103, 2008.

[15] R. H. Venderbosch, A. R. Ardiyanti, J. Wildschut, A. Oasmaa, and H. J. Heeres. Stabilization of biomass-derived pyrolysis oils. *J. Chem. Technol. Biot.*, 85:674–686, 2010.

[16] H. Wenzel. Breaking the biomass bottleneck of the fossil free society. Technical report, Concito, 2010.

[17] P. McKendry. Energy production from biomass (part 1): Overview of biomass. *Bioresource Technol.*, 83:37–46, 2002.

[18] R. L. Naylor, A. J. Liska, M. B. Burke, W. P. Falcon, J. C. Gaskell, S. D. Rozelle, and K. G. Cassman. The ripple effect: Biofuels, food security, and the environment. *Environment*, 49:30–43, 2007.

[19] J. Fargione, J. Hill, D. Tilman, S. Polasky, and P. Hawthorne. Land clearing and the biofuel carbon debt. *Science*, 319:1235–1238, 2008.

[20] S. N. Naik, V. V. Goud, P. K. Rout, and A. K. Dalai. Production of first and second generation biofuels: A comprehensive review. *Renew. Sust. Energ. Rev.*, 14:578–597, 2010.

[21] R. E. H. Sims, W. Mabee, J. N. Saddler, and M. Taylor. An overview of second generation biofuel technologies. *Bioresource Technol.*, 101:1570–1580, 2010.

[22] S. B. Jones, C. Valkenburg, C. W. Walton, D. C. Elliott, J. E. Holladay, D. J. Stevens, C. Kinchin, and S. Czernik. *Production of Gasoline and Diesel from Biomass via Fast Pyrolysis, Hydrotreating and Hydrocracking: a Design Case.* U. S. Department of Energy, February 2009. PNNL-18284.

[23] P. L. Spath and D. C. Dayton. Preliminary screening - technical and economic assessment of synthesis gas to fuels and chemicals with emphasis on the potential for biomass-derived syngas. Technical report, National Renewable Energy Lab., Golden, CO. (US), 2003.

[24] P. L. Spath, M. K. Mann, and W. A. Amos. Update of hydrogen from biomass - determination of the delivered cost of hydrogen. Technical report, U.S. Department of Energy's Hydrogen Program, 2003.

[25] B. Dawson and M. Spannagle. *The Complete Guide to Climate Change.* Routledge: Swansea, 2009.

[26] U. S. energy information administration independent statistics, April 2011. `http://www.eia.doe.gov/oog/info/gdu/gasdiesel.asp`.

[27] Oil-price.net, April 2011. http://www.oil-price.net/.

[28] M. J. A. Tijmensen, A. P. C. Faaij, C. N. Hamelinck, and M. R. M. van Hardeveld. Exploration of the possibilities for production of Fischer Tropsch liquids and power via biomass gasification. *Biomass Bioeng.*, 23:129–152, 2002.

[29] G. W. Huber, S. Iborra, and A. Corma. Synthesis of transportation fuels from biomass: Chemistry, catalysts, and engineering. *Chem. Rev.*, 106:4044–4098, 2006.

[30] K. Göransson, U. Söderlind, J. He, and W. Zhang. Review of syngas production via biomass DFBGs. *Renew. Sust. Energ. Rev.*, 15:482–492, 2011.

[31] T. Damartzis and A. Zabaniotou. Thermochemical conversion of biomass to second generation biofuels through integrated process design - a review. *Renew. Sust. Energ. Rev.*, 15:366–378, 2011.

[32] J. M. Christensen, P. M. Mortensen, R. Trane, P. A. Jensen, and A. D. Jensen. Effects of H_2 and process conditions in the synthesis of mixed alcohols from syngas over alkali promoted cobalt-molybdenum sulfide. *Appl. Catal. A: Gen.*, 366:29–43, 2009.

[33] J. M. Christensen, P. A. Jensen, N. C. Schiødt, and A. D. Jensen. Coupling of alcohols over alkali-promoted cobalt-molybdenum sulfide. *ChemCatChem*, 2:523–526, 2010.

[34] M. Stöcker. Methanol-to-hydrocarbons: catalytic materials and their behavior. *Micropor. Mesopor. Mat.*, 29:3–48, 1999.

[35] F. J. Keil. Methanol-to-hydrocarbons: process technology. *Micropor. Mesopor. Mat.*, 29:49–66, 1999.

[36] P. Grange, E. Laurent, R. Maggi, A. Centeno, and B. Delmon. Hydrotreatment of pyrolysis oils from biomass: reactivity of the various categories of oxygenated compounds and preliminary techno-economical study. *Catal. Today*, 29:297–301, 1996.

[37] J. G. Rogers and J. G. Brammer. Analysis of transport costs for energy crops for use in biomass pyrolysis plant networks. *Biomass Bioeng.*, 33:1367–1375, 2009.

[38] C. Perego and A. Bosetti. Biomass to fuels: The role of zeolite and mesoporous materials. *Micropor. Mesopor. Mat.*, 144:28–39, 2011.

[39] D. C. Elliott. Historical development in hydroprocessing bio-oils. *Energy Fuels*, 21:1792–1815, 2007.

[40] E. Furimsky. Review: Catalytic hydrodeoxygenation. *Appl. Catal. A: Gen.*, 199:144–190, 2000.

[41] Q. Zhang, J. Chang, T. Wang, and Y. Xu. Review of biomass pyrolysis oil properties and upgrading research. *Energ. Convers. Manage.*, 48:87–92, 2007.

[42] A. V. Bridgwater. Review of fast pyrolysis of biomass and product upgrading. *Biomass Bioeng.*, 38:68–94, 2012.

[43] S. Czernik and A. V. Bridgwater. Overview of applications of biomass fast pyrolysis oil. *Energy Fuels*, 18:590–598, 2004.

[44] R. H. Venderbosch and W. Prins. Fast pyrolysis technology development. *Biofuels, Bioprod. Biorefin.*, 4:178–208, 2010.

[45] D. Mohan, C. U. Pittman, and P. H. Steele. Pyrolysis of wood/biomass for bio-oil: A critical review. *Energy Fuels*, 20:848–889, 2006.

[46] D. C. Elliott, E. G. Baker, D. Beckman, Y. Solantausta, V. Tolenhiemo, S.B. Gevert, C. Hörnell, A. Östman, and B. Kjellström. Technoeconomic assessment of direct biomass liquefaction to transportation fuels. *Biomass*, 22:251–269, 1990.

[47] A. V. Bridgwater, S. Czernik, J. Diebold, D. Meier, A. Oasmaa, C. Peakocke, J. Piskorz, and D. Radlein. *Fast Pyrolysis of Biomass: A Handbook.* CPL Press: Newbury, 1999.

[48] J. M. Moffatt and R. P. Overend. Direct liquefaction of wood through solvolysis and catalytic hydrodeoxygenation: an engineering assessment. *Biomass*, 7:99–123, 1985.

[49] A. Demirbas. Mechanisms of liquefaction and pyrolysis reactions of biomass. *Energ. Convers. Manage.*, 41:633–646, 2000.

[50] J. Akhtar and N. A. S. Amin. A review on process conditions for optimum bio-oil yield in hydrothermal liquefaction of biomass. *Renew. Sust. Energ. Rev.*, 15:1615–1624, 2011.

[51] A. A. Peterson, F. Vogel, R. P. Lachance, M. Froling, M. J. Antal, and J. W. Tester. Thermochemical biofuel production in hydrothermal media: A review of sub- and supercritical water technologies. *Energy Environ. Sci.*, 1:32–65, 2008.

[52] T. Bridgwater. Review. biomass for energy. *J. Sci. Food. Agr.*, 86:1755–1768, 2006.

[53] P. C. Badger and P. Fransham. Use of mobile fast pyrolysis plants to densify biomass and reduce biomass handling costs - a preliminary assessment. *Biomass Bioeng.*, 30:321–325, 2006.

[54] K. Raffelt, E. Henrich, A. Koegel, R. Stahl, J. Steinhardt, and F. Weirich. The BTL2 process of biomass utilization entrained-flow gasification of pyrolyzed biomass slurries. *Appl. Biochem. Biotech.*, 129:153–164, 2006.

[55] S. Yaman. Pyrolysis of biomass to produce fuels and chemical feedstocks. *Energ. Convers. Manage.*, 45:651–671, 2004.

[56] A. Demirbas, M. Balat, and H. Balat. Biowaste-to-biofuels. *Energ. Convers. Manage.*, 52:1815–1828, 2011.

[57] A. V. Bridgwater. Production of high grade fuels and chemicals from catalytic pyrolysis of biomass. *Catal. Today*, 29:285–295, 1996.

[58] H. B. Goyal, D. Seal, and R. C. Saxena. Bio-fuels from thermochemical conversion of renewable resources: A review. *Renew. Sust. Energ. Rev.*, 12:504–517, 2008.

[59] C. A. Mullen, A. A. Boateng, N. M. Goldberg, I. M. Lima, D. A. Laird, and K. B. Hicks. Bio-oil and bio-char production from corn cobs and stover by fast pyrolysis. *Biomass Bioeng.*, 34:67–74, 2010.

[60] A. Oasmaa and E. Kuoppala. Fast pyrolysis of foresty residue. 3: storage stability of liquid fuel. *Energy Fuels*, 17:1075–1084, 2003.

[61] A. Oasmaa and D. Meier. Norms and standards for fast pyrolysis liquids 1. round robin test. *J. Anal. Appl. Pyrolysis*, 73:323–334, 2005.

[62] A. V. Bridgwater, S. Czernik, and J. Piskorz. *Progress in Thermochemical Biomass Conversion*, chapter - An overview of Fast Pyrolysis, pages 977–997. Blackwell Wissenschafts-Verlag: Berlin, 2001.

[63] D. Meier, B. van de Beld, A. V. Bridgwater, D. C. Elliott, A. Oasmaa, and F. Preto. State-of-the-art of fast pyrolysis in IEA bioenergy member countries. *Renew. Sust. Energ. Rev.*, 20:619–641, 2013.

[64] L. Qiang, L. Wen-Zhi, and Z. Xi-Feng. Overview of fuel properties of biomass fast pyrolysis oils. *Energ. Convers. Manage.*, 50:1376–1383, 2009.

[65] A. Oasmaa, D. C. Elliott, and J. Korhonen. Acidity of biomass fast pyrolysis bio-oils. *Energy Fuels*, 24:6548–6554, 2010.

[66] M. E. Boucher, A. Chaala, H. Pakdel, and C. Roy. Bio-oils obtained by vacuum pyrolysis of softwood bark as a liquid fuel for gas turbines. part II: Stability and ageing of bio-oil and its blends with methanol and a pyrolytic aqueous phase. *Biomass Bioeng.*, 19:351–361, 2000.

[67] J. D. Adjaye, R. K. Sharma, and N. N. Bakhshi. Characterization and stability analysis of wood-derived bio-oil. *Fuel Process. Technol.*, 31:214–256, 1992.

[68] J. Wildschut, F. H. Mahfud, R. H. Venderbosch, and H. J. Heeres. Hydrotreatment of fast pyrolysis oil using heterogeneous noble-metal catalysts. *Ind. Eng. Chem. Res.*, 48:10324–10334, 2009.

[69] J. D. Adjaye and N. N. Bakhshi. Catalytic conversion of a biomass-derived oil to fuels and chemicals I: Model compound studies and reaction pathways. *Biomass Bioeng.*, 8:131–149, 1995.

[70] J. D. Adjaye and N. N. Bakhshi. Production of hydrocarbons by catalytic upgrading of a fast pyrolysis bio-oil. part II: Comparative catalyst performance and reaction pathways. *Fuel Process. Technol.*, 45:161–183, 1995.

[71] I. Barin. *Thermochemical Data of Pure Substances.* VCH: Weinheim, 1989.

[72] F. E. Massoth, P. Politzer, M. C. Concha, J. S. Murray, J. Jakowski, and J. Simons. Catalytic hydrodeoxygenation of methyl-substituted phenols: correlations of kinetics parameters with molecular properties. *J. Phys. Chem. B*, 110:14283–14291, 2006.

[73] Y. Yunquan, L. He'an, T. Gangsheng, K. J. Smith, and T. C. Thian. Hydrodeoxygenation of phenolic model compounds over MoS_2 catalysts with different structures. *Chin. J. Chem. Eng.*, 16:733–739, 2008.

[74] W. Baldauf, U. Balfanz, and M. Rupp. Upgrading of flash pyrolysis oil and utilization in refineries. *Biomass Bioeng.*, 7:237–244, 1994.

[75] Y. E. Sheu, R. G. Anthony, and E. J. Soltes. Kinetic studies of upgrading pine pyrolysis oil by hydrotreatment. *Fuel Process. Technol.*, 19:31–50, 1988.

[76] D. C. Elliott, T. R. Hart, G. G. Neuenschwander, L. J. Rotness, and A. H. Zacher. Catalytic hydroprocessing of biomass fast pyrolysis bio-oil to produce hydrocarbon products. *Environ. Prog.*, 28:441–449, 2009.

[77] A. Gutierrez, R. K. Kaila, M. L. Honkela, R. Slioor, and A. O. I. Krause. Hydrodeoxygenation of guaiacol on noble metal catalysts. *Catal. Today*, 147:239–246, 2009.

[78] X. Guo, Y. Yan, and T. Li. Influence of catalyst type and regeneration on upgrading of crude bio-oil through catalytical thermal cracking. *Chin. J. Chem. Eng.*, 4:53–58, 2004.

[79] J. D. Adjaye and N. N. Bakhshi. Production of hydrocarbons by catalytic upgrading of a fast pyrolysis bio-oil. part I: Conversion over various catalysts. *Fuel Process. Technol.*, 45:161–183, 1995.

[80] P. T. Williams and P. A. Horne. Characterisation of oils from fluidised bed pyrolysis of biomass with zeolite catalyst upgrading. *Biomass Bioeng.*, 7:223–236, 1994.

[81] S. P. R. Katikaneni, J. D. Adjaye, and N. N. Bakhshi. Performance of aluminophosphate molecular sieve catalysts for the production of hydrocarbons from wood-derived and vegetable oils. *Energy Fuels*, 9:1065–1078, 1995.

[82] A. Corma and G. W. Huber. Synergies between bio- and oil refineries for the production of fuel from biomass. *Angew. Chem. Int. Ed.*, 46:7184–7201, 2007.

[83] A. V. Bridgwater. Catalysis in thermal biomass conversion. *Appl. Catal. A: Gen.*, 116:5–47, 1994.

[84] J. Wildschut. *Pyrolysis Oil Upgrading to Transportation Fuels by Catalytic Hydrotreatment*. PhD thesis, Rijksuniversiteit Groningen, 2009.

[85] F. de Miguel Mercader, M. J. Groeneveld, S. R. A. Kersten, N. W. J. Way, C. J. Schaverien, and J. A. Hogendoorn. Production of advanced biofuels: Co-processing of upgraded pyrolysis oil in standard refinery units. *Appl. Catal. B: Environ.*, 96:57–66, 2010.

[86] M. J. McCall and T. A. Brandvold. Us 2009/0253948 a1, 2009. Fuel and fuel blending components from biomass derived pyrolysis oil.

[87] A. Daudin, L. Bournay, and T. Chapus. Us 2010/0163458 a1, 2010. Method for converting effluents of renewable origin into fuel of excellent quality by using a molybdenum-based catalyst.

[88] K. C. Kwon, H. Mayfield, T. Marolla, B. Nichols, and M. Mashburn. Catalytic deoxygenation of liquid biomass for hydrocarbon fuels. *Renew. Energ.*, 36:907–915, 2011.

[89] J. Gagnon and S. Kaliaguine. Catalytic hydrotreatment of vacuum pyrolysis oils from wood. *Ind. Eng. Chem. Res.*, 27:1783–1788, 1988.

[90] Z. Su-Ping, Y. Yong-Jie, R. Zhengwei, and L. Tingchen. Study of hydrodeoxygenation of bio-oil from the fast pyrolysis of biomass. *Energ. Source*, 25:57–65, 2003.

[91] A. Oasmaa, E. Kuoppala, A. R. Ardiyanti, R. H. Venderbosch, and H. J. Heeres. Characterization of hydrotreated fast pyrolysis liquids. *Energy Fuels*, 24:5264–5272, 2010.

[92] M. C. Samolada, W. Baldauf, and I. A. Vasalos. Production of bio-gasoline by upgrading biomass flash pyrolysis liquids via hydrogen processing and catalytic cracking. *Fuel*, 77:1667–1675, 1998.

[93] R. Nava, B. Pawelec, P. Castaño, M. C. Álvarez Galván, C. V. Loricera, and J. L. G. Fierro. Upgrading of bio-liquids on different mesoporous silica-supported CoMo catalysts. *Appl. Catal. B: Environ.*, 92:154–167, 2009.

[94] T.-R. Viljava, R. S. Komulainen, and A. O. I. Krause. Effects of H_2S on the stability of $CoMo/Al_2O_3$ catalysts during hydrodeoxygenation. *Catal. Today*, 60:83–92, 2000.

[95] A. Centeno, E. Laurent, and B. Delmon. Influence of the support of CoMo sulfide catalysts and of the addition of potassium and platinum on the catalytic performances for hydrodeoxygenation of carbonyl, carboxyl, and guaiacol-type molecules. *J. Catal.*, 154:288–298, 1995.

[96] M. C. Edelman, M. K. Maholland, R. M. Baldwin, and S. W. Cowley. Vapor-phase catalytic hydrodeoxygenation of benzofuran. *J. Catal.*, 111:243–253, 1988.

[97] R. J. French, J. Hrdlicka, and R. Baldwin. Mild hydrotreating of biomass pyrolysis oils to produce a suitable refinery feedstock. *Environ. Prog.*, 29:142–150, 2010.

[98] E.-M. Ryymin, M. L. Honkela, T.-R. Viljava, and A. O. I. Krause. Competitive reactions and mechanisms in the simultaneous HDO of phenol and methyl heptanoate over sulphided $NiMo/\gamma\text{-}Al_2O_3$. *Appl. Catal. A: Gen.*, 389:114–121, 2010.

[99] I. Gandarias, V. L. Barrio, J. Requies, P. L. Arias, J. F. Cambra, and M. B. Güemez. From biomass to fuels: Hydrotreating of oxygenated compunds. *Int. J. Hydrogen Energy*, 33:3485–3488, 2008.

[100] E.-M. Ryymin, M. L. Honkela, T.-R. Viljava, and A. O. I. Krause. Insight to sulfur species in the hydrodeoxygenation of aliphatic esters over sulphided NiMo/γ-Al_2O_3. *Appl. Catal. A: Gen.*, 358:42–48, 2009.

[101] M. Ferrari, S. Bosmans, R. Maggi, B. Delmon, and P. Grange. CoMo/carbon hydrodeoxygenation catalysts: influence of the hydrogen sulfide partial pressure and of the sulfidation temperature. *Catal. Today*, 65:257–264, 2001.

[102] V.N. Bui, D. Laurenti, P. Delichère, and C. Geantet. Hydrodeoxygenation of guaiacol part I: Promoting effect of cobalt on HDO selectivity and activity. *Appl. Catal. B: Environ.*, 111:239–245, 2011.

[103] R. J. French, J. Stunkel, and R. M. Baldwin. Mild hydrotreating of bio-oil: effect of reaction severity and fate of oxygenated species. *Energy Fuels*, 25:3266–3274, 2011.

[104] M. Badawi, J.-F. Paul, S. Cristol, E. Payen, Y. Romero, F. Richard, S. Brunet, D. Lambert, X. Portier, A. Popov, E. Kondratieva, J. M. Goupil, J. E. Fallah, J.-P. Gilson, L. Mariey, A. Travert, and F. Mauge. Effect of water on the stability of Mo and CoMo hydrodeoxygenation catalysts: a combined experimental and DFT study. *J. Catal.*, 282:155–164, 2011.

[105] M. Badawi, S. Cristol, J.-F. Paul, and E. Payen. DFT study of furan adsorption over stable molybdenum sulfide catalyst under HDO conditions. *C. R. Chimie*, 12:754–761, 2009.

[106] Y. Romero, F. Richard, and S. Brunet. Hydrodeoxygenation of 2-ethylphenol as a model compound of bio-crude over sulfided Mo-based catalysts: promoting effect and reaction mechanism. *Appl. Catal. B: Environ.*, 98:213–223, 2010.

[107] H. Topsøe, B. S. Clausen, and F. E. Massoth. *Hydrotreating Catalysis*. Springer-Verlag: Berlin, 1996.

[108] O. I. Senol, T.-R. Viljava, and A. O. I. Krause. Effect of sulphiding agents on the hydrodeoxygenation of aliphatic esters on sulphided catalysts. *Appl. Catal. A: Gen.*, 326:236–244, 2007.

[109] O. I. Senol, E.-M. Ryymin, T.-R. Viljava, and A. O. I. Krause. Effect of hydrogen sulphide on the hydrodeoxygenation of aromatic and aliphatic oxygenates on sulphided catalysts. *J. Mol. Cat. A: Chem.*, 277:107–112, 2007.

[110] R. Prins. *Handbook of Heterogeneous Catalysis*, chapter 13.2: Hydrotreating, pages 2695–2718. John Wiley & Sons, Inc.: New York, 2008.

[111] D. R. Moberg, T. J. Thibodeau, F. G. Amar, and B. G. Frederick. Mechanism of hydrodeoxygenation of acrolein on a cluster model of MoO_3. *J. Phys. Chem. C*, 114:13782–13795, 2010.

[112] A. Gervasini and A. Auroux. Acidity and basicity of metal oxide surfaces. *J. Catal.*, 131:190–198, 1991.

[113] S. Li and D. A. Dixon. Molecular and electronic structures, Brönsted basicity, and Lewis acidities of group VIB transition metal oxide clusters. *J. Phys. Chem. A*, 110:6231–6244, 2006.

[114] V. M. L. Whiffen and K. J. Smith. Hydrodeoxygenation of 4-methylphenol over unsupported MoP, MoS_2, and MoO_x catalysts. *Energy Fuels*, 24:4728–4737, 2010.

[115] S. Echeandia, P. L. Arias, V. L. Barrio, B. Pawelec, and J. L. G. Fierro. Synergy effect in the HDO of phenol over Ni-W catalysts supported on active carbon: Effect of tungsten precursors. *Appl. Catal. B: Environ.*, 101:1–12, 2010.

[116] V. A. Yakovlev, S. A. Khromova, O. V. Sherstyuk, V. O. Dundich, D. Y. Ermakov, V. M. Novopashina, M. Y. Lebedev, O. Bulavchenko, and V. N. Parmon. Development of new catalytic systems for upgraded bio-fuels production from bio-crude-oil and biodiesel. *Catal. Today*, 144:362–366, 2009.

[117] M. J. Mendes, O. A. A. Santos, E. Jordão, and A. M. Silva. Hydrogenation of oleic acid over ruthenium catalysts. *Appl. Catal. A: Gen.*, 217:253–262, 2001.

[118] M. A. Vannice and B. Sen. Metal-support effects on the intramolecular selectivity of crotonaldehyde hydrogenation over platinum. *J. Catal.*, 115:65–78, 1989.

[119] A. Y. Stakheev and L. M. Kustov. Effects of the support on the morpholgy and electronic properties of supported metal clusters; modern concepts and progress in 1990s. *Appl. Catal. A: Gen.*, 188:3–35, 1999.

[120] A. Vargas, T. Bürgi, and A. Baiker. Adsorption of activated ketones on platinum and their reactivity to hydrogenation: a DFT study. *J. Catal.*, 222:439–449, 2004.

[121] A. Vargas, S. Reimann, S. Diezi, T. Mallat, and A. Baiker. Adsorption modes of aromatic ketones on platinum and their reactivity towards hydrogenation. *J. Mol. Cat.*, 282:1–8, 2008.

[122] T. Mallat and A. Baiker. Selectivity enhancement in heterogeneous catalysis induced by reaction modifiers. *Appl. Catal. A: Gen.*, 200:3–22, 2000.

[123] S. D. Lin, D. K. Sanders, and M. A. Vannice. Influence of metal-support effects on acetophenone hydrogenation over platinum. *Appl. Catal. A: Gen.*, 113:59–73, 1994.

[124] M. A. Vannice. Hydrogenation of CO and carbonyl functional groups. *Catal. Today*, 12:255–267, 1992.

[125] J. Wildschut, J. Arentz, C. B. Rasrendra, R. H. Venderbosch, and H. J. Heeres. Catalytic hydrotreatment of fast pyrolysis oil: model studies of reaction pathways for the carbohydrate fraction. *Environ. Prog.*, 28:450–460, 2009.

[126] C. A. Fisk, T. Morgan, Y. Ji, M. Crocker, C. Crofcheck, and S. A. Lewis. Bio-oil upgrading over platinum catalysts using in situ generated hydrogen. *Appl. Catal. A: Gen.*, 358:150–156, 2009.

[127] U. S. Geological Survey. Mineral commodity summaries 2013. Technical report, U.S. Geological Survey, 2013. `http://minerals.usgs.gov/minerals/pubs/mcs/`.

[128] H. Y. Zhao, D. Li, P. Bui, and S. T. Oyama. Hydrodeoxygenation of guaiacol as model compound for pyrolysis oil on transition metal phosphide hydroprocessing catalysts. *Appl. Catal. A: Gen.*, 391:305–310, 2011.

[129] C. Zhao, Y. Kuo, A. A. Lemonidou, X. Li, and J. A. Lercher. Highly selectivte catalytic conversion of phenolic bio-oil to alkanes. *Angew. Chem. Int. Ed.*, 48:3987–3990, 2009.

[130] C. Zhao, Y. Kuo, A. A. Lemonidou, X. Li, and J. A. Lercher. Hydrodeoxygenation of bio-derived phenols to hydrocarbons using raney® Ni and nafion/SiO_2 catalysts. *Chem. Commun.*, 46:412–414, 2010.

[131] C. Zhao, J. He, A. A. Lemonidou, X. Li, and J. A. Lercher. Aqueous-phase hydrodeoxygenation of bio-derived phenols to cycloalkanes. *J. Catal.*, 280:8–16, 2011.

[132] E. Laurent and B. Delmon. Influence of water in the deactivation of a sulfided NiMo/γ-Al_2O_3 catalyst during hydrodeoxygenation. *J. Catal.*, 146:281–291, 1994.

[133] A. Popov, E. Kondratieva, J. M. Goupil, L. Mariey, P. Bazin, J.-P. Gilson, A. Travert, and F. Mauge. Bio-oils hydrodeoxygenation: adsorption of phenolic molecules on oxidic catalyst supports. *J. Phys. Chem. C*, 114:15661–15670, 2010.

[134] D. C. Elliott and T. R. Hart. Catalytic hydroprocessing of chemical models for bio-oil. *Energy Fuels*, 23:631–637, 2009.

[135] K. V. R. Charry, H. Ramakrishna, and G. Murali Dhar. The effect of molybdenum precursor on the dispersion and hydrodesulfurization activity of carbon-supported sulfide catalysts. *J. Mol. Cat.*, 68:L25–L30, 1991.

[136] R. Maggi and B. Delmon. A review of catalytic hydrotreating processes for the upgrading of liquids produced by flash pyrolysis. *Stud. Surf. Sci. Catal.*, 106:99–113, 1997.

[137] A. Popov, E. Kondratieva, J.-P. Gilson, L. Mariey, A. Travert, and F. Mauge. IR study of the interaction of phenol with oxides and sulfided CoMo catalysts for bio-fuels hydrodeoxygenation. *Catal. Today*, 172:132–135, 2011.

[138] V. N. Bui, D. Laurenti, P. Delichère, and C. Geantet. Hydrodeoxygenation of guaiacol part II: Support effect for CoMoS catalysts on HDO activity and selectivity. *Appl. Catal. B: Environ.*, 111:246–255, 2011.

[139] Z. He and X. Wang. Hydrodeoxygenation of model compounds and catalytic systems for pyrolysis bio-oil upgrading. *Catal. Sus. Energy*, 1:28–52, 2012.

[140] Z. He, M. Yang, X. Wang, Z. Zhao, and A. Duan. Effect of the transition metal oxide supports on hydrogen production from bio-ethanol reforming. *Catal. Today*, 194:2–8, 2012.

[141] V. O. Dundich, S. A. Khromova, D. Yu. Ermakov, M. Yu. Lebedev, V. M. Novopashina, V. G. Sister, A. I. Yakimchuk, and V. A. Yakovlev. Nickel catalysts for the hydrodeoxygenation of biodiesel. *Kinet. Catal.*, 51:728–734, 2010.

[142] E. Furimsky and F. E. Massoth. Deactivation of hydroprocessing catalysts. *Catal. Today*, 52:381–495, 1999.

[143] A. Fonseca, P. Zeuthen, and J.B. Nagy. Assignment of an average chemical structure to catalyst carbon deposits on the basis of quantitative ^{13}C n.m.r. spectra. *Fuel*, 75:1413–1423, 1996.

[144] A. Fonseca, P. Zeuthen, and J. Nagy. ^{13}C n.m.r. quantitative analysis of catalyst carbon deposits. *Fuel*, 75:1363–1376, 1996.

[145] S. M. Richardson, H. Nagaishi, and M. R. Gray. Initial carbon deposition on a NiMo/γ-Al_2O_3 bitumen hydrocracking catalyst-the effect of reaction time and hydrogen pressure. *Proceedings of the 210th National Meeting of the American Chemical Society*, 40:455–459, 1995.

[146] Y. Yamamoto, F. Kumata, and F. E. Massoth. Hydrotreating catalyst deactivation by coke from SRC-II oil. *Fuel Process. Technol.*, 19:253–263, 1988.

[147] S. R. A. Kersten, W. P. M. van Swaaij, L. Lefferts, and K. Seshan. *Catalysis for Renewables: From Feedstock to Energy Production*, chapter 6: Options for Catalysis in the Thermochemical Conversion of Biomass into Fuels, pages 119–146. John Wiley & Sons, Inc.: New York, 2007.

[148] J. D. Adjaye and N. N. Bakhshi. Catalytic conversion of a biomass-derived oil to fuels and chemicals II: Chemical kinetics, parameter estimation and model predictions. *Biomass Bioeng.*, 8:265–277, 1995.

[149] S. Vitolo, M. Seggiani, P. Frediani, G. Ambrosini, and L. Polit. Catalytic upgrading of pyrolytic oils to fuel over different zeolites. *Fuel*, 78:1147–1159, 1999.

[150] N. Y. Chen, J. T. F. Degnan, and L. R. Koenig. Liquid fuel from carbohydrates. *Chemtech*, 16:506–511, 1986.

[151] M. Balat, M. Balat, E. Kirtay, and H. Balat. Main routes for thermo-conversion of biomass into fuels and chemicals. part 1: Pyrolysis systems. *Energ. Convers. Manage.*, 50:3147–3157, 2009.

[152] M. Stöcker. Gas phase catalysis by zeolites. *Micropor. Mesopor. Mat.*, 82:257–292, 2005.

[153] R. Xu, W. Pang, J. Yu, Q. Huo, and J. Chen. *Chemisty of Zeolites and Related Porous Material*, chapter 2: Structural Chemistry of Microporus Material, pages 19–116. John Wiley & Sons, Inc.: New York, 2007.

[154] R. Xu, W. Pang, J. Yu, Q. Huo, and J. Chen. *Chemisty of Zeolites and Related Porous Material*, chapter 6: Preparation, Secondary Synthesis, and Modification of Zeolites, pages 345–396. John Wiley & Sons, Inc.: New York, 2007.

[155] J. Weitkamp. Zeolites and catalysis. *Solid State Ionics*, 131:175–188, 2000.

[156] J. M. Thomas, R. G. Bell, and C. R. A. Catlow. *Handbook of Heterogeneous Catalysis*, chapter 2.3: Zeolites and Related Molecular Sieves, pages 286–310. John Wiley & Sons, Inc.: New York, 1997.

[157] H. van Bekkum, E. M. Flanigen, P. A. Jacobs, and J. C. Jansen. *Introduction to Zeolite Science and Practice*. Elsevier: Amsterdam, 2001.

[158] A. Corma, G. W. Huber, L. Sauvanaud, and P. O'Connor. Processing of biomass-derived oxygenates in the oil refinery: catalytic cracking (FCC) reaction pathways and role of catalyst. *J. Catal.*, 247:307–327, 2007.

[159] H. Chiang and A. Bhan. Catalytic consequences of hydroxyl group location on the rate and mechanism of parallel dehydration reactions of ethanol over acidic zeolites. *J. Catal.*, 271:251–261, 2010.

[160] J. D. Adjaye and N. N. Bakhshi. Upgrading of wood-derived oil over various catalysts. *Biomass Bioeng.*, 7:201–211, 1994.

[161] S. Vitolo, B. Bresci, M. Seggiani, and M. G. Gallo. Catalytic upgrading of pyrolytic oil over HZSM-5 zeolite: behaviour of the catalyst when used in repeated upgrading-regenerating cycles. *Fuel*, 80:17–26, 2001.

[162] P. Dejaifve, J. C. Védrine, V. Bolis, and E. G. Derouane. Reaction pathways for the conversion of methanol and olefins on H-ZSM-5 zeolite. *J. Catal.*, 63:331–345, 1980.

[163] H. J. Park, H. S. Heo, J.-K. Jeon, J. Kim, R. Ryoo, K.-E. Jeong, and Y.-K. Park. Highly valuable chemicals production from catalytic upgrading of radiata pine sawdust-derived pyrolytic vapors over mesoporous MFI zeolites. *Appl. Catal. B: Environ.*, 95:365–373, 2010.

[164] J. Huang, W. Long, P. K. Agrawal, and C. W. Jones. Effects of acidity on the conversion of model bio-oil ketone cyclopentanone on H-Y zeolites. *J. Phys. Chem. C*, 113:16702–16710, 2009.

[165] X. X. Zhu, R. G. Mallinson, and D. E. Resasco. Role of transalkylation reactions in the conversion of anisole over HZSM-5. *Appl. Catal. A: Gen.*, 379:172–181, 2010.

[166] B. Valle, A. G. Gayubo, A. T. Aguayo, M. Olazar, and J. Bilbao. Selective production of aromatics by crude bio-oil valorization with an nickel modified HZSM-5 zeolite catalyst. *Energy Fuels*, 24:2060–2070, 2010.

[167] X. Guo, Y. Zheng, B. Zhang, and J. Chen. Analysis of coke precursors on catalyst and study of regeneration of catalyst in upgrading bio-oil. *Biomass Bioeng.*, 33:1469–1473, 2009.

[168] A. G. Gayubo, B. Valle, A. T. Aguayo, M. Olazar, and J. Bilbao. Attenuation of catalyst deactivation by cofeeding methanol for enhancing the valorization of crude bio-oil. *Energy Fuels*, 23:4129–4136, 2009.

[169] L. Hong-yu, Y. Yong-jie, and R. Zheng-wei. Online upgrading of organic vapors from the fast pyrolysis of biomass. *J. Fuel Chem. Technol.*, 36:666–671, 2008.

[170] B. Valle, A. G. Gayubo, A. Atutxa, A. Alonso, and J. Bilbao. Integration of thermal treatment and catalytic transformation for upgrading biomass pyrolysis oil. *Int. J. Chem. React. Eng.*, 5:1–10, 2007.

[171] A. G. Gayubo, A. T. Aguayo, A. Atutxa, B. Valle, and J. Bilbao. Undesired components in the transformation of biomass pyrolysis oil into hydrocarbons on an HZSM-5 zeolite catalyst. *J. Chem. Technol. Biot.*, 80:1244–1251, 2005.

[172] R. V. Pindoria, A. Megaritis, A. A. Herod, and R. Kandiyoti. A two-stage fixed-bed reactor for direct hydrotreatment of volatiles from hydropyrolysis of biomass: effect of catalyst temperature, pressure and catalyst ageing time on product characteristics. *Fuel*, 77:1715–1726, 1998.

[173] R. K. Sharma and N. N. Bakshi. Upgrading of wood-derived bio-oil over HZSM-5. *Bioresource Technol.*, 35:57–66, 1991.

[174] M. Guisnet and P. Magnoux. Organic chemistry of coke formation. *Appl. Catal. A: Gen.*, 212:83–96, 2001.

[175] A. Ausavasukhi, T. Sooknoi, and D. E. Resasco. Catalytic deoxygenation of benzaldehyde over gallium modified ZSM−5 zeolites. *J. Catal.*, 268:68–78, 2009.

[176] M. A. Peralta, T. Sooknoi, T. Danuthai, and D. E. Resasco. Deoxygenation of benzaldehyde over CsNaX zeolites. *J. Mol. Cat.*, 312:78–86, 2009.

[177] E. Brunner, H. Ernst, D. Freude, T. Fröhlich, M. Hunger, and H. Pfeifer. Magic-angle-spinning NMR studies of acid sites in zeolite H-ZSM-5. *J. Catal.*, 127:34–41, 1991.

[178] C. S. Triantafilidis, A. G. Vlessidis, L. Nalbandian, and N. P. Evmiridis. Effect of the degree and type of the dealumination method on the structural, compositional and acidic characteristics of H-ZSM-5 zeolites. *Micropor. Mesopor. Mat.*, 47:369–388, 2001.

[179] Y. Sendoda and Y. Ono. Effect of the pretreatment temperature on the catalytic activity of ZSM-5 zeolites. *Zeolites*, 8:101–105, 1988.

[180] Y. Wang, Y. Fang, T. He, H. Hu, and J. Wu. Hydrodeoxygenation of dibenzofuran over noble metal supported on mesoporous zeolite. *Catal. Commun.*, 12:1201–1205, 2011.

[181] T. Masuda, Y. Fujikata, S. R. Mukai, and K. Hashimoto. Changes in catalytic activity of MFI-type zeolites caused by dealumination in a steam atmosphere. *Appl. Catal. A: Gen.*, 172:73–83, 1998.

[182] W.-C. Cheng, E. T. Habib, K. Rajagopalan, T. G. Roberie, R. F. Wormsbecher, and M. S Ziebarth. *Handbook of Hetrogenoues Catalysis*, chapter 13.2: Fluid Catalytic Cracking, pages 2741–2777. John Wiley & Sons, Inc.: New York, 2008.

[183] S. A. Channiwala and P. P. Parikh. A unified correlation for estimating HHV of solid, liquid and gaseous fuels. *Fuel*, 81:1051–1063, 2002.

[184] Y. Wang, H. Lin, and Y. Zheng. Hydrotreatment of lignocellulosic biomass derived oil using a sulfided NiMo/γ-Al_2O_3 catalyst. *Catal. Sci. Technol.*, In press, 2013.

[185] En 590: Automotive fuels - diesel - requirements and test methods, 2004.

[186] D. A. Bulushev and J. R. H. Ross. Catalysis for conversion of biomass to fuels via pyrolysis and gasification: a review. *Catal. Today*, 171:1–13, 2011.

[187] G. Fogassy, N. Thegarid, G. Toussaint, A. C. van Veen, Y. Schuurman, and C. Mirodatos. Biomass derived feedstock co-processing with vacuum gas oil for second-generation fuel production in FCC units. *Appl. Catal. B: Environ.*, 96:476–485, 2010.

[188] D. Wang, S. Czernik, D. Montané, M. K. Mann, and E. Chornet. Biomass to hydrogen via fast pyrolysis and catalytic steam reforming of the pyrolysis oil or its fractions. *Ind. Eng. Chem. Res.*, 36:1507–1518, 1997.

[189] D. Wang, S. Czernik, and E. Chornet. Production of hydrogen from biomass by catalytic steam reforming of fast pyrolysis oils. *Energy Fuels*, 12:19–24, 1998.

[190] S. Czernik, R. J. French, C. Feik, and E. Chornet. Hydrogen by catalytic steam reforming of liquid byproducts from biomass thermoconversion processes. *Ind. Eng. Chem. Res.*, 41:4209–4215, 2002.

[191] E. C. Vagia and A. A. Lemonidou. Thermodynamic analysis of hydrogen production via steam reforming of selected components of aqueous bio-oil fraction. *Int. J. Hydrogen Energy*, 32:212–223, 2007.

[192] R. Trane, S. Dahl, M. S. Skjøth-Rasmussen, and A. D. Jensen. Catalytic steam reforming of bio-oil. *Int. J. Hydrogen Energy*, 37:6447–6472, 2012.

[193] R. Trane-Restrup, S. Dahl, and A. D. Jensen. Steam reforming of ethanol: Effects of support and additives on Ni-based catalysts. *Int J. Hydrogen Energ.*, 38:15105–15118, 2013.

[194] R. Agrawal and N. R. Singh. Synenergistic routes to liquid fuel for a petroleum-deprived future. *AIChE J.*, 55:1898–1905, 2009.

[195] N. R. Singh, W. N. Delgass, F. H. Ribeiro, and P. K. Agrawal. Estimation of liquid fuel yields from biomass. *Environ. Sci. Technol.*, 44:5298–5305, 2010.

[196] F. S. Mederos, J. Ancheyta, and J. Chen. Review on criteria to ensure ideal behaviors in trickle-bed reactors. *Appl. Catal. A: Gen.*, 355:1–19, 2009.

[197] D. Sanfilippo and P. N Rylander. Hydrogenation and dehydrogenation. In *Ullmann's Encyclopedia of Industrial Chemistry*. John Wiley & Sons, Inc.: New York, 2009.

[198] A. Gianetto and V. Specchia. Trickle-bed reactors: State of art and perspectives. *Chem. Eng. Sci.*, 47:3197–3213, 1992.

[199] H. S. Fogler. *Elements of Chemical Reaction Engineering*. Prentice Hall: New Jersey, 2006.

[200] M. M. Ahmad, M. Fitrir, R. Nordin, and M. Tazli Azizan. Upgrading of bio-oil into high-value hydrocarbons via hydrodeoxygenation. *Am. J. Appl. Sci.*, 7:746–755, 2010.

[201] P. A. Horne and P. T. Williams. The effect of zeolite ZSM-5 catalyst deactivation during the upgrading of biomass-derived pyrolysis vapours. *J. Anal. Appl. Pyrol.*, 34:65–85, 1995.

[202] T. J. Thibodeau, A. S. Canney, W. J. DeSisto, M. C. Wheeler, F. G. Amar, and B. G. Frederick. Composition of tungsten oxide bronzes active for hydrodeoxygenation. *Appl. Catal. A: Gen.*, 388:86–95, 2010.

[203] J. Wildschut, M. Iqbal, F. H. Mahfud, I. M. Cabrera, R. H. Venderbosch, and H. J. Heeres. Insight in the hydrotreatment of fast pyrolysis oil using a ruthenium on carbon catalyst. *Energ. Environ. Sci.*, 3:962–970, 2010.

[204] J. Wildschut, I. Melián-Cabrera, and H. J. Heeres. Catalyst studies on hydrotreatment of fast pyrolysis oil. *Appl. Catal. B: Environ.*, 99:298–306, 2010.

[205] M. V. Bykova, O. A. Bulavchenko, D. Y. Ermakov, M. Y. Lebedev, V. A. Yakovlev, and V. N. Parmon. Guaiacol hydrodeoxygenation in the presence of Ni-containing catalysts. *Biocatalysis*, 3:15–22, 2011.

[206] V. A. Yakovlev, S. A. Khromova, D. Y. Ermakov, M. Y. Lebedev, V. A. Kirillov, and V. N. Parmon. Ru2335340c1, 2007. Catalyst, method of its preparation (versions) and process of hydrodeoxygenation of oxygen-organic products of biomass fast pyrolysis.

[207] J. R. Rostrup-Nielsen. Sulfur-passivated nickel catalysts for carbon-free steam reforming of methane. *J. Catal.*, 85:31–43, 1984.

[208] J. R. Rostrup-Nielsen. *Handbook of Heterogeneous Catalysis*, chapter 13.11: Steam Reforming, pages 2882–2905. John Wiley & Sons, Inc.: New York, 2008.

[209] K. Aasberg-Petersen, T. S. Christensen, I. Dybkjær, J. Sehested, M. Østberg, R. M. Coertzen, M. J. Keyser, and A. P. Steynberg. *Fischer-Tropsch Technology*, chapter 4: Synthesis Gas Production for FT Synthesis, pages 258–405. Elsevier: Amsterdam, 2004.

[210] M. Sau, C. S. L. Narasimhan, and R. P. Verma. A kinetic model for hydrodesulfurisation. In *Hydrotreatment and Hydrocracking of Oil Fractions, Proceedings of the 1st International Symposium/6th European Workshop*. Elsevier: Amsterdam, 1997.

[211] G. Valavarasu, M. Bhaskar, and K. S. Balaraman. Mild hydrocracking - a review of the process, catalysts, reactions, kinetics, and advantages. *Petroleum Sci. Tec.*, 21:1185–1205, 2003.

[212] F. de Miguel Mercader, P. J. J. Koehorst, H. J. Heeres, S. R. A. Kersten, and J. A. Hogendoorn. Competition between hydrotreating and polymerization reactions during pyrolysis oil hydrodeoxygenation. *AIChE J.*, 57:3160–3170, 2011.

[213] P. M. Mortensen, R. Trane-Restrup, and A. Tiedje. Pyrolysis oil converter - high pressure liquid and gas flow reactor system. Technical Report 045-28 POC, Department of Chemical and Biochemical Engineering, CHEC, DTU, 2013.

[214] K. Schofield. The enigmatic mechanism of the flame ionization detector: Its overlooked implications for fossil fuel combustion modeling. *Prog. Energ. Combust.*, 34:330–350, 2008.

[215] C. Baltes, S. Vukojevic, and F. Schüth. Correlations between synthesis, precursor, and catalyst structure and activity of a large set of $CuO/ZnO/Al_2O_3$ catalysts for methanol synthesis. *J. Catal.*, 258:334–344, 2008.

[216] C. H. Bartholomew. Sintering kinetics of supported metals: New perspectives from a unifying GPLE treatment. *Appl. Catal. A: Gen.*, 107:1–57, 1993.

[217] J. Sehested. Sintering of nickel steam-reforming catalysts. *J. Catal.*, 217:417–426, 2003.

[218] J. Sehested. Four challenges for nickel steam-reforming catalysts. *Catal. Today*, 111:103–110, 2006.

[219] C. Louis, Z. X. Cheng, and M. Che. Characterization of Ni/SiO_2 catalysts during impregnation and further thermal activation treatment leading to metal particles. *J. Phys. Chem.*, 97:5703–5712, 1993.

[220] M. Ferrari, B. Delmon, and P. Grange. Influence of the impregnation order of molybdenum and cobalt in carbon-supported catalysts for hydrodeoxygenation reactions. *Carbon*, 40:497–511, 2002.

[221] P. L. Llewellyn, E. Bloch, and S. Bourelly. *Characterization of Solid Material and Heterogenous Catalysts*, chapter 19: Surface Area/Porosity, Adsorption, Diffusion, pages 853–880. Wiley-VCH: Weinheim, 2012.

[222] J.-D. Grunwaldt, S. Hannemann, J. Göttlicher, S. Mangold, M. Denecke, and A. Baiker. X-ray absorption spectroscopy on heterogeneous catalysts at the new XAS beamline at ANKA. *Phys. Scripta*, T115:769–772, 2005.

[223] J.-D. Grunwaldt, M. Caravati, S. Hannemann, and A. Baiker. X-ray absorption spectroscopy under reaction conditions: suitability of different reaction cells for combined catalyst characterization and time-resolved studies. *Phys. Chem. Chem. Phys.*, 6:3037–3047, 2004.

[224] J.-D. Grunwaldt, N. van Vegten, and A. Baiker. Insight into the structure of supported palladium catalysts during the total oxidation of methane. *Chem. Commun.*, 44:4635–4637, 2007.

[225] O.V. van Beek, W.and Safonova, G. Wiker, and H. Emerich. SNBL, a dedicated beamline for combined in situ X-ray diffraction, X-ray absorption and raman scattering experiments. *Phase Transit.*, 84:726–732, 2011.

[226] G. Bergerhoff and I.D. Brown. Crystallographic databases. Technical report, International Union of Crystallography, 1987.

[227] B. Ravel and M. Newville. *ATHENA*, *ARTEMIS*, *HEPHAESTUS*: data analysis for X-ray absorption spectroscopy using *IFEFFIT*. *J. Synchrotron Radiat.*, 12:537–541, 2005.

[228] J. J. Rehr, J. J. Kas, M. P. Prange, A. P. Sorini, Y. Takimoto, and F. D. Vila. Ab initio theory and calculations of X-ray spectra. *C. R. Phys.*, 10:548–559, 2009.

[229] I. Graca, J. M. Lopes, H. S. Cerqueira, and M. F. Ribeiro. Bio-oils upgrading for second generation biofuels. *Ind. Eng. Chem. Res.*, 52:275–287, 2012.

[230] Q. Bu, H. Lei, A. H. Zacher, L. Wang, S. Ren, J. Liang, Y. Wei, Y. Liu, J. Tang, Q. Zhang, and R. Ruan. A review of catalytic hydrodeoxygenation of lignin-derived phenols from biomass pyrolysis. *Bioresource Technol.*, 124:470–477, 2012.

[231] M. S. A. Moraes, M. V. Migliorini, F. C. Damasceno, F. Georges, S. Almeida, C. A. Zini, R. A. Jacques, and E. B. Caramão. Qualitative analysis of bio oils of agricultural residues obtained through pyrolysis using comprehensive two dimensional gas chromatography with time-of-flight mass spectrometric detector. *J. Anal. Appl. Pyrol.*, 98:51–64, 2012.

[232] I. Chorkendorff and J. W. Niemantsverdriet. *Concepts of Modern Catalysis and Kinetics*. John Wiley & Sons, Inc.: New York, 2007.

[233] G. C. Chinchen, P. J. Denny, D. G. Parker, M. S. Spencer, K. C. Waugh, and D. A. Whan. Mechanism of methanol synthesis from $CO_2/CO/H_2$ mixtures over copper/zinc oxide/alumina catalysts: use of ^{14}C-labelled reactants. *Appl. Catal.*, 30:333–338, 1987.

[234] P. B. Rasmussen, P. M. Holmblad, T. Askgaard, C. V. Ovesen, P. Stoltze, J. K. Nørskov, and I. Chorkendorff. Methanol synthesis on Cu(100) from a binary gas mixture of CO_2 and H_2. *Catal. Lett.*, 26:373–381, 1994.

[235] T. Askgaard, J. K. Nørskov, C. V. Ovesen, and P. Stoltze. A kinetic model of methanol synthesis. *J. Catal.*, 156:229–242, 1995.

[236] N. Shuikin and L. Erivanskaya. Catalytic hydrogenation of phenols. *Russ. Chem. Rev.*, 29:309–320, 1960.

[237] E.-J. Shin and M. A. Keane. Gas-phase hydrogenation/hydrogenolysis of phenol over supported nickel catalysts. *Ind. Eng. Chem. Res.*, 39:883–892, 2000.

[238] X. Zhang, T. Wang, L. Ma, Q. Zhang, X. Huang, and Y. Yu. Production of cyclohexane from lignin degradation compounds over Ni/ZrO_2-SiO_2 catalysts. *Appl. Energ.*, 112:533–538, 2013.

[239] H. Ohta, H. Kobayashi, K. Hara, and A. Fukuoka. Hydrodeoxygenation of phenols as lignin models under acid-free conditions with carbon-supported platinum catalysts. *Chem. Commun.*, 47:12209–12211, 2011.

[240] C. Zhao, S. Kasakov, J. He, and J. A. Lercher. Comparison of kinetics, activity and stability of Ni/HZSM-5 and Ni/Al_2O_3-HZSM-5 for phenol hydrodeoxygenation. *J. Catal.*, 296:12–23, 2012.

[241] S. Kozuch and J. M. L. Martin. "Turning over" definitions in catalytic cycles. *ACS Catal.*, 2:2787–2794, 2012.

[242] S. W. Benson. *Thermochemical Kinetics: Methods for estimation of thermochemical data and rate parameters.* John Wiley & Sons, Inc.:New York, 1968.

[243] Stephen J. Hurff and Michael T. Klein. Reaction pathway analysis of thermal and catalytic lignin fragmentation by use of model compounds. *Ind. Eng. Chem. Fundam.*, 22:426–430, 1983.

[244] M. V. Bykova, S. G. Zavarukhin, L. I. Trusov, and V. A. Yakovlev. Guaiacol hydrodeoxygenation kinetics with catalyst deactivation taken into consideration. *Kinet. Catal.*, 54:40–48, 2013.

[245] G. M. Kontogeorgis, M. L. Michelsen, G. K. Folas, S. Derawi, N. von Solms, and E. H. Stenby. Ten years with the CPA (cubic-plus-association) equation of state. part 1. pure compounds and self-associating systems. *Ind. Eng. Chem. Res.*, 45:4855–4868, 2006.

[246] G. M. Kontogeorgis, M. L. Michelsen, G. K. Folas, S. Derawi, N. von Solms, and E. H. Stenby. Ten years with the CPA (cubic-plus-association) equation of state. part 2. cross-associating and multicomponent systems. *Ind. Eng. Chem. Res.*, 45:4869–4878, 2006.

[247] T. Prasomsri, T. Nimmanwudipong, and Y. Román-Leshkov. Effective hydrodeoxygenation of biomass-derived oxygenates into unsaturated hydrocarbons by MoO_3 using low H_2 pressures. *Energy. Environ. Sci.*, 6:1732–1738, 2013.

[248] A. R. Adriyanti, S. A. Khromova, R. H. Venderbosch, V. A. Yakovlev, and H. J. Heeres. Catalytic hydrotreatment of fast-pyrolysis oil using non-sulfided bimetallic Ni-Cu catalysts on a δ-Al_2O_3 support. *Appl. Catal. B: Environ.*, 117-118:105–117, 2012.

[249] R. R. Davda, J. W. Shabaker, G. W. Huber, R. D. Cortright, and J. A. Dumesic. A review of catalytic issues and process conditions for renewable hydrogen and alkanes by aqueous-phase reforming of oxygenated hydrocarbons over supported metal catalysts. *Appl. Catal. B: Environ.*, 56:171–186, 2005.

[250] C. R. Lee, J. S. Yoon, Y.-W. Suh, J.-W. Choi, J.-M. Ha, D. J. Suh, and Y.-K. Park. Catalytic roles of metals and supports on hydrodeoxygenation of lignin monomer guaiacol. *Catal. Commun.*, 17:54–58, 2012.

[251] A. R. Adriyanti, A. Gutierrez, M. L. Honkela, A. O. I. Krause, and H. J. Heeres. Hydrotreatment of wood-based pyrolysis oil using zirconia-supported mono- and bimetallic (Pt, Pd, Rh) catalysts. *Appl. Catal. A: Gen.*, 407:56–66, 2011.

[252] J. K. Nørskov, J. Rossmeisl, A. Logadottir, L. Lindqvist, J. R. Kitchin, T. Bligaard, and H. Jonsson. Origin of the overpotential for oxygen reduction at a fuel-cell cathode. *J. Phys. Chem. B*, 108:17886–17892, 2004.

[253] A. J. Foster, P. T. M. Do, and R. F. Lobo. The synergy of the support acid function and the metal function in the catalytic hydrodeoxygenation of m-cresol. *Top. Catal.*, 55:118–128, 2012.

[254] J. Zielinski. Effect of water on the reduction of nickel/alumina catalysts - catalyst characterization by temperature-programmed reduction. *J. Chem. Soc. Faraday Trans.*, 93:3577–3580, 1997.

[255] M. E. Dry. High quality diesel via the Fischer-Tropsch process - a review. *J. Chem. Technol. Biot.*, 77:43–50, 2001.

[256] M. E. Dry. The Fischer-Tropsch process: 1950-2000. *Catal. Today*, 71:227–241, 2002.

[257] M. E. Dry. *Fischer-Tropsch Technology*, chapter 7: FT catalysts, pages 533–593. Elsevier: Amsterdam, 2004.

[258] J. Filley and C. Roth. Vanadium catalyzed guaiacol deoxygenation. *J. Mol. Cat.*, 139:245–252, 1999.

[259] R. L. Burwell, A. B. Littlewood, M. Cardew, G. Pass, and C. T. H. Stodhart. Reactions between hydrocarbons and deuterium on chromium oxide gel. 1. general. *J. Am. Chem. Soc.*, 82:6272–6280, 1960.

[260] R. L. Burwell, K. C. Taylor, and G. L. Haller. Texture of chromium oxide catalysts. *J. Phys. Chem.*, 71:4580–4581, 1967.

[261] J. A. Rodriguez, J. C. Hanson, A. I. Frenkel, J. Y. Kim, and M. Perez. Experimental and theoretical studies on the reaction of H_2 with NiO: Role of O vacancies and mechanism for oxide reduction. *J. Am. Chem. Soc.*, 124:346–354, 2002.

[262] H. H. Kung. *Transition Metal Oxides: Surface Chemistry and Catalysis*, chapter 4: Surface Coordinative Unsaturation, pages 53–71. Elsevier: Amsterdam, 1989.

[263] D. G. Rethwisch and J. A. Dumesic. Effect of metal-oxygen bond strength on the properties of oxides. 1. infrared spectroscopy of adsorbed CO and CO_2. *Langmuir*, 2:73–79, 1986.

[264] H. Idriss and M. A. Barteau. Active sites on oxides: From single crystals to catalysts. *Adv. Catal.*, 45:261–331, 2000.

[265] H. Liu, T. Jiang, B. Han, S. Liand, and Y. Zhou. Selective phenol hydrogenation to cyclohexanone over a dual supported Pd-lewis acid catalyst. *Science*, 326:1250–1252, 2009.

[266] S. Velu, M. P. Kapoor, S. Inagaki, and K. Suzuki. Vapor phase hydrogenation of phenol over palladium supported on mesoporous CeO_2 and ZrO_2. *Appl. Catal. A: Gen.*, 245:317–331, 2003.

[267] J. Matos and A. Corma. Selective phenol hydrogenation in aqueous phase on Pd-based catalysts supported on hybrid TiO_2-carbon materials. *Appl. Catal. A: Gen.*, 404:103–112, 2011.

[268] J. P. Boitiaux, J. Cosyns, and E. Robert. Liquid phase hydrogenation of unsaturated hydrocarbons on palladium, platinum and rhodium catalysts. part i: kinetic study of 1-butene, 1,3-butadiene and 1-butyne hydrogenation on platinum. *Appl. Catal.*, 32:145–168, 1987.

[269] P. Ponec and G. C. Bond. *Catalysis by Metals and Alloys*, volume 95, chapter 11: Catalytic hydrogenation and dehydrogenation, pages 477 – 539. Elsevier: Amsterdam, 1995.

[270] F. Gracia and E. E. Wolf. Monte Carlo simulations of the effect of crystallite size on the activity of a supported catalyst. *Chem. Eng. J.*, 82:291–301, 2001.

[271] A. P. Umpierre, E. de Jesús, and J. Dupont. Carbonyl numbers and soluble metal nanoparticles. *ChemCatChem*, 3:1413–1418, 2011.

[272] G Jones, J. G. Jakobsen, S. S. Shim, J. Kleis, M. P. Andersson, J. Rossmeisl, F. Abild-Pedersen, T. Bligaard, S. Helveg, B. Hinnemann, J. R. Rostrup-Nielsen, I. Chorkendorff, J. Sehested, and J. K. Nørskov. First principle calculations and experimental insight into methane steam reforming over transition metal catalysts. *J. Catal.*, 259:147–160, 2008.

[273] D. A. J. M. Lighthart, R. A. van Santen, and E. J. M. Hensen. Influence of particle size on the activity and stability in steam methane reforming of supported Rh nanoparticles. *J. Catal.*, 280:206–220, 2011.

[274] J. Wei and E. Iglesia. Mechanism and site requirements for activation and chemical conversion of methane on supported Pt clusters and turnover rate comparisons among noble metals. *J. Phys. Chem. B*, 108:4094–4103, 2004.

[275] J. Engbæk, O. Lytken, J. H. Nielsen, and I. Chorkendorff. CO dissociation on Ni: the effect ofsteps and of the nickel carbonyl. *Surf. Sci.*, 602:733–743, 2008.

[276] M. P. Andersson, F. Abild-Pedersen, I. N. Remediakis, T. Bligaard, G. Jones, J. Engbæk, O. Lytken, S. Horch, J. H. Nielsen, J. Sehested, J. R. Rostrup-Nielsen, J. K. Nørskov, and I. Chorkendorff. Structure sensitivity of the methanation reaction: H_2-induced CO dissociation on nickel surfaces. *J. Catal.*, 255:6–19, 2008.

[277] V. Ragaini, R. Carli, C. L. Bianchi, D. Lorenzetti, G. Predieri, and P. Moggi. Fischer-Tropsch synthesis on alumina-supported ruthenium catalysts II. influence of morphological factors. *Appl. Catal. A: Gen.*, 139:31–42, 1996.

[278] J. P. den Breejen, P. B. Radstake, G. L. Bezemer, J. H. Bitter, V. Frøseth, A. Holmen, and K. P. de Jong. On the origin of the cobalt particle size effects in the Fischer-Tropsch catalysis. *J. Am. Chem. Soc.*, 131:7197–7203, 2009.

[279] J. Yang, E. Z. Tveten, D. Chen, and A. Holmen. Understanding the effect of cobalt particle size on Fischer-Tropsch synthesis: Surface species and mechanistic studies by SSITKA and kinetic isotope effect. *Langmuir*, 26:16558–16567, 2010.

[280] J. M. G. Carballo, J. Yang, A. Holmen, S. García-Rodríguez, S. Rojas, M. Ojeda, and J. L. G. Fierro. Catalytic effects of ruthenium particle size on the Fischer-Tropsch synthesis. *J. Catal.*, 284:102–108, 2011.

[281] J.-D. Grunwaldt, M. Maciejewski, O. S. Becker, P. Fabrizioli, and A. Baiker. Comparative study of Au/TiO_2 and Au/ZrO_2 catalysts for low-temperature CO oxidation. *J. Catal.*, 186:458–469, 1999.

[282] B. Hvolbæk, T. V. W. Janssens, B. S. Clausen, H. Falsig, C. H. Christensen, and J. K. Nørskov. Catalytic activity of Au nanoparticles. *Nanotoday*, 2:14–18, 2007.

[283] T. V. W. Janssens, A. Carlsson, A. Puig-Molina, and B. S. Clausen. Relation between nanoscale Au particle structure and activity for CO oxidation on supported gold catalysts. *J. Catal.*, 240:108–113, 2006.

[284] N. Lopez, T. V. W. Janssens, B. S. Clausen, Y. Xu, M. Mavrikakis, T. Bligaard, and J. K. Nørskov. On the origin of the catalytic activity of gold nanoparticles for low-temperature CO oxidation. *J. Catal.*, 223:232–235, 2004.

[285] A. Boubnov, S. Dahl, E. Johnson, A. P. Molina, S. B. Simonsen, F. M. Cano, S. Helveg, L. J. Lemus-Yegres, and J.-D. Grunwaldt. Structure-activity relationships of Pt/Al_2O_3 catalysts for CO and NO oxidation at diesel exhaust conditions. *Appl. Catal. B: Environ.*, 126:315–325, 2012.

[286] M. Shao, A. Peles, and K. Shoemaker. Electrocatalysis on platinum nanoparticles: particle size effect on oxygen reduction reaction activity. *Nano Lett.*, 11:3714–3719, 2011.

[287] C. Wang, D. van der Vliet, K.-C. Chang, H. You, D. Strmchnik, J. A. Schlueter, N. M. Markovic, and V. R. Stamenkovic. Monodisperse Pt_3Co nanoparticles as a catalyst for the oxygen reduction reaction: size-dependent activity. *J. Phys. Chem. C*, 113:19365–19368, 2009.

[288] A. Borodzinski and M. Bonarowska. Relation between crystallite size and dispersion on supported metal catalysts. *Langmuir*, 13:5613–5620, 1997.

[289] C. L. Cleveland and U. Landman. The energetics and structure of nickel clusters: size dependence. *J. Chem. Phys.*, 94:7376–7396, 1991.

[290] R. E. Benfield. Mean coordinate numbers and the non-metal transition in clusters. *J. Chem. Soc. Faraday Trans.*, 88:1107–1110, 1992.

[291] H. S. Bengaard, J. K. Nørskov, J. Sehested, B. S. Clausen, L. P. Nielsen, A. M. Molenbroek, and J. R. Rostrup-Nielsen. Steam reforming and graphite formation on Ni catalysts. *J. Catal.*, 209:365–384, 2002.

[292] N. Lopez, J. K. Nørskov, T. V. W. Janssens, A. Carlsson, A. Puig-Molina, B. S. Clausen, and J.-D. Grunwaldt. The adhesion and shape of nanosized Au particles in a Au/TiO_2 catalyst. *J. Catal.*, 225:86–94, 2004.

[293] K. V. R. Chary, D. Naresh, V. Vishwanathan, M. Sadakane, and W. Ueda. Vapour phase hydrogenation of phenol over Pd/C catalysts: a relationship between dispersion, metal area, and hydrogenation activity. *Catal. Commun.*, 8:471–477, 2007.

[294] G. A. Martin and J. A. Dalmon. Benzene hydrogenation over nickel catalysts at low and high temperature: structure-sensitivity and copper alloying effects. *J. Catal.*, 75:233–242, 1982.

[295] M. García-Diéguez and E. Iglesia. Structure sensitivity via decoration of low-coordinated exposed metal atoms: CO oxidation catalysis on Pt clusters. *J. Catal.*, 301:198–209, 2013.

[296] D. Y. Murzin. Kinetic analysis of cluster size dependent activity and selectivity. *J. Catal.*, 276:85–91, 2010.

[297] D. Y. Murzin. Size-dependent heterogeneous catalytic kinetics. *J. Mol. Cat. A: Chem.*, 315:226–230, 2010.

[298] D. Y. Murzin. Nanokinetics for nanocatalysis. *Catal. Sci. Technol.*, 1:380–384, 2011.

[299] D. Y. Murzin. On cluster size dependent activity and selectivity in heterogeneous catalysis. *Catal. Lett.*, 142:1279–1285, 2012.

[300] Y. Xiang, L. Ma, L. Chunshan, Q. Zhang, and X. Li. Aqueous system for the improved hydrogenation of phenol and its derivatives. *Green Chem.*, 10:939–943, 2008.

[301] M. V. Bykova, D. Y. Ermakov, V. V. Kaichev, O. Bulavchenko, A. A. Saraev, M. Y. Lebedev, and V. A. Yakovlev. Ni-based sol-gel catalysts as promising systems for crude bio-oil upgrading: Guaiacol hydrodeoxygenation study. *Appl. Catal. B: Environ.*, 113-114:296–307, 2012.

[302] E. Furimsky. Hydroprocessing challenges in biofuels production. *Catal. Today*, 217:13–56, 2013.

[303] T. V. Choudhary and C. B. Phillips. Renewable fuels via catalytic hydrodeoxygenation. *Appl. Catal. A: Gen.*, 397:1–12, 2011.

[304] H. Wang, J. Male, and Y. Wang. Recent advances in hydrotreating of pyrolysis bio-oil and its oxygen-containing model compounds. *ACS Catal.*, 3:1047–1070, 2013.

[305] T. N. Trinh, P. A. Jensen, H. R. Sørensen, K. Dam-Johansen, and S. Hvilsted. Comparison of lignin, macroalgae, wood, and straw fast pyrolysis. *Energy Fuels*, 27:1399–1409, 2013.

[306] P. R. Patwardhan, R. C. Brown, and B. H. Shanks. Understanding the fast pyrolysis of lignin. *ChemSusChem*, 4:1629–1636, 2011.

[307] E. Laurent, A. Centeno, and B. Delmon. Coke formation during the hydrotreating of biomass pyrolysis oils: influence of guaiacol type compounds. *Stud. Surf. Sci. Catal.*, 88:573–578, 1994.

[308] Y.-C. Lin, C.-L. Li, H.-P. Wan, H.T. Lee, and C.-F. Liu. Catalytic hydrodeoxygenation of guaiacol on Rh-based and sulfided CoMo and NiMo catalysts. *Energy Fuels*, 25:890–896, 2011.

[309] B. Peng, C. Zhao, I. Mejía-Centeno, G. A. Fuentes, A. Jentys, and J. A. Lercher. Comparison of kinetics and reaction pathways for hydrodeoxygenation of C_3 alcohols on Pt/Al_2O_3. *Catal. Today*, 183:3–9, 2012.

[310] J. Ryu, S. M. Kim, J.-W. Choi, J.-M. Ha, D. J. Ahn, D. J. Suh, and Y.-W. Suh. Highly durable Pt-supported niobia-silica aerogel catalysts in the aqueous-phase hydrodeoxygenation of 1-propanol. *Catal. Commun.*, 29:40–47, 2012.

[311] P. M. Mortensen, J.-D. Grunwaldt, P. A. Jensen, and A. D. Jensen. Structure sensitivity of nickel based catalysts for the hydrodeoxygenation of phenol. *Submitted to ChemCatChem*, 2013.

[312] T. Borowiecki. Nickel catalysts for steam reforming of hydrocarbons; size of crystallites and resistance to coking. *Appl. Catal.*, 4:223–231, 1982.

[313] J. R. Rostrup-Nielsen, J. Sehested, and J. K. Nørskov. Hydrogen and synthesis gas by steam- and CO_2 reforming. *Adv. Catal.*, 47:65–139, 2002.

[314] G. Tavoularis and M. A. Kean. Gas phase catalytic dehydrochlorination and hydrodechlorination of aliphatic and aromatic systems. *J. Mol. Cat. A: Chem.*, 142:187–199, 1999.

[315] C. Menini, C. Park, E.-J. Shin, G. Tavoularis, and M. A. Keane. Catalytic hydrodehalogenation as a detoxification methodology. *Catal. Today*, 62:355–366, 2000.

[316] B. Schrick, J. L. Blough, A. D. Jones, and T. E. Mallouk. Hydrodechlorination of trichloroethylene to hydrocarbons using bimetallic nickel-iron nanoparticles. *Chem. Mater.*, 14:5140–5147, 2002.

[317] M. A. Keane. Supported transition metal catalysts for hydrodechlorination reactions. *ChemCatChem*, 3:800–821, 2011.

[318] S. Park, J. O. Baker, M. E. Himmel, P. A. Parilla, and D. K. Johnson. Cellulose crystallinity index: measurement techniques and their impact on interpreting cellulase performance. *Biotechnol. Biofuel.*, 3, 2010.

[319] Y. Ohtsuka. Influence of hydrogen chloride treatment on the dispersion of nickel particles supported on carbon. *J. Mol. Cat.*, 54:225–235, 1989.

[320] K. Jurek and O. Gedeon. Volume and composition surface changes in alkali silicate glass irradiated with electrons. *Microchim. Acta.*, 161:377–380, 2008.

[321] S. Hodson and J. Marshall. Migration of potassium out of electron-microscope specimens. *J. Microsc.*, 93:49–53, 1971.

[322] S. Sasaki, K. Fujino, and Y. Takeuchi. X-ray determination of electron-density distributions in oxides, MgO, MnO, CoO, and NiO, and atomic scattering factors of their constituent atoms. *Proc. Jpn. Acad., Ser. B*, 55:43–48, 1979.

[323] J. R. Rostrup-Nielsen. Chemisorption of hydrogen sulfide on a supported nickel catalyst. *J. Catal.*, 11:220–227, 1968.

[324] T. Rosenqvist. A thermodynamic study of iron, cobalt, and nickel sulphides. *J. Iron Steel I.*, 176:37–57, 1954.

[325] J. L. Oliphant, R. W. Fowler, R. B. Pannell, and C. H. Bartholomew. Chemisorption of hydrogen sulfide on nickel and ruthenium catalysts: I. desorption isotherms. *J. Catal.*, 51:229 – 242, 1978.

[326] C. H. Bartholomew, G. D. Weatherbee, and G. A. Jarvi. Sulfur poisoning of nickel methanation catalysts: I. in situ deactivation by H_2S of nickel and nickel bimetallics. *J. Catal.*, 60:257 – 269, 1979.

[327] J. R. Rostrup-Nielsen. Some principle relating to the regeneration of sulfur-poisoned nickel catalyst. *J. Catal.*, 21:171–178, 1971.

[328] H. Oudghiri-Hassani, N. Abatzoglou, S. Rakass, and P. Rowntree. Regeneration of an n-decanethiol-poisoned nickel catalyst. *J. Power Sources*, 171:811–817, 2007.

[329] T. S. Christensen. Adiabatic prereforming of hydrocarbons - important step in syngas production. *Appl. Catal. A: Gen.*, 138:285–309, 1996.

[330] M. Kiskinova and D. W. Goodman. Modification of chemisorption properties by electronegative adatoms: H_2 and CO on chlorided, sulfided, and phosphide Ni(100). *Surf. Sci.*, 108:64–76, 1981.

[331] J. T. Richardson, J. D. Ortego, N. Coute, and M. V. Twigg. Chloride poisoning of water-gas shift activity in nickel catalysts during steam reforming. *Catal. Lett.*, 41:17–20, 1996.

[332] J. D. Ortego, J. T. Richardson, and M. V. Twigg. Catalytic steam reforming of chlorocarbons: methyl chloride. *Appl. Catal. B: Environ.*, 12:339–355, 1997.

[333] J. P. Trembly, R. S. Gemmen, and D. J. Bayless. The effect of coal syngas containing HCl on the performance of solid oxide fuel cells: Investigations into the effect of operational temperature and HCl concentration. *J. Power Sources*, 169:347–354, 2007.

[334] R. B. Levy and M. Boudart. Platinum-like behavior of tungsten carbide in surface catalysis. *Science*, 4099:547–549, 1973.

[335] L. Leclercq, K. Imura, S. Yoshida, T. Barbee, and M. Boudart. Synthesis of new catalytic materials: Metal carbides of the group VI B elements. *Stud. Surf. Sci. Catal.*, 3:627–639, 1979.

[336] A. J. Medford, A. Vojvodic, F. Studt, F. Abild-Pedersen, and J. K. Nørskov. Elementary steps of syngas reactions on $Mo_2C(001)$: Adsorption thermochemistry and bond dissociation. *J. Catal.*, 290:108–117, 2012.

[337] S. Ramanathan and S. T. Oyama. New catalysts for hydroprocessing: transition metal carbides and nitrides. *J. Phys. Chem.*, 99:16365–16372, 1995.

[338] B. Dhandapani, T. Clair, and S. T. Oyama. Simultaneous hydrodesulfurization, hydrodeoxygenation, and hydrogenation with molybdenum carbide. *Appl. Catal. A: Gen.*, 168:219–228, 1998.

[339] E. Furimsky. Metal carbides and nitrides as potential catalysts for hydroprocessing. *Appl. Catal. A: Gen.*, 240:1–28, 2003.

[340] P. Rodríguez, J. L. Brito, A. Albornoz, M. Labadí, C. Pfaff, S. Marrero, D. Moronta, and P. Betancourt. Comparison of vanadium carbide and nitride catalysts for hydrotreating. *Catal. Commun.*, 5:79–82, 2004.

[341] H. Ren, W. Yu, M. Salciccioli, Y. Chen, Y. Huang, K. Xiong, D. G. Vlachos, and J. G. Chen. Selective hydrodeoxygenation of biomass-derived oxygenates to unsaturated hydrocarbons using molybdenum carbide catalysts. *ChemSusChem*, 6:798–801, 2013.

[342] J. Han, J. Duan, P. Chen, H. Lou, X. Zheng, and H. Hong. Nanostructured molybdenum carbides supported on carbon nanotubes as efficient catalysts for one-step hydrodeoxygenation and isomerization of vegetable oils. *Green Chem.*, 13:2561–2568, 2011.

[343] J. Han, J. Duan, P. Chen, H. Lou, X. Zheng, and H. Hong. Carbon-supported molybdenum carbide catalysts for the conversion of vegetable oils. *ChemSusChem*, 5:727–733, 2012.

[344] R. W. Gosselink, D. R. Stellwagen, and J. H. Bitter. Tungsten-based catalysts for selective deoxygenation. *Angew. Chem. Int. Ed.*, 52:5089–5092, 2013.

[345] Y. Qin, P. Chen, J. Duan, J. Han, H. Lou, X. Zheng, and H. Hong. Carbon nanofibers supported molybdenum carbide catalysts for hydrodeoxygenation of vegetable oils. *RSC Adv.*, 3:17485–17491, 2013.

[346] S. A. W. Hollak, R. W. Gosselink, D. S. Van Es, and J. H. Bitter. The comparison of tungsten and molybdenum carbide catalysts for the hydrodeoxygenation of oleic acid. *ACS Catal.*, 3:2837–2844, 2013.

[347] W. Zhang, Y. Zhan, L. Zhao, and W. Wei. Catalytic activities of NiMo carbide supported on SiO_2 for the hydrodeoxygenation of ethyl benzoate, acetone, and acetaldehyde. *Energy Fuels*, 24:2052–2059, 2010.

[348] J. Chang, T. Danuthai, S. Dewiyanti, C. Wang, and A. Borgna. Hydrodeoxygenation of guaiacol over carbon-supported metal catalysts. *ChemCatChem*, 5:3041–3049, 2013.

[349] A. L. Jongerius, R. W. Gosselink, J. Dijkstra, J. H. Bitter, P. C. A. Bruijnincx, and B. M. Weckhuysen. Carbon nanofiber supported transition-metal carbide catalysts for the hydrodeoxygenation of guaiacol. *ChemCatChem*, 5:2964–2972, 2013.

[350] S. Boullosa-Eiras, R. Lødeng, H. Bergem, M. Stöckerc, L. Hannevold, and E. A. Blekkan. Catalytic hydrodeoxygenation (HDO) of phenol over supported molybdenum carbide, nitride, phosphide and oxide catalysts. *Catal. Today*, In press, 2013.

[351] K. C. Pratt, J. V. Sanders, and V. Christov. Morphology and activity of MoS_2 on various supports: Genesis of the active phase. *J. Catal.*, 124:416–432, 1990.

[352] M. Breysse, J. L. Portefaix, and M. Vrinat. Support effects on hydrotreating catalysts. *Catal. Today*, 10:489–505, 1991.

[353] T. Leisegang, A. A. Levin, J. Walter, and D. C. Meyer. In situ X-ray analysis of MoO_3 reduction. *Cryst. Res. Technol.*, 40:95–105, 2005.

[354] K. Page, J. Li, R. Savinelli, H. N. Szumila, J. Zhang, J. K. Stalick, T. Proffen, S. L. Scott, and R. Seshadri. Reciprocal-space and real-space neutron investigation of nanostructured Mo_2C and WC. *Solid State Sci.*, 10:1499–1510, 2008.

[355] B. S. Gevert, J.-E. Otterstedt, and F. E. Massoth. Kinetics of the HDO of methyl-substituted phenols. *Appl. Catal.*, 31:119–131, 1987.

[356] E. Laurent and B. Delmon. Influence of oxygen-, nitrogen-, and sulfur-containing compounds on the hydrodeoxygenation of phenols over sulfided CoMo/γ-Al_2O_3 and NiMo//γ-Al_2O_3 catalysts. *Ind. Eng. Chem. Res.*, 32:2516–2524, 1993.

[357] T.-R. Viljava, S. Komulainen, T. Selvam, and A. O. I. Krause. Stability of CoMo/Al_2O_3 catalysts: Effect of HDO cycles on HDS. In G.F. Froment B. Delmon and P. Grange, editors, *Hydrotreatment and hydrocracking of oil fractions*, volume 127 of *Studies in Surface Science and Catalysis*, pages 145 – 152. Elsevier: Amsterdam, 1999.

[358] D. D. Laskar, B. Yang, H. Wang, and J. Lee. Pathways for biomass-derived lignin to hydrocarbon fuels. *Biofuels, Bioprod. Biorefin.*, 7:602–626, 2013.

[359] J. B. Claridge, A. P. E. York, A. J. Brungs, C. Marquez-Alvarez, J. Sloan, S. C. Tsang, and M. L. H. Green. New catalysts for the conversion of methane to synthesis gas: molybdenum and tungsten carbide. *J. Catal.*, 180:85–100, 1998.

[360] I. Barin and O. Knacke. *Thermochemical properties of inorganic substances.* Springer-Verlag: Berlin, 1973.

[361] D. R. Burgess. Thermochemical data. In *NIST Chemistry WebBook, NIST Standard Reference Database Number 69.* National Institute of Standards and Technology, retrieved September 18 2013. http://webbook.nist.gov,.

[362] C.-T. Liu and W. T. Lindsay. Vapor pressure of D_2O from 106 to 300°C. *J. Chem. Eng. Data*, 15:510–513, 1970.

[363] R. V. Chaudhari, A. Torres, X. Jin, and Subramaniam. Multiphase catalytic hydrogenolysis/hydrodeoxygenation processes for chemicals from renewable feedstocks: Kinetics, mechanism, and reaction engineering. *Ind. Eng. Chem. Res.*, 52:15226–15243, 2013.

[364] H. Topsøe, K. G. Knudsen, L. S. Byskov, J. K. Nørskov, and B. S. Clausen. Advances in deep desulfurization. In *Science and Technology in Catalysis*, volume 121 of *Studies in Surface Science and Catalysis*, pages 13–22. Elsevier: Amsterdam, 1999.

[365] P. Raybaud. Understanding and predicting improved sulfide catalysts: Insights from first principles modeling. *Appl. Catal. A: Gen.*, 322:76–91, 2007.

[366] M. Marafi, A. Stanislaus, and E. Furimsky. *Handbook of Spent Hydroprocessing Catalysts*, chapter 3: Hydroprocessing of Petroleum, pages 17–49. Elsevier: Amsterdam, 2010.

[367] S. Helveg, J. V. Lauritsen, E. Lægsgaard, I. Stensgaard, J. K. Nørskov, B. S. Clausen, H. Topsøe, and F. Besenbacher. Atomic-scale structure of single-layer MoS_2 nanoclusters. *Phys. Rev. Lett.*, 84:951–954, 2000.

[368] R. Prins. Catalytic hydrodenitrogenation. *Adv. Catal.*, 46:399–464, 2001.

[369] J. V. Lauritsen, J. Kibsgaard, S. Helveg, H. Topsøe, B. S. Clausen, E. Laegsgaard, and F. Besenbacher. Size-dependent structure of MoS_2 nanocrystals. *Nat. Nanotechnol.*, 2:53–58, 2007.

[370] F. Besenbacher, M. Brorson, B.S. Clausen, S. Helveg, B. Hinnemann, J. Kibsgaard, J.V. Lauritsen, P.G. Moses, J. K. Nørskov, and H. Topsøe. Recent STM, DFT and HAADF-STEM studies of sulfide-based hydrotreating catalysts: Insight into mechanistic, structural and particle size effects. *Catal. Today*, 130:86–96, 2008.

[371] M. Badawi, J.-F. Paul, S. Cristol, and E. Payen. Guaiacol derivatives and inhibiting species adsorption over MoS_2 and CoMoS catalysts under HDO conditions: A DFT study. *Catal. Commun.*, 12:901–905, 2011.

[372] J. K. Nørskov, B. S. Clausen, and H. Topsøe. Understanding the trends in hydrodesulfurization activity of the transition metal sulfides. *Catal. Lett.*, 13:1–8, 1992.

[373] W. Mu, H. Ben, A. Ragauskas, and Y. Deng. Lignin pyrolysis component and upgrading - technology review. *Bioenerg. Res.*, 6:1183–1204, 2013.

[374] A. L. Jongerius, J. R. Copeland, G. S. Foo, J. P. Hofmann, P. C. A. Bruijnincx, C. Sievers, and B. M. Weckhuysen. Stability of Pt/γ-Al_2O_3 catalysts in lignin and lignin model compounds solutions under liquid phase reforming reaction conditions. *ACS Catal.*, 3:464–473, 2013.

[375] D. Kubicka and J. Koracek. Deactivation of HDS catalysts in deoxygenation of vegetable oils. *Appl. Catal. A: Gen.*, 394:9–17, 2011.

[376] A. Y. Bunch, X. Wang, and U. S. Ozkan. Hydrodeoxygenation of benzofuran over sulfided and reduced Ni-Mo/γ-Al_2O_3 catalysts: Effect of H_2S. *J. Mol. Cat. A: Chem.*, 270:264–272, 2007.

[377] A. Andersen, S. M. Kathmann, M. A. Lilga, K. O. Albrecht, R. T. Hallen, and D. Mei. Adsorption of potassium on MoS_2 (100) surface: A first principle investigation. *J. Phys. Chem. C*, 115:9025–9040, 2011.

[378] J. P. Chen, M. A. Buzanowski, R. T. Yang, and J. E. Cichanowicz. Deactivation of the vanadia catalyst in the selective catalytic reduction process. *J. Air Waste Manage.*, 40:1403–1409, 1990.

[379] Y. Zheng, A. D. Jensen, and J. E. Johnsson. Laboratory investigation of selective catalytic reduction catalysts: Deactivation by potassium compounds and catalyst regeneration. *Ind. Eng. Chem. Res.*, 43:941–947, 2004.

[380] M. Marafi, A. Stanislaus, and E. Furimsky. *Handbook of Spent Hydroprocessing Catalysts*, chapter 4: Catalyst Deactivation, pages 51–92. Elsevier: Amsterdam, 2010.

[381] P. Stoltze and J. K. Nørskov. *Handbook of Heterogeneous Catalysis*, chapter 13.11: Theoretical Modeling of Catalytic Reactions, pages 1479–1492. John Wiley & Sons, Inc.: New York, 2008.

[382] P. Bui, J. A. Cecilia, S. Oyama, A. Takagaki, A. Infantes-Molina, H. Zhao, D. Li, E. Rodríguez-Castellón, and A. Jiménez López. Studies of the synthesis of transition metal phosphides and their activity in the hydrodeoxygenation of a biofuel model compound. *J. Catal.*, 294:184–198, 2012.

[383] J. A. Cecilia, A. Infantes-Molina, E. Rodríguez-Castellón, A. Jiménez López, and S. Oyama. Oxygen-removal of dibenzofuran as a model compound in biomass derived bio-oil on nickel phosphide catalysts: Role of phosphorus. *Appl. Catal. B: Environ.*, 136-137:140–149, 2013.

[384] X. Xu, C. Zhang, Y. Liu, Y. Zhai, and R. Zhang. Two-step catalytic hydrodeoxygenation of fast pyrolysis oil to hydrocarbon liquid fuels. *Chemosphere*, 93:652–660, 2013.

[385] A. K. Datye. Electron microscopy of catalysts: recent achievements and future prospects. *J. Catal.*, 216:144–154, 2003.

[386] Shima Kadkhodazadeh. High resolution STEM of quantum dots and quantum wires. *Micron*, 44:75–92, 2013.

[387] R. S. Rai and S. Subramanian. Role of transmission electron microscopy in the semiconductor industry for process development and failure analysis. *Prog. Cryst. Growth Ch.*, 55:63 – 97, 2009.

[388] T. W. Hansen, J. B. Wagner, and R. E. Dunin-Borkowski. Aberration corrected and monochromated environmental transmission electron microscopy: challenges and prospects for materials science. *Mater. Sci. Technol.*, 26:1338–1344, 2010.

[389] E. A. Stach. Real-time observations with electron microscopy. *Mater. Today*, 11, Supplement:50–58, 2008.

[390] R. Sharma. Kinetic measurements from in situ TEM observations. *Microsc. Res. Techniq.*, 72:144–152, 2009.

[391] E. D. Boyes and P. L. Gai. Environmental high resolution electron microscopy and applications to chemical science. *Ultramicroscopy*, 67:219–232, 1997.

[392] K. Kishita, H. Sakai, H. Tanaka, H. Saka, K. Kuroda, M. Sakamoto, A. Watabe, and T. Kamino. Development of an analytical environmental TEM system and its application. *J. Elec. Microsc.*, 58:331–339, 2009.

[393] Comsol. *COMSOL - Chemical Engineering Module User's Guide*, 2005. Version 3.2.

[394] R. B. Bird, W. E. Stewart, and E. N. Lightfoot. *Transport Phenomena.* John Wiley & Sons, Inc.: New York, 2007.

[395] W. M. Haynes, editor. *CRC Handbook of Chemistry and Physics 92th Edition (Internet Version 2012).* CRC Press, April 2010.

[396] J. B. Mehl, M. L. Huber, and A. H. Harvey. Ab initio transport coefficients of gaseous hydrogen. *Int. J. Thermophys.*, 31:740–755, 2010.

[397] E. J. Owens and G. Thodos. Thermal-conductivity-reduced-state correlation for the inert gases. *A.I.Ch.E. J.*, 3:454–461, 1957.

[398] The engineering toolbox, November 2011. `http://www.engineeringtoolbox.com`.

[399] Comsol. *COMSOL Multiphysics - Reference Guide*, 2010. Version 4.0a.

[400] C. R. Wilke and P. Chang. Correlation of diffusion coefficients in dilute solutions. *AIChE J.*, 1:264–270, 1955.

[401] T. Shinomiya. Dielectric dispersion and intermolecular association for 28 pure liquid alcohols the position dependence of hydroxyl group in the hydrocarbon chain. *B. Chem. Soc. Jpn.*, 62:908–914, 1989.

[402] C. N. Satterfield and T. K. Sherwood. *The Role of Diffusion in Catalysis.* Addison-Wesley: London, 1963.

[403] C. T. Campbell, S. C. Parker, and D. E. Starr. The effect of size-dependent nanoparticle energetics on catalyst sintering. *Science*, 298:811–814, 2002.

[404] V. N. Parmon. Thermodynamic analysis of the effect of the nanoparticle size of the active component on the adsorption equilibrium and the rate of heterogeneous catalytic processes. *Dokl. Phys. Chem.*, 413:42–48, 2007.

Appendices

Appendix A

Modeling of Temperature Profiles in an Environmental Transmission Electron Microscope using Computational Fluid Dynamics

Abstract

The temperature gradient and pressure drop inside an environmental transmission electron microscope have been addressed by means of computational fluid dynamics. Heating the sample area by a furnace type TEM holder gives rise to temperature gradients over the sample area. Three majors mechanism have been identified with respect to heat transfer in the sample area: radiation, conduction in the grid and conductivity in the gas. The sample temperature was affected by the conductivity of the gas, the emissivity of the sample grid, and the conductivity of the grid. Ideally the grid should be polished and of a good conductive material, like conventionally used Cu. With hydrogen gas, which have the highest conductivity of the studied gases, the temperature difference over the TEM grid is less than 5°C, at what must be considered typical conditions, and it is concluded that close to isothermal conditions can be achieved in the ETEM.

A.1 Introduction

Since its invention, transmission electron microscopy (TEM) has been an invaluable addition to the materials science toolbox. It has been routinely used in fields such as catalysis, semiconductors and photonics [385–387]. No other tool provides the versatility of spatial information at high resolution along with simultaneous acquisition of spectroscopic information. More recently, *in situ* experimentation within the TEM has also become possible [388–390]. Scientists are now routinely exposing samples to heat, gas, liquid, stress, and light while performing electron microscopical investigations.

In order to expose samples to a gaseous environment, certain modifications have to be made. Gas can be introduced either via the microscope column or via the sample holder. In the former case, the microscope column itself is fitted with a gas inlet through the objective lens and differential pumping apertures in the upper and lower pole pieces. This setup is known as the differentially pumped column and is described by Boyes *et al.* [391]. The other option is to inject gases via the sample holder. This has been described by Kishita *et al.* [392]. In either case, microscopes capable of exposing samples to a gaseous atmosphere are now known as environmental transmission electron microscopes or ETEMs.

In order to simulate the working environment of e.g. an industrial catalyst, a gas atmosphere along with an ability to heat the sample is necessary. Heating is typically done using a heating holder. However, this also represents a challenge to conventional knowledge of TEM experimentation. Conventionally, heating experiments in the TEM has been carried out in high vacuum. This means that very little power is needed to heat the entire sample region (traditionally a metal grid of 3 mm in diameter) as there is virtually no gas atmosphere to remove heat from the sample. In an ETEM however, there is a flow of gas and thus a heat sink around the sample. Hence additional heat needs to be supplied in order to maintain a certain set temperature. Furthermore, as heat (in traditional heating holders) is supplied via the periphery of the 3 mm metal grid, there may be a temperature gradient across the sample, rendering the center of the 3 mm grid at a lower temperature than what is measured at the furnace supplying the heat. However, to the best knowledge of the authors, the level of non-uniformity of the sample holder temperature field has not been investigated previously.

In order to understand the significance of the temperature gradient across the sample, CFD modeling of the interior of the microscope, sample holder, and sample grid have been employed in this work.

Using a simplified model of the inside of an objective lens, the gas flow inside the ETEM chamber in steady state is calculated. Based on this flow, the temperature field is obtained and thereby the temperature distribution in the sample area. The simulation were made using the Weakly Compressible Navier-Stokes and General Heat Transfer packages of the commercial software program Comsol ® were used.

A.2 CFD Model

The CFD model was defined and solved using Comsol ®; a commercial multiphysics modeling and simulation software. Figure A.1(a), A.1(b), and A.1(c) show a two

dimensional cross section of the modeled geometry of respectively the x-y-plane, y-z-plane, and x-z-plane.

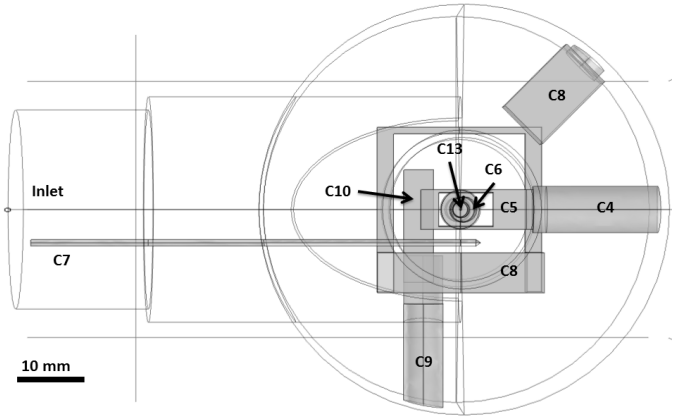

(a) x-y-plane

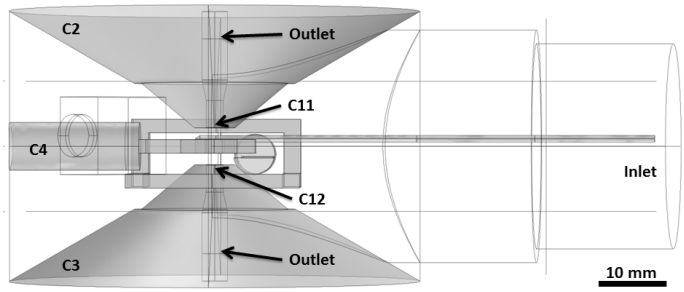

(b) y-z-plane

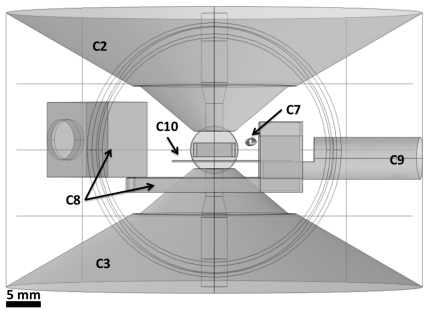

(c) x-z-plane

Figure A.1: *Cross section of the structure of the CFD model used in the evaluation of the ETEM.*

The model is divided into thirteen regions, denoted as CX, where X denotes a specific region.. Table A.1 describes the function of each of these regions and their nature.

A sample holder is inserted from the left of Figure A.1(b). This consists of three sections: the holder barrel (C4), the holder around the heating coil (C5), and the heating coil (C6). When using the ETEM the sample is placed in the center of the heating coil on a grid (C13); the center of this grid is used as origin in the drawings of Figure A.1. A cold trap (C8) is placed around the holder and beneath the holder is the objective aperture which consist of an objective aperture barrel (C9) and the objective diaphragm (C10). A sniffer (C7) connected to a quadropole mass spectrometer is placed parallel to the gas flow with the orifice facing the sample. Above and below the sample are the upper and lower pole pieces (truncated cones, C2 and C3), which have a Pt 250 μm diaphragm (C11 and C12) at the cone center.

The gas (C1 and white area in Figure A.1) enters the system through the boundary to the right in Figure A.1(b) and leaves the system through exits at the top and bottom after the diaphragms (C11 and C12), see Figure A.1(b) for clarification. The hole in the diaphragms have a diameter of 250 μm and a height of 50 μm and are therefore barely visible on Figure A.1(b). Pole pieces and diaphragms are kept at a constant temperature of 20 °C by cooling water.

Table A.1: Regions of the CFD model.

Region	Description	Material
C1	Gas phase	H_2/N_2
C2	Upper pole piece	304 steel
C3	Lower pole piece	304 steel
C4	Holder barrel	304 steel
C5	Holder	Brass
C6	Heating coil	Brass
C7	Sniffer	304 steel
C8	Cold trap	Copper
C9	Objective aperture barrel	Brass
C10	Objective diaphragm	Platinum
C11	Top 250 μm Pt diaphragm	Platinum
C12	Bottom 250 μm Pt diaphragm	Platinum
C13	Sample Cu grid	Copper & H_2/N_2

A.2.1 Weakly Compressible Navier-Stokes Equations

In the evaluation of the velocity field in the reactor the calculations are based on a weakly compressible Navier-Stokes model implemented in Comsol ®. The equations being solved for the gas phase are thus:

$$\rho \cdot \left(\frac{\partial \underline{v}}{\partial t} + \underline{v} \cdot \nabla \underline{v} \right) = -\nabla P + \rho \cdot g + \mu \nabla^2 \underline{v} - \nabla \cdot \left(\frac{2 \cdot \mu}{3} + \kappa \right) (\nabla \cdot \underline{v}) \tag{A.1}$$

$$\frac{\partial \rho}{\partial t} + (\nabla \cdot \rho \underline{v}) = 0 \tag{A.2}$$

Where $\underline{v}$ is the vector describing the velocity at a given point, ρ the density of the medium, P the total pressure, g the gravitational acceleration, μ the dynamic viscosity, and κ the dilatational viscosity. In this case where steady state is examined, the term $\partial \underline{v}/\partial t$ is zero.

These equations are based on the traditional Navier-Stokes equation and the equation of continuity, but with the introduction of the $(2 \cdot \mu/3 + \kappa)(\nabla \cdot \underline{v})$ term in the Navier-Stokes equation in order to compensate for the changes in the fluid as a function of temperature. This form of the Navier-Stokes equations can be used in the case where the Mach number is below 0.3, where relatively small changes in density occur as a function of temperature, and no change in internal energy occur as a function of either expansion or compression [393]. In the current system the Mach number is generally found to be in the order of 10^{-4}, only very localized around the 250 μm pressure limiting apertures the Mach number is higher. Viscosity increases by a factor of ca. 2 when the temperature increases from 25 to 500 °C, similarly the density decreases by a factor of ca. 0.4 in the same temperature interval. Furthermore, these changes do not occur along the major streamlines in the system. Thus, this overall justifies the use of this modified form of the Navier-Stokes equation in the current case.

The gas phase equations should be solved in C1 and C13, as the other regions are solids where momentum is not relevant. In principle C13 is a Cu grid with a porosity

of 0.5, but as the grid is only 15 μm thick and it was realized that the gas flow at the center was very small it was chosen to treat this part of the model as gas.

In order to solve this system, the gas viscosity and density must be known; both parameters which are dependent on temperature. κ is known to be zero for all monatomic gases at low density and for simple gas compositions behaving similar to ideal gases [394], thus it is assumed that it is zero in all cases treated, which is a fair assumption.

Viscosity data [395] for H_2 was fitted to a 5th order expression with Excels least square method. In this way the following expression was obtained for the viscosity:

$$\begin{aligned}\mu_{\mathrm{H}_2} = &+ 4.48 \cdot 10^{-20} T^5 - 7.50 \cdot 10^{-17} T^4 + 3.83 \cdot 10^{-14} T^3 \\ &- 1.44 \cdot 10^{-11} T^2 + 2.68 \cdot 10^{-8} T + 1.62 \cdot 10^{-6} \quad [Pa \cdot s]\end{aligned} \tag{A.3}$$

Inserting T in Kelvin.

As nitrogen was used as gas phase for some of the simulations a similar expression was derived for this in the temperature interval from -100-400 °C with data from CRC [395]:

$$\mu_{\mathrm{N}_2} = -2.93 \cdot 10^{-11} T^2 + 6.53 \cdot 10^{-8} T + 8.60 \cdot 10^{-7} \quad [Pa \cdot s] \tag{A.4}$$

Inserting T in Kelvin.

The density in the gas phase was calculated on the basis of the ideal gas law:

$$\rho_{gas} = \frac{P_{in}}{R \cdot T} \cdot \sum_i M_i \cdot x_i \tag{A.5}$$

Where P_{in} is the inlet pressure, R the ideal gas constant, M_i the molar mass of component i, and x_i the mole fraction of component i. It was chosen to fix the pressure to the inlet pressure in Eq. A.5, as this did not change much inside the ETEM. The inlet pressure was found from experiments.

A.2.1.1 Boundary conditions

At the inlet, the linear gas velocity is specified as:

$$v_0 = \frac{F}{A} \tag{A.6}$$

With F being the volumetric flow and A the cross sectional area.

The boundaries to C2-C12 are all specified as no slip, meaning that the linear velocity on these surfaces is equal to zero, as shown in Eq. A.7:

$$\underline{v} = 0 \tag{A.7}$$

At the outlet of the reactor no viscous stress with a constant pressure is specified. This generates a fix point for the pressure simulation in the chamber. This pressure is measured during ETEM experiments.

A.2.2 General Heat Transfer

The temperature field and energy transport in the system is simulated on the basis of the equation of energy:

$$\rho \cdot C_p \cdot \left(\frac{\partial T}{\partial t} + \underline{v} \cdot \nabla T \right) = k \cdot \nabla^2 T + Q \tag{A.8}$$

Where C_p is the heat capacity, k the thermal conductivity, and Q the supplied heat. This equation must be solved in all regions. At steady state the $\partial T/\partial t$ term is zero.

To calculate the temperature field in C1, the density (ρ), heat capacity (C_p), and conductivity (k) are needed. ρ has already been defined in eq. A.5. C_p and k are defined similarly to the viscosity in Eq. A.3, on the basis of table values from 0-800 °C [395, 396]:

$$\begin{aligned} C_{p,\mathrm{H_2}} &= -7.61 \cdot 10^{-9}T^4 + 2.40 \cdot 10^{-5}T^3 - 2.59 \cdot 10^{-2}T^2 \\ &\quad + 12.1T + 1.24 \cdot 10^4 \quad [J/kg/°C] \end{aligned} \tag{A.9}$$

$$\begin{aligned} k_{\mathrm{N_2}} &= +1.80 \cdot 10^{-15}T^5 - 3.63 \cdot 10^{-12}T^4 + 2.75 \cdot 10^{-9}T^3 \\ &\quad - 1.25 \cdot 10^{-6}T^2 + 8.42 \cdot 10^{-4}T - 4.46 \cdot 10^{-3} \quad [W/m/°C] \end{aligned} \tag{A.10}$$

Inserting T in Kelvin.

Similar expressions were also derived for N_2 in the temperature interval from -100-400 °C with data from CRC [395]:

$$C_{p,\mathrm{N_2}} = -3.32 \cdot 10^{-7}T^3 + 7.95 \cdot 10^{-4}T^2 - 3.88 \cdot 10^{-1}T + 1.09 \cdot 10^3 \quad [J/kg/°C] \tag{A.11}$$

$$k_{\mathrm{N_2}} = -4.05 \cdot 10^{-8}T^2 + 9.89 \cdot 10^{-5}T + 1.00 \cdot 10^{-5} \quad [W/m/°C] \tag{A.12}$$

Inserting T in Kelvin.

No pressure correction is introduced for the thermal conductivities, as this does not have any significant effect in the current case [397].

In C2-C12, solids are treated, where heat transfer is only by conduction and the left side of eq. A.8 is therefore set to zero. Physical parameters for these areas are assumed independent of temperature as a first approximation and summarized in Table A.2.

Table A.2: *Parameters for the solid regions in the CFD model. Data from references [395, 398].*

Region	Material	ρ [kg/m^3]	C_p [J/kg/°C]	k [W/m/°C]	ϵ
C2-C4, C7	304 steel	7900	500	21	0.6
C5, C6, C9	Brass	8470	377	100	0.22
C8	Copper	8960	385	401	0.03
C10-C13	Platinum	21500	133	72	0.08

As C13 is porous it was chosen to simulate the physical parameters of this layer by accounting for the porosity (ϕ), i.e.:

$$\rho_{\mathrm{Cu}-grid} = \rho_{\mathrm{Cu}} \cdot (1-\phi) + \rho_{gas} \cdot \phi \tag{A.13}$$

$$C_{p,\mathrm{Cu}-grid} = C_p, \mathrm{Cu} \cdot (1-\phi) + C_{p,gas} \cdot \phi \tag{A.14}$$

$$k_{\mathrm{Cu}-grid} = k_{\mathrm{Cu}} \cdot (1-\phi) + k_{gas} \cdot \phi \tag{A.15}$$

The porosity of a 60×60 μm Cu grid was calculated to be 0.498.

A.2.2.1 Boundary conditions

At the inlet of C1, room temperature is specified as boundary condition. Top face and bottom face of C2 and C3, respectively, was specified as 25 °C. Additionally the surface of C6 was fixed to the desired temperature of the heating coil.

Internal boundaries between C1 and C2-C13 are specified by continuity in the heat flux, which satisfies the following condition:

$$-\underline{n_u} \cdot (-k_u \cdot \nabla T_u) - \underline{n_d} \cdot (-k_d \cdot \nabla T_d) = 0 \tag{A.16}$$

Here $\underline{n_i}$ is the normal vector, k_i the conductivity, and T_i the temperature, index u and d indicate upward and downward. This expression specify that the the normal heat flux on the upside of the boundary is equal to the normal heat flux on the downside of the boundary.

At the outlet of C1 a conductive flux is specified:

$$-\underline{n} \cdot (-k \cdot \nabla T) = 0 \tag{A.17}$$

So the gradient across the boundary must be zero, which is true in the case of uniform temperature. Similarly the edges of C1 are described as insulation, which means that the same expression should be satisfied:

$$-\underline{n} \cdot (-k \cdot \nabla T) = 0 \tag{A.18}$$

Thus, no heat is transferred over these boundaries.

The objects surrounding the heating coil are treated as radiative surfaces, Figure A.2 shows the relevant surfaces. At this interface the heat transfer by radiation is defined as:

$$\begin{aligned} \epsilon \cdot (G - \sigma \cdot T^4) &= -\underline{n_u} \cdot (-k_u \cdot \nabla T_u) - \underline{n_d} \cdot (-k_d \cdot \nabla T_d) \\ J - \epsilon \cdot \sigma \cdot T^4 &= (1 - \epsilon) \cdot G \end{aligned} \tag{A.19}$$

Here ϵ is the emissivity, G the irradiation, J the radiosity, and σ the Stefan-Boltzmann constant.

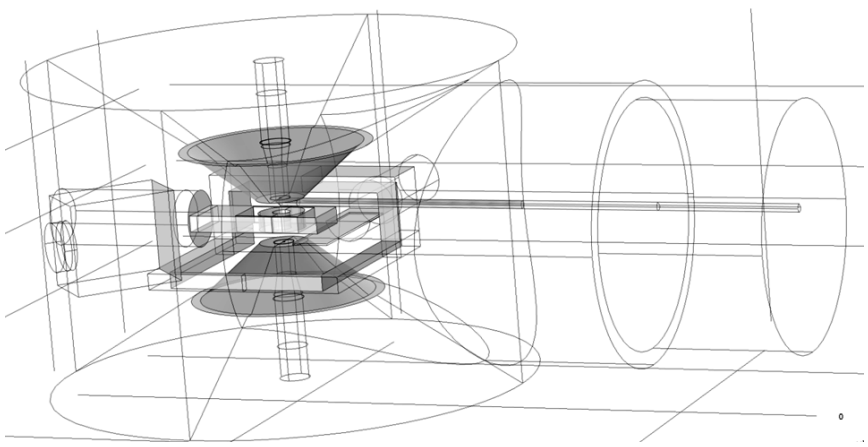

Figure A.2: *Surfaces simulated with respect to radiation in the model.*

The net heat flux ($q_{rad,net}$) into the object is given as the difference between the irradiation and radiosity:

$$q_{rad,net} = G - J \tag{A.20}$$

ϵ is assumed independent of temperature. The values of this parameter of the surfaces of the different regions are given in Table A.2.

At the surface of region C6 a constant temperature is defined as well as radiation, thus:

$$(1 - \epsilon) \cdot G = J - \epsilon \cdot \sigma \cdot T_{coil}^4 \tag{A.21}$$

Where T_{coil} is the surface temperature of the coil.

A.2.3 Mesh and Model Evaluation

The mesh used for the simulations was automatically created by Comsol ® by the Delaunay algorithm [399]. Figure A.3 shows the general distribution and size of the elements used in the simulations. Smaller elements were used in the more narrow regions of the geometry, with very small elements around the 250 μm apertures, and larger toward the entrance to the microscope.

To evaluate the quality of the mesh, a mesh sensitivity analysis was made on the basis of the predefined mesh in Comsol ®. Figure A.4 shows the variance in the simulated pressure drop over the pressure limiting apertures and center temperature with varying mesh quality. The center temperature was not particularly influenced by the quality of the grid, as this changed less than 0.5 °C from the coarsest to the finest mesh. The pressure drop was influenced more by the change in the mesh, as this varied in the range from 3.6 mbar to 5.11 mbar, but stabilizes when the mesh number is larger than 300,000.

Based on the mesh analysis it was decided to use a mesh consisting of ca. 330,000 elements.

As discussed in Section A.2.2.1 only the surfaces shown in Figure A.2 were simulated with respect to radiation. Limiting the model to only include these surfaces was done in order to save computational power and increase calculation speed. To evaluate the error introduced by this choice, a simulation was performed where all

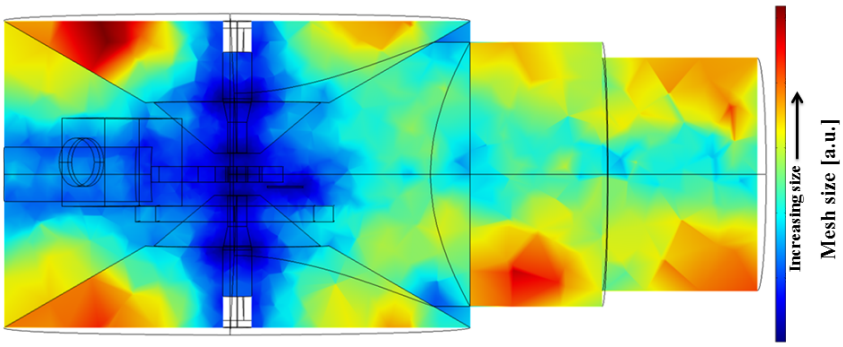

Figure A.3: *Distribution and size of elements in the mesh used for the simulation viewed in the cross-section of the y-z-plane. The current case is equivalent to a mesh of ca. 380,000 elements. Inlet flow = 10 Nml/min, Coil temperature = 500 °C, Gas phase: H_2.*

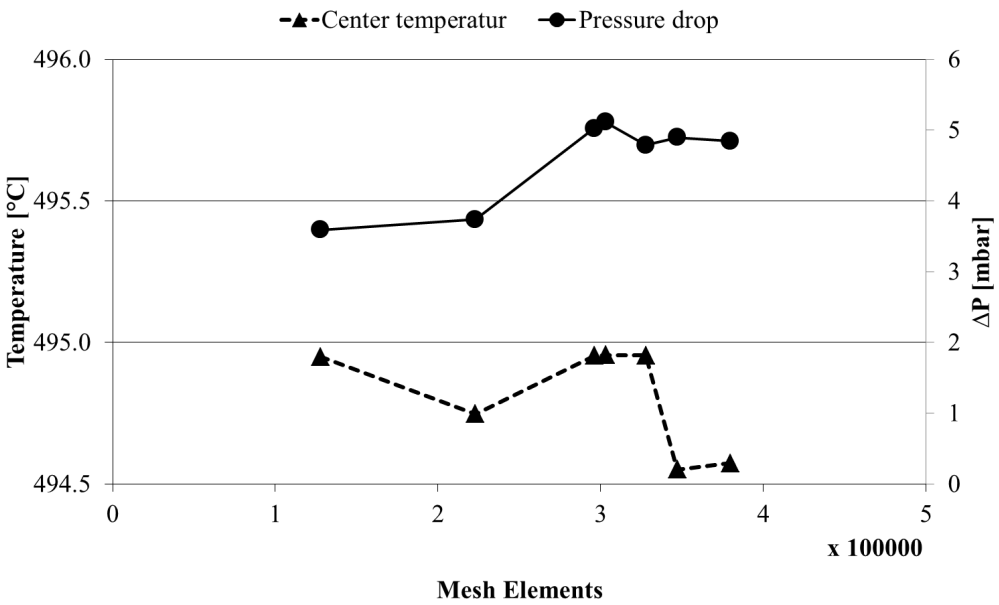

Figure A.4: *Dependency of simulated center temperature (middle of Cu-grid) and pressure drop in the system as a function of the quality of the used mesh. Inlet flow = 10 Nml/min, Coil temperature = 500 °C, Gas phase: H_2.*

surfaces were treated as active with respect to radiation in a case with a flow of 5 Nml/min H_2 and a coil temperature of 500 °C. The center temperature was 496.430 °C when only simulating radiation on the surfaces shown in Figure A.2 and 496.425 °C when simulating for all surfaces. Thus, limiting the radiation simulation to the surfaces of Figure A.2 seems as a fair assumption as the difference between the two cases is only 0.005 °C.

A.3 Results and Discussion

A.3.1 General Model Analysis

A general model analysis was made of a case with a feed flow of 10 Nml/min H_2 and a coil temperature of 500 °C.

Figure A.5(a) shows the velocity field around the sample in the ETEM. The flow rate near the gas inlet is in the order of <0.1m/s (see also Figure A.5(b)), but approaching the apertures (2-5 mm from the constriction) the gas velocity increases. Looking at both Figure A.5(a) and A.5(b) shows that the gas speed in this region is ca. 5 m/s, but in the narrow aperture the gas velocity increases to around 300 m/s; the acceleration from ca. 10 m/s to around the 300 m/s takes place over a length in the order of 0.5 mm. At this velocity the model might be insufficient to fully describe what is occurring. However it gives a clear indication of the very turbulent behavior of the system around this very narrow constriction. A relatively fast deceleration takes place on the low pressure side of the aperture, but due to the more narrow dimensions, the velocity ends at about 3 m/s.

The stream lines in Figure A.5(b), show the same pattern as in Figure A.5(a). The gas enters the microscope and is evenly distributed throughout the microscope.

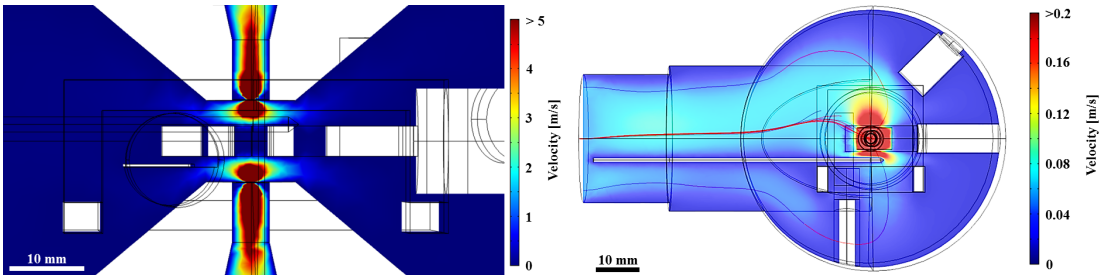

(a) y-z-plane through the center (b) x-y-plane parallel to the sniffer

Figure A.5: *Cross sections of the velocity field and stream lines around the center of the ETEM. Dark red area indicates an area where the velocity is greater than the maximum of the scale bars. White regions indicate solids. Red lines in (b) are streamlines. Inlet flow = 10 Nml/min, Coil temperature = 500 °C, Gas phase:* H_2.

Approaching the apertures, all streamlines are however converging, showing that all gas must pass the same narrow region.

In the region inside the heating coil, where the sample is placed, the velocity is very close to 0 m/s. This means that practically no flow passes the center. Thus, the primary gas transport mechanism to the sample in the ETEM is by diffusion.

Looking at the velocity field in the x-y-plane parallel to the sniffer and in the region between the sample holder and the upper aperture in Figure A.5(b), the flow entering the ETEM is laminar. Approaching the center, the streamlines distribute in the void around the sample holder and then converges toward the apertures. In this region the flow is accelerated. Due to the sniffer an asymmetric profile is observed, where the gas more easily passes on the side where the sniffer is not placed.

Additionally, the model shows that the void of the ETEM practically has the same pressure. The only pressure drop is found across the apertures.

The good heat conductivity of the steel of the pole pieces means that the surface temperature of these is very close to 25 °C. As the coil is 500 °C, the temperature drops 480 °C over a length of only ca. 5 mm in the vertical direction. The heat is on the other hand better distributed in the horizontal direction. This is better illustrated in Figure A.6(b), where the surroundings of the heating coil is heated. Most notable is how the solid part of the microscope is heated more efficient than the gas. The holder rod has a temperature of ca. 150 °C and the aperture rod has a temperature of ca. 75 °C. With respect to the gas phase, this is practically not heated anywhere except very close (<5mm) to the heating coil.

The temperature profile across the sample is shown in Figure A.7. Here the same trends are observed as discussed above, i.e. a higher temperature of the holder compared to the gas; 5 mm into the gas phase from the holder edge the temperature has dropped to below 100 °C. At the center, where the sample is placed, a small drop in temperature is observed when approaching the center of the grid. This temperature drop is symmetric around the center. The minimum temperature in the current case is 496.9 °C, compared to 500 °C at the coil.

In conclusion, it is apparent that the temperature of the grid is close to the set point of the coil in the current case, with a deviation in the order of only 3-4 °C.

In Figure A.8 an overview of the heat transfer by radiation on the surfaces close

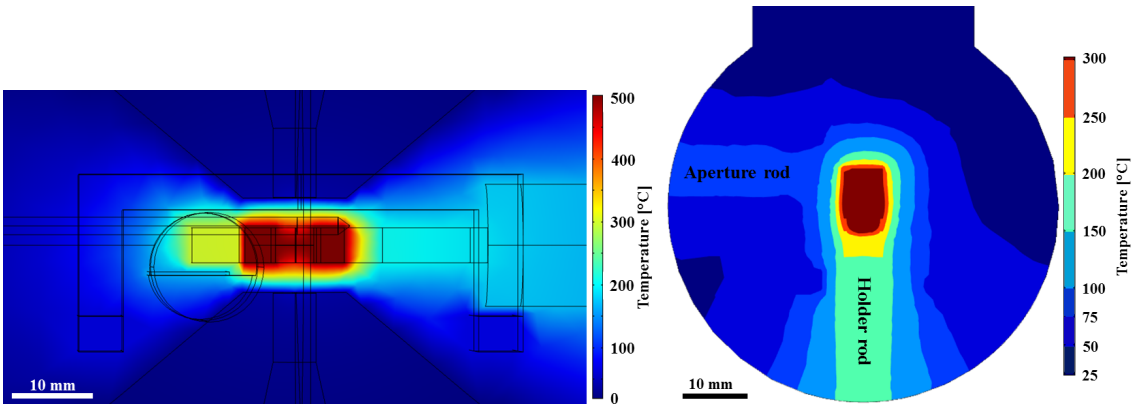

(a) Temperature profile in the y-z-plane crossing the center

(b) Contours of temperature zones in the x-y-plane crossing the center

Figure A.6: *Temperature profiles in the ETEM. (a) shows the the y-z cross section view of the temperature around the center of the ETEM and (b) shows the contour plot in the x-y-plane. Inlet flow = 10 Nml/min, Coil temperature = 500 °C, Gas phase:* H_2.

to the center of the ETEM is shown. Here a relatively high net loss of energy takes place on the heating coil. The holder radiates a significant amount of energy as well, but on the sides facing the heating coil also a high irradiation is present and the effective radiation heat flux is therefore close to zero. The area of the pole piece closest to the sample receives relative large amounts of energy by radiation, which is due to their direct placement opposite the heating coil. The net radiation heat flux on the platinum diaphragms is, however, significantly lower. This is due to the markedly lower value of the emissivity of platinum relative to the steel (cf. Table A.2) which in practice means that a large amount of the radiation on the platinum surface is reflected.

A.3.2 Parameter Analysis

A series of simulations were carried out to evaluate the effect on the center temperature of the grid at different conditions, i.e. referring to the point denoted (0, 0, 0) in the current geometry. In the following ΔT will be used as descriptive parameter for the temperature drop and is defined as:

$$\Delta T = T_{Coil} - T_{Center} \tag{A.22}$$

Here T_{Center} is the temperature at (0, 0, 0).

Initially, variations in the feed flow were investigated. Figure A.9 shows the variation in the pressure drop (corresponding to the system pressure due to the very high vacuum on the backside of the apertures) and the center temperature as a function of feed flow variations between 0 and 20 Nml/min of H_2. Obviously, the pressure drop increases with the flow. The figure shows pressure drop data from simulations with coil temperatures at both 25 °C and 500 °C and also experimentally determined pressure drops at 25 °C. Comparing the simulation and the data, these were of the same magnitude. In the low flow range (0-10 Nml/min) the data and

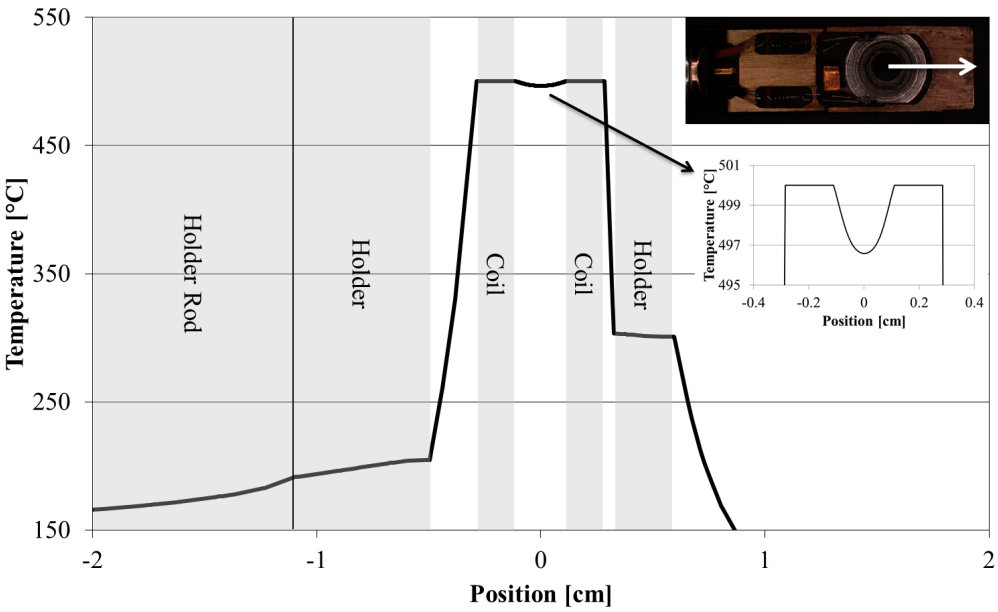

Figure A.7: *Temperature along the y-axis in the x-y-plane crossing the center. The insert shows the localized temperature profile around the sample. Orientation of the profile is shown on the image of the sample holder. Inlet flow = 10 Nml/min, Coil temperature = 500 °C, Gas phase:* H_2.

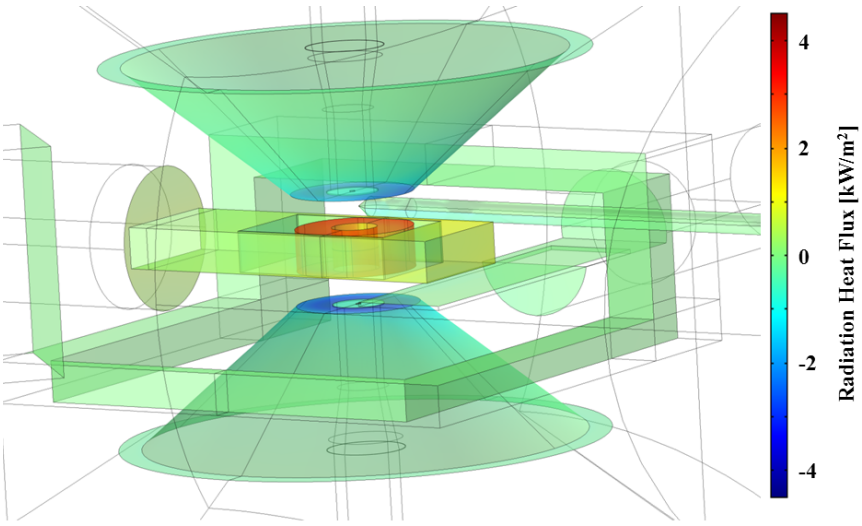

Figure A.8: *Surface radiation in the ETEM expressed as the effective heat flux, i.e. the difference between the irradiation and radiosity. Positive values indicate a higher radiosity compared to irradiation and therefore a net removal of heat. Inlet flow = 10 Nml/min, Coil temperature = 500 °C, Gas phase:* H_2.

the model agree well, deviating less than 0.5 mbar. As the inlet flow increased, the difference however increased and at 20 Nml/min the difference was 2.1 mbar. The reason for the increased difference may be be explained by an increased turbulent behavior of the gas, especially around the apertures, which was not taken into account in the model.

Comparing the simulated pressure drop at the 25 °C and 500 °C coil temperatures showed that the pressure drop increased in the order of 10% when increasing the coil temperature. This is associated with the increasing viscosity of gasses at higher temperatures [394]. This increase in the pressure drop occurs despite the gas passing through the aperture is very close to the 25 °C of the pole pieces, as seen in Figure A.6(a), and the increased pressure drop must therefore be occurring in the heated gas accelerated in the vicinity of the coil.

For the case with 500 °C coil temperature, ΔT is shown as a function of the feed flow in Figure A.9. The temperature difference increased with the feed flow, from a value of 2.1 °C with practically no flow (0.001 Nml/min) to 4.6 °C at 20 Nml/min. This increase in the temperature drop shows that some heat is removed from the system by convection. However, as there is a notable temperature drop in the case with no flow, it is clear that other mechanisms, such as radiation, also plays a role.

The coil temperature was varied between 100 °C and 1000 °C to investigate the effect of this parameter on ΔT; this is shown in Figure A.10. At a coil temperature of 100 °C the temperature difference was only 0.5 °C, but this increased approximately linearly with the coil temperature to a value of 7.2 °C at a coil temperature of 1000 °C.

Figure A.10 also shows the average heat flux by radiation on both sides of the Cu grid as a function of the coil temperature. The heat flux increased in an exponential way as a function of the coil temperature. This is because the heat transfer by radiation varies with the temperature of the surface to the power of 4, as seen from Eq. A.19.

To understand the driving mechanisms for the results in Figure A.9 and A.10 the effect on changing the emissivity and conductivity of the some of the key materials in the systems were investigated.

In Figure A.11 the changes in ΔT as a function of the emissivity of respectively the diaphragm surfaces (C10-C12), the grid surfaces (C13), and the holder surfaces (C5 and C6) are shown. From Figure A.8 these surfaces were evaluated as crucial with respect to the radiation heat flux.

In the case of the diaphragms, ΔT increased only slightly when increasing the emissivity, and in practice it did not influence the result. However, by increasing the value of the emissivity the reflective tendency of the diaphragm surfaces observed in Figure A.8 decreased. Evaluating the average radiation flux in the cases with diaphragms emissivities of 0.08 and 0.96 gives respectively -580 W/m^2 and -6297 W/m^2, despite the irradiation in the two cases is approximately the same, respectively 7799 W/m^2 and 7113 W/m^2. Thus significantly more heat is absorbed when the emissivity of the apertures is increased. This, however, does not influence the center temperature.

Figure A.11 shows that changing the emissivity of the holder, which from Figure A.8 was observed to be a highly radiative surfaces, only had negligible influence on

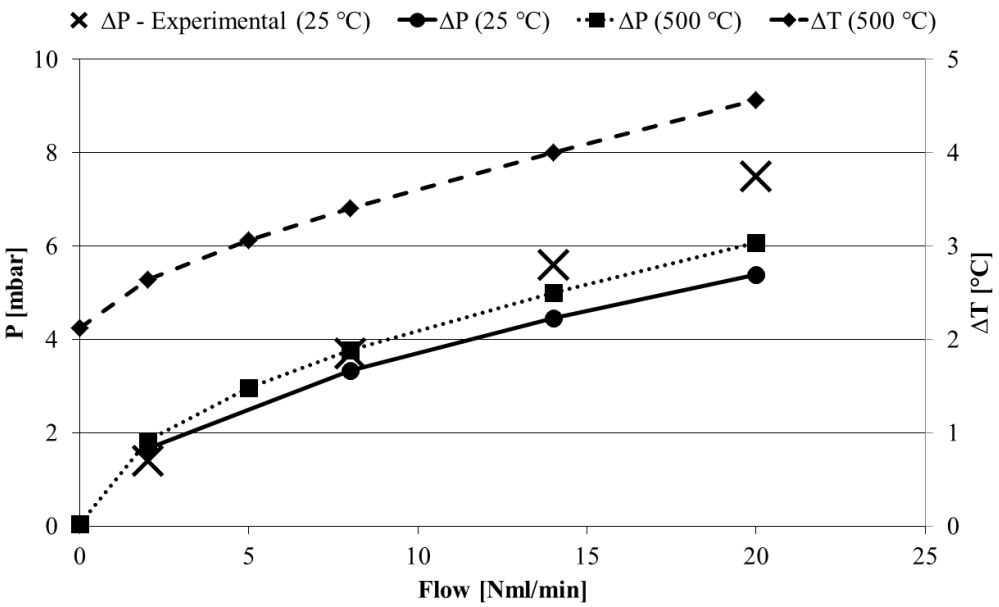

Figure A.9: *Pressure drop and ΔT as a function of the inlet flow. ΔP corresponds closely to the absolute pressure in the microscope. The experimentally determined Δ T was at 25 °C. Gas phase: H_2.*

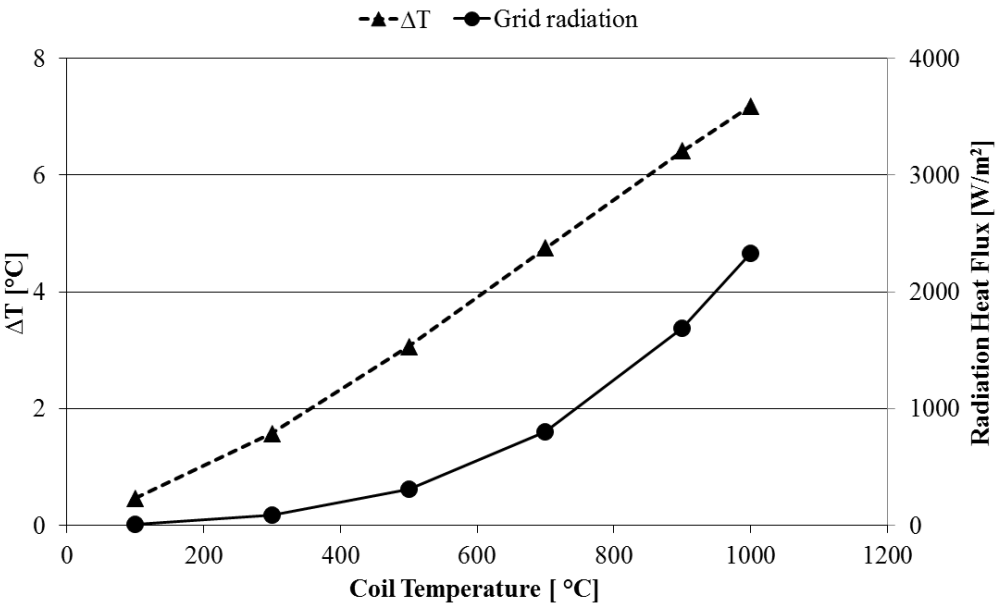

Figure A.10: *Development in ΔT and the average heat radiation flux from the copper grid as a function of the coil temperature. The average heat flux by radiation is evaluated from both sides of the grid. Inlet flow = 5 Nml/min, Gas phase: H_2.*

the center temperature. This indicates that radiation is not the primary heat transfer mechanism for the grid, which also follows from the low temperature difference between the coil surface and the grid surface.

From Figure A.11 it can be seen that the emissivity of the grid is the parameter which influence the center temperature the most. The reference value from Table 3 for the emissivity of copper is 0.03, but increasing this to 0.95 increased ΔT from

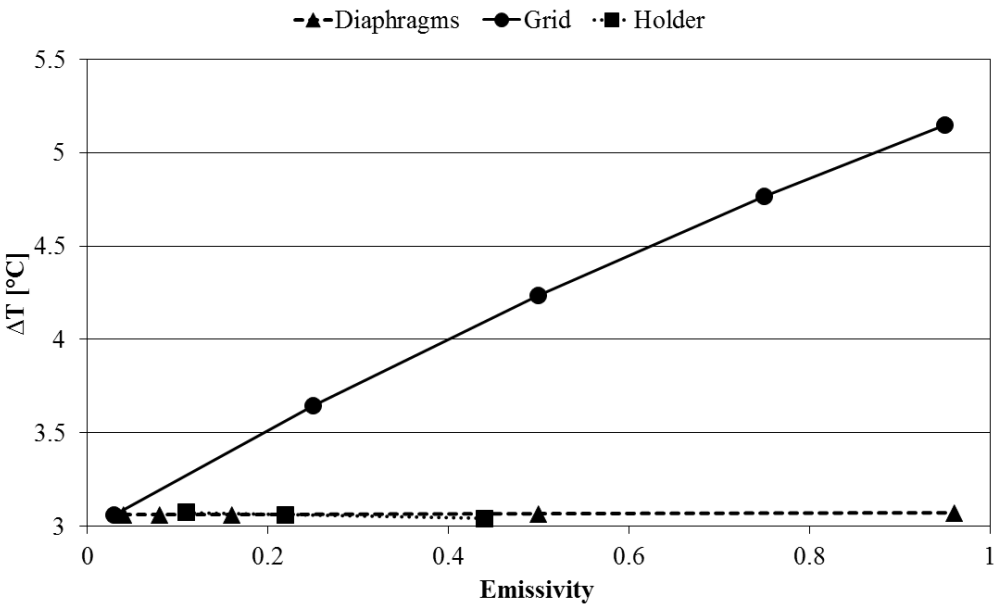

Figure A.11: *Sensitivity of ΔT with respect to changes in the emissivities of the aperture surfaces (C10-C12), the grid surfaces (C13), and the holder surfaces (C5 and C6). Inlet flow = 5 Nml/min, Coil temperature = 500 °C, Gas phase: H_2.*

3.1 °C to 5.1 °C, i.e. an increase by 65%. This must however still be considered minor. Increasing the emissivity has two effects; the reflected energy is decreased and the radiosity from the surface is increased. The first effect means that all energy transferred to the surface from the surroundings is absorbed, however this effect is not very significant as discussed earlier. The second effect describes the radiosity of the surface and this roughly scales with $\epsilon \cdot \sigma \cdot T^4_{surface}$, i.e. the emissivity. From this term it follows that the energy leaving the surface scales with the emissivity. This therefore also explains why ΔT scales more or less linearly with the emissivity of the grid surface.

Figure A.12 shows the influence of varying the conductivity of the holder (C5 and C6) and the grid (C13). In the case of the holder, changing the conductivity had practically no effect on ΔT. Instead this parameter affected the distribution of the heat in the system. Using the interface temperature between the sample holder (C5) and the sample rod (C4) as example, this temperature was 173.6 °C in the case with a conductivity of 70 W/m/°C, but 202.9 °C in the case with a conductivity of 130 W/m/°C. Thus, the latter case would probably result in a longer stabilization time to reach steady state and probably also a higher power on the heating coil.

Figure A.12 also shows the effect on the center temperature when changing the conductivity of the grid. A significant decrease in the center temperature occurred when the conductivity was low, with a conductivity of 500 W/m/°C ΔT was only 2.4 °C, but with a conductivity of 0.1 W/m/°C ΔT increased markedly to 21.7 °C. The latter case corresponds to a case where the grid is an insulator. From the analysis it is clear that it is of high importance that the grid has a high heat conductivity to avoid large temperature variations over the sample. This result, and the analysis for the emissivities in Figure A.11, shows that the primary heat transfer mechanism to the grid is conduction, while radiation is the primary mechanism for transfer of heat

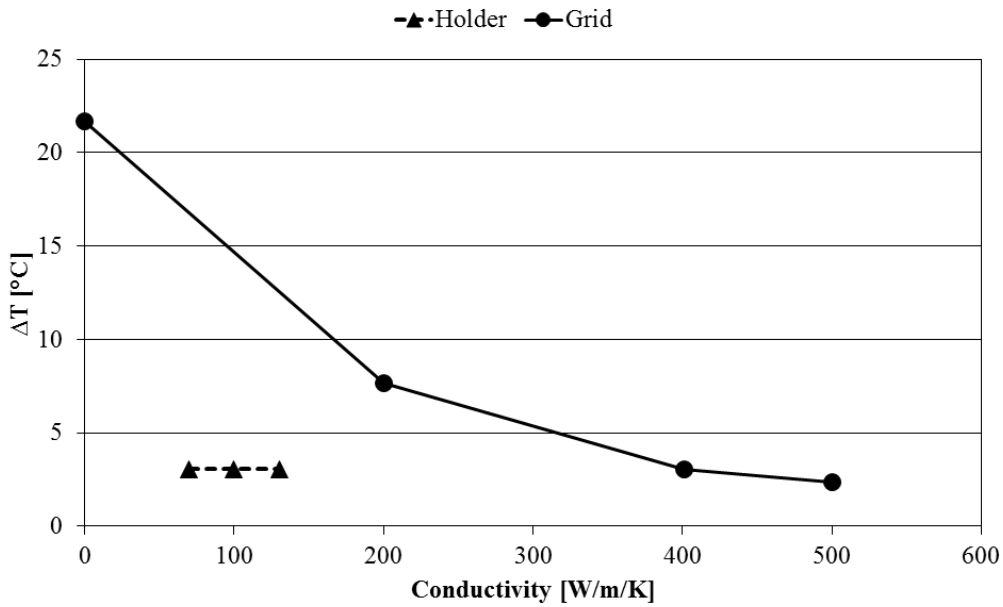

Figure A.12: *Sensitivity of ΔT with respect to changes in the conductivity of the holder (C5 and C6) and the grid (C13). Inlet flow = 5 Nml/min, Coil temperature = 500 °C, Gas phase: H_2.*

away from the grid.

To evaluate the effect of changing the gas, a simulation was made with nitrogen as gas phase instead of hydrogen. The histogram in Figure A.13 displays the major differences between the two cases. For ΔT it is apparent that the temperature drop in hydrogen is much larger compared to nitrogen, 3.1 °C and 0.5 °C respectively. This is most likely because the much higher conductivity of hydrogen compared to nitrogen, as the conductivity of hydrogen at 500 °C is 374 mW/m/°C compared to 54 mW/m/°C for nitrogen [395]. To further investigate this, a case was simulated where the conductivity of hydrogen was lowered to practically 0; this case is also shown in the histogram of Figure A.13. Here a ΔT of 0.2 °C was found, i.e. lower than the case with nitrogen. This shows that the heat loss from the grid is influenced by the conductivity of the gas, and the higher it is the more heat is lost to the surroundings.

Looking at the pressure drop for the case with N_2 compared to H_2 shows a pressure drop of 4.3 mbar for N_2 and 3.0 mbar for H_2. The higher pressure drop observed for nitrogen follows from the markedly higher viscosity, as the viscosity of nitrogen at 500 °C is 36 μPa · s compared to 17 μPa · s for H_2.

Figure A.13 also shows the results from a case study where the grid was removed from the simulation and the zone instead was simulated as part of the gas phase. A significant temperature drop occurred, with a ΔT of 18.8 °C. This result is in continuation of the results observed in Figure A.12, however in this case the radiation was also removed and therefore the temperature drop was less than the case with k_{grid} = 0.1 W/m/°C in Figure A.12. Overall it clearly follows that conduction in the metal grid is an important mechanism to achieve isothermal conditions in the sample region of the ETEM.

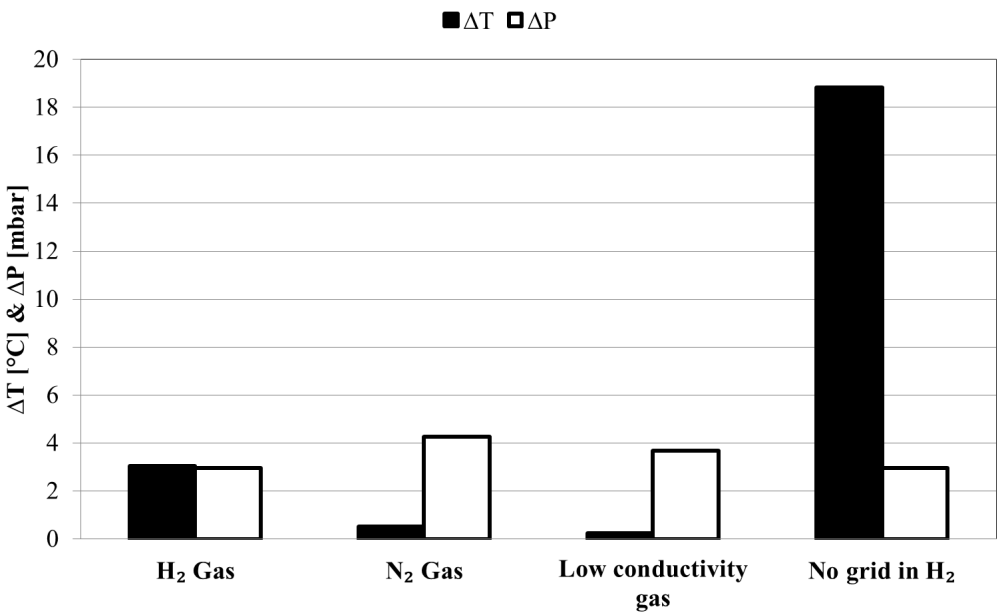

Figure A.13: *Comparison of case studies: a case with H_2 as gas phase, a case with N_2 as gas phase, a case with a gas phase of a conductivity of 1 mW/m/°C (otherwise similar to H_2), and a case without a grid in the sample holder and with H_2 as gas phase. Inlet flow = 5 Nml/min, Coil temperature = 500 °C.*

A.4 Operation Recommendations

Based on the results of the present work, some general guidelines can be given to achieve the most isothermal zone in the ETEM sampleholder. Three main mechanisms have been identified with respect to supplying/removing heat from the sample zone: radiation, conduction in the grid, and conduction in the gas.

The key parameter with respect to radiation is the emissivity of the grid. This should be as low as possible, as the heat flux by radiation scales directly with this parameter. The emissivity of Cu is 0.03 for a pure and polished surface and this is therefore a good choice as grid material. Other highly reflective surfaces are noble metals: silver (0.02-0.03) and gold (0.025) [398]. However, the low emissivity of these materials can be altered by contamination of the surface. Scratches, dirt etc. will increase the value. Even application of the sample and the carbon film will probably result in an increase of the emissivity. In general, it is recommended to keep the surface as polished as possible to minimize the heat loss by radiation.

The heat conductivity of the grid can on the basis of Figure A.12 and A.13 be seen to be of key importance for the transport of heat from the furnace to the sample zone. Copper is a very good conductor, only surpassed by silver among the pure metals as the conductivities of these are 401 W/m/°C and 429 W/m/°C, respectively. Also gold would be a good candidate for the grid material, with a conductivity of 317 W/m/°C. In conclusion, the current analysis indicates that silver could be a slightly better grid material compared to copper.

As the last important parameter, the conductivity of the gas was identified. Due to its very high heat conductivity, hydrogen was found to lead to the largest tem-

perature drop over the sample. Thus, whenever possible it is advised to operate the microscope with gases of low conductivity in order to achieve most isothermal conditions at the sample. H_2 and He are among the gases with the highest conductivities (231 mW/m/°C and 190 mW/m/°C at 127 °C respectively) and should therefore only be used when absolutely needed. As seen from Figure A.13, good isothermal conditions can be achieved with N_2, but if very isothermal conditions are sought krypton or xenon can be considered (as carrier gas) with even lower conductivities of respectively 12 mW/m/°C and 7 mW/m/°C at 127 °C.

Additionally it can be mentioned that having a good insulator as holder material and low reflective diaphragms (e.g. as highly polished Pt) will decrease the heat loss to the surroundings. Besides saving energy, this will decrease the stabilization time for the system.

A.5 Conclusion

A Computational Fluid Dynamics study of flow and temperature fields in an Environmental Transmission Electron Microscope has been made to evaluate the temperature profile over the sample holder. The aim was to calculate how closely the temperature measured on the sample holder/heating coil reflected the actual temperature on the sample grid. The temperature drop from the heating coil to the center of the sample grid was less than or in the order of 5-10 °C when simulating typical operating conditions and it is therefore fair to assume isothermal conditions in most instances.

Three heat transfer mechanisms were found to be important for the temperature at the center of the sample grid: heat transfer by convection in the gas phase, conduction in the grid material, and radiation from the grid surface. Convection is influenced by which gas and what flow is used. Gases with high conductivity (as H_2) and high flow rates increased the heat loss from the sample and increased the temperature difference between coil and sample. Conduction of heat through the grid was found as the most important mechanism for heating the sample. It is advised to use a high conducting material like Cu for the grid to achieve most isothermal conditions. Radiation of heat away from the grid caused loss of heat from the sample region. This scaled with the temperature of the grid and the emissivity. High emissivity (i.e. high radiosity) resulted in an increased temperature drop from the coil to the sample grid. This scaled additionally with the temperature applied. Radiation was indicated to be the primary mechanism for transfer of heat away from the grid.

Appendix B

Evaluation of the Temperature in the Batch Reactor

The temperature in the batch reactor was evaluated by inserting a thermocouple in between the heating jacket and the steel reactor, as illustrated in Figure B.1. The temperatures in the reactor was followed in two cases:

- A case where the reactor was filled with hydrogen and heated from room temperature to a setpoint of 325 °C at 4 bar.
- A case where the reactor was filled with 50 g of phenol and hydrogen as balance and heated from room temperature to a setpoint of 275 °C with a final pressure of 100 bar.

Figure B.2 summarizes the temperature difference between the temperature measured between the heating jacket and the reactor (T2) and the temperature measured in the thermopocket suspended in the reactor (T1). When the reactor is filled with gas, the temperature difference between the outside of the reactor and the reaction medium was 115 °C at its highest and 61 °C at steady state. If a catalyst is loaded to the bottom of the reactor, the temperature of this would probably be closest to the external measured temperature.

In the case where a liquid phase is present in the reactor, the temperature difference was 83 °C at its highest during the heating, but only 17 °C in steady state. Thus, the liquid medium will probably have a temperature very close to the set point.

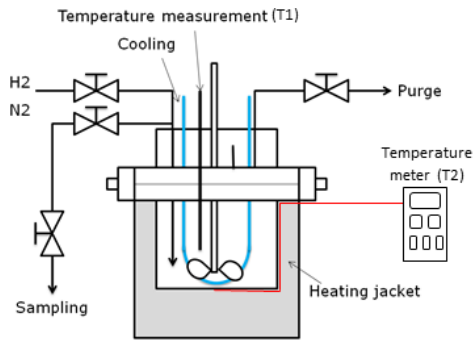

Figure B.1: *Schematic drawing of the batch reactor, illustrating the placement of the two thermocouples during evaluation of the temperature.*

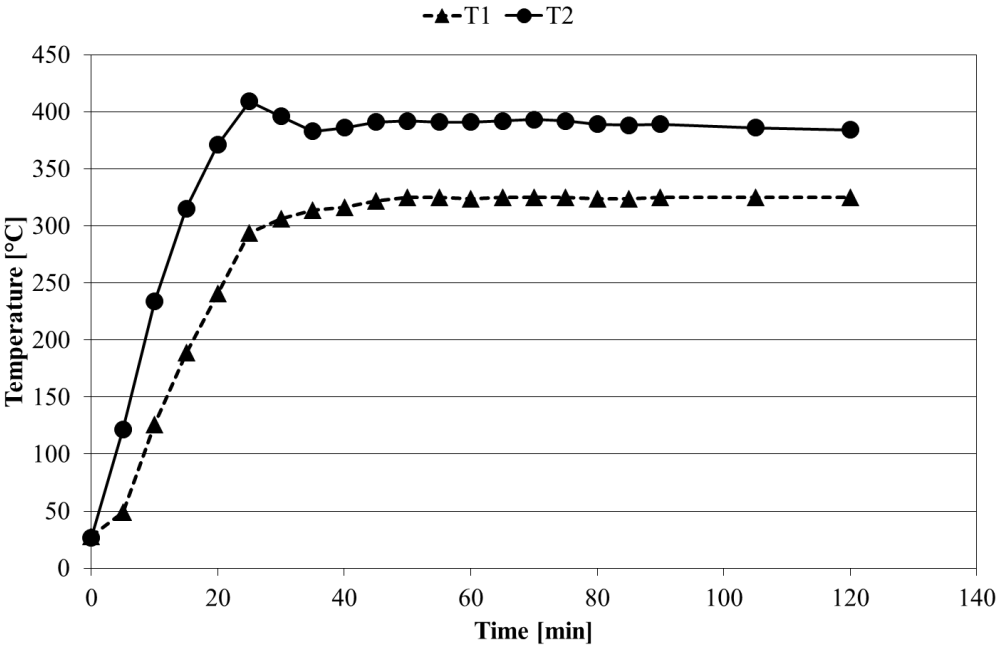

(a) Gas phase in reactor.

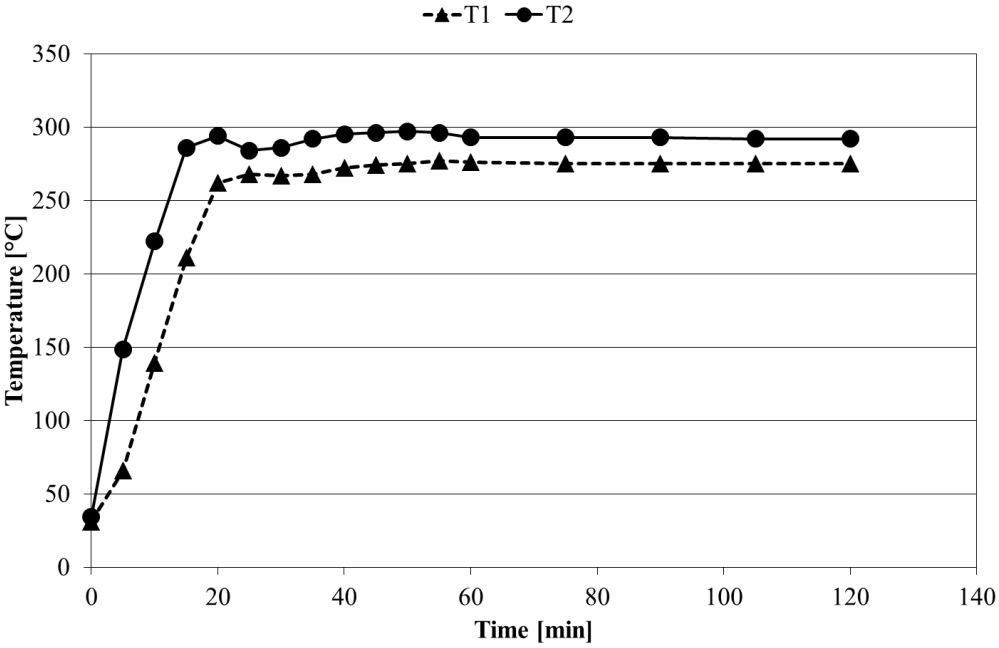

(b) Liquid phase in reactor.

Figure B.2: *Temperature difference between T2 and T1 (cf. Figure B.1) in a case where the reactor is filled with hydrogen (a) and one where it is filled with 50 g of phenol and hydrogen (b).* $T_{Set,gas} = 325\,°C$, $P_{Set,gas} = 5$ *bar,* $T_{Set,liquid} = 275\,°C$, $P_{Set,liquid} = 100$ *bar*

Appendix C

Transport Limitations of Catalysts

C.1 Mears' Criterion

To evaluate the effect of the external diffusion, Mears' criterion for external diffusion was used. This states that the external diffusion limitations can be neglected if [199]:

$$C_M = \frac{r'(obs) \cdot \rho_b \cdot d_p \cdot n}{2 \cdot k_c \cdot C_{Ab}} < 0.15 \tag{C.1}$$

Here $r'(obs)$ is a measured reaction rate, ρ_b is the bulk density of the catalyst bed, d_p is the diameter of the catalyst particles, n is the reaction order, k_c is the mass transfer coefficient, and C_{Ab} is the concentration of reactant A in the bulk.

Mears' criterion is an evaluation of the external diffusion of one compound. Below an example with hydrogenation of guaiacol in 1-octanol is evaluated.

The reaction rate is evaluated on the basis of the kinetic model developed for the system and the reaction rate in the inlet to the system is used:

$$r_1 = k_1' \cdot C_{0,\text{Guaiacol}} \cdot (1 - X_1) \tag{C.2}$$

$$= 500ml/(kg \cdot min) \cdot 900mol/m^3 \cdot (1 - 0) = 7.5 \cdot 10^{-3} mol/(kg \cdot s) \tag{C.3}$$

The particle diameter was controlled by sieving the catalyst, obtaining a particle size in the range from 300 μm to 600 μm. In order to consider the worst case scenario, the largest particle diameter was used in the calculations.

The reaction order was assumed to be 1.

The diffusion in a binary system, D_{AB}, was estimated from the Wilke-Chang method [400]:

$$D_{AB} = 7.4 \cdot 10^{-8} \cdot \frac{\sqrt{\psi_B \cdot M_B} \cdot T}{\mu \cdot \tilde{V_A}^{0.6}} \tag{C.4}$$

Here ψ_B is an association parameter assumed to be 1 for 1-octanol [394], M_B the molar mass of 1-octanol (130.23 g/mol), T the temperature in Kelvin, μ the viscosity of the mixture in cP (0.65 cP for 1-Octanol [401]), and $\tilde{V_A}$ is the molar volume of guaiacol in cm^3/mol (111.6 cm^3/mol). In this way the diffusion coefficient for guaiacol in 1-octanol can be found as $4.01 \cdot 10^{-9}$ m^2/s.

For self-diffusion, D_{AA}, the modified Stokes-Einstein equation was used:

$$D_{AB} = \frac{\kappa \cdot T}{2 \cdot \pi \cdot \mu} \cdot \left(\frac{N_A}{\tilde{V_A}}\right)^{1/3} \tag{C.5}$$

Here κ is Boltmann's constant and N_A the Avogadro constant.

The diffusion coefficient is needed to calculate k_c, which was done from the correlation between the Reynolds number (Re), the Schmidt number (Sc) and the Sherwood number (Sh). The Reynolds and Schmidt numbers are:

$$Re = \frac{\frac{F}{A} \cdot d_p \cdot \rho_l}{\mu} \tag{C.6}$$

$$= \frac{\frac{0.2ml/min}{5 \cdot 10^{-5}m^2} \cdot 0.6mm \cdot 0.824g/ml}{0.65cP} = 0.13 \tag{C.7}$$

$$Sc = \frac{\mu}{\rho_l \cdot D_{AB}} \tag{C.8}$$

$$= \frac{0.65cP}{0.824g/ml \cdot 4.01 \cdot 10^{-9}m^2/s} = 197 \tag{C.9}$$

Here F is the flow, A the cross section area, and ρ_l the density of the liquid. These can be used to calculate the Sherwood number (Sh) [199]:

$$Sh = \left(\frac{0.765}{Re^{0.82}} + \frac{0.365}{Re^{0.386}}\right) \frac{Sc^{1/3} \cdot Re}{1 - \phi_b} \tag{C.10}$$

$$= \left(\frac{0.765}{0.13^{0.82}} + \frac{0.365}{0.13^{0.386}}\right) \frac{197^{1/3} \cdot 1.45}{1 - 0.14} = 4.26 \tag{C.11}$$

Here ϕ_b is the porosity of the bed, which was calculated as:

$$\phi_b = 1 - \frac{\rho_b}{\rho_c} \tag{C.12}$$

$$= 1 - \frac{950kg/m^3}{1100kg/m^3} = 0.14 \tag{C.13}$$

Here ρ_c is the density of the catalyst which is 1100 kg/m^3.

The mass transfer coefficient was obtained from the Sherwood number:

$$k_c = \frac{Sh \cdot D_{AB}}{d_p} \tag{C.14}$$

$$= \frac{4.26 \cdot 4.01 \cdot 10^{-9}m^2/s}{0.6mm} = 8.55 \cdot 10^{-5}m/s \tag{C.15}$$

From this, Mears' was found to be 0.06, which is significantly lower than 0.15 and thereby indicating that the reaction was not limited by external diffusion.

C.2 Weisz-Prater Criterion

Based on the previous results for the Mears' criterion on no external diffusion limitation, the Weisz-Prater criteria can be used in the estimation of internal diffusion

limitations [199]:

$$C_{wp} = \frac{r'(obs) \cdot \rho_c \cdot \left(\frac{d_p}{2}\right)^2}{D_e \cdot C_{As}} \tag{C.16}$$

Here D_e is the effective diffusion coefficient, and C_{As} is the concentration of the investigated compound at the surface of the catalyst.

$r'(obs)$ was determined analogously to what was done in Eq. C.2, and d_p is the same catalyst particle diameter as discussed above. C_{As} can be assumed equal to the concentration in the bulk, because it was concluded that there was no external diffusion limitation.

The effective diffusion coefficient was determined as:

$$D_e = \frac{\phi_c \cdot \vartheta_c}{\tau_c} \cdot \frac{1}{\frac{1}{D_K} + \frac{1}{D_{AB}}} \tag{C.17}$$

Here ϕ_c is the porosity of the catalyst, ϑ_c is the constriction factor, and τ_c is the tortuosity.

The Knudsen diffusivity, D_K, is given by [402]:

$$D_K = 9700 \cdot a \cdot \left(\frac{T}{M_A}\right)^{1/2} \tag{C.18}$$

$$= 9700 \cdot 2 \cdot 10^{-6} cm \cdot \left(\frac{523K}{124.14 g/mol}\right)^{1/2} = 0.0398 cm^2/s = 3.98 \cdot 10^{-6} m^2/s \tag{C.19}$$

Here a is the radius of the pores inside the catalyst. This parameter was set to 20 nm which is the average pore size for the given catalyst. The bulk diffusion coefficient is the same as that determined in Eq. C.4.

ϕ_c, ϑ_c, and τ_c have the respective values of 0.33, 0.8, and 2.5. Whereby the effective diffusion coefficient was calculated as:

$$D_e = \frac{0.33 \cdot 0.8}{2.5} \cdot \frac{1}{\frac{1}{3.98 \cdot 10^{-6} m^2/s} + \frac{1}{4.01 \cdot 10^{-9} m^2/s}} = 4.23 \cdot 10^{-10} m^2/s \tag{C.20}$$

Hereby C_{wp} was found to be 1.9 and as this criterion states that if $C_{wp} \ll 1$ no interior diffusion problems exist, it is indicated that internal transport limitation probably exist for the largest particles. With a particle size of 300 μm C_{wp} was 0.49.

Table C.1 summarizes Mears' and Weisz-Prater criteria parameters for all the investigated catalysts. The batch reactor experiment with Ni/SiO_2 did not appear to be transport limited. Similar continuous flow experiments with Mo_2C/ZrO_2 was not transport limited at all. On the other hand, both Ni/ZrO_2 and $Ni\text{-}MoS_2/ZrO_2$ appeared to be limited to some extent by internal transport limitations both for the guaiacol, phenol, and 1-octanol reactions, as the Weisz-Prater criterion parameters were above 1 in these systems.

Table C.1: *Mears' and Weisz-Prater criteria parameters for the investigated reactions. Ni/SiO$_2$ was evaluated in the batch reactor setup, the other catalysts were evaluated in the continuous flow setup.*

Catalyst	Ni/SiO_2	Ni/ZrO_2	Mo_2C/ZrO_2	$Ni\text{-}MoS_2/ZrO_2$
d_p [μm]	125	600	180	600
Feed	Phenol	Guaiacol/ Octanol	Phenol/ Octanol	Phenol/ Octanol
Reactant	Phenol	Guaiacol	Phenol	Phenol
k_i [ml/kg$_{\text{cat}}$/min]	1830	500	25	50
C_M	0.0003	0.06	0.0003	0.006
C_{wp}	0.19	1.9	0.007	0.17
Reactant	-	Octanol	Octanol	Octanol
k_i [ml/kg$_{\text{cat}}$/min]	-	500	80	250
C_M	-	0.08	0.002	0.038
C_{wp}	-	2.88	0.039	1.36

C.3 Effectiveness Factor

To further evaluate the internal transport limitations, the effectiveness factor (η_{eff}) of a single catalyst pellet was evaluated for the guaiacol and 1-octanol reaction over Ni/ZrO_2, which for a first order reaction is given by [199]:

$$\eta_{eff} = \frac{3}{\phi^2} \cdot (\phi \cdot \coth \phi - 1), \tag{C.21}$$

$$\phi^2 = \frac{\rho_c \cdot k_1 \cdot (d_p/2)^2}{D_e} \tag{C.22}$$

In Figure C.1, η_{eff} is plotted for both the guaiacol and 1-octanol reaction over Ni/ZrO_2 as a function of particle size. The smaller particles in this catalyst batch (radius of 150 μm) has an effectiveness in the order of 95-97 %, but the larger (radius of 300 μm) are in the order of 85-89%. Thus, the internal transport limitation is not pronounced and as both the Ni/ZrO_2 and $Ni\text{-}MoS_2/ZrO_2$ were tested for stability and not kinetics, this slight uncertainty will probably not interfere with the results.

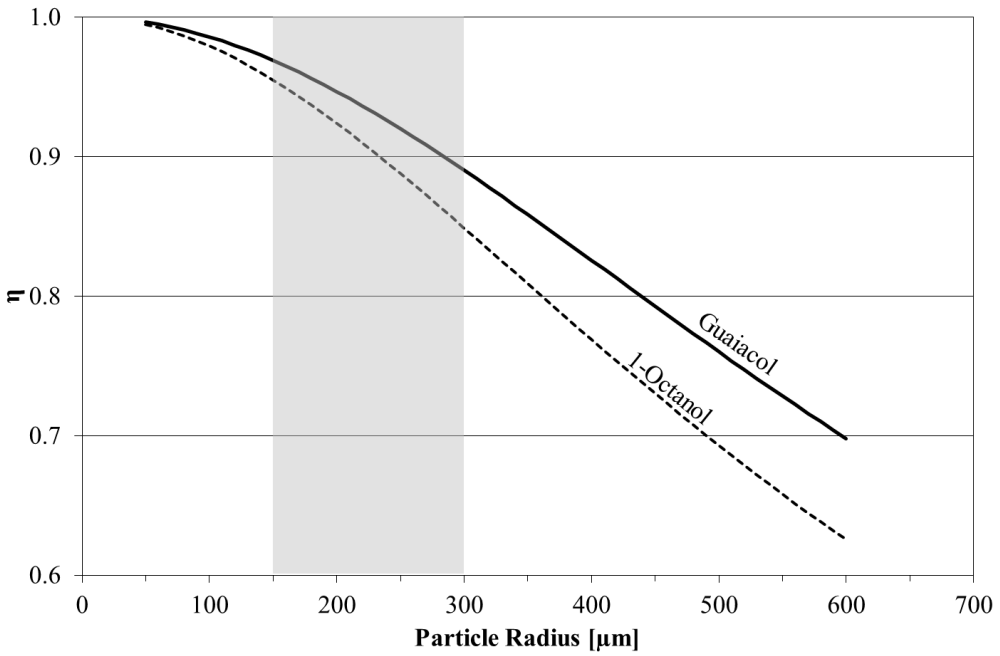

Figure C.1: *Effectiveness factor as a function of particle radius for the given system of hydrogenation of guaiacol. Grey area indicate the used particle fraction.*

Appendix D

Temperature Programmed Reduction of Catalysts

TPR was done for Ni/SiO_2, Ni/Al_2O_3, Ni/ZrO_2, $Ni/MgAl_2O_4$, Ni/CeO_2, Ni/CeO_2-ZrO_2, Ni-V_2O_5/SiO_2, and Co/SiO_2 according to the procedure described in Table D.1 by TGA. All TPR profiles are displayed below as change in mass ($\Delta m/\Delta T$) as a function of temperature.

Table D.1: *Heating profile of TGA during TPR experiments. Gas: 5% H_2 in N_2 , Flow: 100 Nml/min*

Start temperature [°C]	End temperature [°C]	Heating rate [°C/min]
50	300	5
300	500	1
500	700	5

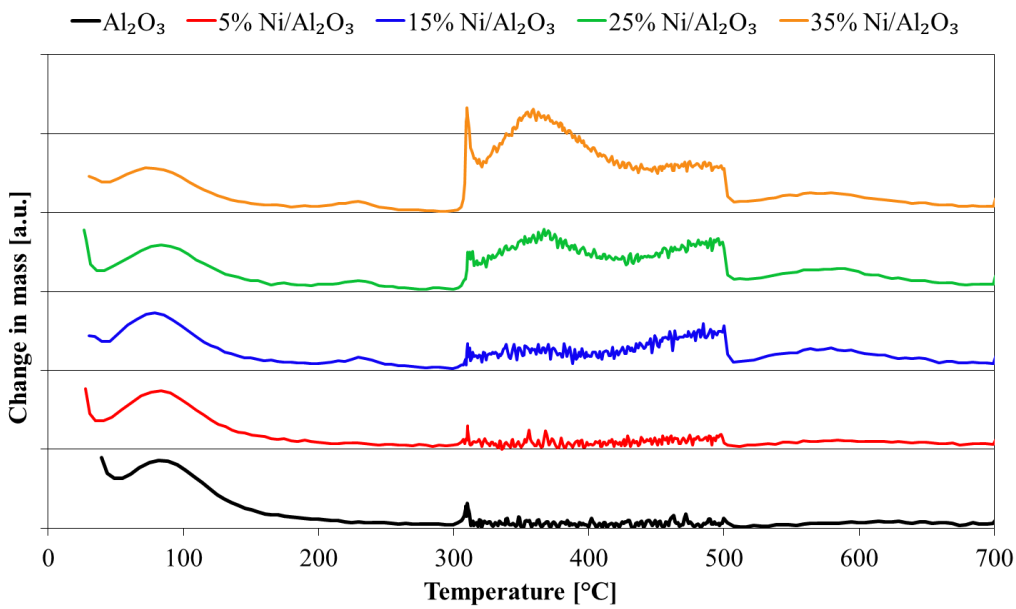

Figure D.1: *TPR profile of Ni/Al_2O_3 compared to the pure support.*

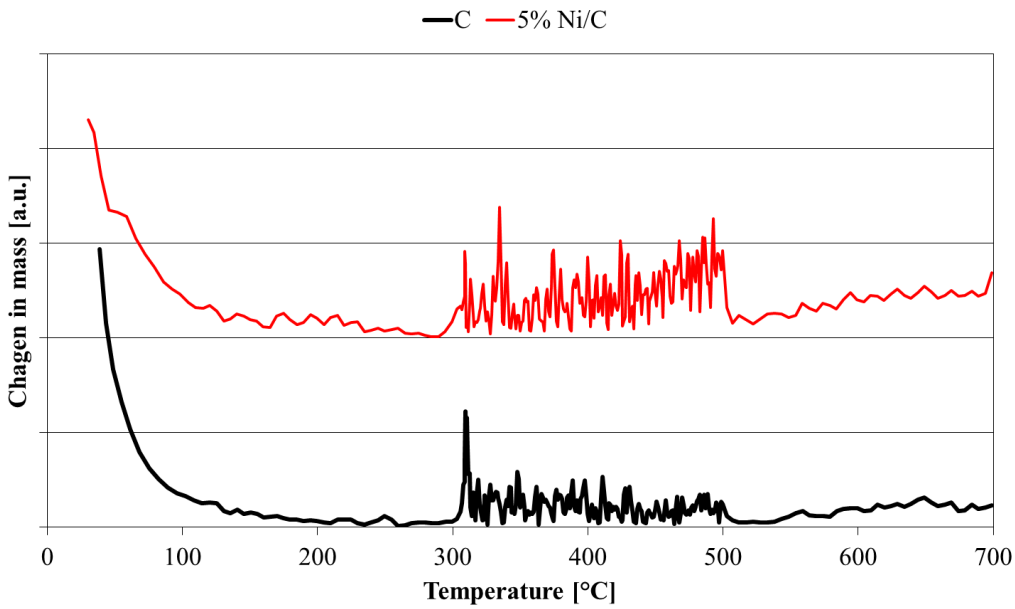

Figure D.2: *TPR profile of Ni/C compared to the pure support.*

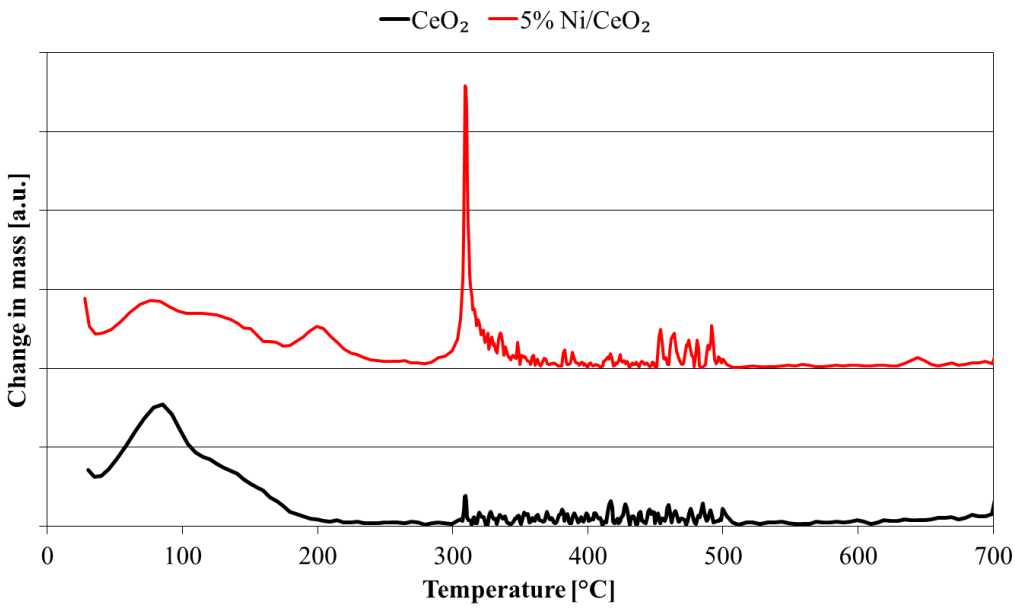

Figure D.3: *TPR profile of Ni/CeO_2 compared to the pure support.*

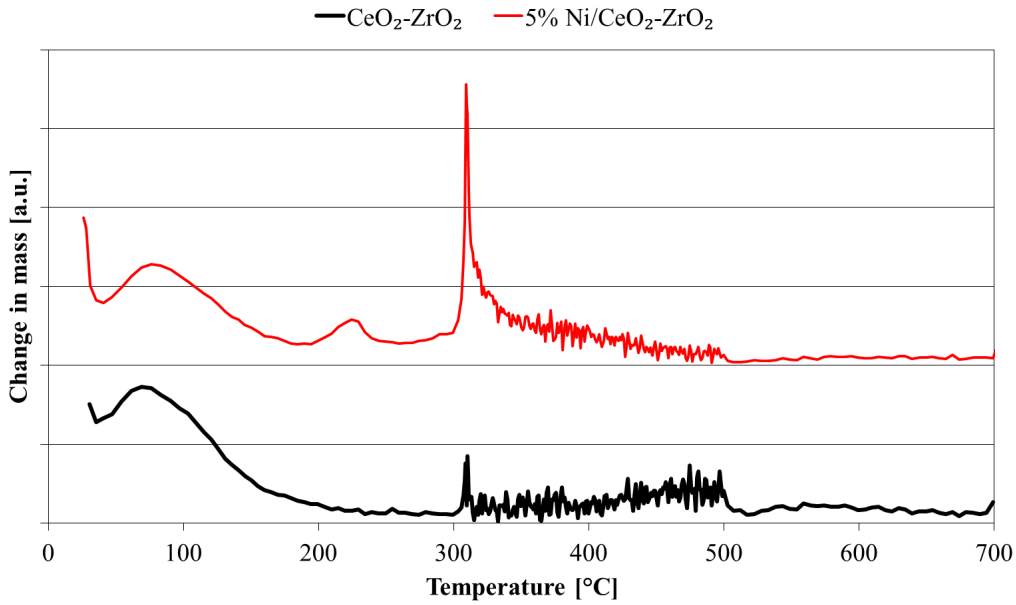

Figure D.4: *TPR profile of Ni/CeO_2-ZrO_2 compared to the pure support.*

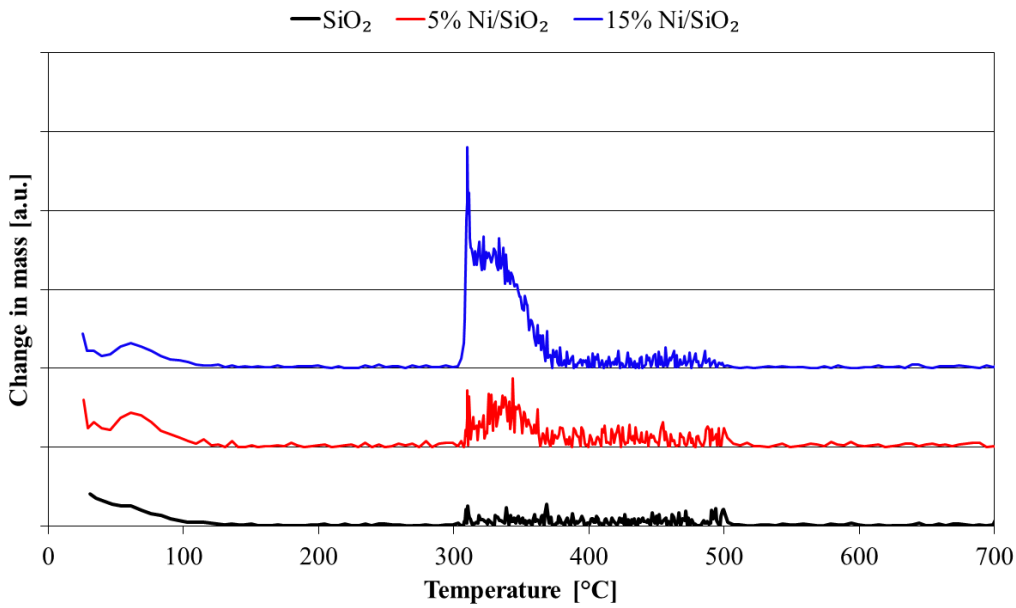

Figure D.5: *TPR profile of Ni/SiO_2 compared to the pure support.*

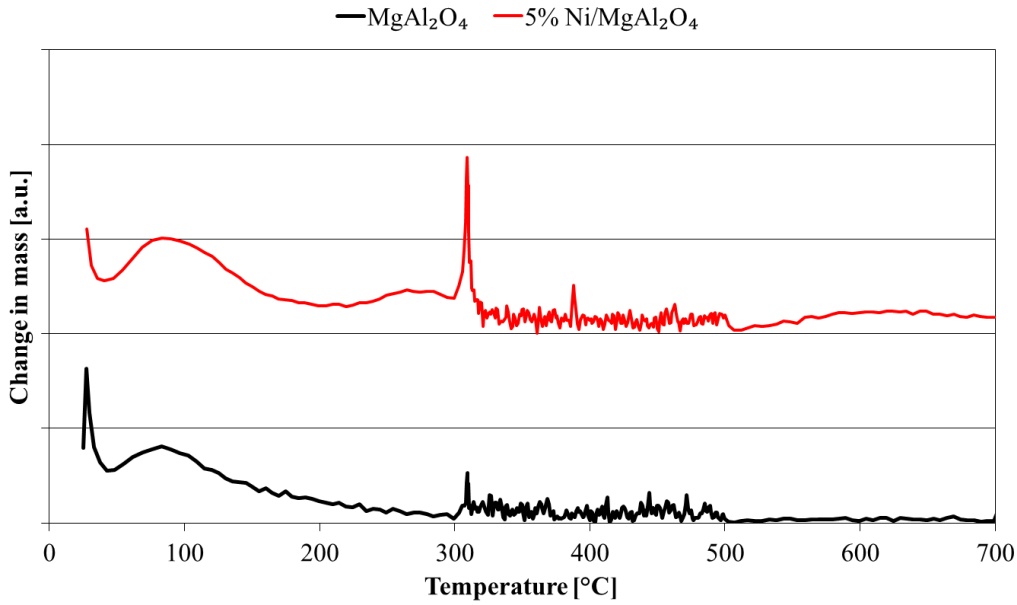

Figure D.6: *TPR profile of $Ni/MgAl_2O_4$ compared to the pure support.*

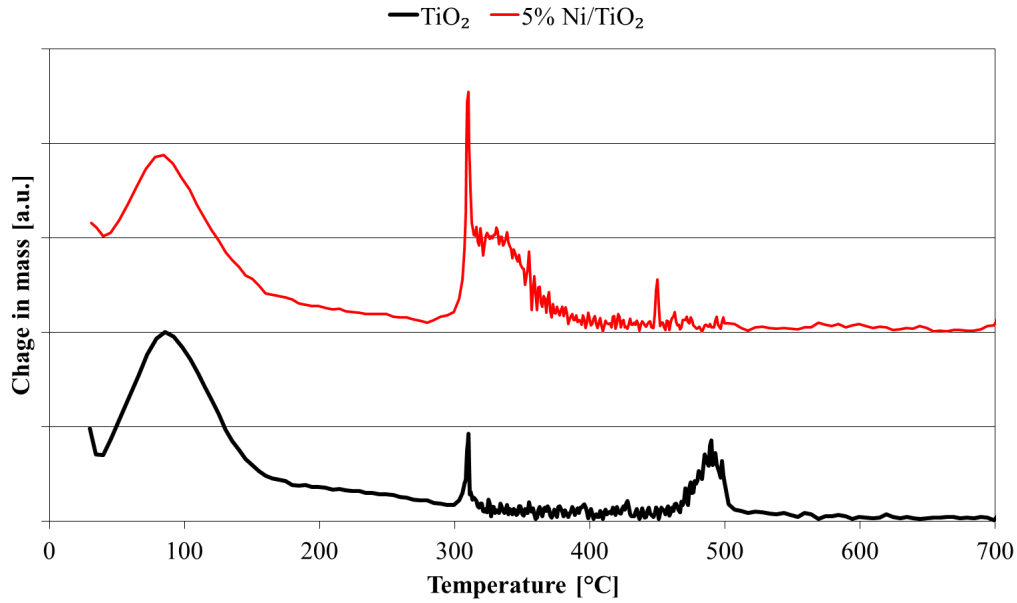

Figure D.7: *TPR profile of Ni/TiO_2 compared to the pure support.*

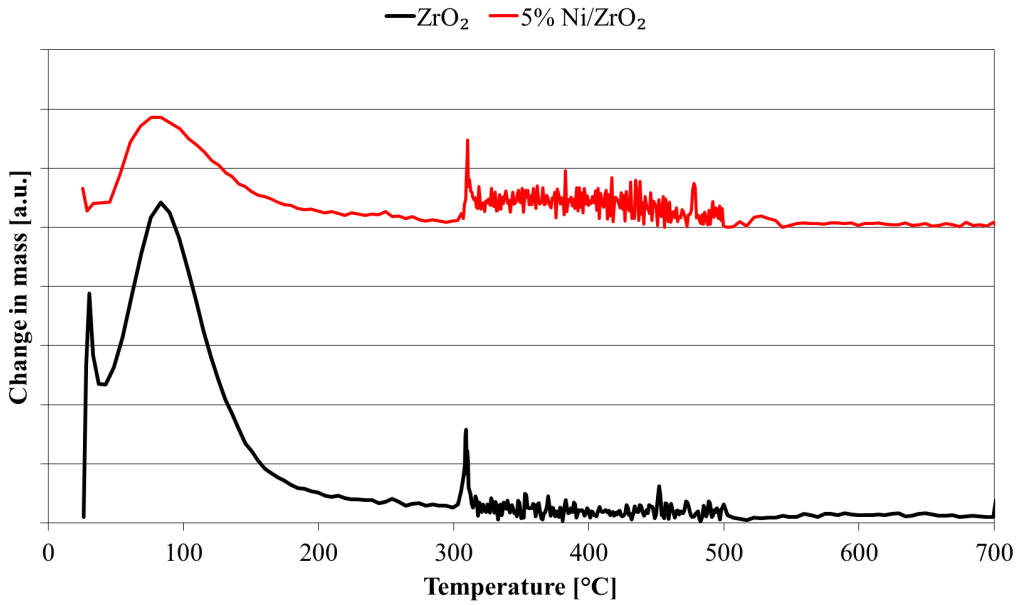

Figure D.8: *TPR profile of Ni/ZrO_2 compared to the pure support.*

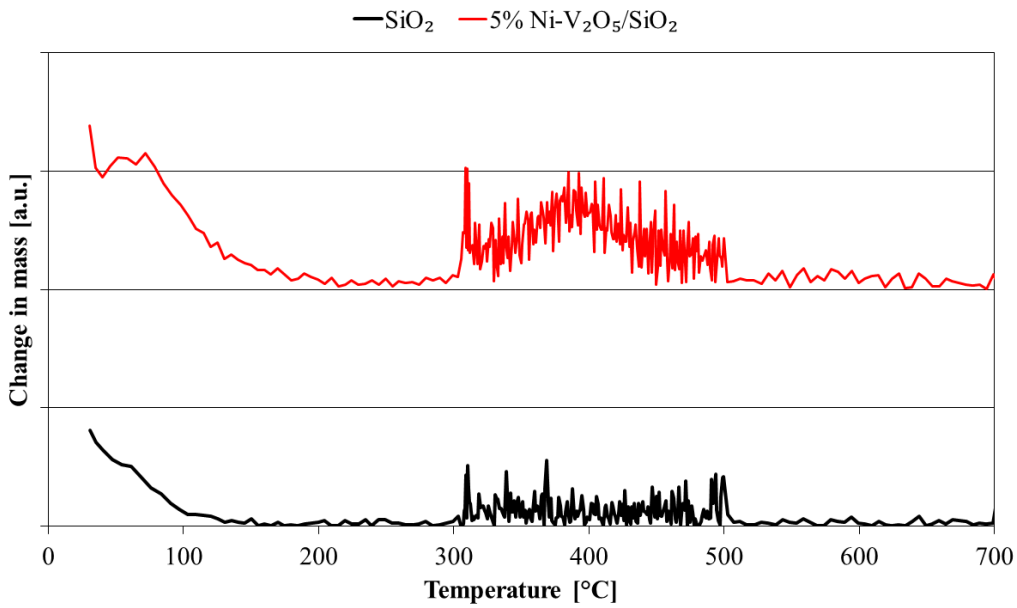

Figure D.9: *TPR profile of $Ni\text{-}V_2O_5/SiO_2$ compared to the pure support.*

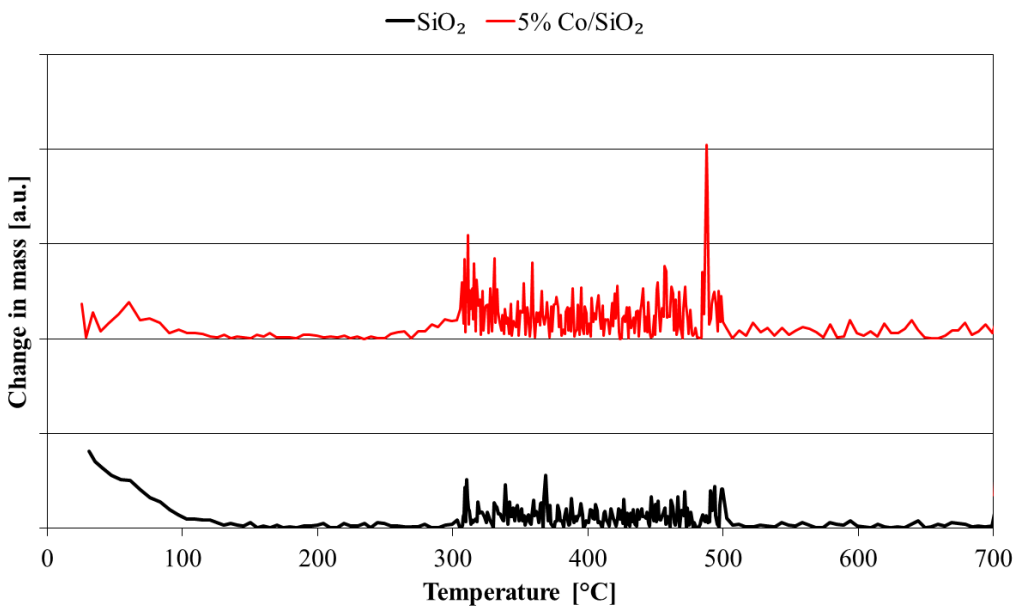

Figure D.10: *TPR profile of Co/SiO_2 compared to the pure support.*

Appendix E

Langmuir-Hinshelwood Model of Phenol Hydrogenation

To evaluate if a site blocking mechanism was causing the development in the hydrogenation rate of phenol in the present work, a Langmuir-Hinshelwood kinetic model was set up [232]. Figure E.1 summarizes the elementary steps of the hydrogenation reaction. Phenol is assumed to adsorb on oxygen vacancy sites in the oxide as discussed in Section 4.5 and thus is dependent on a separate type of sites, denoted #. Hydrogen and cyclohexanol are both adsorbing on nickel sites which are denoted *.

As the intermediates formed in reaction 3-6 all are regarded as relative unstable, subsequent reactions with these intermediates would probably be relative fast. Therefore reaction 3 is assumed to be the rate determining step. Assuming further that reaction 3 is irreversible and that all other elementary steps are in quasi equilibrium, the rate of reaction is given as:

$$r = r_3^+ = k_3 \cdot \Theta_{\mathrm{Ph}}^{\#} \cdot \Theta_{\mathrm{H}}^{*} \tag{E.1}$$

Here k_3 is the forward rate constant of reaction 3, $\Theta_{\mathrm{Ph}}^{\#}$ is the surface coverage of phenol, and Θ_{H}^{*} is the surface coverage of hydrogen.

The surface coverage of phenol can be found from reaction 1:

$$r_1 = k_1^+ \cdot C_{\mathrm{Ph}} \cdot \Theta_{\#} - k_1^- \cdot \Theta_{\mathrm{Ph}}^{\#} = 0 \Leftrightarrow \tag{E.2}$$

$$\Theta_{\mathrm{Ph}}^{\#} = K_{\mathrm{Ph}} \cdot C_{\mathrm{Ph}} \cdot \Theta_{\#}, \quad K_{\mathrm{Ph}} = \frac{k_1^+}{k_1^-} \tag{E.3}$$

Here K_{Ph} is the equilibrium constant for the phenol coverage at the # sites. The coverage of hydrogen is found from reaction 2 as:

$$r_2 = k_2^+ \cdot C_{\mathrm{H_2}} \cdot \Theta_*^2 - k_2^- \cdot \Theta_{\mathrm{H}}^{*\,2} = 0 \Leftrightarrow \tag{E.4}$$

$$\Theta_{\mathrm{H}}^{*} = \sqrt{K_{\mathrm{H_2}} \cdot C_{\mathrm{H_2}}} \cdot \Theta_*, \quad K_{\mathrm{H_2}} = \frac{k_2^+}{k_2^-} \tag{E.5}$$

Here $K_{\mathrm{H_2}}$ is the equilibrium constant for the hydrogen coverage at the * sites. The concentration of H_2 in the liquid phase is used as this will be the relevant parameter describing the coverage at the catalyst surface.

Using this in Eq. E.1 gives:

$$r = k_3 \cdot K_{\mathrm{Ph}} \cdot C_{\mathrm{Ph}} \cdot \Theta_{\#} \cdot \sqrt{K_{\mathrm{H_2}} \cdot C_{\mathrm{H_2}}} \cdot \Theta_* \tag{E.6}$$

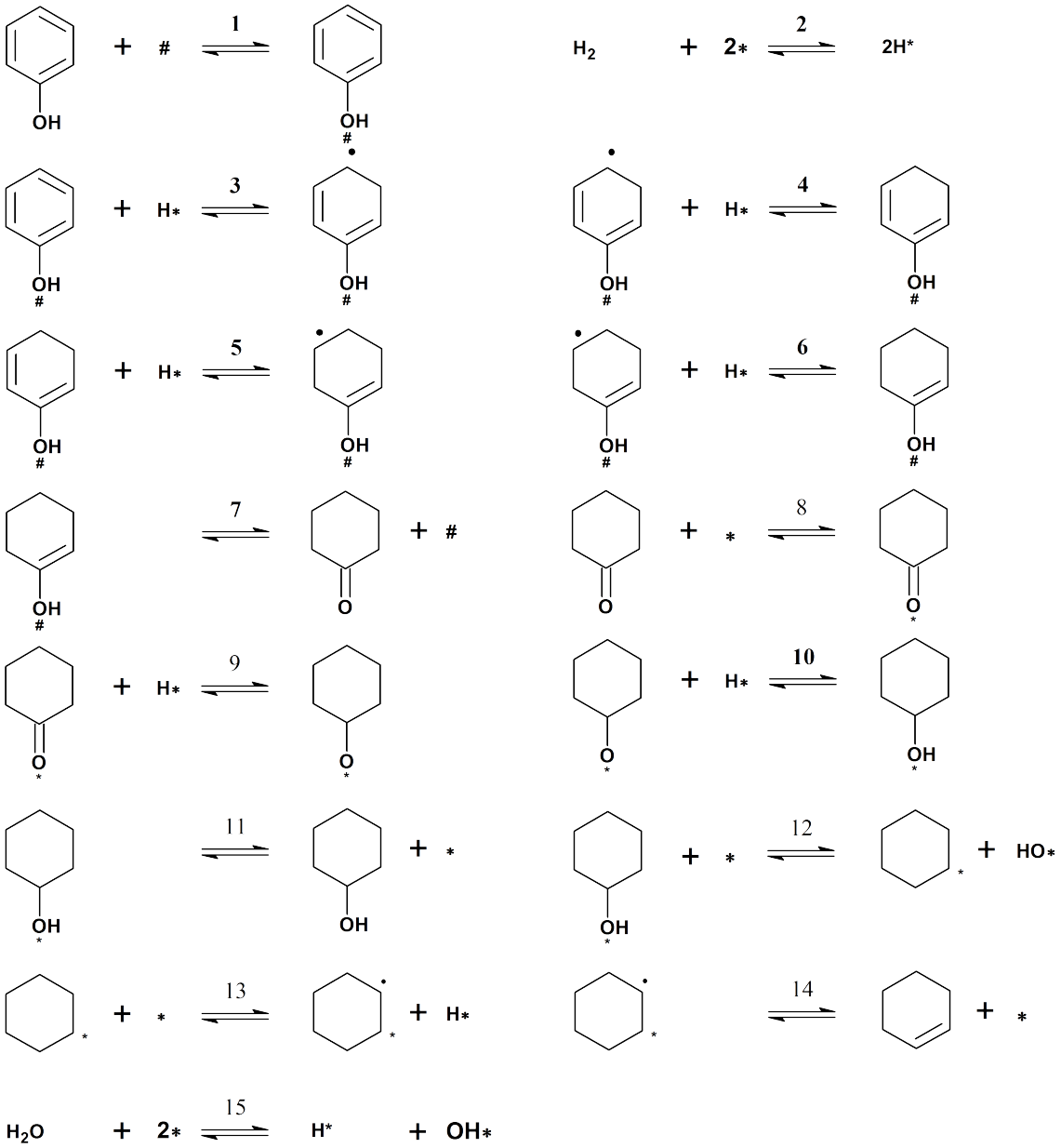

Figure E.1: *Proposed elementary steps for hydrogenation of phenol over a Ni/SiO_2 catalyst.*

The fraction of free sites j is given as:

$$\Theta_j = 1 - \sum_i \Theta_{j,i} \tag{E.7}$$

For the # sites this is given as:

$$\Theta_\# = 1 - \Theta_{\mathrm{Ph}}^\# \Leftrightarrow \tag{E.8}$$

$$= \frac{1}{1 + K_{\mathrm{Ph}} \cdot C_{\mathrm{Ph}}} \tag{E.9}$$

The * sites will also be covered by hydrogen, but also intermediates from the subsequent deoxygenation reaction could be thought to interfere. In the derivation only coverage of cyclohexanol (Θ_{Ch}, reaction 11) and OH groups (Θ_{OH}, reaction 15) are considered as potential surface groups, but reaction 8-10 and 12-14 could also be thought to contribute to the surface coverage. With this assumption, the fraction of free * sites becomes:

$$\Theta_* = 1 - \Theta_{\mathrm{H}}^* - \Theta_{\mathrm{Ch}}^* - \Theta_{\mathrm{OH}}^* \tag{E.10}$$

The coverage of cyclohexanol can be derived from reaction 11 in Figure E.1 as:

$$r_{11} = k_{11}^+ \cdot \Theta_{\mathrm{Ch}}^* - k_{11}^- \cdot C_{\mathrm{Ch}} \cdot \Theta_* = 0 \Leftrightarrow \tag{E.11}$$

$$\Theta_{\mathrm{Ch}}^* = K_{\mathrm{Ch}} \cdot C_{\mathrm{Ch}} \cdot \Theta_*, \quad K_{\mathrm{Ch}} = \frac{k_{11}^+}{k_{11}^-} \tag{E.12}$$

Here K_{Ch} is the equilibrium constant for the cyclohexanol coverage.

Similarly, the coverage of OH can be derived from reaction 15 in Figure E.1 as:

$$r_{15} = k_{15}^+ \cdot C_{\mathrm{H_2O}} \cdot \Theta_*^2 - k_{15}^- \cdot \Theta_{\mathrm{OH}}^* \cdot \Theta_{\mathrm{H}}^* = 0 \Leftrightarrow \tag{E.13}$$

$$\Theta_{\mathrm{OH}}^* = \frac{K_{\mathrm{H_2O}} \cdot C_{\mathrm{H_2O}} \cdot \Theta_*^2}{\Theta_{\mathrm{H}}^*} \tag{E.14}$$

$$\Theta_{\mathrm{OH}}^* = \frac{K_{\mathrm{H_2O}} \cdot C_{\mathrm{H_2O}} \cdot \Theta_*}{\sqrt{K_{\mathrm{H_2}} \cdot C_{\mathrm{H_2}}}}, \quad K_{\mathrm{Ch}} = \frac{k_{15}^+}{k_{15}^-} \tag{E.15}$$

Here $K_{\mathrm{H_2O}}$ is the equilibrium constant for the H_2O coverage.

Using this in Eq. E.10 gives:

$$\Theta_* = 1 - \sqrt{K_{\mathrm{H_2}} \cdot C_{\mathrm{H_2}}} \cdot \Theta_* - K_{\mathrm{Ch}} \cdot C_{\mathrm{Ch}} \cdot \Theta_* - \frac{K_{\mathrm{H_2O}} \cdot C_{\mathrm{H_2O}} \cdot \Theta_*}{\sqrt{K_{\mathrm{H_2}} \cdot C_{\mathrm{H_2}}}} \Leftrightarrow \tag{E.16}$$

$$= \frac{1}{1 + \sqrt{K_{\mathrm{H_2}} \cdot C_{\mathrm{H_2}}} + K_{\mathrm{Ch}} \cdot C_{\mathrm{Ch}} + \frac{K_{\mathrm{H_2O}} \cdot C_{\mathrm{H_2O}}}{\sqrt{K_{\mathrm{H_2}} \cdot C_{\mathrm{H_2}}}}} \tag{E.17}$$

Ultimately the rate term then becomes:

$$r = k_3 \cdot K_{\mathrm{Ph}} \cdot C_{\mathrm{Ph}} \cdot \sqrt{K_{\mathrm{H_2}} \cdot C_{\mathrm{H_2}}} \cdot \Theta_* \cdot \Theta_\# \tag{E.18}$$

$$\Theta_* = \frac{1}{1 + \sqrt{K_{\mathrm{H_2}} \cdot C_{\mathrm{H_2}}} + K_{\mathrm{Ch}} \cdot C_{\mathrm{Ch}} + \frac{K_{\mathrm{H_2O}} \cdot C_{\mathrm{H_2O}}}{\sqrt{K_{\mathrm{H_2}} \cdot C_{\mathrm{H_2}}}}}$$

$$\Theta_\# = \frac{1}{1 + K_{\mathrm{Ph}} \cdot C_{\mathrm{Ph}}}$$

The adsorption equilibrium constants on metal sites will be dependent on the size of the nano-particle and thereby the fraction of available facet and step sites [296–299, 403, 404]. Murzin [296, 299] showed that this relationship could be described as:

$$K_i(D) = K_i \cdot e^{-\chi_i \cdot D} \tag{E.19}$$

Here $K_i(D)$ is the adsorption equilibrium constant as a function of dispersion (D), K_i is the adsorption equilibrium constant at facets, and χ_i is the difference in the Gibbs free energy (ΔG) for adsorption at step and facet sites and is defined as:

$$\chi_i = \frac{\Delta G_{ads,i,step} - \Delta G_{ads,i,facet}}{R \cdot T} \tag{E.20}$$

Here R is the gas constant.

Hydrogen is known to have a relative low activation energy of 0-10 kJ/mol for adsorption on either facets or steps on nickel particles and is therefore generally regarded as structure insensitive [313]. Thus, it is reasonable to assume that the difference in the Gibbs free energy for adsorption between facet and step sites probably is close to 0 for hydrogen and $\chi_{\mathrm{H_2}}$ thereby is 0. Contrary, as deoxygenation was found to mainly take place on low coordinated sites, it follows that cyclohexanol preferentially adsorbs at these sites. Furthermore, OH groups will be deposited at low coordinated sites as the product from the deoxygenation reaction. Thus, both species will probably have a significant difference between $\Delta G_{ads,step}$ and $\Delta G_{ads,facet}$. Incorporating this in Eq. E.10 gives:

$$\Theta_* = \frac{1}{1 + \sqrt{K_{\mathrm{H_2}} \cdot C_{\mathrm{H_2}}} + C_{\mathrm{Ch}} \cdot K_{\mathrm{Ch}} \cdot e^{-\chi_{\mathrm{Ch}} \cdot D} + \dfrac{C_{\mathrm{H_2O}} \cdot K_{\mathrm{H_2O}} \cdot e^{-\chi_{\mathrm{H_2O}} \cdot D}}{\sqrt{K_{\mathrm{H_2}} \cdot C_{\mathrm{H_2}}}}} \tag{E.21}$$

As phenol is assumed to adsorb on an oxygen vacancy site in the support, K_{Ph} will not depend on the dispersion.

The reaction rate in Eq. E.18 scales with the TOF as:

$$TOF = r \cdot \frac{N_A}{N_S} \tag{E.22}$$

And N_S scales linear with dispersion (cf. Figure 5.4). Thus, the TOF for hydrogenation of phenol over $\mathrm{Ni/SiO_2}$ can be described as:

$$TOF = k_3 \cdot K_{\mathrm{Ph}} \cdot \sqrt{K_{\mathrm{H_2}}} \cdot C^{\circ 3/2} \cdot \Theta_* \cdot \Theta_\# \cdot \frac{N_A}{D \cdot N_{S,s} + N_{S,0}} \tag{E.23}$$

$$\Theta_* = \frac{1}{1 + \sqrt{K_{\mathrm{H_2}} \cdot C^\circ} + K_{\mathrm{Ch}} \cdot e^{-\chi_{\mathrm{Ch}} \cdot D} \cdot C^\circ + \dfrac{K_{\mathrm{H_2O}} \cdot e^{-\chi_{\mathrm{H_2O}} \cdot D} \cdot C^\circ}{\sqrt{K_{\mathrm{H_2}} \cdot C^\circ}}}$$

$$\Theta_\# = \frac{1}{1 + K_{\mathrm{Ph}} \cdot C^\circ}$$

Here $N_{S,s}$ and $N_{S,0}$ are scaling parameters of N_S with dispersion. All concentrations are set to the standard concentration (C°) to normalize the TOF.

Appendix F

Plug Flow Reactor Kinetic Model Derivation

Based on the experimental observations as summarized in Figure F.1, four main reactions were identified during HDO of guaiacol and 1-octanol over Ni/ZrO_2, giving the following kinetic system:

$$r_1 = k_1 \cdot C_{\text{Guaiacol}} \cdot P_{\text{H}_2}^n \tag{F.1}$$

$$r_2 = k_2 \cdot C_{\text{2-Methoxy-cyclohexanol}} \cdot P_{\text{H}_2}^m \tag{F.2}$$

$$r_3 = k_3 \cdot C_{\text{Cyclohexanol}} \cdot P_{\text{H}_2}^l \tag{F.3}$$

$$r_4 = k_4 \cdot C_{\text{1-Octanol}} \cdot P_{\text{H}_2}^k \tag{F.4}$$

Here r_i is the rate of reaction i, k_i is the rate constant for reaction i, C_i is the concentration of compound i, P_{H_2} is the partial pressure of H_2, and n-k are the unknown reaction orders of hydrogen. The reaction orders for all the hydrocarbons were assumed to be first order.

As a significant excess of hydrogen was used in all experiments the partial pressure of hydrogen was assumed constant and therefore the kinetic expressions reduce to:

$$r_1 = k_1' \cdot C_{\text{Guaiacol}} \tag{F.5}$$

$$r_2 = k_2' \cdot C_{\text{2-Methoxy-cyclohexanol}} \tag{F.6}$$

$$r_3 = k_3' \cdot C_{\text{Cyclohexanol}} \tag{F.7}$$

$$r_4 = k_4' \cdot C_{\text{1-Octanol}} \tag{F.8}$$

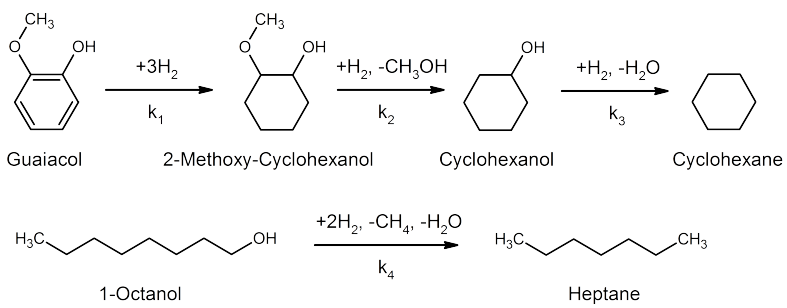

Figure F.1: *Observed reaction path of guaiacol and 1-octanol.*

By defining X_1 as the degree of conversion in reaction 1 relative to the initial guaiacol concentration, X_2 as the degree of conversion in reaction 2 relative to the initial guaiacol concentration, X_3 as the degree of conversion in reaction 3 relative to the initial guaiacol concentration, and X_4 as the degree of conversion in reaction 4 relative to the initial 1-octanol concentration and assuming constant volume, the rate expressions can be defined as:

$$r_1 = k_1' \cdot C_{0,\text{Guaiacol}} \cdot (1 - X_1) \tag{F.9}$$
$$r_2 = k_2' \cdot C_{0,\text{Guaiacol}} \cdot (X_1 - X_2) \tag{F.10}$$
$$r_3 = k_3' \cdot C_{0,\text{Guaiacol}} \cdot (X_2 - X_3) \tag{F.11}$$
$$r_4 = k_4' \cdot C_{0,\text{1-Octanol}} \cdot (1 - X_4) \tag{F.12}$$

The reaction takes place in a plug flow reactor (PFR), for which the mole balances are [199]:

$$C_{0,\text{Guaiacol}} \cdot v \cdot \frac{dX_1}{dW} = r_1 \tag{F.13}$$
$$C_{0,\text{Guaiacol}} \cdot v \cdot \frac{dX_2}{dW} = r_2 \tag{F.14}$$
$$C_{0,\text{Guaiacol}} \cdot v \cdot \frac{dX_3}{dW} = r_3 \tag{F.15}$$
$$C_{0,\text{1-Octanol}} \cdot v \cdot \frac{dX_4}{dW} = r_4 \tag{F.16}$$

Here v is the feed flow and W is the mass of catalyst. Using zero as initial conditions of the conversions, the differential equation can be solved algebraically as:

$$X_1 = 1 - \exp\left(-k_1' \cdot \frac{W}{v}\right) \tag{F.17}$$
$$X_2 = 1 - \frac{k_1' \cdot \exp\left(-k_2' \cdot \frac{W}{v}\right) - k_2' \cdot \exp\left(-k_1' \cdot \frac{W}{v}\right)}{k_1' - k_2'} \tag{F.18}$$
$$X_3 = 1 - \frac{k_3' \cdot k_2' \cdot \exp\left(-k_1' \cdot \frac{W}{v}\right)}{(k_1' - k_3') \cdot (k_1' - k_2')} + \frac{k_3' \cdot k_1' \cdot \exp\left(-k_2' \cdot \frac{W}{v}\right)}{(k_1' - k_2') \cdot (k_2' - k_3')} - \frac{k_1' \cdot k_2' \cdot \exp\left(-k_3' \cdot \frac{W}{v}\right)}{(k_2' - k_3') \cdot (k_1' - k_3')} \tag{F.19}$$
$$X_4 = 1 - \exp\left(-k_4' \cdot \frac{W}{v}\right) \tag{F.20}$$

This can be used to evaluate the kinetic parameters of the system, where k_1' corresponds to the rate of hydrogenation, k_2' corresponds to the rate of hydrogenolysis, k_3' corresponds to the rate of hydrodeoxygenation, and k_4' corresponds to the rate of cracking/decarbonylation.

Appendix G

Detailed Product Development of Stability Tests with Ni/ZrO_2

In the stability experiments with Ni/ZrO_2 described in Chapter 6, all liquid samples were analyzed by GC-MS/FID and detailed product compositions were obtained in all experiments. This is summarized in the following figures. All experiments were conducted at 250 °C and 100 bar, with an oil flow of 0.2 ml/min (WHSV = 4.0 h^{-1}) and gas flow of 400 Nml/min.

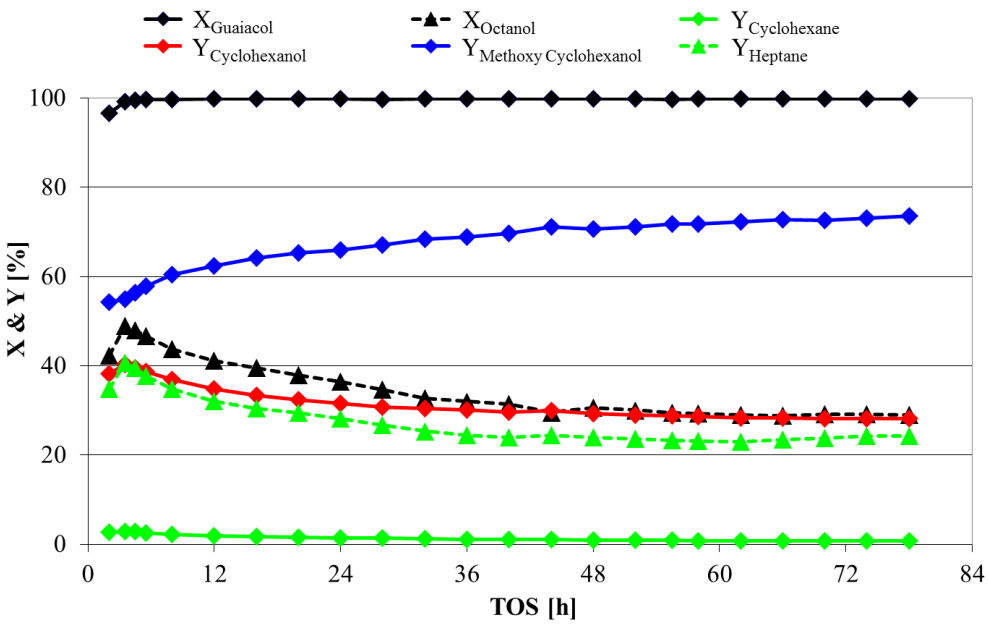

Figure G.1: *Conversion of guaiacol and 1-octanol and yield of heptane, cyclohexane, cyclohexanol, 2-methoxy-cylclohexanol DOD for a calcined 5 wt% Ni/ZrO_2 as a function of TOS. $T = 250\,°C$, $P = 100$ bar, $F_{oil} = 0.2$ ml/min, WHSV = 4.0 h^{-1}.*

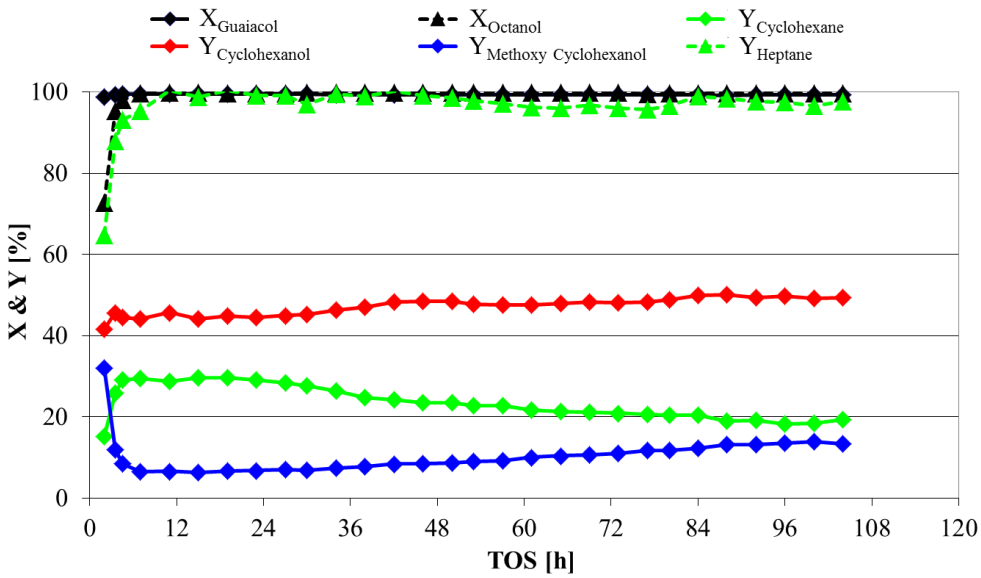

Figure G.2: *Conversion of guaiacol and 1-octanol and yield of heptane, cyclohexane, cyclohexanol, 2-methoxy-cylclohexanol DOD for an un-calcined 5 wt% Ni/ZrO_2 as a function of TOS. $T = 250\,°C$, $P = 100$ bar, $F_{oil} = 0.2$ ml/min, $WHSV = 4.0\ h^{-1}$.*

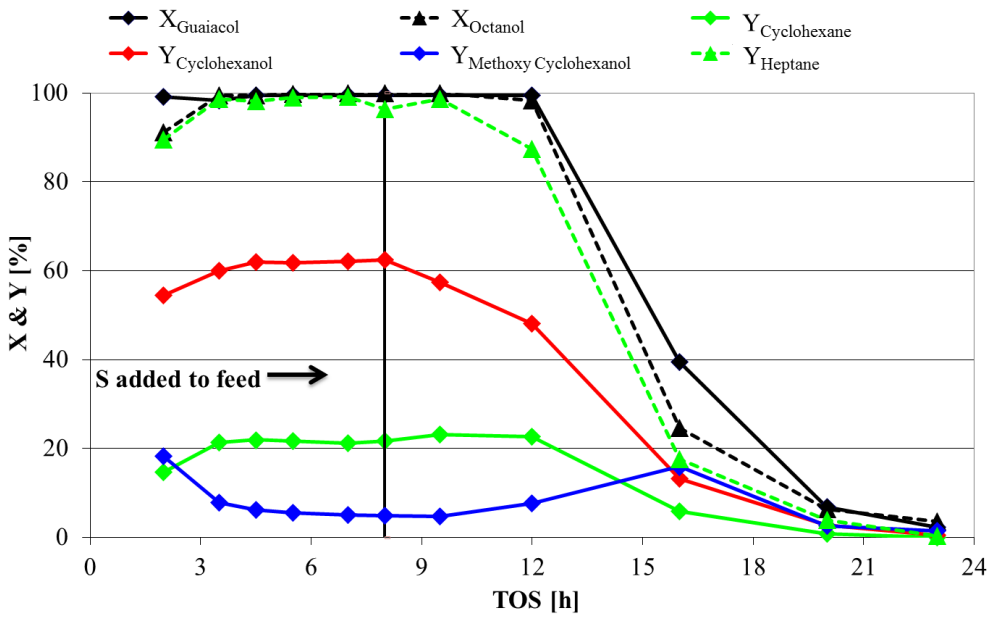

Figure G.3: *Conversion of guaiacol and 1-octanol and yield of heptane, cyclohexane, cyclohexanol, 2-methoxy-cylclohexanol DOD for an un-calcined 5 wt% Ni/ZrO_2 as a function of TOS deactivated by 0.05 wt% sulfur from 8 h of TOS. $T = 250\,°C$, $P = 100$ bar, $F_{oil} = 0.2$ ml/min, $WHSV = 4.0\ h^{-1}$.*

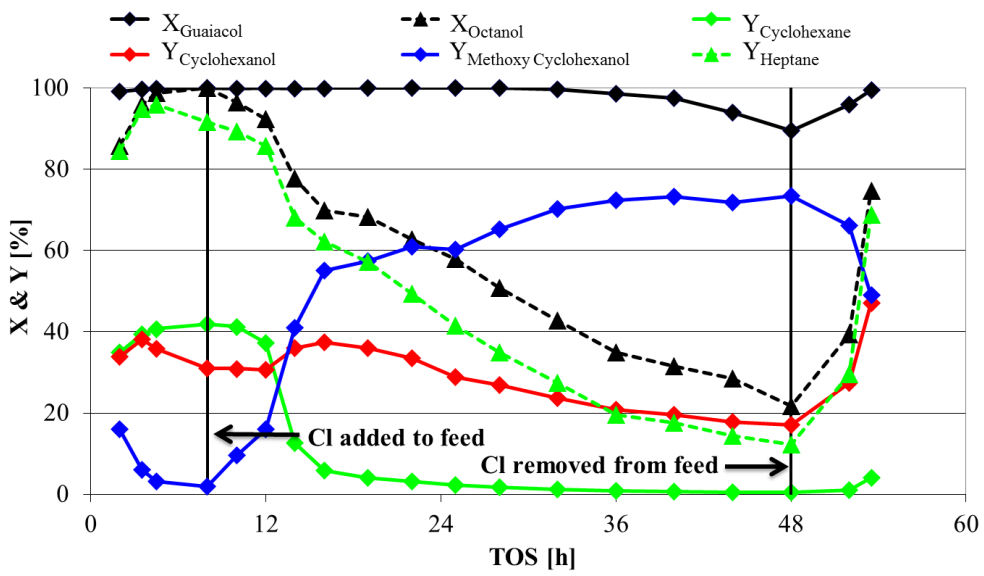

Figure G.4: *Conversion of guaiacol and 1-octanol and yield of heptane, cyclohexane, cyclohexanol, 2-methoxy-cylclohexanol DOD for an un-calcined 5 wt% Ni/ZrO_2 as a function of TOS deactivated by 0.05 wt% chlorine from 8 h to 48 h of TOS. $T = 250$ °C, $P = 100$ bar, $F_{oil} = 0.2$ ml/min, $WHSV = 4.0\ h^{-1}$.*

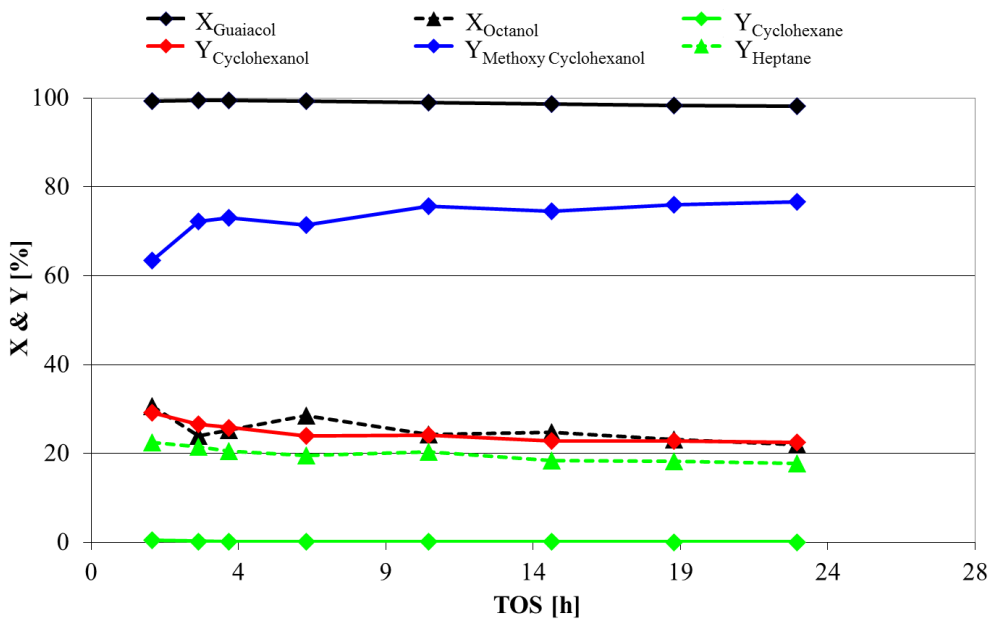

Figure G.5: *Conversion of guaiacol and 1-octanol and yield of heptane, cyclohexane, cyclohexanol, 2-methoxy-cylclohexanol DOD for an un-calcined 5 wt% Ni/ZrO_2 impregnated with KCl as a function of TOS. $T = 250$ °C, $P = 100$ bar, $F_{oil} = 0.2$ ml/min, $WHSV = 4.0\ h^{-1}$.*

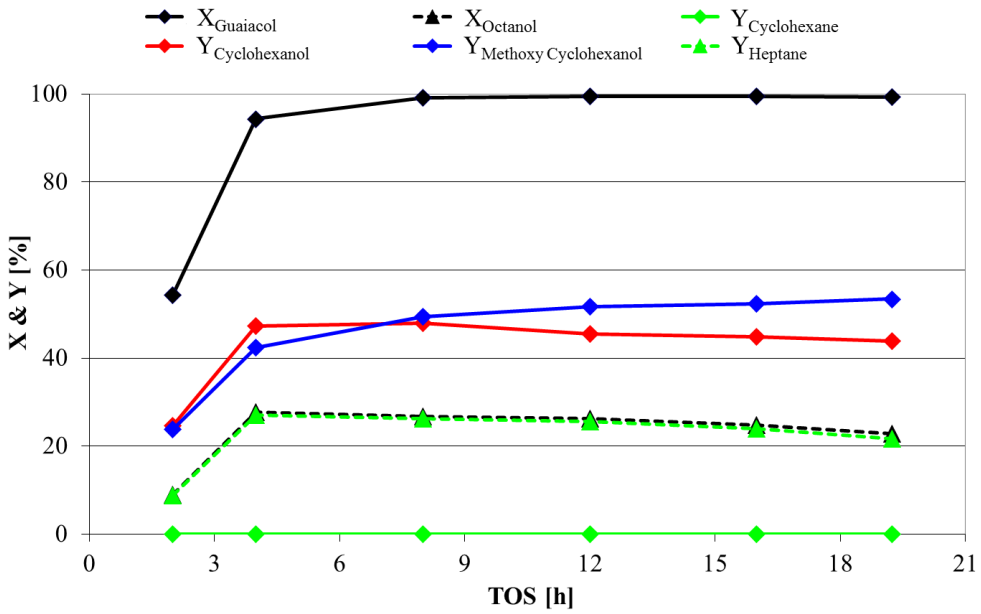

Figure G.6: *Conversion of guaiacol and 1-octanol and yield of heptane, cyclohexane, cyclohexanol, 2-methoxy-cylclohexanol DOD for an un-calcined 5 wt% Ni/ZrO_2 impregnated with KNO_3 as a function of TOS. $T = 250\,°C$, $P = 100$ bar, $F_{oil} = 0.2$ ml/min, $WHSV = 4.0\ h^{-1}$.*

Appendix H

EXAFS of Poisoned Ni/ZrO_2 Catalysts

Table 6.2 is the product of analysis of EXAFS spectra for all poisoned Ni/ZrO_2 catalysts. The detailed data can be found in the following.

Due to the shoulder below 2 Å at the Fourier transformed EXAFS spectra (highlighted in Figure B-H.1(a)), the refinements of carbon, chlorine, KNO_3 and KCl poisoned catalyst were carried out considering one and two shells. The best results were found for the two shells approach. Below all refinements and Fourier Transformed EXAFS spectra are presented.

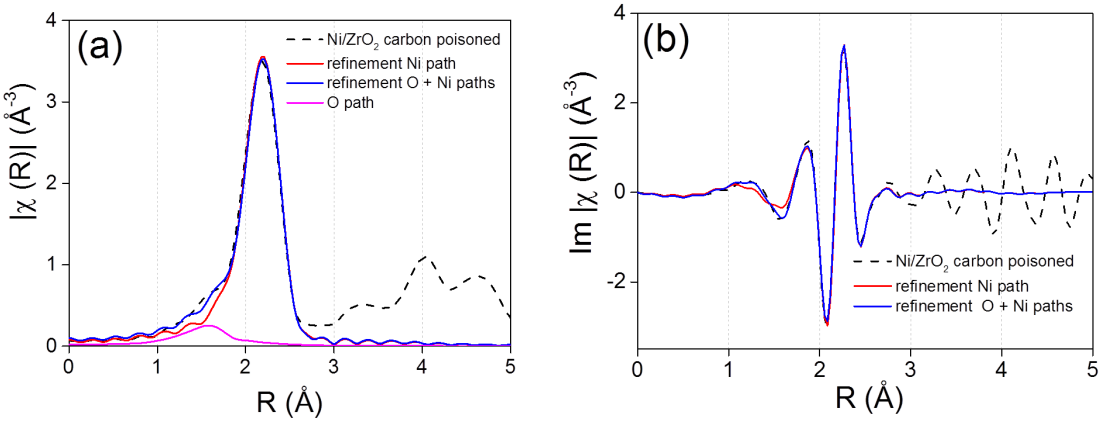

Figure H.1: *Fourier transformed EXAFS spectra of carbon poisoned Ni/ZrO_2 catalysts.*

Table H.1: *Results of the data fits of the Ni-K-edge EXAFS spectra for the carbon poisoned Ni/ZrO_2 catalysts. N is the number of neighboring atoms, r the distance, σ^2 the mean-square disorder in the atomic distances, and ρ the misfitting between the experimental data and the theory. Index f and c respectively indicates fitted and constrained. R-Range: 1.0-3.0 Å, $S_0^2 = 0.78$, 1st model: $\Delta E_0 = 6.6 \pm 0.8$, 2nd: $\Delta E_0 = 5.8 \pm 0.9$*

Sample	Model	Atom	N	r [Å]	$\sigma^2 \cdot 10^{-3}$ [Å^2]	ρ [%]
Carbon	1st	Ni	8.6 ± 0.9^f	2.49 ± 0.01^f	6.2 ± 1.0^f	2.6
	2nd	O	0.8 ± 0.3^f	1.98 ± 0.05^f	$7.1 \pm 0.1^{f\,a}$	0.5
		Ni	8.7 ± 0.9^f	2.48 ± 0.01^f	6.3 ± 1.0^f	

[a]Ni-O σ^2 was constrained and fitted together with $NiCO_3$ reference

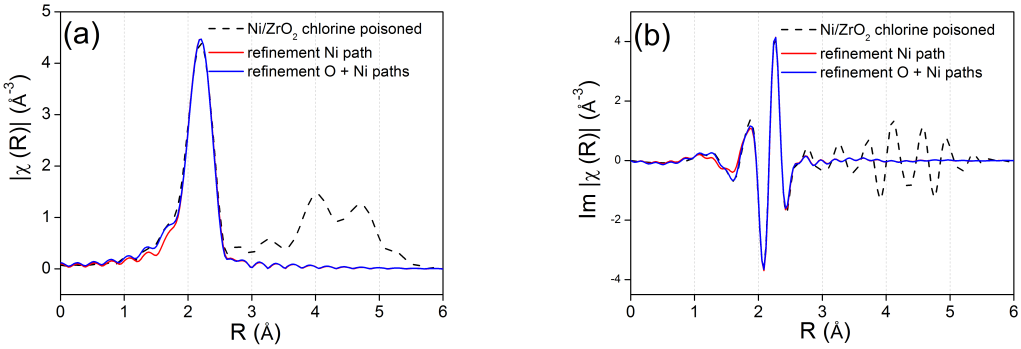

Figure H.2: *Fourier transformed EXAFS spectra of chlorine poisoned Ni/ZrO_2 catalysts.*

Table H.2: *Results of the data fits of the Ni-K-edge EXAFS spectra for the chlorine poisoned Ni/ZrO_2 catalysts. N is the number of neighboring atoms, r the distance, σ^2 the mean-square disorder in the atomic distances, and ρ the misfitting between the experimental data and the theory. Index f and c respectively indicates fitted and constrained. R-Range: 1.0-3.0 Å, $S_0^2 = 0.78$, 1st model: $\Delta E_0 = 7.0 \pm 0.0$, 2nd model: $\Delta E_0 = 6.6 \pm 1.4$*

Sample	Model	Atom	N	r [Å]	$\sigma^2 \cdot 10^{-3}$ [Å^2]	ρ [%]
Chlorine	1st	Ni	8.6 ± 0.8^f	2.49 ± 0.01^f	4.6 ± 1.0^f	1.9
	2nd	O	0.8 ± 0.2^f	2.00 ± 0.04^f	$7.2 \pm 0.1^{f\,a}$	0.9
		Ni	$8.5 \pm 0.6f$	$2.48^b \pm 0.01^f$	4.5 ± 1.0^f	

[a] Ni-O σ^2 was constrained and fitted together with $NiCO_3$ reference
[b] Fitted uncertainty less than 1%

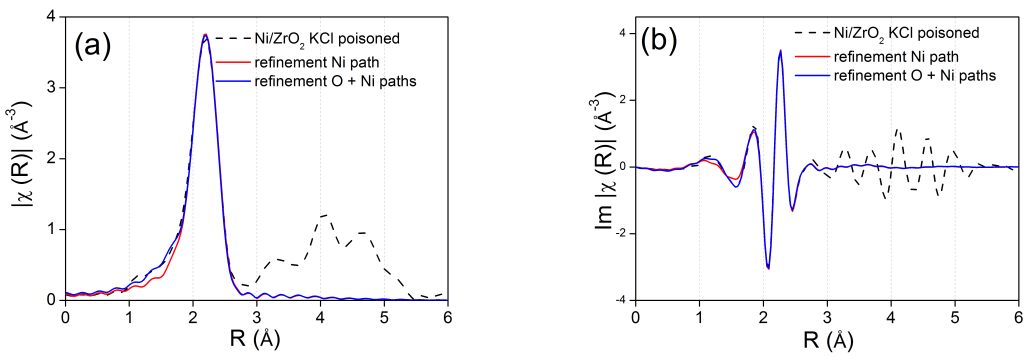

Figure H.3: *Fourier transformed EXAFS spectra of KCl poisoned Ni/ZrO_2 catalysts.*

Table H.3: *Results of the data fits of the Ni-K-edge EXAFS spectra for the KCl poisoned Ni/ZrO_2 catalysts. N is the number of neighboring atoms, r the distance, σ^2 the mean-square disorder in the atomic distances, and ρ the misfitting between the experimental data and the theory. Index f and c respectively indicates fitted and constrained. R-Range: 1.0-3.0 Å, $S_0^2 = 0.78$, 1st model: $\Delta E_0 = 7.1 \pm 0.7$, 2nd model: $\Delta E_0 = 6.7 \pm 0.3$*

Sample	Model	Atom	N	r [Å]	$\sigma^2 \cdot 10^{-3}$ [Å^2]	ρ [%]
KCl	1st	Ni	10.0 ± 0.8^f	2.49 ± 0.01^f	7.0 ± 1.0^f	1.2
	2nd	O	0.6 ± 0.1^f	2.00 ± 0.04^f	7.2 ± 0.1^{fa}	0.9
		Ni	9.9 ± 0.4^f	2.48^{fb}	6.8 ± 0.5^f	

[a]Ni-O σ^2 was constrained and fitted together with $NiCO_3$ reference
[b]Fitted uncertainty less than 1%

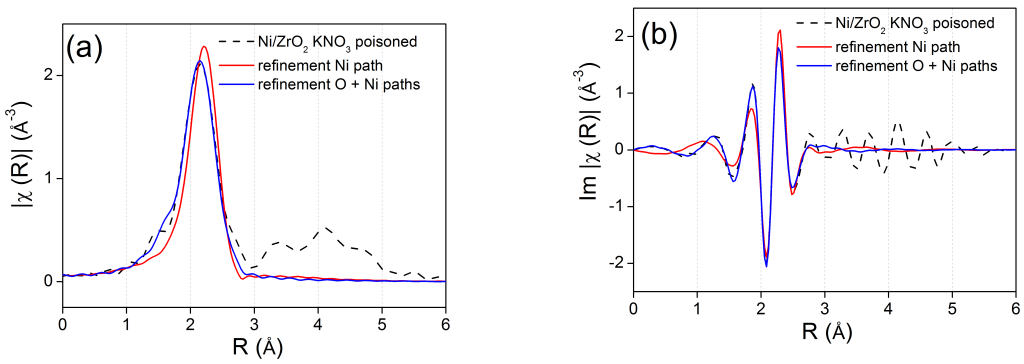

Figure H.4: *Fourier transformed EXAFS spectra of KNO_3 poisoned Ni/ZrO_2 catalysts.*

Table H.4: *Results of the data fits of the Ni-K-edge EXAFS spectra for the KNO_3 poisoned Ni/ZrO_2 catalysts. N is the number of neighboring atoms, r the distance, σ^2 the mean-square disorder in the atomic distances, and ρ the misfitting between the experimental data and the theory. Index f and c respectively indicates fitted and constrained. R-Range: 1.0-3.0 Å, $S_0^2 = 0.78$, 1st model: $\Delta E_0 = 3.3 \pm 2.0$, 2nd model: $\Delta E_0 = 6.6 \pm 1.0$*

Sample	Model	Atom	N	r [Å]	$\sigma^2 \cdot 10^{-3}$ [Å^2]	$C_3 \cdot 10^{-4}$ [Å^3]	ρ [%]
KNO_3	1st	Ni	7.5 ± 1.4^f	2.49 ± 0.01^f	8.5 ± 1.6^f	-	5.4
	2nd	O	1.1 ± 0.3^f	1.96 ± 0.01^f	7.9 ± 4.5^{fa}		1.3
		Ni	8.3 ± 0.9^f	$2.48 \pm 0.01f$	9.2 ± 1.0^f	4.9 ± 1.0^f	

[a]Ni-O σ^2 was constrained and fitted together with $NiCO_3$ reference

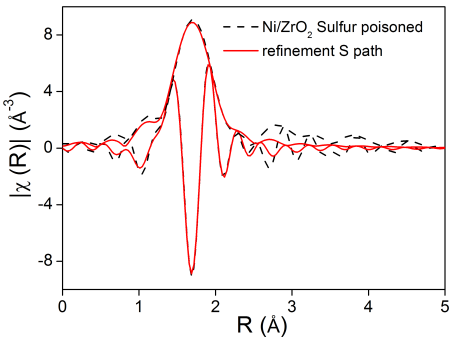

Figure H.5: *Fourier transformed EXAFS spectra of sulfur poisoned Ni/ZrO_2 catalysts.*

Table H.5: *Results of the data fits of the Ni-K-edge EXAFS spectra for the sulfur poisoned Ni/ZrO_2 catalysts. N is the number of neighboring atoms, r the distance, σ^2 the mean-square disorder in the atomic distances, and ρ the misfitting between the experimental data and the theory. Index f and c respectively indicates fitted and constrained. R-Range: 1.11-2.50 Å, $S_0^2 = 0.78$, $\Delta E_0 = -8.4 \pm 0.5$*

Sample	Atom	N	r [Å]	$\sigma^2 \cdot 10^{-3}$ [Å^2]	ρ [%]
Suflur	S	5.0^c	2.22 ± 0.01^f	7.6 ± 0.4^f	2.5

Appendix I

Linear Combination Analysis of XAS Data During Carburization

The references used for the liner combination is an important parameter. In the comparison of the recorded spectra and the bulk references of the relevant phases, a poor match was found, as shown in Figure I.1. Thus, the bulk materials do not represent the phases obtained during the carburization.

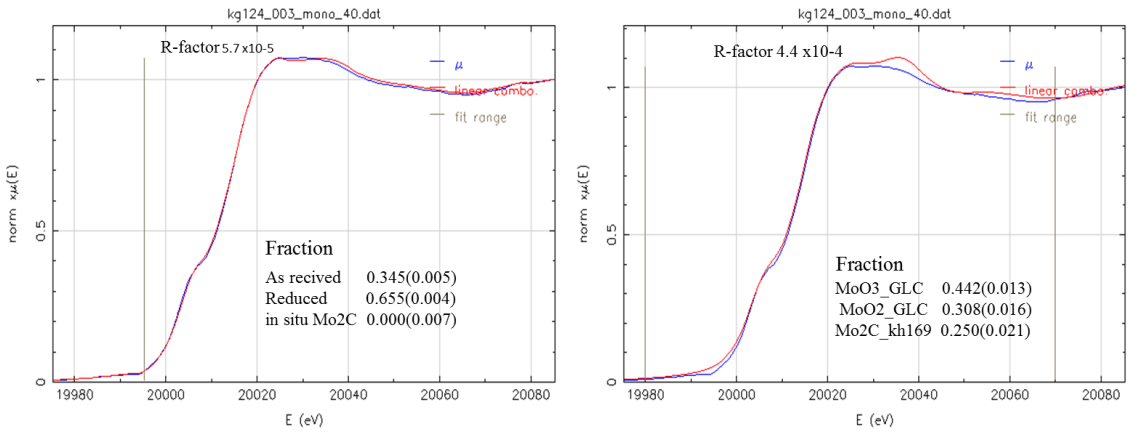

(a) Recroded spectra (b) Bulk reference spectra

Figure I.1: *(a) linear combination using the spectra recorded during the carburization process and (b) linear combination using the reference bulk spectra. The spectra Reduced in (a) was recorded at 411 °C.*

Figure I.2 shows the linear combination results using the bulk compounds as references. Poor consistency was found, especially the decreasing trend of the Mo_2C ratio during the isothermal treatment at 550 °C does not make sense.

Instead the references was handpicked from the analysis. Figure I.3 shows the reference handpicked spectra used for the linear combination analysis. The species called reduced was stable over 40 °C and is most likely related to MoO_2.

The error in the fitting using the "handpicked" references compared to the bulk references was significantly lower, as evidenced by comparing the error bars for the linear combinations with the two references, as shown in Figure I.4. The disagreement

obtained using the handpicked references is lower than the one using bulk references. Thus, the "handpicked"' spectra were used for the linear combination.

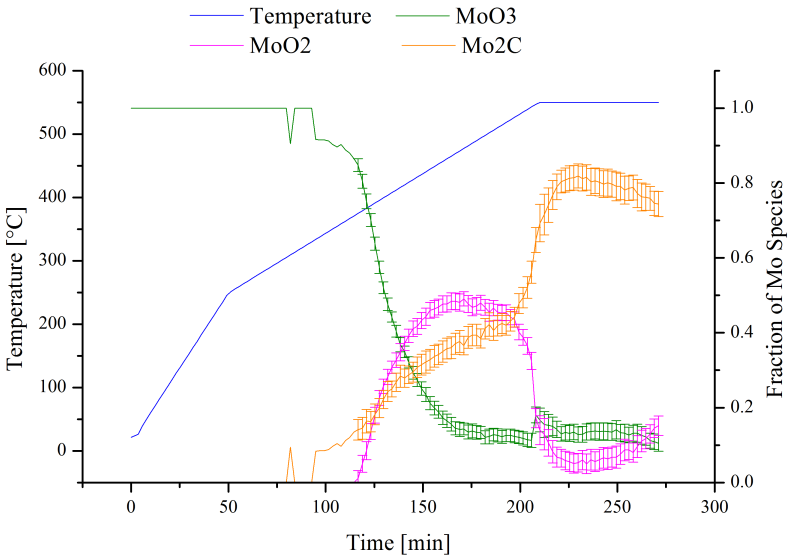

Figure I.2: *Linear combination results using bulk reference compounds.*

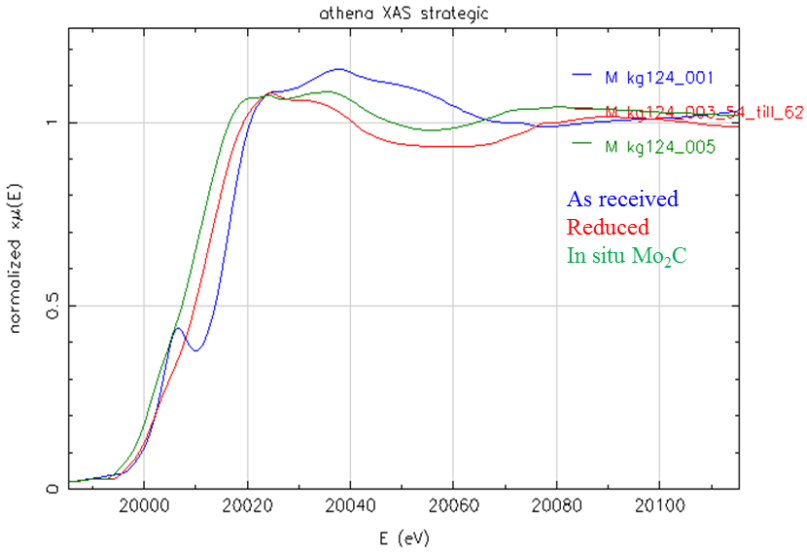

Figure I.3: *References used for the linear combination analysis.*

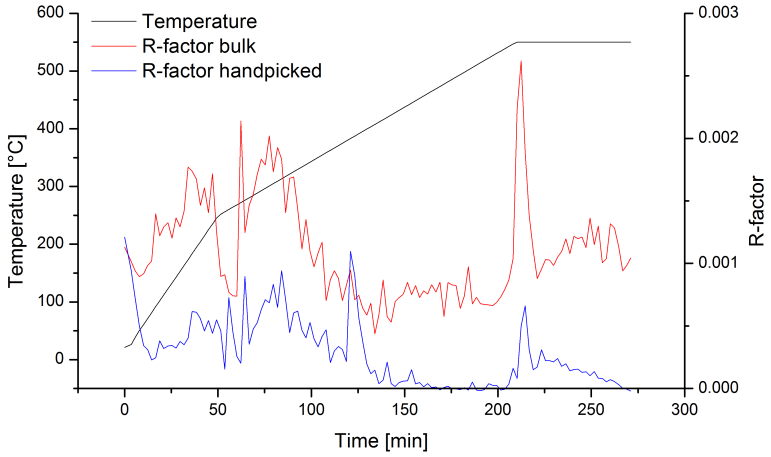

Figure I.4: *R-factor (disagreement) of the linear combinations using bulk and hand-picked references.*

Appendix J

Thermodynamic Data of MoS_2 Oxidation

To evaluate the stability of the bulk part of the MoS_2 phase in the presence of water, thermodynamic calculations were made as presented below.

Table J.1: *Gibbs free energy of the reaction between MoS_2 and water. Data for bulk molybdenum compounds was used in the calculations. Calculations done on the basis of thermodynamic data from Barin [71, 360] and NIST [361].*

#	Reaction	ΔG [kJ/mol]		
	Temperature [°C]	200	300	400
1	$MoS_2(s) + 2\,H_2O(g) \rightleftharpoons MoO_2(s) + 2\,H_2S(g)$	122	120	119
2	$MoS_2(s) + 2\,H_2O(l) \rightleftharpoons MoO_2(s) + 2\,H_2S(g)$	101	81	62
3	$MoS_2(s) + 3\,H_2O(g) \rightleftharpoons MoO_3(s) + 2\,H_2S(g) + H_2(g)$	219	220	220
4	$MoS_2(s) + 3\,H_2O(l) \rightleftharpoons MoO_3(s) + 2\,H_2S(g) + H_2(g)$	188	160	136

Appendix K

Real Bio-oil Tests

To make a final evaluation of the progress in the catalyst and process development work for HDO during the span of this Ph.D. project, a final series of test were made with real bio-oil. Initially it was realized that some modification was needed to the setup presented in Section 3.2 to make it possible to operate with the significantly more complex bio-oil. Specifically the downstream section was modified, implementing the following changes:

- Thermocouple inserted from the bottom of the reactor was removed to avoid the narrow section out of the bottom flange.
- The pipe from the bottom flange to the separator was replaced with a 1/4" pipe with minimum amount of bends. Three-way valve V30 was removed completely.
- The pipe from the reactor to the separator was heat traced at 50 °C.
- The condensator (C1) was bypassed.

Table K.1 summarizes the experiments performed with real bio-oil, including catalyst, loading profile (in accordance with Figure K.2), feed, and operating temperature. In all experiments the bio-oil was diluted in an alcohol. This was done because the used bio-oil was inhomogeneous due to too long storage. Methanol was used as solvent initially, but to give a more consistent flow of the oil, 2-butanol was chosen instead in the later experiments. The bio-oil was made from wood and produced in Canada.

For all experiment, the pressure drop over the reactor (ΔP, difference in PIC7 and PI8, cf. Figure 3.3) increased as a function of TOS. This was used as an indication for the shape of the catalyst bed. Figure K.1 shows ΔP as a function of TOS for all experiments.

In Exp. 1-3, only 2-3.5 h of operation was maintained before ΔP increased sharply. Especially Exp. 1 had a sharp increase from ca. 0.4 bar to >10 bar in less than 20 min. The rapid development in ΔP in Exp. 1 was due to plugging of the initial part of the reactor, prior to the catalyst bed. Thus, it was realized that the reactive zone should have a graduated temperature profile, with catalyst from the liquid inlet to the isothermal zone as shown in Figure K.2.

By having the graduated temperature profile, the HDO reaction was started already at ca. 200 °C at the inlet of the reactor. This should serve to convert some

Table K.1: *Experiments with real bio-oil feed. The Ni/ZrO_2 and $Ni\text{-}MoS_2/ZrO_2$ catalysts are the same as those used in Chapter 6 and 8,respectively. Top and central cat. refers to the loading profile shown in Figure K.2.*

Exp. #	Catalyst	Feed	Central cat. [g]	Top cat. [g]	T [°C]
1[a]	$Ni\text{-}MoS_2/ZrO_2$	50% CH_3OH/50% bio-oil	4	-	300
2[a]	$Ni\text{-}MoS_2/ZrO_2$	50%CH_3OH/50%bio-oil	4	3	260
3[a]	Ni/ZrO_2	50%2-Butanol/50%bio-oil	4	3	175
4	Ni/ZrO_2	50%2-Butanol/50%bio-oil	6	4	260
5	$Ni\text{-}MoS_2/Al_2O_3$[b]	50%2-Butanol/50%bio-oil	6.5[c]	6.5[c]	300

[a]Experiment performed prior to setup modifications.
[b]Catalyst from Haldor Topsøe A/S.
[c]Not diluted in glass beads.

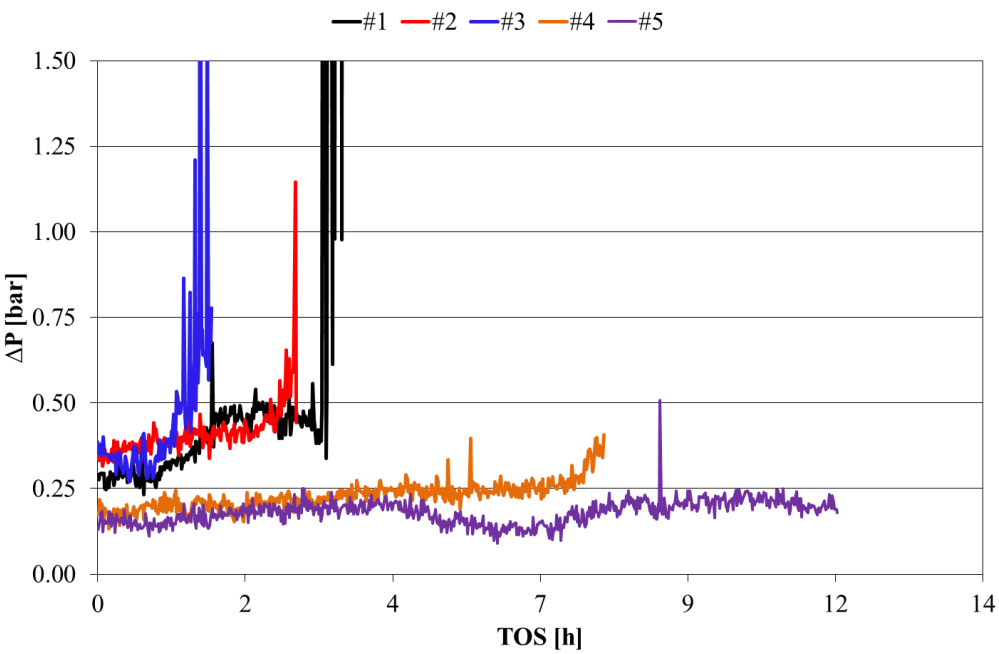

Figure K.1: *Development in ΔP in Exp. 1-5 as a function of TOS.*

of the most reactive compounds to less carbon prone species at an early stage in the reactor.

Exp. 2 and 3 had graduated temperature profiles, but here the temperature was chosen too low, which resulted in a too low activity. Thus, plugging of the reactor took place, because insufficient hydrogenation took place, and the bio-oil was instead left polymerizing on its own (cf. Figure K.1).

From the initial tests, it was realized that the stability of catalyst was dependent on sufficient activity. Additionally, upgrading of the bio-oil required a catalyst able to perform HDO at relative low temperatures, to avoid plugging of the low temperature zone of the reactor. Thus, in Exp. 4 Ni/ZrO_2 was used as catalyst, as this is more

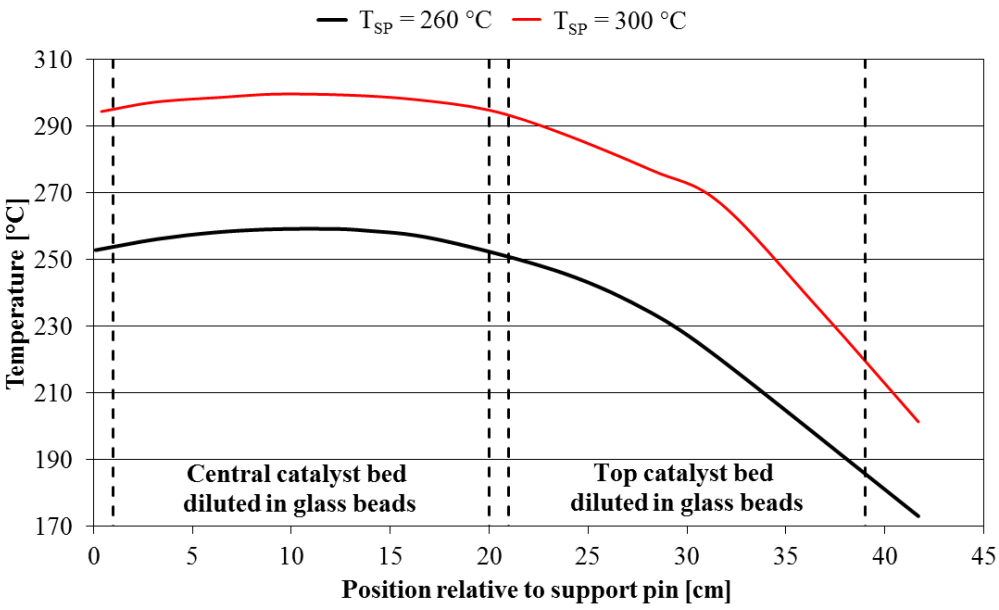

Figure K.2: *Temperature and loading profile of experiments with real bio-oil as feed at oven set points of both 260 and 300 °C. The catalyst was diluted in 212-245 μm glass beads.*

active at low temperatures compared to Ni-MoS_2/ZrO_2 (cf. Chapter 6 and 8), and the loading was increased. In this way much longer TOS was achieved, with the pressure drop remaining stable for >8 h of operation (cf. Figure K.1). However, looking at the gas product, as an online indicator of the activity, the formation of methane decreased as a function of TOS, from a maximum of 1.4 mol% to 0.25 mol% after 8.5 h of operation, as shown in Figure K.3. Despite a slow increase in the CO_2 in the gas product, the total carbon in the product gas decreased during the experiment. This indicates that the activity of the catalyst decreased as a function of TOS. Thus, it is indicated that the catalyst bed plugs after severe deactivation of the catalyst. Similar to Exp. 2 and 3, this resulted in plugging of the reactor as the bio-oil no longer was hydrogenated, but left for polymerizing reactions with itself.

Looking at the spent catalyst in the reactor after Exp. 4 by cutting it open lengthwise showed that carbon formation had occurred along the entire catalytic bed. No carbon plugs could be found but rather a general particle agglomeration. Thus, it appears that the graduated temperature profile serves to at least disperse the carbon formation in the catalytic zone.

Realizing that maintaining sufficient activity was essential in avoiding plugging of the reactor, the commercial Ni-MoS_2/Al_2O_3 from Haldor Topsøe A/S was used in Exp. 5 where the entire reactor was loaded with pre-sulphided catalyst. In this experiment (in contrast to the other) a production of a separate oil phase product was achieved. Figure K.4 shows the appearance of the oil phase as a function of TOS. The initial oil product, was a clear free flowing liquid, but as a function of TOS a more distinct yellow/brown tint was visible in the oil product.

Analyzing the oil-product by CHN-S elemental analysis, revealed that the oxygen content was practically zero in the initial liquid product, but this slowly increased during the experiment and ended in the order of 17 wt% (cf. Table K.2).

Table K.2: *Elemental composition of oil product from Exp. 5. Catalyst: Commercial Ni-MoS_2/Al_2O_3, T = 300 °C, P = 100 bar, F_{oil} = 0.2 ml/min, $WHSV_{total}$ = 0.9 h^{-1}.*

TOS [h]	C [wt%]	H [wt%]	O [wt%]	DOD [wt%]	H/C [mol/mol]
Feed	38	8	54	-	-
4-6	85	15	0	100	2.1
6-8	80	14	6	90	2.1
8-10	80	13	6	88	2.0
10-12	72	11	17	69	1.9

The H/C ratio in the produced oil was 2.1 in the first oil sample, which is equivalent to the desired value from crude oil (cf. Table 2.7). This value, however, slowly

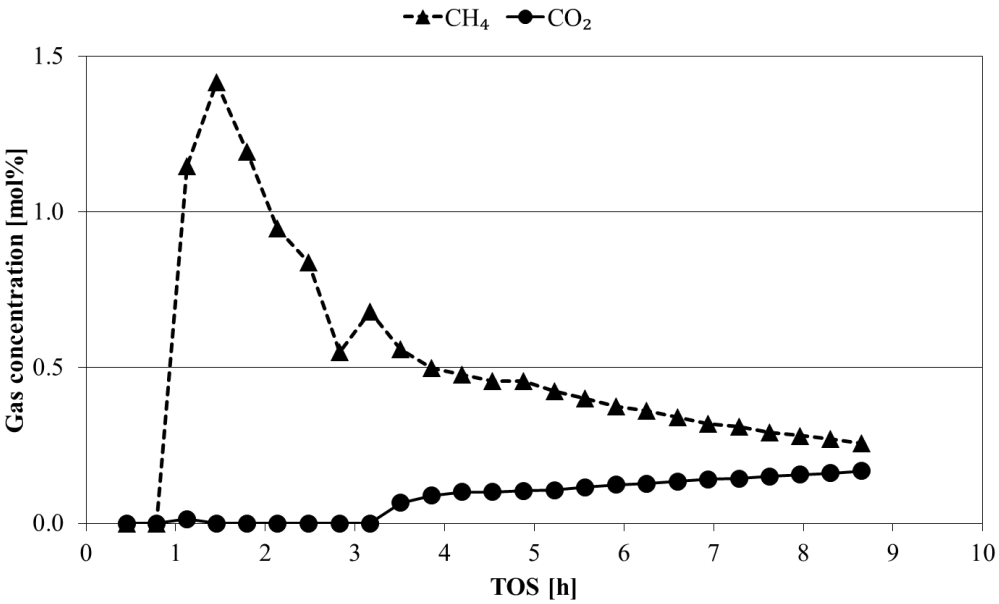

Figure K.3: *Development in gas concentration during HDO of 50% bio-oil in 2-butanol over a Ni/ZrO_2 catalyst. T = 260 °C, P = 100 bar, F_{oil} = 0.2 ml/min, $WHSV_{total}$ = 1.2 h^{-1}.*

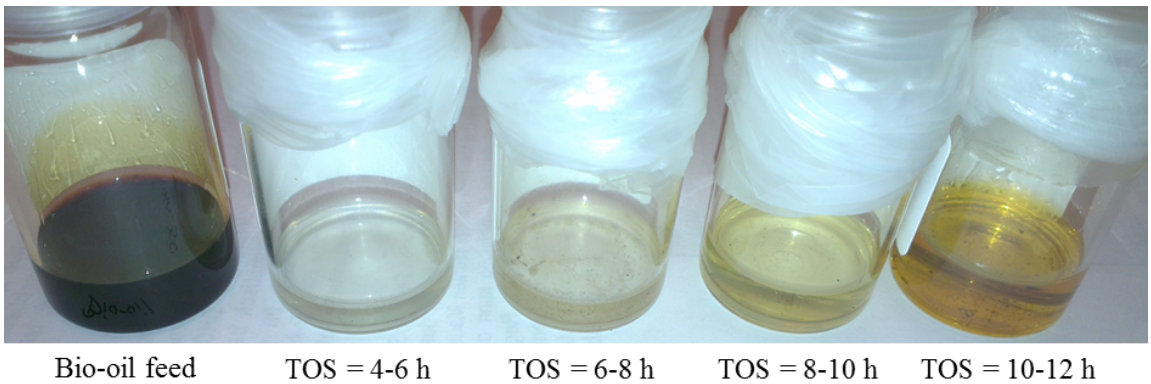

Figure K.4: *Oil product from HDO of 50% bio-oil in 2-butanol over a commercial Ni-MoS_2/Al_2O_3 catalyst, as a function of TOS. T = 300 °C, P = 100 bar, F_{oil} = 0.2 ml/min, $WHSV_{total}$ = 0.9 h^{-1}.*

decreased as the catalyst lost activity and ended at 1.9 after 12 h of operation.

Further analyzing the oil product at TOS 4-6 h with GC-MS showed that the product was primarily composed of naphtenes (in the order of 65%) and linear/branched hydrocarbons (in the order of 25%). Among major compounds identified were methyl, ethyl, or propyl substituted cyclohexane (∼20%), methyl substituted hexane (∼5%), and methyl and ethyl substituted cyclopentane (∼5%).

The DOD in Table K.2 and the color of the liquid samples in Figure K.4 reveal that the activity of the catalyst decreased during the experiment. The exact source of deactivation was not identified and is left for future work. However, a potential source for deactivation can be lack of sulfur, as this was not present in the feed, and (as found in Section 8.2) this results in slow deactivation of the catalyst by transformation of MoS_2 to MoO_2.

Commonly, experiment 1-5 show that finding stable catalysts is a crucial and apparent task for HDO. It is possible to upgrade bio-oil to fuel grade standard (cf. Table K.2), however, deactivation is fast. Which deactivation mechanism is the primary cannot be deduced from the current analysis, but probably a combination of several are occurring. The experiments also highlight that the catalysts developed in the current project (Ni/ZrO_2 and $Ni\text{-}MoS_2/ZrO_2$) probably have insufficient activity, as the oil product only was obtained with the commercial $Ni\text{-}MoS_2/Al_2O_3$ (experimental conditions are however not similar in the comparison). Thus, it is indicated that a lot can be gained by directing effort in developing a single catalytic system, like optimizing loading, application of additives, etc. This is left for future work to address.

Appendix L

Supporting Documents

Besides this dissertation a series of documents have been written or in other ways procured during this Ph.D. Below some of the most important documents are summarized and also were they can be found (at the time of writting). Additionally, many manuals for the POC unit can be found in the POC file folder in CHEC department share folder: "K:\Chec Laboratories\setups\045-28 POC Pyrolysis Oil Converter (ant)\06 Literature".

Title:	Pyrolysis Oil Converter: High Pressure Liquid and Gas Flow Reactor System
Authors:	Peter Mølgaard Mortensen, Rasmus Trane-Restrup, and Anders Tiedje
Year:	2013
Digital Copy:	In the case file folder in CHEC department share folder: K:\Chec Laboratories\setups\045-28 POC Pyrolysis Oil Converter (ant)\02 Instructions\POC documentation
Physical Copy:	A physical copy is placed at the setup
Description:	Detailed description of the POC setup

Title:	Valorization of Biomass to Chemicals and Fuels: Input to DONG Roadmap
Authors:	Peter Mølgaard Mortensen and Anker Degn Jensen
Year:	2012
Digital Copy:	Anker Degn Jensen is assigned as corresponding author
Description:	Input for DONG roadmap made in spring 2012 to highlight prospective chemical engineering routes to bio-chemicals

Title:	Affald fra Marken bliver CO_2-neutrale Brændstoffer
Authors:	Peter Mølgaard Mortensen and Rasmus Trane
Book title	Energi på Lager
Chapter	4: Affald på Tanken
Year:	2011
Digital Copy:	Available at:

	www.energi.case.dtu.dk/Biomasse/Laer-mere_kap4
Description:	Popular scientific description on utilization of bio-oil, as an addition to a Danish municipal primary and lower secondary school book

Title:	GC-2014 Instruction Manual
Author:	Jörn Hannum
Year:	2011
Digital Copy:	In the case file folder in CHEC department share folder: K:\Chec Laboratories\setups\045-28 POC Pyrolysis Oil Converter (ant)\02 Instructions
Physical Copy:	A physical copy is placed at the setup
Description:	Description of the GC-TCD dedicated to the POC setup

Title:	Operating Instruction Manual for 4560 Mini Bench Top Reactors
Author:	Parr Instrument Company
Year:	2008
Digital Copy:	In the case file folder in CHEC department share folder: K:\Chec Laboratories\setups\037-03 Batch reactors (ant)\037-03 High Pressure Batch Reactor 1 Parr 4566 (small) (ant)\02 Instructions
Physical Copy:	A physical copy is placed at the setup
Description:	Description of the batch reactor from Parr

Title:	GAS Chromaograph-Mass Spectrometer: GCMS-QP2010 System Package
Author:	Shimadzu
Physical Copy:	A physical copy is placed at the setup
Description:	Description of the GC-MS from Shimadzu

Title:	EuroEA 3000-single: Instruction Manual (v.3.0. Single-2007)
Author:	EuroVector SpA
Physical Copy:	A physical copy is placed at the setup
Description:	Description of the CHN-S elemental analyzer from EuroVector